UNIVERSITÀ
DEGLI STUDI
DI PADOVA

Sede Amministrativa: Università degli Studi di Padova

Dipartimento di Ingegneria Industriale

SCUOLA DI DOTTORATO DI RICERCA IN: INGEGNERIA INDUSTRIALE
INDIRIZZO: INGEGNERIA DELL'ENERGIA
CICLO XXVI

EXPERIMENTAL AND NUMERICAL ANALYSIS OF MICROSTRUCTURED SURFACES

Direttore della Scuola: Ch.mo Prof. Paolo Colombo
Coordinatore d'indirizzo: Ch.mo Prof. Luisa Rossetto
Supervisore: Ch.mo Prof. Luisa Rossetto

Dottorando: Andrea Diani

Contents

Abstract

Heat dissipation is one of the most important issues for the reliability of electronics equipment. Up today, air represents the most safe, cheap, and common working fluid for electronics thermal management applications. Due to its poor heat transfer characteristics, air always flow through enhanced surfaces, such as plain and louvered fins, pin fins, offset strip fins and wire screens, in order to increase the heat transfer area and to create turbulence. Recently, metal foams have been proposed as promising enhanced surfaces to improve the overall heat transfer performance of the cooling system.

In several applications air might be not enough for high level of heat dissipation, thus two-phase systems can represent a viable solution. Boiling is the heat transfer mechanism with the highest heat transfer coefficients, thus it can be used to spread high heat fluxes to maintain the wall temperature at low values with compact heat sinks. Microstructured surfaces, such as metal foams and microfin tubes, can exploit positive benefits on the flow boiling mechanism, i.e. they can promote bubble nucleation, reduce onset of nucleate boiling, augment two-phase mixing, enhance critical heat flux. On the other hand, the environmental issues associated to the use of synthetic refrigerants call for a continuous improvement of the technical solutions. Recently, new low-GWP refrigerants, in particular R1234ze(E) and R1234yf, have been proposed as possible alternatives of the traditional R134a.

This PhD thesis explores the use of microstructured surfaces for thermal management applications. Metal foams, plain finned and pin finned surfaces are experimentally and numerically investigated during air forced convection. In addition, single- and two-phase flow (vaporization) of refrigerants through a copper foam and in a microfin tube is experimentally studied.

The first chapter is focused on the air forced convection through metal foams.

Nine copper foams are experimentally tested, and the overall heat transfer coefficients and pressure drops are calculated from the experimental measurements. The effects of the geometrical parameters (foam core height, pore density, and porosity) on the thermal and hydraulic behaviour of such materials are discussed. The experimental data points, coupled with other measurements previously obtained on aluminum foams, have permitted the development of a new semi-empirical equation for the estimation of the foam finned surface efficiency and of the heat transfer coefficient.

The air forced convection through plain finned and pin fin surfaces is discussed in the second chapter. Numerical simulations are performed on different geometrical configurations of fin thickness, pitch, and height for the plain finned surfaces, and different configurations of pin diameter, longitudinal and transverse pin pitch, and pin height for the pin fin surfaces. The effects of the geometrical characteristics on the thermal and hydraulic behaviour are reported. From the numerical results, four correlations have been developed for the estimation of the Colburn j-factor and friction factor for plain finned and pin fin surfaces. In the end, an optimization of a plain finned surface is reported.

The third chapter proposes a numerical approach to study the air forced convection through metal foams. The real structure of four copper foams, whose experimental results are reported in the first chapter, is obtained by micro-computed tomography scanned images. Once reconstructed, the real foams are meshed and the air flow simulated with a commercial software. Numerical results of pressure drop and heat transfer coefficient are compared against the experimental values.

The design and development of a new experimental facility to study the phenomenon of the flow boiling inside microstructured surfaces is reported in the fourth chapter. The numerical design of the test section, which hosts a 200 mm long metal foam, is presented. Every component of the set up is discussed in details. The results of the calibration tests are reported.

The flow boiling of refrigerants inside a metal foam is shown in the fifth chapter. The tested copper foam is 200 mm long, 10 mm wide, and 5 mm high. Three different refrigerants are studied: R134a, R1234ze(E), and R1234yf. R1234ze(E) and R1234yf (GWP=6 and 4, respectively) are possible substitutes of R134a (GWP=1400). Tests are run at a saturation temperature of 30 °C, which can be considered suitable for

the case of electronic cooling applications, at different working conditions, in order to highlight the effects of the vapour quality, mass velocity, and heat flux on the thermal and hydraulic performance.

Finally, the sixth chapter reports some results about the flow boiling of refrigerants inside a 3.4 ID microfin tube. Three different refrigerants are studied: R134a, R1234ze(E), and R1234yf. As for the case of flow boiling inside a metal foam, tests are run at a saturation temperature of 30 °C under different working conditions, i.e. different vapour quality, mass velocity, and heat flux. The experimental results of heat transfer coefficient, vapour quality at the onset of the dryout, and pressure drop are compared against values predicted by correlations from the open literature.

Sommario

Lo smaltimento di calore è uno degli aspetti più importanti per l'affidibilità di componenti elettronici. Ad oggi, l'aria è il più sicuro, economico e utilizzato fluido operativo in applicazioni di raffreddamento di componentistica elettronica. A causa delle sue scarse qualità di scambio termico, l'aria fluisce attraverso superficie estese, come alette piane, cilindriche e louvered, "offset strip fins" e "wire screens", per aumentare la superficie di scambio termico e per creare turbolenza. Recentemente, le schiume metalliche sono state proposte come promettenti superfici estese per incrementare le prestazioni termiche del sistema di raffreddamento.

Tuttavia, l'aria potrebbe non essere sufficiente nel caso in cui i flussi termici da asportare siano particolarmente alti e pertanto i sistemi bifase possono essere una soluzione attuabile. La vaporizzazione è il meccanismo di scambio termico con i maggiori coefficienti di scambio termico, pertanto può essere usato per dissipare elevati flussi termici e mantenere la temperatura di parete del dissipatore entro limiti che siano compatibili con quelli delle apparecchiature elettroniche. Superfici microstrutturate, come schiume metalliche e tubi microalettati, possono avere benefici nella vaporizzazione, cioè possono incrementare i siti di nucleazione delle bolle, anticipare l'ebollizione nucleata, aumentare il miscelamento tra la fase liquida e vapore, aumentare il flusso termico critico. Importanti sono anche gli aspetti ambientali associati a refrigeranti sintetici, situazione che richiede un miglioramento delle soluzioni tecniche attualmente impiegate. Recentemente, nuovi refrigeranti a basso impatto ambientale, in particolare l'R1234ze(E) e l'R1234yf, sono stati proposti come alternative al tradizionale R134a.

Questa tesi di dottorato esplora l'uso di superfici microstrutturate in sistemi di raffreddamento. Sono state studiate sperimentalmente e numericamente schiume metalliche, alette piane e cilindriche durante la convezione forzata di aria. Inoltre,

è stato sperimentalmente studiato il deflusso monofase e bifase (vaporizzazione) di refrigeranti in una schiuma metallica in rame e all'interno di un tubo microalettato.

Il primo capitolo si focalizza sulla convezione forzata di aria attraverso schiume metalliche. Nove schiume in rame sono sperimentalmente studiate e dalle misure sperimentali vengono calcolati i coefficienti globali di scambio termico e le perdite di carico. Vengono discussi gli effetti dei parametri geometrici (altezza della schiuma, densità di pori e porosità) sul comportamento termico e idraulico di tali materiali. I punti sperimentali raccolti, insieme ad altre misure sperimentali precedentemente ottenute su schiume in alluminio, hanno permesso lo sviluppo di una correlazione per la stima dell'efficienza e del coefficiente di scambio termico.

La convezione forzata di aria attraverso alette piane e cilindriche è discussa nel secondo capitolo. Sono state condotte simulazioni numeriche su differenti configurazioni geometriche di spessore, passo e altezze delle alette nel caso di alette piane, e di diametro, passo longitudinale e trasversale e altezza nel caso di alette cilindriche. Vengono riportati gli effetti delle caratteristiche geometriche sul comportamento termico e idraulico. Dai risultati numerici, sono state sviluppate quattro correlazioni per la stima del fattore j di Colburn e del fattore f di attrito per alette piane e cilindriche. Infine, è riportato un esempio di ottimizzazione di una superficie con alette piane.

Il terzo capitolo propone un approccio numerico alla modellizzazione della convezione forzata di aria in schiume metalliche. La reale struttura di quattro schiume in rame, i cui risultati sperimentali sono riportati nel primo capitolo, è ottenuta mediante immagini ottenute con la tecnica della microtomografia. Il deflusso di aria è quindi simulato con un software commerciale. I risultati numerici relativi alle perdite di carico e ai coefficienti di scambio termico sono quindi confrontati con i risultati sperimentali.

Il dimensionamento e lo sviluppo di un nuovo impianto sperimentale per lo studio del fenomeno della vaporizzazione in superfici microstrutturate è riportato nel quarto capitolo. Viene presentato lo sviluppo mediante un codice numerico della sezione di prove, che alloggerà una schiuma metallica lunga 200 mm. Ogni componente dell'impianto è discusso in dettaglio. Infine vengono riportati i risultati della calibrazione dell'impianto.

I risultati relativi alla vaporizzazione di refrigeranti all'interno di una schiuma

metallica sono presentati nel quinto capitolo. La schiuma metallica in rame è lunga 200 mm, larga 10 mm e alta 5 mm. Tre diversi refrigeranti sono studiati: R134a, R1234ze(E), and R1234yf. L'R1234ze(E) e l'R1234yf (GWP=6 e 4, rispettivamente) sono possibili sostituti dell'R134a (GWP=1400). Le prove sperimentali sono state condotte ad una temperatura di saturazione di 30 °C, che è un valore idoneo al caso di raffreddamento di componenti elettronici, in diverse condizioni operative, al fine di evidenziare gli effetti del titolo di vapore, della portata specifica e del flusso termico sulle performance termiche ed idrauliche.

Nel sesto ed ultimo capitolo vengono riportati alcuni risultati sulla vaporizzazione di refrigeranti all'interno di tubo microalettato avente un diametro interno di 3.4 mm. Tre diversi refrigeranti sono studiati: R134a, R1234ze(E), and R1234yf. Come nel caso precedente, le prove sono state condotte ad una temperatura di saturazione di 30 °C in diverse condizioni operative, cioè a diverso titolo di vapore, portata specifica e flusso termico. I risultati sperimentali del coefficiente di scambio termico, del titolo di vapore all'inizio della crisi termica e delle perdite di carico sono confrontati con i valori stimati da alcune correlazioni empiriche proposte in letteratura.

Chapter 1

Experimental analysis of the air forced convection through metal foams

1.1 Introduction

A cellular solid is one made up of an interconnected network of solid struts or plates which form the edges and faces of cells. Three typical structures exist. The simplest is a two-dimensional array of polygons which pack to fill a plane area like the hexagonal cells of the bee, and for this reason these materials are called *honeycombs*. More commonly, the cells are polyhedra which pack in the three dimensions to fill space: these materials are called *foams*. If the solid of which the foam is made is contained in the cell edges only (so that the cells are connected through open faces), the foam is said to be open-celled. If the faces are solid too, so that each cell is sealed off from its neighbors, it is said to be closed-celled; and, of course, some foams are partly open and partly closed.

Almost any material can be foamed [1]. Polymers, of course, are the most common. But also metals can be fabricated into cells. Metallic foams can be made using either liquid or solid state processing, as suggested by Shapalov [2] and by Davies and Zhen [3]. Powdered metal and powdered titanium hydride or zirconium hydride can be mixed, compacted and then heated to the melting point of the metal to evolve

hydrogen as a gas and form the foam. Liquid metals can also be infiltrated around granules which are then removed: for instance, carbon beads can be burned off or salt granules can be leached out. Metals can be coated onto an open-cell polymer foam substrate using electroless deposition, electrochemical deposition or chemical vapor deposition. Metal foams can also be made by a eutectic transformation: the metal is melted in an atmosphere of hydrogen and then cooled through the eutectic point, yielding the gas as a separate phase within the metal. Solid state processes usually use powder metallurgy. In the powder sintering method, the powdered material is mixed with a spacing agent which decomposes or evaporates during sintering. Alternatively, a slurry of metal powder mixed with a foaming agent in an organic vehicle can be mechanically agitated to form a foam which is then heated to give the porous metal. Metal foams can also be formed by coating an organic sponge with a slurry of powdered materials, drying the slurry and firing to remove the organic sponge. In another solution, single crystal silicon can be made porous by anodization: a silicon wafer is immersed in a solution of hydrofluoric acid, ethanol and water and subjected to a current for a brief time. The anodizing process tunnels, giving an interconnected network of pores with cell size of 10 nm and a relative density as low as 0.1; yet the material remains a single crystal.

Metal foams can also be fabricated without directly foaming the metal. For this technique a polymer foam is used as a starting point. The polymer foam is processed into a structure with open pores by manipulating the foaming process or by a subsequent reticulation treatment. The resulting foam is then filled with a slurry of heat resistant material, e.g. a mixture of mullite, phenolic resin and calcium carbonate. After drying the polymer is removed and molten metal is cast into the resulting open voids which exactly represent the original foam structure. After removal of the mould material (e.g. by water under high pressure) a metallic foam is obtained which is an exact image of the original polymer foam. The foams under investigation in this thesis work are made by ERG Material and Aerospace [4], and they are made with this last technique. This kind of metal foams are called DUOCEL foams. Duocel foams can be specified by defining two independent characteristics.

Pore size

Each bubble structure in the open-celled foam generally consists of 14 reticulated windows or facets. The polygonal opening through each open window is referred to as a ”pore” (see figure 1.1). In any given bubble, the polygonal pores actually are of two or three different characteristic sizes and shapes, but for material designation purposes, they are simplified to an average size and circular shape. The number of these pores that would subtend one inch designates the foam ”pore size”. Duocel metal foams are generally manufactured from 5 to 40 pores per inch, while Duocel carbon and ceramic foams are manufactured from 5 to 100 pores per inch. An average pore diameter is about 50% to 70% the diameter of its parent bubble, thus a 10 pore per inch (PPI) foam would have roughly 5 to 7 bubbles per inch.

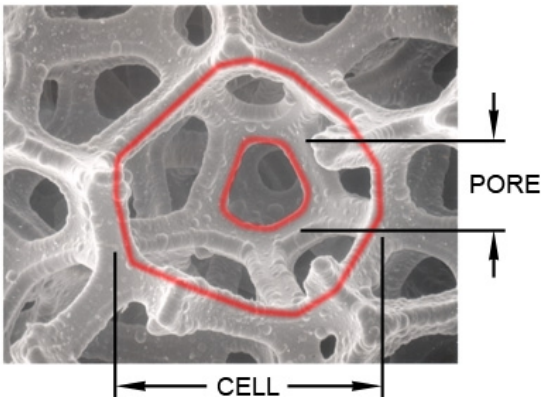

Figure 1.1: Cells and pores in a Duocel foam.

Foam pore size defines how finely the raw material of a foam is divided. The bubble and strut structural shape is always constant, but a 5 pore per inch (PPI) will visually appear more open than a 40 or 100 PPI foam. Accordingly, the foam pore size directly affects nominal ligament length and cross section size, and pore diameter. In turn, these micro-structural features influence specific surface area, fluid flow resistance, and electromagnetic transmission or absorption.

Relative density

Relative density is the density of a foam divided by the density of the solid parent material of the struts. In other words, it is the mass of real material in a block of

foam compared to what it would be if it were a solid block of the same material. Typical relative densities for Duocel foams run from about 2% to 15% depending on the material being foamed and the application. Due to the physics of small-scale structures, the majority of Duocel foams are manufactured in the 3-10% density range. It should be noted that this characteristic has also been historically defined as "mass density", "void volume", "porosity", "solid fraction", and a number of other terms depending on the author and industry. "Relative density" is currently the standard designation for this dimensionless characteristic as it is a more accurate and unambiguous description, and it correlates directly with the affected material properties to be discussed below. Relative density is denoted by $\frac{\rho^*}{\rho_s}$, where ρ^* indicates the density of the foam, and ρ_s the density of the foamed material.

Figure 1.2: Ligament cross section.

While pore size controls the number and nominal size of the foam ligaments, the relative density controls the ligament cross-section shape and actual size, as showed in figure 1.2. Since foams can be compared to miniature three-dimensional truss structures, it is apparent that the cross section and moment of inertia of the struts or ligaments is a primary driver of foam mechanical properties like stiffness, rush strength, electrical conductivity, and thermal conductivity.

1.2 State of the art

Metal foams have interesting characteristics, such as a high heat transfer area per unit of volume, good stiffness and strength, enhanced flow mixing capabilities, which makes them suitable for applications in cryogenics, combustion chambers, cladding on buildings, strain isolation, buffer between a stiff structure and a fluctuating

temperature field, geothermal operations, petroleum reservoirs, compact heat exchangers for airborne equipment, air cooled condensers, and heat sinks for power electronics.

In the past decades, several different research groups have studied both experimentally and analytically the heat transfer and fluid flow through metal foams. Calmidi and Mahajan [5] studied the air forced convection in high porosity ($\varepsilon = 0.89 - 0.87$) aluminum metal foams, with PPI ranging from 5 to 40, and with air as fluid medium. They obtained Nusselt numbers as a function of the pore Reynolds number. In the numerical part, they considered a semi-empirical volume-averaged form of the governing equation, obtaining the velocity profiles and the interstitial heat transfer coefficients. Agreement was achieved between experimental and numerical results.

Hisieh et al. [6] investigated the effect of porosity, pore density, and air velocity on the heat transfer characteristics of aluminum-foam heat sink. They performed experiments on foams having 10 to 40 PPI, and a porosity from 0.87 to 0.96. They found that both the porosity and the pore density affect the cooling performance of aluminum-foam heat sinks: the Nusselt number increases with the increase of the porosity and of the pore density.

Kim et al. [7] experimentally studied the impact of the presence of an aluminum foam on the flow and convective heat transfer in an asymmetrically heated channel. The aluminum foams tested had the same porosity (0.92), but different number of pores per linear inch (10, 20, and 40). These foams were placed inside a channel, in which the upper wall was maintained at a constant temperature, while the lower wall was thermally isolated. Results indicated that the friction factor is much lower at lower PPI, while significant enhancement in the Nusselt number is obtained.

Hwang et al. [8] examined the combined effects of foams porosity (ε=0.70, 0.80, and 0.95) and of flow Reynolds number (Re=1900-7800), on the hydraulic and thermal performance of aluminum foams. Results showed that both the friction factor and the volumetric heat transfer coefficient increase with decreasing the foam porosity at constant Reynolds number. In addition, the aluminum foam with a porosity of 0.80 has the best thermal performance under the same pumping power constraint among the considered foams. They also proposed empirical correlations for pore Nusselt number in terms of pore Reynolds number under various porosities.

Dukhan et al. [9] investigated the pressure drop of air flowing though nine compressed and uncompressed aluminum foams, having different porosities (0.679 - 0.924) and pore densities (10, 20, and 40 PPI). The pressure drop was found to have a quadratic dependence on velocity, following the Forchheimer equation, and was significantly higher for the compressed foams.

Mancin et al. [10, 11] carried out experimental measurements on heat transfer and pressure drop during air flow through metal foams. A total amount of 7 aluminum foams were tested: these samples permitted to highlight the effects of the number of pores per linear inch, porosity and foam core height on the hydraulic and thermal behavior of such materials. The experimental measurements also permitted to develop two semi-empirical models for the estimation of the overall heat transfer coefficient and of the pressure drop.

Aluminum foams are the most studied metal foams, however other materials can also be foamed. Giani et al. [12] characterized foam samples made of FeCrAlloy and copper with 10 and 20 PPI by performing non-steady state cooling measurements. Heat transfer experiments were run on each foam sample for eight different flow velocities, and the heat transfer coefficient was calculated.

Zhang et al. [13] experimentally investigated the fluid flow and heat transfer of liquid cooled foam heat sinks. Eight copper foams with 60 and 100 PPI and four porosities from 0.6 to 0.9 were bonded onto copper base plates. For the four 60 PPI foams, the one with the lowest porosity of 0.6 is found to possess the lowest thermal resistance level with the largest pressure drop. Generally the foams with 100 PPI had slightly lower thermal resistances at the same flow rates but much larger pressure drops than those with 60 PPI.

Next to the efforts about basic research, researchers have focused their attention also to the applied research in order to study the feasibility of metal foams in real systems. Odabaee and Hooman [14] studied the feasibility of metal foams as air-cooled condensers for geothermal power plants. They proposed two optimization techniques, based on the first and second law of thermodynamics, to optimize the metal foam heat exchanger. The new design was compared to a conventional air-cooled condensers: while the heat transfer rate increases significantly (by an order of magnitude) compared to the traditional one, the pressure drop is within an acceptable range.

Ribeiro and Barbosa [15] conducted an experimental work to compare the thermal-hydraulic performance of cross-flow microchannel condensers using louvered fins and metal foams as extended surfaces. They used three metal foams with 10 and 20 PPI with a porosity of 0.893 and 0.947, and three louvered fins with lengths of 27 mm and 32 mm (in the flow direction) and heights of 5 mm and 7.5 mm, with air flowing at a velocity ranging between 2.1 and 7.7 m/s. A comparison based on the thermal conductance and air-side pumping power showed that the surfaces enhanced with louvered fins performed better than the metal foams under all the investigated conditions.

A possible implementation of foams as extended surfaces in HVAC heat exchangers was considered by De Schampheleiere et al. [16], who compared a traditional commercially available high quality louvered fin heat exchanger against a prototype in-house made heat exchanger using 10 PPI aluminum foam. Surprisingly, the friction factor of the louvered fin heat exchanger was higher than that of the metal foam heat exchanger. Nevertheless, the air side resistance of the foam heat exchanger was higher due to its lower available heat transfer area of the foam structure, which is 66% of that of the louvered fin heat exchanger. Thus, a metal foam with a higher linear porosity or with a more conductive material (for instance copper) can lead to a better performance.

Yang et al. [17] conducted experiments to study the possible implementation of foams to cool a LED module. A total amount of six heat sink modules were made and implemented on a typical LED light bulb. The thermal resistance of the heat sink was the dominant one. The thermal resistance for the carbon foam having an embedded metal plate shows the least thermal resistance, followed by carbon foam, and metal foam. A further improvement is the reduced weight of the heat sink.

Huang et al. [18] presented a numerical analysis of forced pulsating convection flow in a parallel-channel of solar water collector mounted with multiple metal-foam blocks. The results showed that the periodic alteration in the structure of recirculation flows, caused by metal-foam blocks and flow pulsation, significantly enhance the heat transfer rate on heat source surface.

As it appears from this brief introduction, there is a great interest in the research community about the use of porous media in many applications, which cover different field of the engineering. Both heat transfer and fluid flow characteristics are closely

linked to the geometrical properties of the metal foams, such as: porosity, pore density, fiber thickness and fiber length, foam height, material, and are linked also to the operating conditions: air mass flow rate, pressure, and temperature. Thus, reliable measurements of heat transfer coefficient and pressure drop are needed in a large database of metal foams, covering a number of variables as large as possible, in order to develop and validate empirical models. These models can help engineers to design metal foams heat exchangers.

1.3 Copper metal foams

Nine Duocel copper foams were acquired from ERG Material and Aerospace [4]. The test samples consist of a 20 mm or 40 mm high foam core height brazed between two 10 mm high copper plates, and foams have different characteristics, in terms of pores per linear inch (PPI) and relative density, so that it is possible to study how each geometrical parameter affects air heat transfer and fluid flow through such materials.

As suggested by Gibson and Ashby [1], the structure of metal foams can be well described by a tetrakaidecahedron unit cell where the fiber thickness and the fiber length are the thickness and the length of the edges of the hexagonal window. The fiber length, l, and the fiber thickness, t, are two important geometrical parameters, which are linked to the morphological structure of the foams. Gibson and Ashby [1] proposed an equation that links these two parameters to the relative density, $\frac{\rho^*}{\rho_s}$, defines as:

$$\frac{\rho^*}{\rho_s} = 1 - \varepsilon = 1.06\left(\frac{t}{l}\right) \tag{1.1}$$

Mancin et al. [10] proposed a simplified procedure to measure both the length and thickness of the fibers of the foam structure. The fiber thickness is the mean value of the thickness of the edges of the pores, whereas the length of the edges, which connects two adjacent vertices, is considered as the length of the fiber. This procedure permits to obtain the results summarized in table 1.1, where a_{sv} is the total heat transfer area per unit of volume. As shown in figure 1.3, the model proposed by Gibson and Ashby [1] is able to predict the values of the porosity from

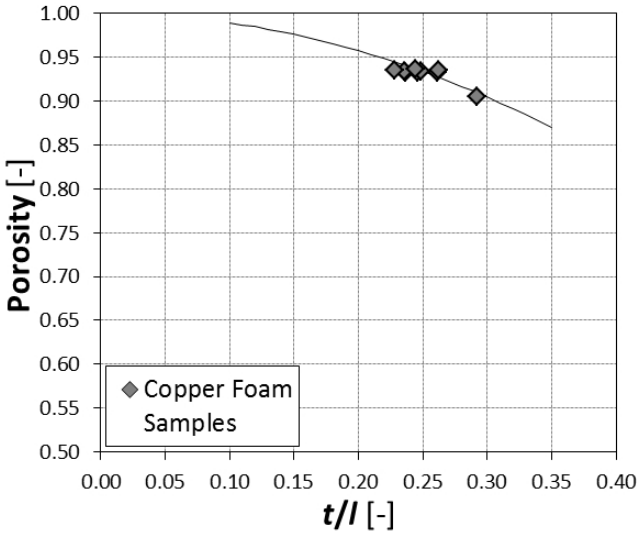

Figure 1.3: Model of Gibson and Ashby [1] compared against experimental measurements.

Table 1.1: Major geometrical characteristics of the tested metal foams during air forced convection.

Sample	PPI [in^{-1}]	Porosity [-]	H [mm]	a_{sv} [m^{-1}]	t [mm]	l [mm]
Cu-5-6.7	5	0.933	0.04	299	0.500	1.913
Cu-10-6.7	10	0.933	0.04	698	0.390	1.583
Cu-10-9.5	10	0.905	0.04	831	0.403	1.378
Cu-20-6.7	20	0.933	0.04	1148	0.293	1.236
Cu-40-6.6	40	0.934	0.04	1635	0.262	1.109
Cu-5-6.5	5	0.935	0.02	292	0.495	1.890
Cu-10-6.6	10	0.934	0.02	692	0.432	1.739
Cu-20-6.5	20	0.935	0.02	1134	0.320	1.402
Cu-40-6.4	40	0.936	0.02	1511	0.244	0.999

the measured values of fiber thickness and length, with an average deviation of 1%.

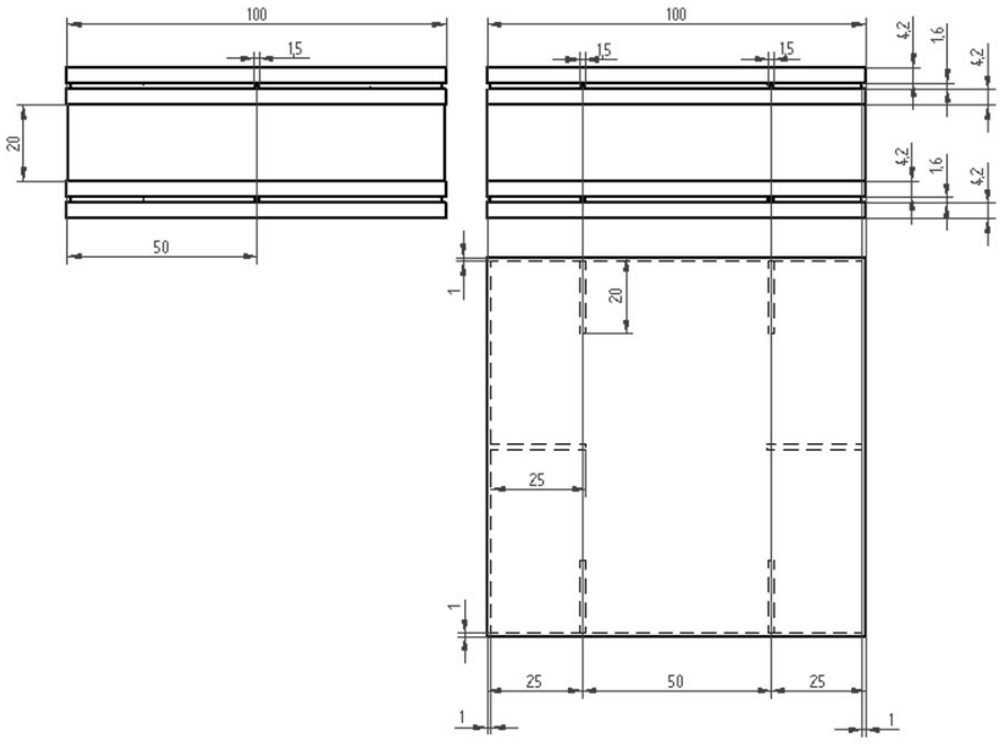

Figure 1.4: Location of the holes for the thermocouples in the bottom and top plates.

The bottom and top plates, between which the metal foam is brazed, have been machined in order to obtain six holes in each plate. A total amount of 12 T-type thermocouples are located in these holes, in order to monitor the wall temperature distribution. The location of the holes for the thermocouples is reported in figure 1.4.

1.4 Experimental apparatus

The experimental set up is located at the Dipartimento di Ingegneria Industriale of the University of Padova. The test rig is an open-circuit wind tunnel with a rectangular cross section and it has been designed and developed to study heat transfer and fluid flow of air through different enhanced surfaces. It can be subdivided into two main sections: the air compression one and the test section.

Air compression section

The main components of the air compression section are: a screw compressor (1), a drier (2), a charcoal filter (3), and an air receiver (4). A schematic of the air compression section is given in figure 1.5. The compressor is a single stage, oil

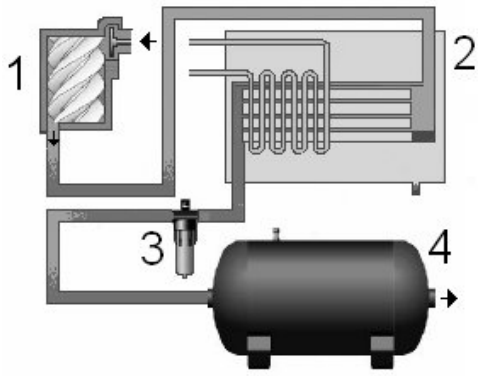

Figure 1.5: Air compression section.

injected machine driven by an electric motor with inverter driver, which is able to supply a variable air flow rate up to 90 $m^3\ h^{-1}$ at a constant gauge pressure of 7 bar. The humid compressed air is first dehydrated in order to remove water: air flows into the direct expansion evaporator of a drier, at the exit of which the specific humidity is lower than $0.6 \times 10^{-3}\ g_v/\,kg_a$. The dry air is then filtered by a set of filters in order to remove oil and any particulate materials. An additional charcoal filter eliminates oil residuals down to 3 ppm. Air finally reaches a 500 L receiver.

Experimental test section

The compressed air at 7 bar is drawn from the air receiver to the test part, which is the actual experimental test section. The main components of this part are reported in figure 1.6, and are: a pressure control valve, an air flowmeter, a 70 L calm chamber, an inlet tube, the test section, and an air flow control valve.

First of all, the compressed air is elaborated by the pressure control valve designed for pressure reduction down to the atmospheric pressure; after that, according to EN ISO 5167-1:1991/A1:1998 Standard [19], an orifice flowmeter, equipped

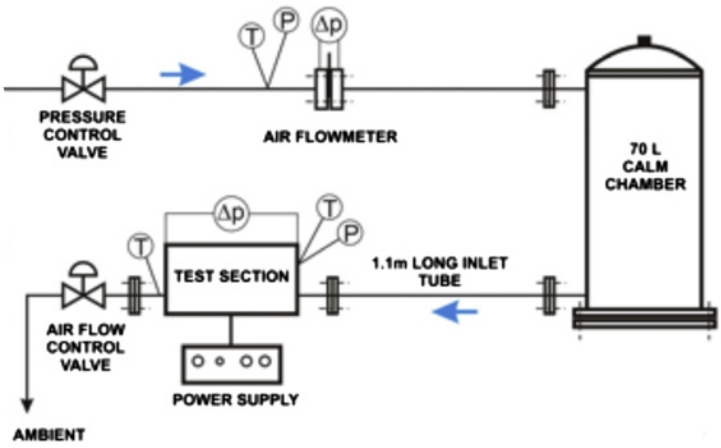

Figure 1.6: Experimental test part.

with a high precision differential transducer, measures the air flow rate. The uncertainty of the calibrated orifice flowmeter, calculated according to EN ISO 5167-1:1991/A1:1998 Standard [19], including the differential pressure transducer accuracy, always complies within ±0.8%. The differential pressure transducer has an uncertainty of ±2 Pa. A T-type thermocouple and an absolute pressure transducer are placed at the inlet of the orifice, so that it is possible to know the thermodynamic state of the air. This absolute pressure transducer has an uncertainty of ±330 Pa. It is possible to measure a wide range of flow rates by using different orifices. The upstream and downstream tube has an inner diameter of 51 mm.

The air flows into a 70 L calm chamber and then through the inlet tube to the test section. This tube has a rectangular cross section, it is 100 mm wide, and the height depends on the height of the foam under investigation: it is 20 mm high for 20 mm high samples, whereas it is 40 mm high for 40 mm high samples. After that the air reaches the test section, then the flow rate control valve and it is discharged into the atmosphere.

The test section is made of stainless steel AISI 316L, and it is 300 mm wide, 300 mm long, and 200 mm high, and contains a Bakelite channel, in which the foam specimen is located. It consists of three parts: the top and bottom plates, which are bolted in order to allow inspections and maintenance operations, and the core where the test sample is inserted. The Bakelite channel is inserted into the stainless

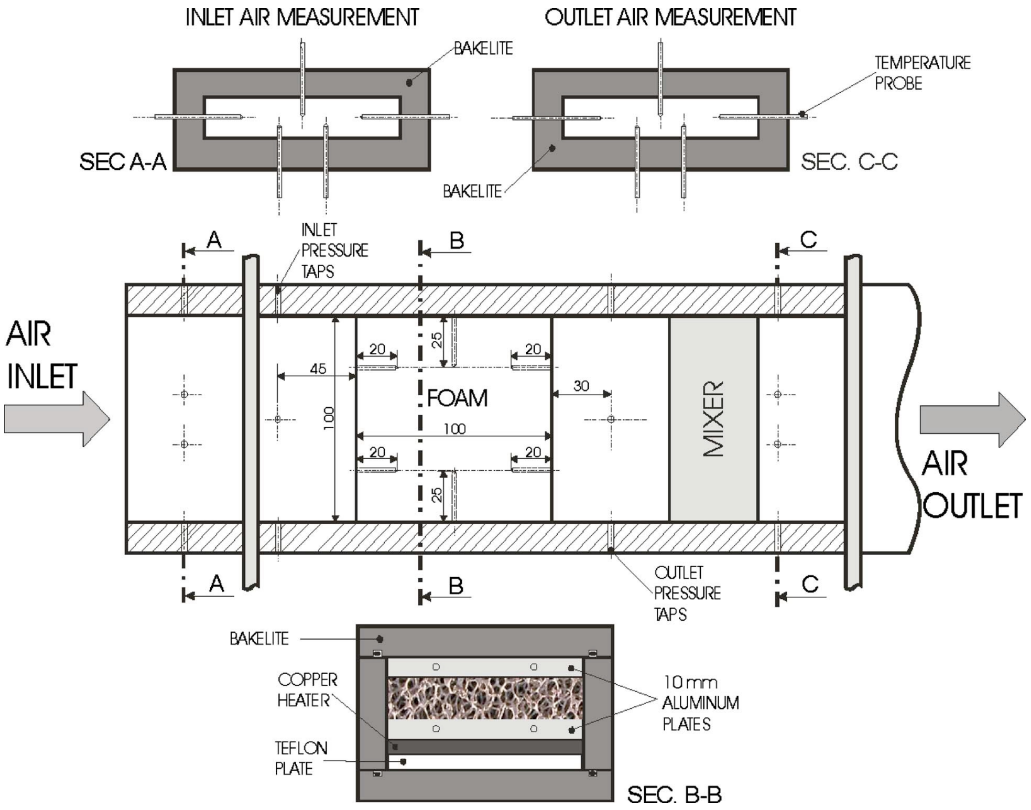

Figure 1.7: Schematic of the Bakelite channel [20].

steel box to permit the experimental heat transfer and pressure drop measurements.

A top view of the Bakelite channel with several cross sections that display the location of thermocouples and of the pressure pressure taps is reported in figure 1.7. The temperature of the air entering into the test section is measured by means of several T-type thermocouples (5 in case of 20 mm high sample, or 8 in case of 40 mm high sample), evenly distributed in a cross section. Then four pressure taps (two on the lateral sides, one on the top and one on the bottom) are connected to an absolute pressure transducer (uncertainty of ± 330 Pa) to measure the inlet pressure. Other four pressure taps can be found downstream to the foam: these taps and the upstream ones are connected to a differential pressure transducer (uncertainty of ± 2.5 Pa), in order to measure the pressure drop across the sample. A mixer is inserted upstream to the outlet pressure taps and before the temperature measurements, in order to reduce air temperature non-uniformities.

Foam samples are located over an electric heater, which is a 7 mm high copper

plate with the same test sample base area. A guide is milled in the copper plate to hold a Nichel-Chrome wire resistance. The electric power is given by a stabilized direct current power supplier. This heating technique was proved to be suitable and reliable by Mancin et al. [10]. The electric power is indirectly measured by means of a calibrated reference resistance (shunt) and by the measurements of the electrical potential difference (EDP) of the resistance wire inserted in the heater. From the Ohm's law and from the knowledge of the EDP across the shunt, it is possible to calculate the current in the heater, and thus the electric power can be obtained. It has been estimated that the accuracy of the electrical power supplied to the sample is within ±0.13% of the measured value. The uncertainties of the transducers are reported in Table 1.2.

Table 1.2: Uncertainties of transducers.

Transducer	Uncertainty
T-type thermocouples	±0.05 K
Absolute pressure transducer (full scale FS=0.6 MPa)	±0.055 FS %
Differential pressure transducer (orifice, full scale FS=2000 Pa)	±0.10 FS %
Differential pressure transducer (test section, full scale FS=1000 Pa)	±0.25 FS %
Electric power	±0.13% of the reading
Air flow rate	±0.80% of the reading

Acquisition system

The experimental apparatus is connected to a real-time acquisition system which permits to control the principal parameters through the facility. The signals coming from the experimental transducers are recorded with an acquisition system consisting of a digital switch multimeter connected to a PC through a GPIB port. The recorded signals are elaborated and displayed with Labview 9.0 [21]. The acquisition program displays the measurements in terms of graphs or numerical values of the rielaborated electric signals: graphs report the desired parameter as a function of the reading. This program permits to identify whether or not a steady state condition is reached.

The following parameters are recorded in an Excel output file:

- number of the reading [-];
- 6 bottom wall temperatures of the sample [°C];
- 6 top wall temperatures of the sample [°C];
- 5 or 8 inlet air temperatures [°C];
- 5 or 8 outlet air temperatures [°C];
- air temperature at the orifice flowmeter [°C];
- pressure drop across the orifice [mbar];
- air inlet pressure at the test section [bar];
- air inlet pressure at the orifice [bar];
- air pressure drop across the sample [Pa];
- current supplied to the electric heater[A];
- voltage across the electric heater [V].

1.5 Data reduction

1.5.1 Heat transfer

First of all, the heat balance between the electric power and the air side heat flow rate must be checked; in other words:

$$P_{EL} = \dot{m}_{air} \cdot c_{p,air} \cdot (t_{air,out} - t_{air,in}) \tag{1.2}$$

where P_{EL} is the heat flow rate supplied by the electric heater, $\dot{m}_{air}$ the air mass flow rate, $c_{p,air}$ the air specific heat at constant pressure, calculated at the mean

value of temperature and pressure. $t_{air,in}$ and $t_{air,out}$ are the inlet and outlet air temperature, respectively, and are calculated as follows:

$$t_{air,in} = \frac{\sum_{n=1}^{n_{tc}} t_{air,in,i}}{n_{tc,air,in}} \tag{1.3}$$

$$t_{air,out} = \frac{\sum_{n=1}^{n_{tc}} t_{air,out,i}}{n_{tc,air,out}} \tag{1.4}$$

For every test, the difference between the two sides of equation 1.2 is always lower than 5%, thus the heat balance is checked.

The experimental measurements allow calculations of heat transfer coefficients, which has to be referred to a reference surface. In case of metal foams, there are two different ways to define this parameter: the first one uses the base area as reference surface, allowing the calculation of the overall heat transfer coefficient, HTC^*. Thus, HTC^* is defined as the product between the heat transfer coefficient HTC and the foam finned surface efficiency Ω^*, as:

$$HTC^* = HTC \cdot \Omega^* = \frac{P_{EL}}{A_{base} \cdot \Delta T_{ml}} \tag{1.5}$$

where the base area of the test sample, A_{base}, is the reference surface, and ΔT_{ml} is the logarithmic mean temperature difference calculated between wall and air temperatures, defined as:

$$\Delta T_{ml} = \frac{(t_{w,in} - t_{air,in}) - (t_{w,out} - t_{air,out})}{\ln \dfrac{t_{w,in} - t_{air,in}}{t_{w,out} - t_{air,out}}} \tag{1.6}$$

where $t_{w,in}$ and $t_{w,out}$ indicate the heated wall temperatures at the inlet and outlet of the base plate, respectively.

The second way uses the overall heat transfer area of the metal foams as reference surface, leading to the determination of the interstitial heat transfer coefficient, defined as:

$$\alpha^* = \alpha \cdot \Omega^* = \frac{HTC^*}{1 + a_{sv} \cdot H} \tag{1.7}$$

The foam can be considered as an extended surface that enhances the heat transfer area where the heat sink is attached on. However, not the entire height of

the foam is at the base temperature, therefore a foam finned surface efficiency must be taken into account, as shown in equations 1.5 and 1.7.

Another important parameter is the normalized mean wall temperature, which can be useful to compare performances at different ambient conditions. In the hypothesis that the product between the heat transfer coefficient and the foam-finned surface efficiency is constant along the length of the sample and it does not vary with air temperature because air properties change moderately, with reference to the mean air temperature across the sample, $\bar{t}_{air}$, it is possible to calculate a normalized mean wall temperature, $\bar{t}_w$, as:

$$\bar{t}_w = \bar{t}_{air} + \frac{P_{EL}}{\Omega^* \cdot HTC \cdot A_{base}} \tag{1.8}$$

Since $\bar{t}_w$ depends on $\bar{t}_{air}$, reference is made to a normalized mean wall temperature $\bar{t}_{w,25°C}$, at which the inlet air temperature is 25 °C. The corresponding outlet air temperature is given by:

$$\bar{t}_{air,out,25°C} = 25 + \frac{P_{EL}}{\dot{m}_a \cdot c_{p,air}} \tag{1.9}$$

Thus:

$$\bar{t}_{w,25°C} = \bar{t}_{air,25°C} + \frac{P_{EL}}{\Omega^* \cdot HTC \cdot A_{base}} \tag{1.10}$$

where

$$\bar{t}_{air,25°C} = \frac{25 + \bar{t}_{air,out,25°C}}{2} \tag{1.11}$$

1.5.2 Pressure drop

The experimental pressure gradient in a porous medium can be approximated with the following equation:

$$-\frac{\mathrm{d}p}{\mathrm{d}z} = \frac{\mu}{K}u + f\frac{\rho}{\sqrt{K}}u^2 \tag{1.12}$$

The first term on the right side of equation 1.12 is the Darcy's term, which accounts for the linear dependence of the pressure drop on flow velocity at low velocities. K is the permeability of the porous media, which, according to Darcy's law, is the measure of the flow conductance of the matrix and it is expressed in m^2. The second

term reports the quadratic dependence of pressure drop on velocity and defines the inertia coefficient, f. The other quantities are the air dynamic viscosity, μ, the air density, ρ, calculated at the mean value of temperature and pressure, and the air pores velocity, u, defined as:

$$u = \frac{\dot{m}_{air}}{A_{front} \cdot \rho \cdot \varepsilon} \tag{1.13}$$

The experimental results show that the ratio between pressure gradient and the pores velocity is a linear function of the velocity; therefore, equation 1.12 can be rearranged as follows:

$$\left(\frac{\mathrm{d}p}{\mathrm{d}z}\right)_{Exp} \cdot \frac{1}{u} = \frac{\mu}{K} + f\frac{\rho}{\sqrt{K}}u = a + b \cdot u \tag{1.14}$$

From the linear least square error regression it is possible to obtain the values of the two constants a and b, and so the values of permeability and of inertia coefficient:

$$K = \frac{\mu}{a} \tag{1.15}$$

$$f = \frac{b\sqrt{K}}{\rho} \tag{1.16}$$

All thermophysical properties are evaluated using Refprop 9.0 [22].

1.6 Uncertainty analysis

1.6.1 Theory on uncertainty analysis of indirect measurements

Suppose that a physical quantity is a function of n independent parameters:

$$y = f(x_1, x_2, ..., x_n) \tag{1.17}$$

and the independent parameters have their uncertainty i_i; thus, the physical quantity y has its uncertainty i_y:

$$y \pm i_y = f(x_1 \pm i_1, x_2 \pm i_2, ..., x_n \pm i_n) \tag{1.18}$$

With a first order Taylor expansion:

$$f(x_1 \pm i_1, x_2 \pm i_2, ..., x_n \pm i_n) \approx f(x_1, x_2, ..., x_n) \pm \left(\frac{\partial f}{\partial x_1} i_1 + \frac{\partial f}{\partial x_2} i_2 + ... + \frac{\partial f}{\partial x_n} i_n \right) \quad (1.19)$$

and so:

$$i_y \approx \pm \frac{\partial f}{\partial x_1} i_1 \pm \frac{\partial f}{\partial x_2} i_2 \pm ... \pm \frac{\partial f}{\partial x_n} i_n = \pm \vartheta_1 i_1 \pm \vartheta_2 i_2 \pm ... \pm \vartheta_n i_n \quad (1.20)$$

where ϑ_i are called sensitivity coefficients and are evaluated in the point x_i. If uncertainties i_i are normally distributed and their average value is zero, the uncertainty on the physical quantity i_y can be calculated as:

$$i_y = \sqrt{\sum_{i=1}^{n} \left(\frac{\partial f}{\partial x_i} i_i \right)^2} = \sqrt{\sum_{i=1}^{n} \left(\vartheta_i i_i \right)^2} \quad (1.21)$$

1.6.2 Uncertainty analysis on the experimental measurements

Uncertainty on the logarithmic mean temperature difference

The logarithmic mean temperature difference is defined as:

$$\Delta t_{ml} = \frac{\Delta_2 - \Delta_1}{\ln \frac{\Delta_2}{\Delta_1}} \quad (1.22)$$

and in this case:

$$\Delta_1 = t_{w,in} - t_{air,in} \quad (1.23)$$

$$\Delta_1 = t_{w,out} - t_{air,out} \quad (1.24)$$

Deriving:

$$\frac{\partial \Delta_1}{\partial t_{w,in}} = \frac{\partial \Delta_2}{\partial t_{w,out}} = 1 \quad (1.25)$$

$$\frac{\partial \Delta_1}{\partial t_{air,in}} = \frac{\partial \Delta_2}{\partial t_{air,out}} = -1 \quad (1.26)$$

and thus the uncertainties on Δ_1 and Δ_2 become:

$$i_{\Delta_1} = \sqrt{\left(\frac{\partial \Delta_1}{\partial t_{w,in}} i_{t_{w,in}}\right)^2 + \left(\frac{\partial \Delta_1}{\partial t_{air,in}} i_{t_{air,in}}\right)^2} \tag{1.27}$$

$$i_{\Delta_2} = \sqrt{\left(\frac{\partial \Delta_2}{\partial t_{w,out}} i_{t_{w,out}}\right)^2 + \left(\frac{\partial \Delta_2}{\partial t_{air,out}} i_{t_{air,out}}\right)^2} \tag{1.28}$$

Substituting equations 1.25 and 1.26 into 1.27 and 1.28, considering a temperature measurement accuracy of ± 0.05 K, it is:

$$i_{\Delta_1} = i_{\Delta_2} = \pm 0.07 \text{ K} \tag{1.29}$$

The partial derivatives of the logarithmic mean temperature difference with respect to Δ_1 and Δ_2 are:

$$\frac{\partial \Delta t_{ml}}{\partial \Delta_1} = \frac{\left(\frac{\Delta_2 - \Delta_1}{\Delta_1}\right) - \ln \frac{\Delta_2}{\Delta_1}}{\left(\ln \frac{\Delta_2}{\Delta_1}\right)^2} \tag{1.30}$$

$$\frac{\partial \Delta t_{ml}}{\partial \Delta_2} = \frac{\left(\frac{\Delta_1 - \Delta_2}{\Delta_2}\right) + \ln \frac{\Delta_2}{\Delta_1}}{\left(\ln \frac{\Delta_2}{\Delta_1}\right)^2} \tag{1.31}$$

Thus the uncertainty on the logarithmic mean temperature difference can be calculated as:

$$i_{\Delta t_{ml}} = \sqrt{\left(\frac{\partial \Delta t_{ml}}{\partial \Delta_1} i_{\Delta_1}\right)^2 + \left(\frac{\partial \Delta t_{ml}}{\partial \Delta_2} i_{\Delta_2}\right)^2} \qquad [\text{K}] \tag{1.32}$$

and the percentage uncertainty as:

$$i_{\Delta t_{ml\%}} = \frac{i_{\Delta t_{ml}}}{\Delta t_{ml}} \cdot 100 \qquad [\%] \tag{1.33}$$

From this error propagation analysis, the maximum and mean uncertainties on the logarithmic mean temperature difference are 0.17% and 0.12%, respectively.

Uncertainty on the overall heat transfer coefficient

The overall heat transfer coefficient was previously defined as:

$$HTC^* = HTC \cdot \Omega^* = \frac{P_{EL}}{A_{base} \cdot \Delta T_{ml}} \tag{1.5}$$

Deriving:

$$\frac{\partial HTC^*}{\partial P_{el}} = \frac{1}{A_{base} \Delta T_{ml}} \tag{1.34}$$

$$\frac{\partial HTC^*}{\partial \Delta t_{ml}} = -\frac{P_{el}}{A_{base} \Delta T_{ml}^2} \tag{1.35}$$

$$\frac{\partial HTC^*}{\partial A_{base}} = -\frac{P_{el}}{\Delta T_{ml} A_{base}^2} \tag{1.36}$$

and thus the uncertainty on the overall heat transfer coefficient can be calculated with the following equations:

$$i_{HTC^*} = \sqrt{\left(\frac{\partial HTC^*}{\partial P_{el}} i_{P_{el}}\right)^2 + \left(\frac{\partial HTC^*}{\partial \Delta T_{ml}} i_{\Delta T_{ml}}\right)^2 + \left(\frac{\partial HTC^*}{\partial A_{base}} i_{A_{base}}\right)^2} \qquad \left[\frac{\mathrm{W}}{\mathrm{m^2K}}\right] \tag{1.37}$$

where

$$i_{P_{el}} = 0.0013 \cdot P_{el} \qquad [\,\mathrm{W}] \tag{1.38}$$

and $i_{\Delta t_{ml}}$ is expressed with equation 1.32, and $i_{A_{base}} = 0.0001\,[\,\mathrm{m^2}]$. The percentage uncertainty can be calculated as:

$$i_{HTC^*\%} = \frac{i_{HTC^*}}{HTC^*} \cdot 100 \qquad [\%] \tag{1.39}$$

From this error propagation analysis, it is estimated that the overall heat transfer coefficient has an uncertainty of $\pm 1.5\%$.

Uncertainty on permeability and inertia coefficient

The coefficients a and b of equation 1.14 are calculated from a linear least square error regression:

$$a = \frac{\sum x_i^2 \sum y_i - \sum x_i \sum (x_i y_i)}{\Delta} \tag{1.40}$$

and

$$b = \frac{N \sum (x_i y_i) - \sum x_i \sum y_i}{\Delta} \tag{1.41}$$

where

$$\Delta = N \sum x_i^2 - \left(\sum x_i \right)^2 \tag{1.42}$$

and

$$x_i = u_i \qquad\qquad y_i = \left[\left(-\frac{\mathrm{d}p}{\mathrm{d}z} \right) \frac{1}{u} \right]_i \tag{1.43}$$

From the error propagation analysis, the uncertainties on the coefficients a and b can be calculated as follows:

$$i_a = \sqrt{\left(\frac{\partial a}{\partial x_i} i_{x_i} \right)^2 + \left(\frac{\partial a}{y_i} i_{y_i} \right)^2} \tag{1.44}$$

$$i_b = \sqrt{\left(\frac{\partial b}{\partial x_i} i_{x_i} \right)^2 + \left(\frac{\partial b}{y_i} i_{y_i} \right)^2} \tag{1.45}$$

where i_x and i_y are the uncertainties on the velocity and on the first term of equation 1.14.

Velocity is calculated as ratio between mass flow rate and product between density and frontal area, thus the uncertainty on the velocity is defined as follows:

$$i_u = i_{x_i} = \sqrt{\left(\frac{\partial u}{\partial \dot{m}_a} i_{\dot{m}_a} \right)^2 + \left(\frac{\partial u}{\partial A_{sezione}} i_{A_{sezione}} \right)^2 + \left(\frac{\partial u}{\partial \rho} i_\rho \right)^2} \tag{1.46}$$

where $i_{\dot{m}_a} = \pm 0.8\%$ of the reading, $i_{A_{sezione}} = \pm 1\%$ of the measurement, and $i_\rho = \pm 1\%$ of the measurement. The uncertainty on the term $\left(-\frac{\mathrm{d}p}{\mathrm{d}z} \right) \frac{1}{u}$ is:

$$i_{y_i} = \sqrt{\left(\frac{\partial y}{\partial p} i_p \right)^2 + \left(\frac{\partial y}{\partial z} i_z \right)^2 + \left(\frac{\partial y}{\partial u} i_u \right)^2} \tag{1.47}$$

with $i_z = \pm 1\%$ of the measurement. Thus, since:

$$K = \frac{\mu}{a} \tag{1.15}$$

$$f = \frac{b\sqrt{K}}{\rho} \tag{1.16}$$

it is possible to calculate the uncertainty on permeability and inertia coefficient, and their mean values are: ±1.0% and ±0.7%, respectively.

1.7 Experimental results

Heat transfer coefficient and pressure drop measurements during air forced convection through nine copper foams were carried out. The main geometrical characteristics of these foams are summarized in table 1.1. The measurements were taken by imposing two or three heat fluxes (25.0, 32.5, and 40.0 kW m^{-2}), which correspond to heat flow rates of 250, 325, and 400 W, respectively. The air flow rate was varied between 0.005 and 0.0125 kg s^{-1} for the samples with a foam core height of 20 mm, and between 0.010 and 0.025 kg s^{1}, to which a frontal air velocity from 2.5 to 5.0 m s^{-1} corresponds. The air pressure and temperature were always set around the value of that of ambient conditions. The operating test conditions are summarized in table 1.3.

Table 1.3: Operating test conditions.

Parameter	Range
Air mass flow rate (20 mm high sample)	0.005 - 0.0125 kg s^{-1}
Air mass flow rate (40 mm high sample)	0.010 - 0.025 kg s^{-1}
Air frontal velocity	2.5 - 5.0 m s^{-1}
Heat flux	25.0, 32.5, 40.0 kW m^{-2}
Heat flow rate	250, 325, 400 W
Absolute pressure	Near Ambient Conditions
Inlet air temperature	Near Ambient Conditions

In the following, the results in terms of overall heat transfer coefficient, mean wall temperature, and pressure gradient for the nine copper foam samples are presented.

1.7.1 Cu-40-6.6, H=20 mm

The experimental measurements of the Cu-40-6.6 with a foam core height of 20 mm are here reported. Figure 1.8 reports the overall heat transfer coefficient plotted against the air mass velocity for three different heat fluxes (HF=25.0, 32.5, and 40.0 kW m^{-2}). The global heat transfer coefficient appears to be independent on the imposed heat flux. It increases with increasing the air mass velocity, and it varies from 763 to 1087 W m^{-2} K^{-1}. The mean wall temperature, reported in figure 1.9, calculated with an inlet air velocity of 25 °C, decreases when the air flow rate increases; at a constant mass velocity, the mean wall temperature increases with the imposed heat flux. Finally, the pressure gradient as a function of the air mass velocity is reported in figure 1.10. It appears that the pressure gradient increases as the mass velocity increases, according to the Forchheimer equation, and it varies from 3282 to 10690 Pa m^{-1}. The heat flux has no effect on the pressure gradient in the tested working conditions. From the procedure reported in equations 1.15 and 1.16, it is possible to calculate the permeability and the inertia coefficient, and they are 0.439×10^{-7} m^2 and 0.0600, respectively.

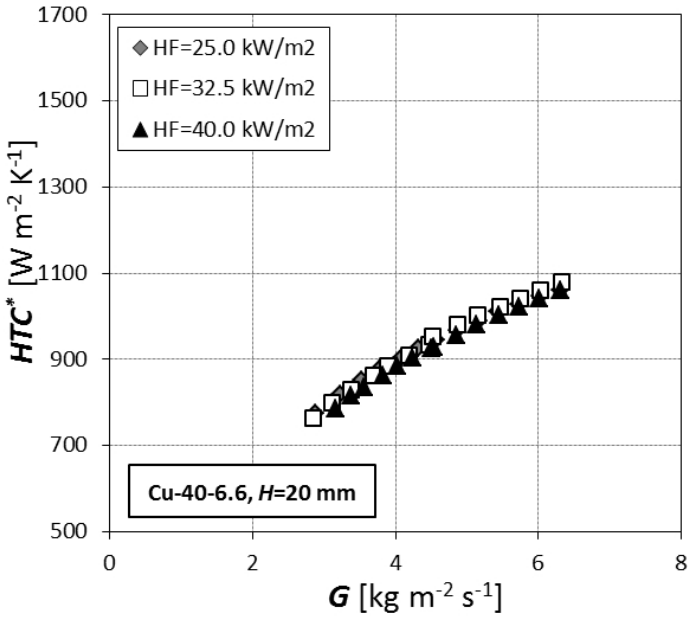

Figure 1.8: Overall heat transfer coefficient for the Cu-40-6.6 foam with a core foam height of 20 mm.

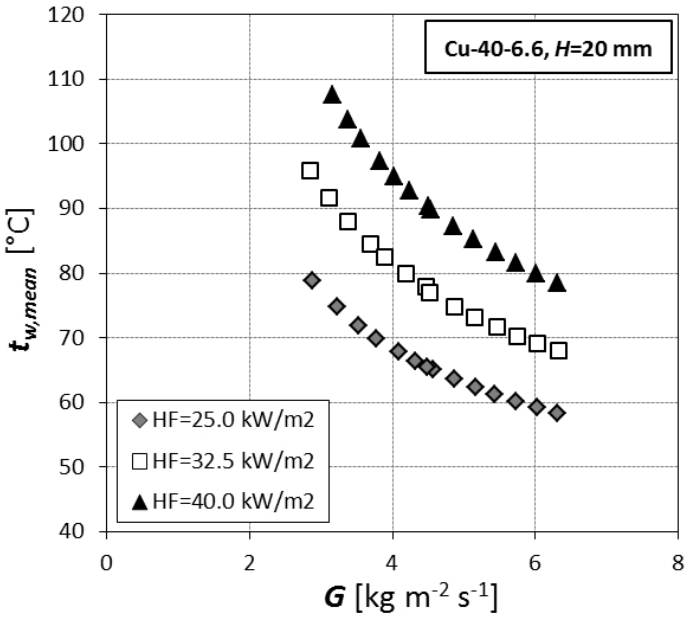

Figure 1.9: Mean wall temperature for the Cu-40-6.6 foam with a core foam height of 20 mm.

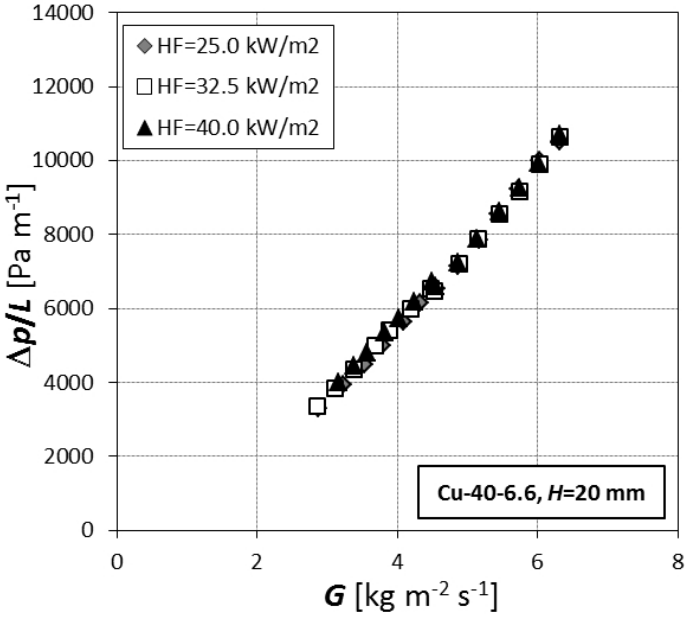

Figure 1.10: Pressure gradient for the Cu-40-6.6 foam with a core foam height of 20 mm.

1.7.2 Cu-20-6.7, H=20 mm

The experimental measurements of the Cu-20-6.7 with a foam core height of 20 mm are here reported. Figure 1.11 reports the overall heat transfer coefficient plotted against the air mass velocity for three different heat fluxes (HF=25, 32.5, and 40.0 kW m^{-2}). The global heat transfer coefficient appears to be independent on the imposed heat flux. It increases with increasing the air mass velocity, and it varies from 777 to 1149 W m^{-2} K^{-1}. The mean wall temperature, reported in figure 1.12, calculated with an inlet air velocity of 25 °C, decreases when the air flow rate increases; at a constant mass velocity, the mean wall temperature increases with the imposed heat flux. Finally, the pressure gradient as a function of the air mass velocity is reported in figure 1.13. It appears that the pressure gradient increases as the mass velocity increases, according to the Forchheimer equation, and it varies from 2558 to 8311 Pa m^{-1}. The heat flux has no effect on the pressure gradient in the tested working conditions. From the procedure reported in equations 1.15 and 1.16, it is possible to calculate the permeability and the inertia coefficient, and they are 0.409×10^{-7} m^2 and 0.0389, respectively.

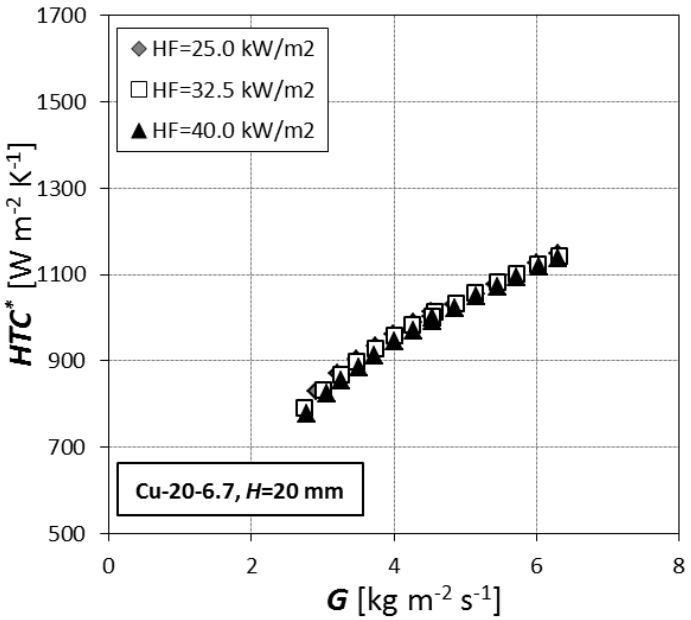

Figure 1.11: Overall heat transfer coefficient for the Cu-20-6.7 foam with a core foam height of 20 mm.

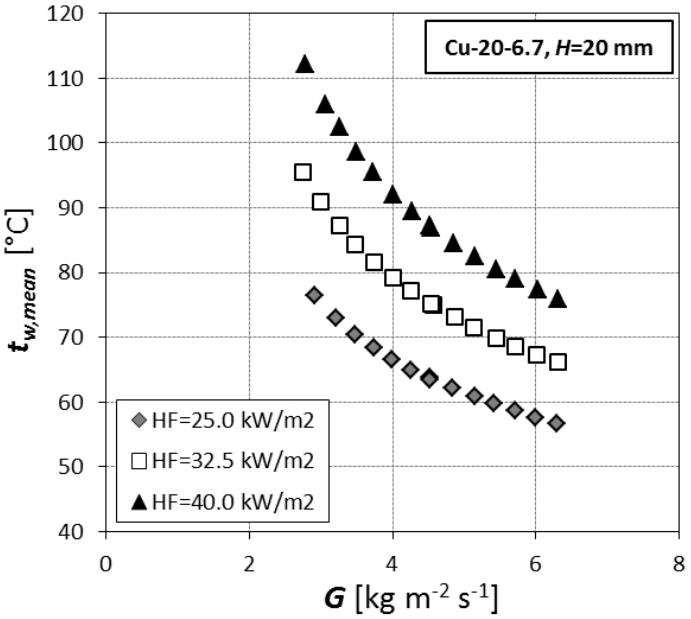

Figure 1.12: Mean wall temperature for the Cu-20-6.7 foam with a core foam height of 20 mm.

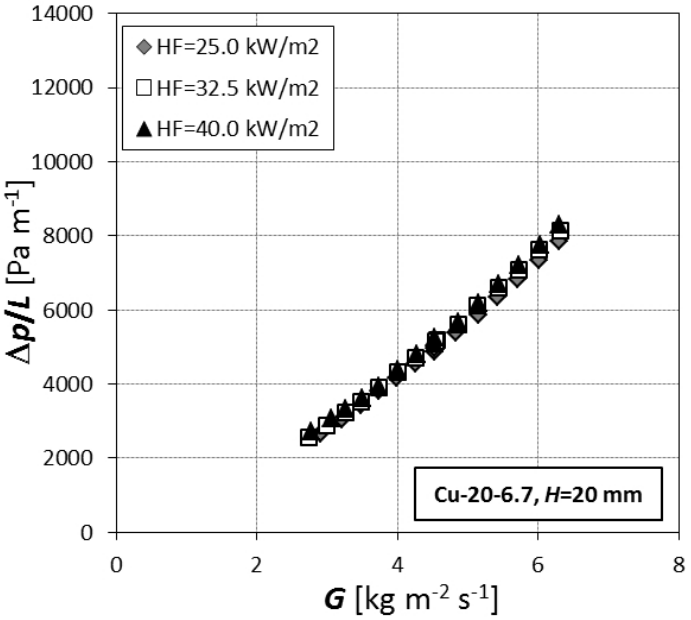

Figure 1.13: Pressure gradient for the Cu-20-6.7 foam with a core foam height of 20 mm.

1.7.3 Cu-10-9.5, H=20 mm

The experimental measurements of the Cu-10-9.5 with a foam core height of 20 mm are here reported. Figure 1.14 reports the overall heat transfer coefficient plotted against the air mass velocity for two different heat fluxes (HF=25.0, 32.5 kW m^{-2}). The global heat transfer coefficient appears to be independent on the imposed heat flux. It increases with increasing the air mass velocity, and it varies from 1127 to 1503 W m^{-2} K^{-1}. The mean wall temperature, reported in figure 1.15, calculated with an inlet air velocity of 25 °C, decreases when the air flow rate increases; at a constant mass velocity, the mean wall temperature increases with the imposed heat flux. Finally, the pressure gradient as a function of the air mass velocity is reported in figure 1.16. It appears that the pressure gradient increases as the mass velocity increases, according to the Forchheimer equation, and it varies from 1806 to 5698 Pa m^{-1}. The heat flux has no effect on the pressure gradient in the tested working conditions. From the procedure reported in equations 1.15 and 1.16, it is possible to calculate the permeability and the inertia coefficient, and they are 1.210×10^{-7} m^2 and 0.0555, respectively.

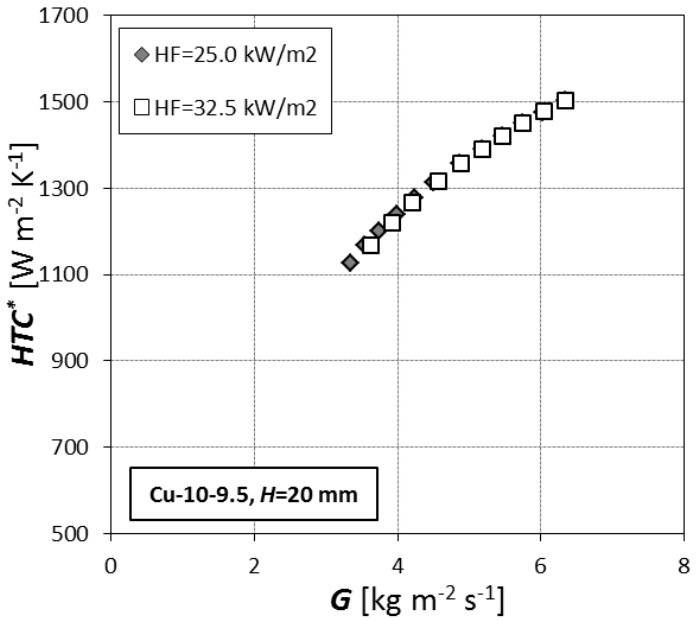

Figure 1.14: Overall heat transfer coefficient for the Cu-10-9.5 foam with a core foam height of 20 mm.

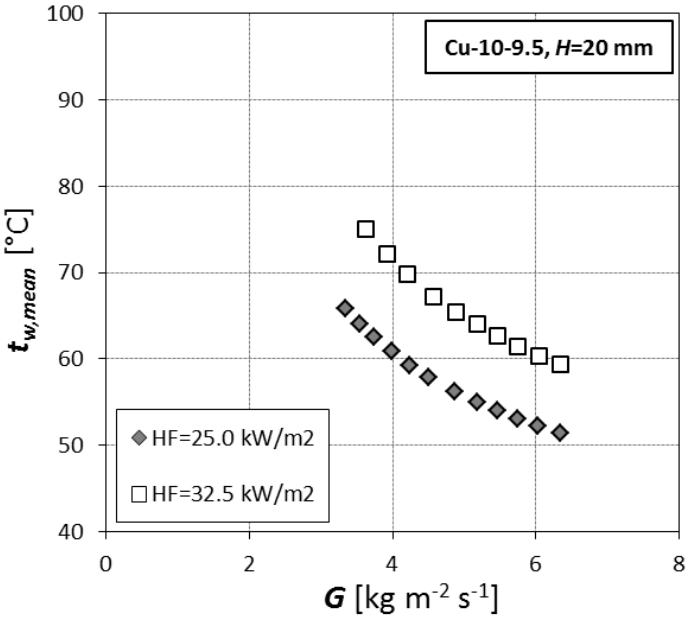

Figure 1.15: Mean wall temperature for the Cu-10-9.5 foam with a core foam height of 20 mm.

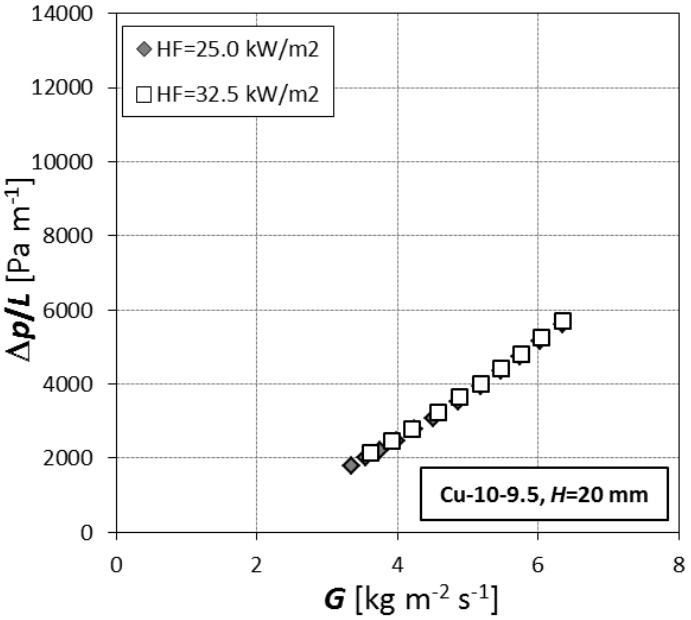

Figure 1.16: Pressure gradient for the Cu-10-9.5 foam with a core foam height of 20 mm.

1.7.4 Cu-10-6.7, H=20 mm

The experimental measurements of the Cu-10-6.7 with a foam core height of 20 mm are here reported. Figure 1.17 reports the overall heat transfer coefficient plotted against the air mass velocity for two different heat fluxes (HF=25.0, 32.5 kW m^{-2}). The global heat transfer coefficient appears to be independent on the imposed heat flux. It increases with increasing the air mass velocity, and it varies from 852 to 1172 W m^{-2} K^{-1}. The mean wall temperature, reported in figure 1.18, calculated with an inlet air velocity of 25 °C, decreases when the air flow rate increases; at a constant mass velocity, the mean wall temperature increases with the imposed heat flux. Finally, the pressure gradient as a function of the air mass velocity is reported in figure 1.19. It appears that the pressure gradient increases as the mass velocity increases, according to the Forchheimer equation, and it varies from 1895 to 5759 Pa m^{-1}. The heat flux has no effect on the pressure gradient in the tested working conditions. From the procedure reported in equations 1.15 and 1.16, it is possible to calculate the permeability and the inertia coefficient, and they are 2.088×10^{-7} m^2 and 0.0916, respectively.

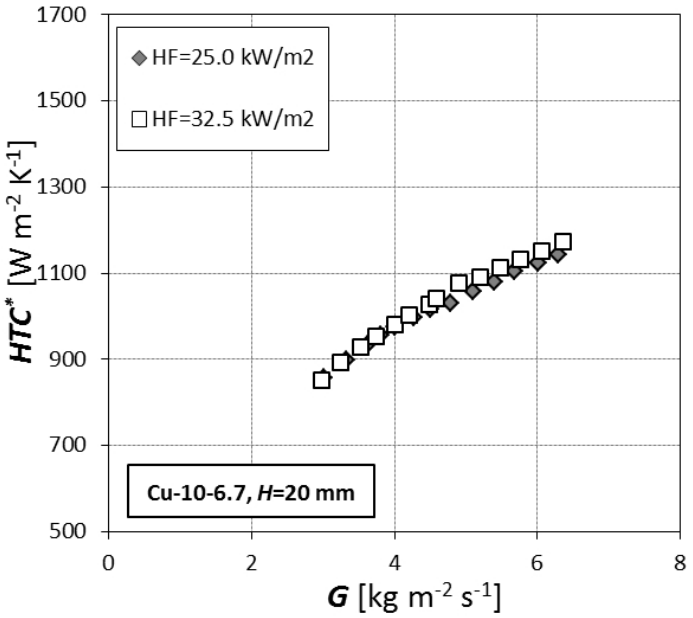

Figure 1.17: Overall heat transfer coefficient for the Cu-10-6.7 foam with a core foam height of 20 mm.

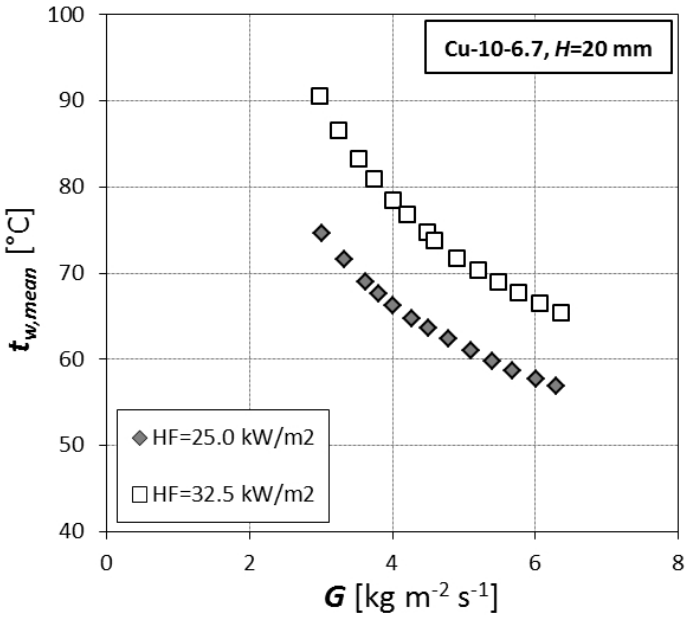

Figure 1.18: Mean wall temperature for the Cu-10-6.7 foam with a core foam height of 20 mm.

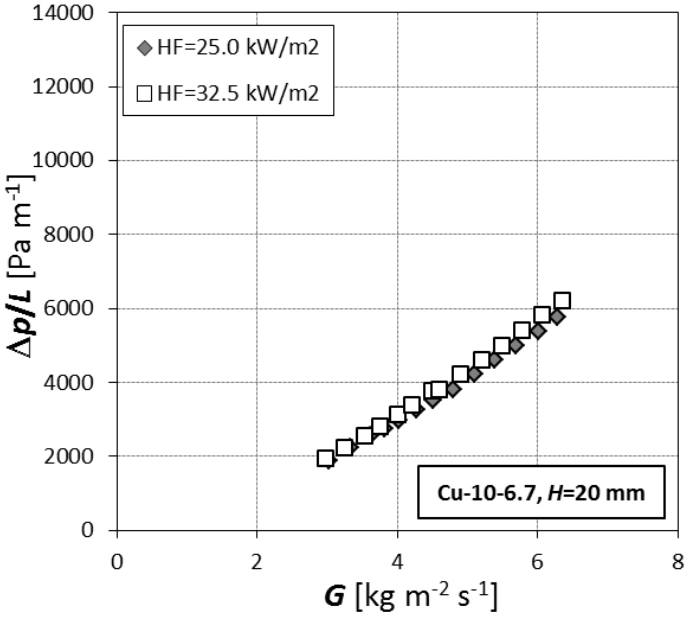

Figure 1.19: Pressure gradient for the Cu-10-6.7 foam with a core foam height of 20 mm.

1.7.5 Cu-5-6.7, H=20 mm

The experimental measurements of the Cu-5-6.7 with a foam core height of 20 mm are here reported. Figure 1.20 reports the overall heat transfer coefficient plotted against the air mass velocity for two different heat fluxes (HF=25.0, 32.5 kW m^{-2}). The global heat transfer coefficient appears to be independent on the imposed heat flux. It increases with increasing the air mass velocity, and it varies from 853 to 1192 W m^{-2} K^{-1}. The mean wall temperature, reported in figure 1.21, calculated with an inlet air velocity of 25 °C, decreases when the air flow rate increases; at a constant mass velocity, the mean wall temperature increases with the imposed heat flux. Finally, the pressure gradient as a function of the air mass velocity is reported in figure 1.22. It appears that the pressure gradient increases as the mass velocity increases, according to the Forchheimer equation, and it varies from 1777 to 5354 Pa m^{-1}. The heat flux has no effect on the pressure gradient in the tested working conditions. From the procedure reported in equations 1.15 and 1.16, it is possible to calculate the permeability and the inertia coefficient, and they are 0.966×10^{-7} m^2 and 0.0509, respectively.

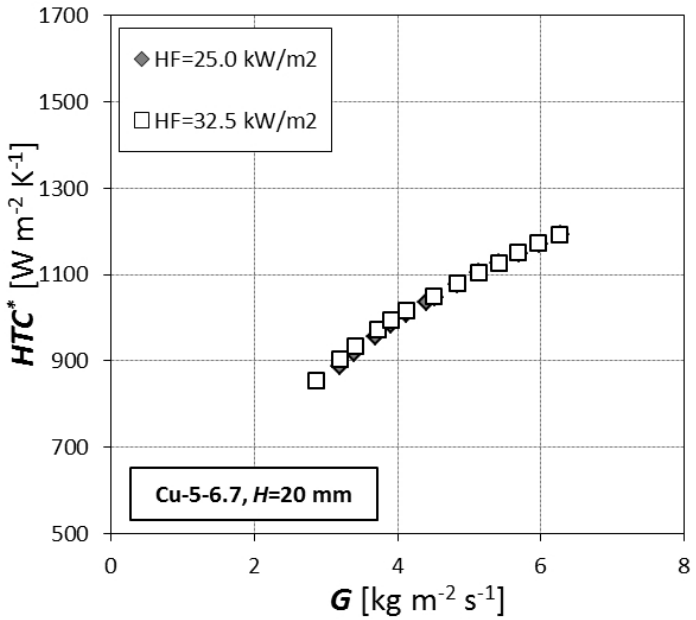

Figure 1.20: Overall heat transfer coefficient for the Cu-5-6.7 foam with a core foam height of 20 mm.

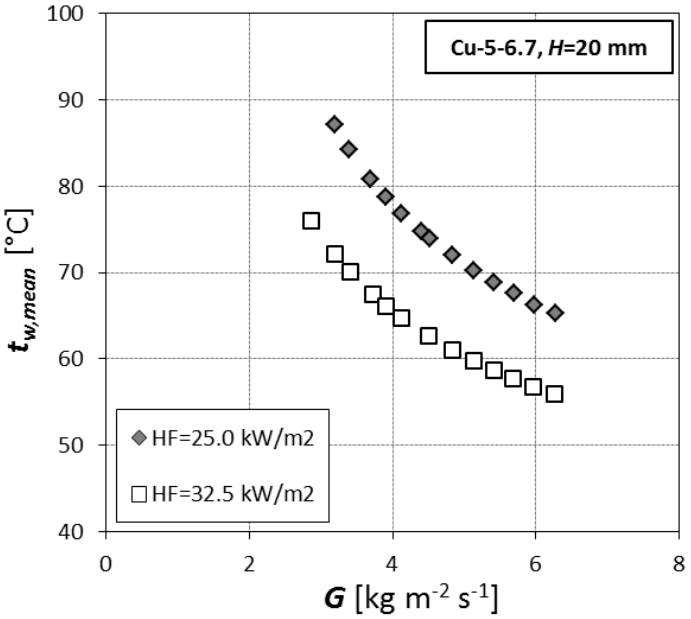

Figure 1.21: Mean wall temperature for the Cu-5-6.7 foam with a core foam height of 20 mm.

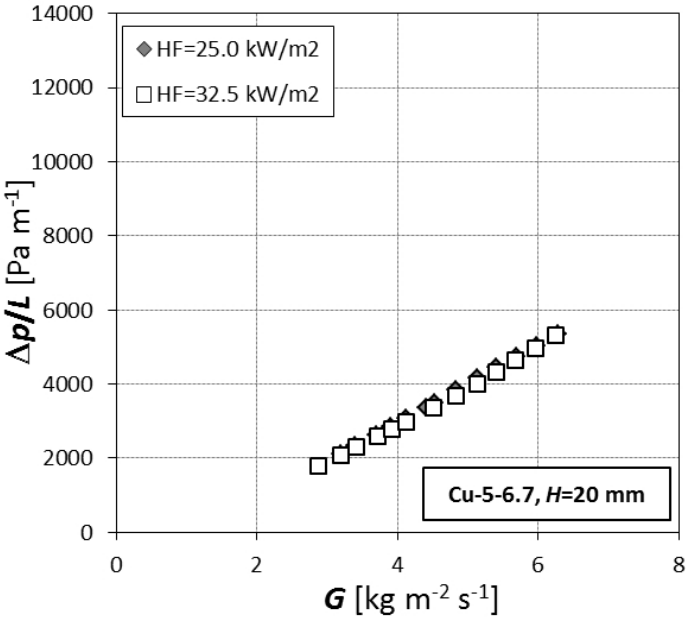

Figure 1.22: Pressure gradient for the Cu-5-6.7 foam with a core foam height of 20 mm.

1.7.6 Cu-40-6.4, H=40 mm

The experimental measurements of the Cu-40-6.4 with a foam core height of 40 mm are here reported. Figure 1.23 reports the overall heat transfer coefficient plotted against the air mass velocity for two different heat fluxes (HF=25.0, 32.5 kW m^{-2}). The global heat transfer coefficient appears to be independent on the imposed heat flux. It increases with increasing the air mass velocity, and it varies from 712 to 1041 W m^{-2} K^{-1}. The mean wall temperature, reported in figure 1.24, calculated with an inlet air velocity of 25 °C, decreases when the air flow rate increases; at a constant mass velocity, the mean wall temperature increases with the imposed heat flux. Finally, the pressure gradient as a function of the air mass velocity is reported in figure 1.25. It appears that the pressure gradient increases as the mass velocity increases, according to the Forchheimer equation, and it varies from 1779 to 12124 Pa m^{-1}. The heat flux has no effect on the pressure gradient in the tested working conditions. From the procedure reported in equations 1.15 and 1.16, it is possible to calculate the permeability and the inertia coefficient, and they are 4.500×10^{-7} m^2 and 0.2206, respectively.

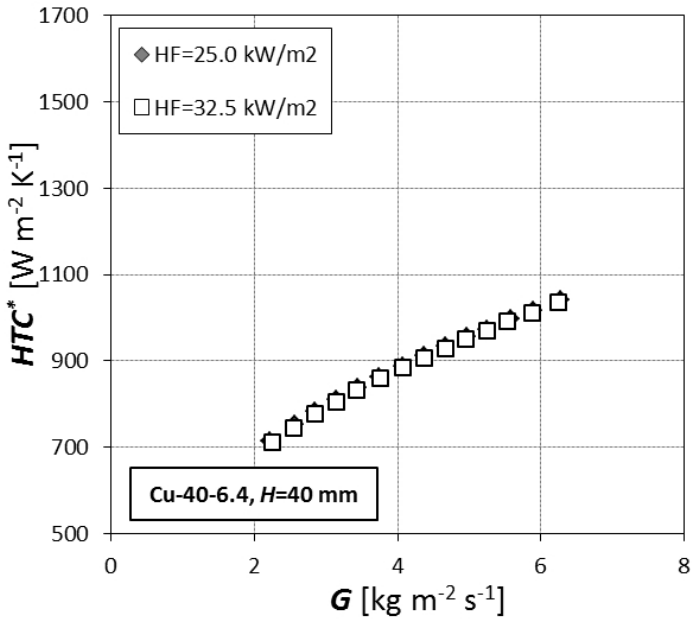

Figure 1.23: Overall heat transfer coefficient for the Cu-40-6.4 foam with a core foam height of 40 mm.

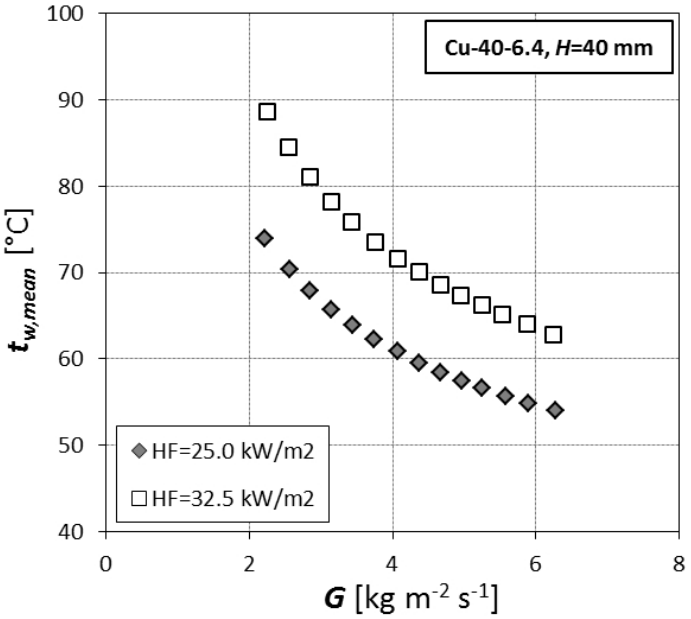

Figure 1.24: Mean wall temperature for the Cu-40-6.4 foam with a core foam height of 40 mm.

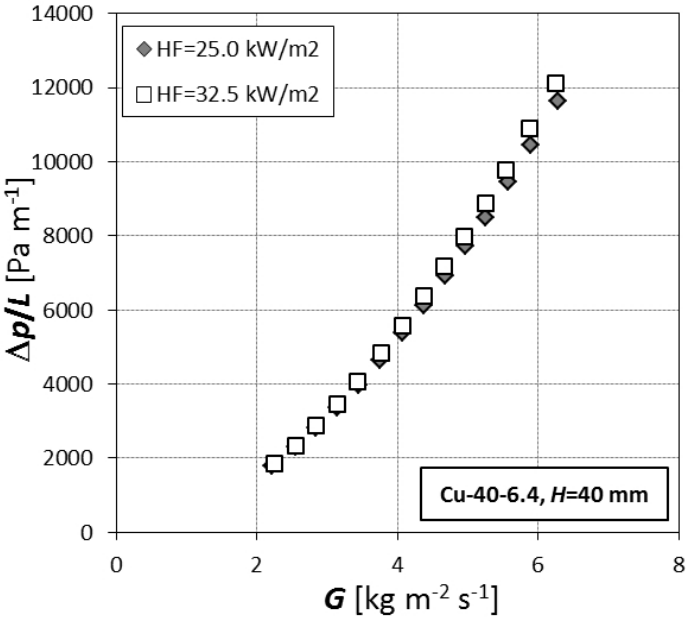

Figure 1.25: Pressure gradient for the Cu-40-6.4 foam with a core foam height of 40 mm.

1.7.7 Cu-20-6.5, H=40 mm

The experimental measurements of the Cu-20-6.5 with a foam core height of 40 mm are here reported. Figure 1.26 reports the overall heat transfer coefficient plotted against the air mass velocity for two different heat fluxes (HF=25.0, 32.5 kW m^{-2}). The global heat transfer coefficient appears to be independent on the imposed heat flux. It increases with increasing the air mass velocity, and it varies from 748 to 1073 W m^{-2} K^{-1}. The mean wall temperature, reported in figure 1.27, calculated with an inlet air velocity of 25 °C, decreases when the air flow rate increases; at a constant mass velocity, the mean wall temperature increases with the imposed heat flux. Finally, the pressure gradient as a function of the air mass velocity is reported in figure 1.28. It appears that the pressure gradient increases as the mass velocity increases, according to the Forchheimer equation, and it varies from 1645 to 9073 Pa m^{-1}. The heat flux has no effect on the pressure gradient in the tested working conditions. From the procedure reported in equations 1.15 and 1.16, it is possible to calculate the permeability and the inertia coefficient, and they are 1.770×10^{-7} m^2 and 0.1230, respectively.

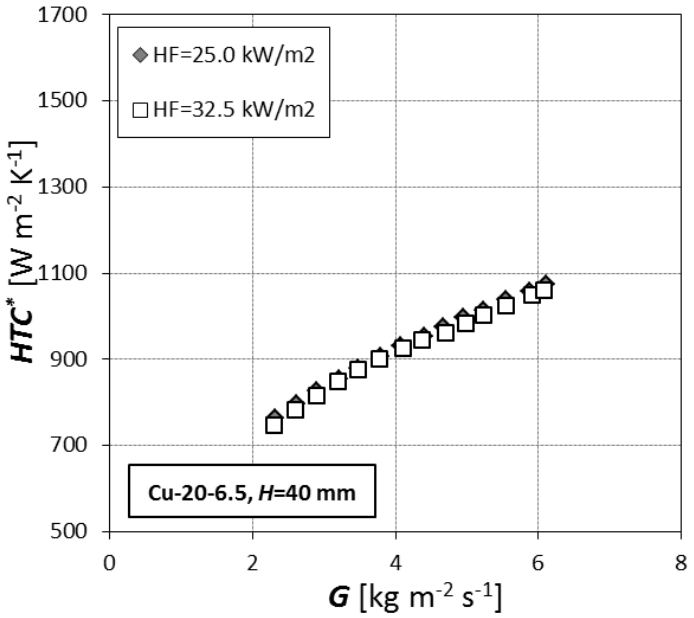

Figure 1.26: Overall heat transfer coefficient for the Cu-20-6.5 foam with a core foam height of 40 mm.

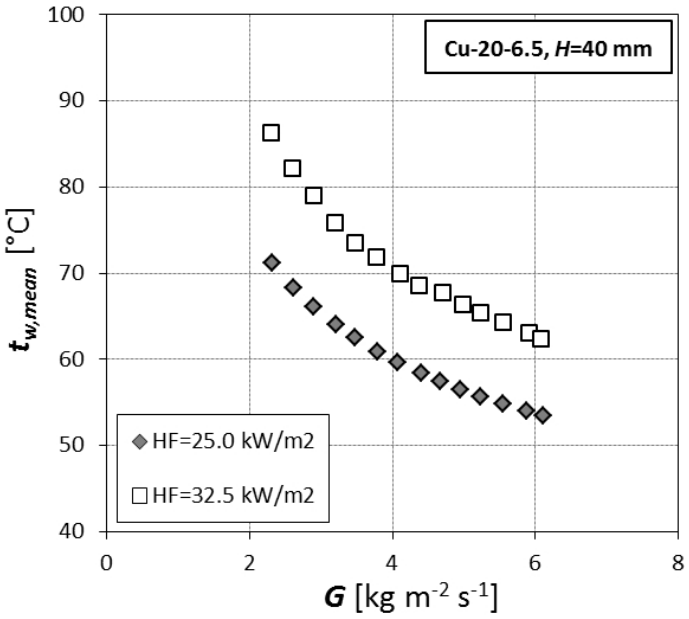

Figure 1.27: Mean wall temperature for the Cu-20-6.5 foam with a core foam height of 40 mm.

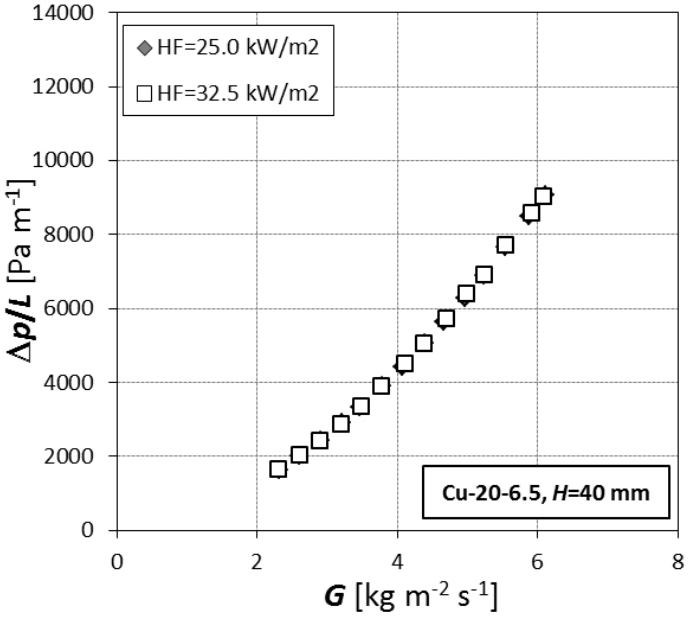

Figure 1.28: Pressure gradient for the Cu-20-6.5 foam with a core foam height of 40 mm.

1.7.8 Cu-10-6.6, H=40 mm

The experimental measurements of the Cu-10-6.6 with a foam core height of 40 mm are here reported. Figure 1.29 reports the overall heat transfer coefficient plotted against the air mass velocity for two different heat fluxes (HF=25.0, 32.5 kW m^{-2}). The global heat transfer coefficient appears to be independent on the imposed heat flux. It increases with increasing the air mass velocity, and it varies from 720 to 1043 W m^{-2} K^{-1}. The mean wall temperature, reported in figure 1.30, calculated with an inlet air velocity of 25 °C, decreases when the air flow rate increases; at a constant mass velocity, the mean wall temperature increases with the imposed heat flux. Finally, the pressure gradient as a function of the air mass velocity is reported in figure 1.31. It appears that the pressure gradient increases as the mass velocity increases, according to the Forchheimer equation, and it varies from 1110 to 6777 Pa m^{-1}. The heat flux has no effect on the pressure gradient in the tested working conditions. From the procedure reported in equations 1.15 and 1.16, it is possible to calculate the permeability and the inertia coefficient, and they are 2.582×10^{-7} m^2 and 0.1032, respectively.

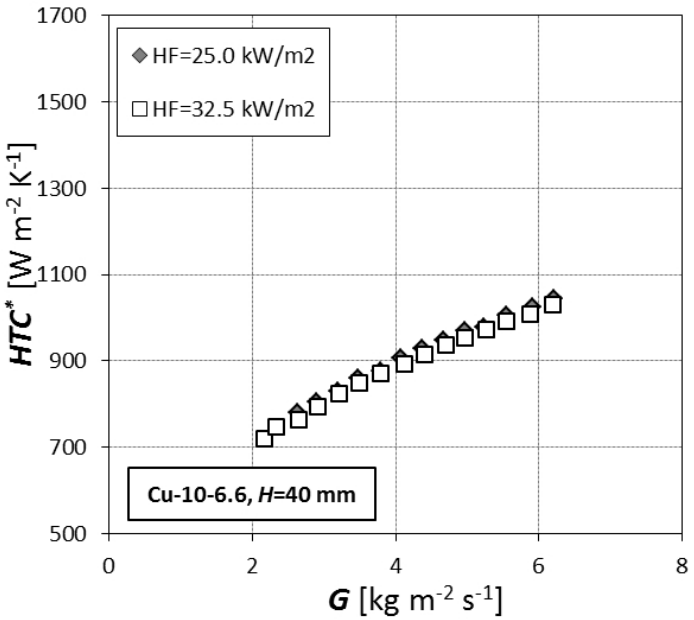

Figure 1.29: Overall heat transfer coefficient for the Cu-10-6.6 foam with a core foam height of 40 mm.

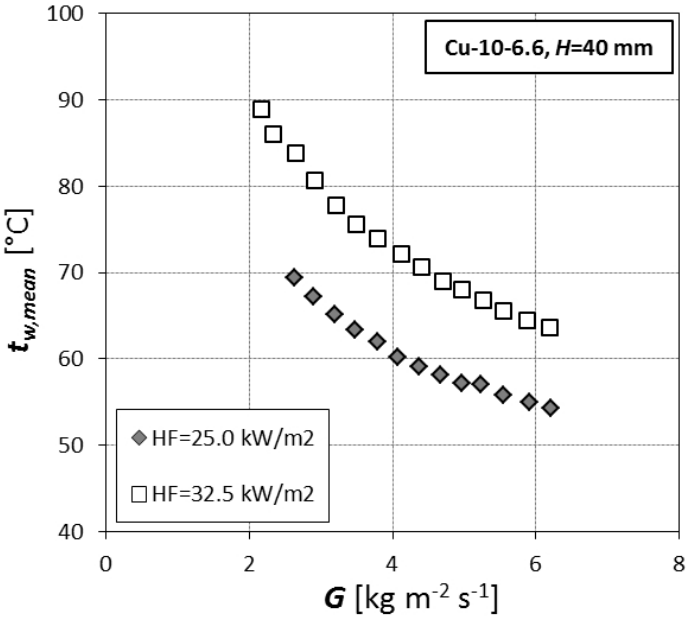

Figure 1.30: Mean wall temperature for the Cu-10-6.6 foam with a core foam height of 40 mm.

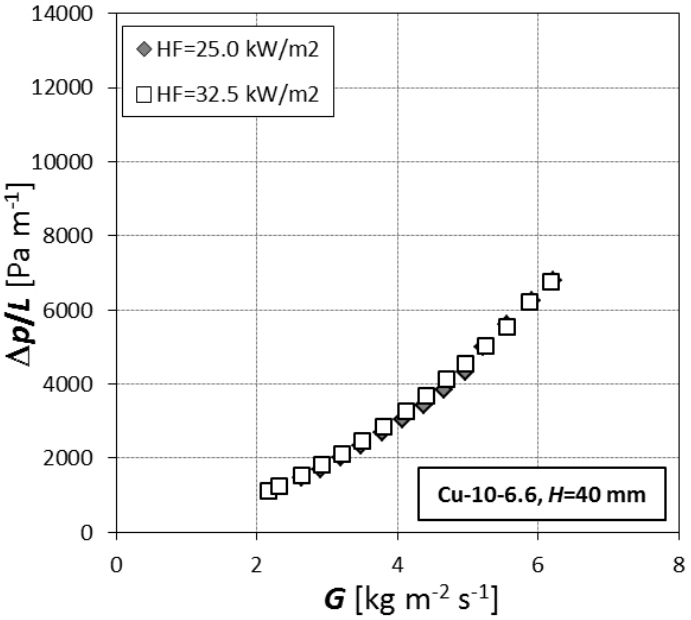

Figure 1.31: Pressure gradient for the Cu-10-6.6 foam with a core foam height of 40 mm.

1.7.9 Cu-5-6.5, H=40 mm

The experimental measurements of the Cu-5-6.5 with a foam core height of 40 mm are here reported. Figure 1.32 reports the overall heat transfer coefficient plotted against the air mass velocity for two different heat fluxes (HF=25.0, 32.5 kW m^{-2}). The global heat transfer coefficient appears to be independent on the imposed heat flux. It increases with increasing the air mass velocity, and it varies from 777 to 1089 W m^{-2} K^{-1}. The mean wall temperature, reported in figure 1.33, calculated with an inlet air velocity of 25 °C, decreases when the air flow rate increases; at a constant mass velocity, the mean wall temperature increases with the imposed heat flux. Finally, the pressure gradient as a function of the air mass velocity is reported in figure 1.34. It appears that the pressure gradient increases as the mass velocity increases, according to the Forchheimer equation, and it varies from 1146 to 6384 Pa m^{-1}. The heat flux has no effect on the pressure gradient in the tested working conditions. From the procedure reported in equations 1.15 and 1.16, it is possible to calculate the permeability and the inertia coefficient, and they are 4.190×10^{-7} m^2 and 0.1170, respectively.

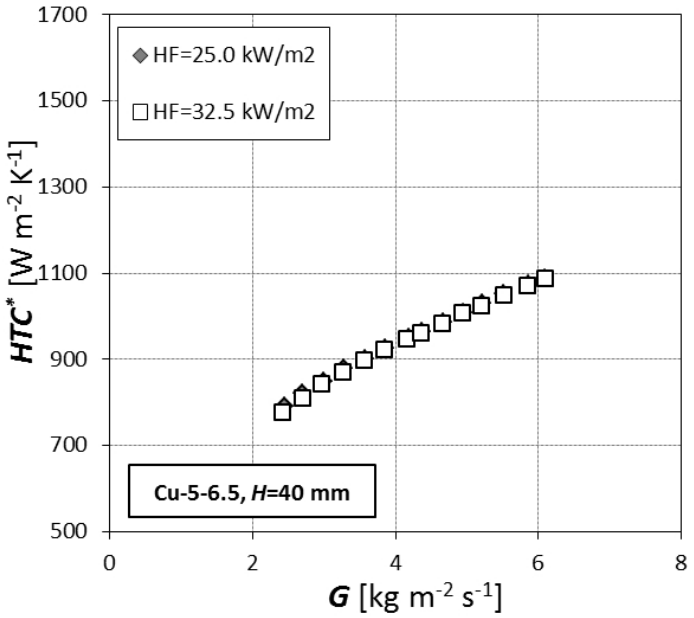

Figure 1.32: Overall heat transfer coefficient for the Cu-5-6.5 foam with a core foam height of 40 mm.

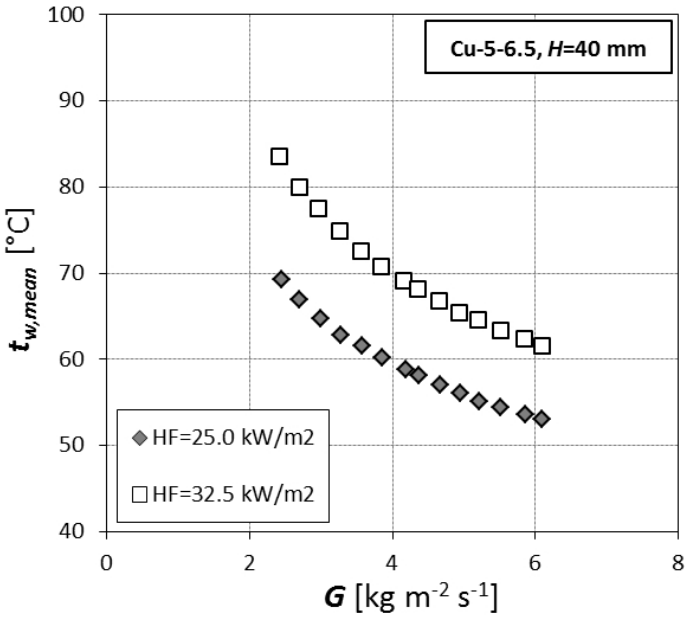

Figure 1.33: Mean wall temperature for the Cu-5-6.5 foam with a core foam height of 40 mm.

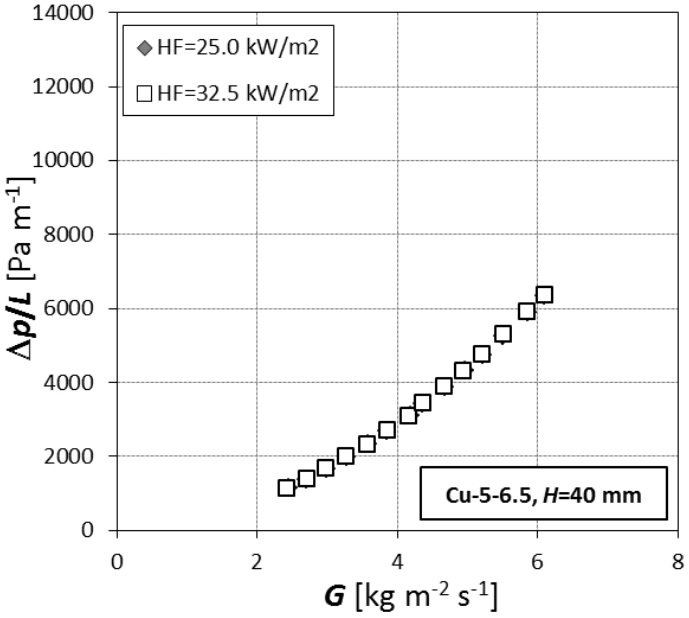

Figure 1.34: Pressure gradient for the Cu-5-6.5 foam with a core foam height of 40 mm.

1.8 Comparison among the tested copper foams

1.8.1 Overall heat transfer comparisons

The following analysis of the experimental results aims to highlight the effects of each geometrical parameter, i.e. number of pores per linear inch (PPI), porosity, and foam core height, on the thermal performance of such materials.

Effect of the pore density

Figure 1.35 compares the heat transfer performance of the four copper foams each with a different number of pores per inch (5, 10, 20, and 40 PPI) but almost constant porosity ($\varepsilon = 0.933 - 0.934$) and the same foam core height (H=20 mm). For the sake of clarity, since it is proved that the heat flux has no effect on the overall heat transfer coefficient, only results at 25.0 kW m^{-2} are reported in the next figures. All the copper foams exhibit the same behavior, the overall heat transfer coefficient

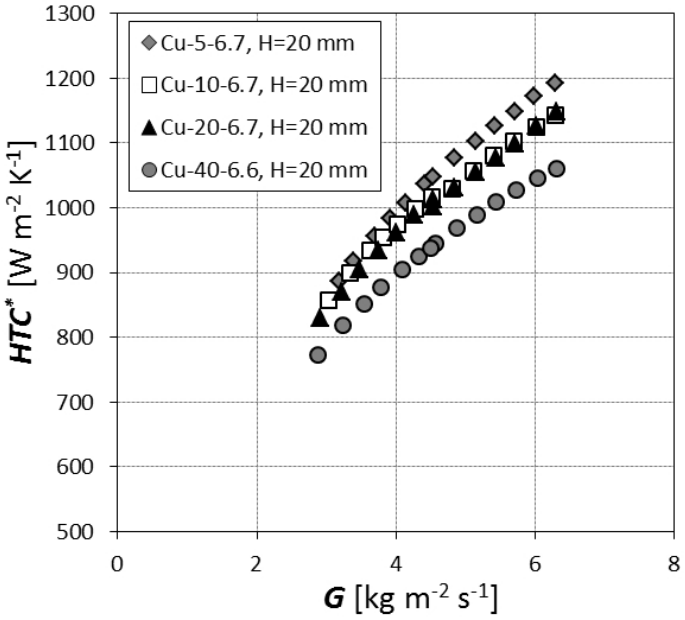

Figure 1.35: Pore density effects at constant porosity ($\varepsilon = 0.93$) and foam height (H = 20 mm) on the overall heat transfer coefficient plotted against the mass velocity.

increases with the air mass velocity; the data can be interpolated with the following simple equation:

$$HTC^* = A \cdot \dot{m}_{air}^B \tag{1.48}$$

Table 1.4: Coefficients A and B of equation 1.48 for the five copper foams with a foam core height of 20 mm.

Foam	A	B
Cu-5-6.7	7511	0.42
Cu-10-6.7	6052	0.38
Cu-10-9.5	10559	0.44
Cu-20-6.7	6903	0.41
Cu-40-6.6	6132	0.40

Table 1.4 reports the values of the coefficients A and B of equation 1.48. It is worthy to underline that the values of the exponent B of equation 1.48 are 0.42 for Cu-5-6.7, 0.38 for Cu-10-6.7, 0.41 for Cu-20-6.7, and 0.40 for Cu-40-6.6. This means that the tested copper foams show almost the same dependence on the air mass velocity.

Even if the values of the exponent B are similar for the four samples, the Cu-5-6.7 foam sample shows the highest overall heat transfer coefficients, while the lowest values are relative to the Cu-40-6.6 sample, being around 10-12% lower than those of Cu-5-6.7. This can be explained by comparing the values of the constant A of equation 1.4: for the 5 PPI foam is 7511, whereas for the 40 PPI foam is 6132.

The experimental measurements for the 10 PPI and 20 PPI do not differ much; this transfer behavior can be explained by considering the different foam finned surface efficiency of these two copper foams. As listed in table 1.1, the surface area per unit of volume of the 20 PPI copper foam ($a_{sv} = 1148\,\mathrm{m^2\,m^{-3}}$) is 1.64 times higher than that of 10 PPI ($a_{sv} = 698\,\mathrm{m^2\,m^{-3}}$); this means that the two foams might exploit the same overall heat transfer coefficient only if the foam finned surface efficiency of the 10 PPI is some 60-70% higher than that of the 20 PPI sample. Further, referring to the classical fin-theory [23], the fin efficiency depends on the fin thickness and length, more precisely it increases as the fin thickness increases and fin length decreases. Considering the measured fiber thickness and

length reported in table 1.1, Cu-10-6.7 presents longer and thicker fibers than Cu-20-6.7, but fewer pores. Therefore, the equivalent length of an ideal fin of Cu-10-6.7 should be shorter and the fin thickness greater than that of Cu-20-6.7. This consideration quantitatively confirms that the foam finned surface efficiency of Cu-10-6.7 is higher than that of Cu-20-6.7.

Effect of the porosity

The porosity effects on the heat transfer behavior are highlighted in figure 1.36, where the overall heat transfer coefficient is plotted against the mass velocity for two copper foams with the same pore density (10 PPI) and the same foam core height (20 mm).

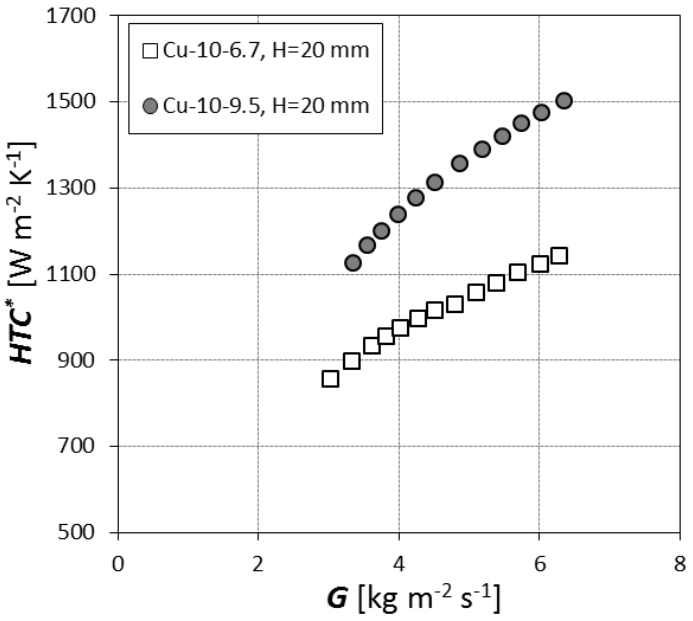

Figure 1.36: Porosity effects at constant pore density (10 PPI) and foam height (H = 20 mm) on the overall heat transfer coefficient plotted against the mass velocity.

The heat transfer performance improves when porosity decreases. As listed in table 1.4, Cu-10-9.5 shows the highest values of coefficients A and B, being 10559 and 0.44, respectively. In particular, the Cu-10-9.5 sample, which presents a porosity of ε=0.905, exploits 1.25-1.31 times higher overall heat transfer coefficients than those measured for Cu-10-6.7, which presents a porosity of ε=0.933. According to table

1.1, the mere increase of the heat transfer surface between Cu-10-9.5 and Cu-10-6.7 is about 19%: this means that the measured heat transfer enhancement is also due to the higher foam finned surface efficiency exhibited by the Cu-10-9.5, since it presents a slightly thicker fiber than that of Cu-10-6.7.

Effect of the foam core height

The effects of the foam core height are reported in figure 1.37, where the overall heat transfer coefficient is plotted against the mass velocity for two 10 PPI foams and two 40 PPI foams having the same porosity but different core foam height.

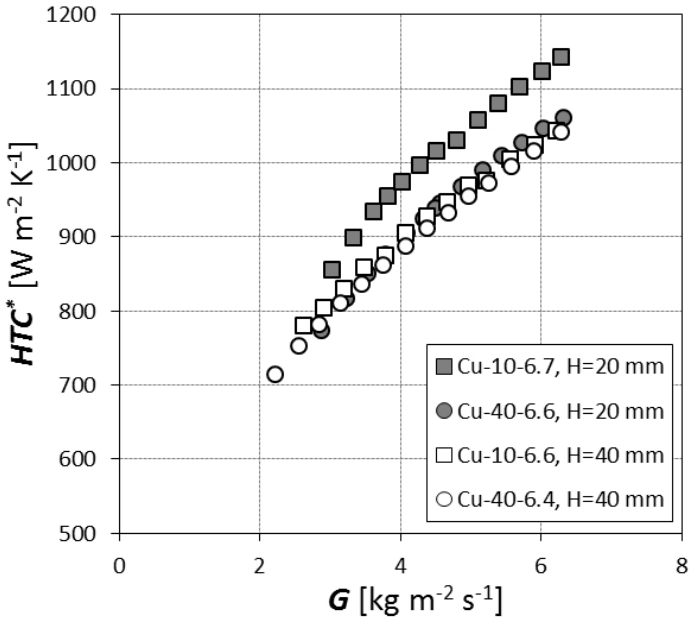

Figure 1.37: Porosity effects at porosity (ε=0.93) on the overall heat transfer coefficient plotted against the mass velocity.

Considering first the effect of the foam core height on the 10 PPI copper foams, it can be seen that the 20 mm high foam presents higher overall heat transfer coefficients than those of the 40 mm high sample. These two copper foams present almost the same porosity and accordingly, as reported in table 1.1, they have almost the same surface area per unit of volume (around 695 m^2 m^{-3}). This means that the 20 mm high foam has half heat transfer area than the 40 mm high foam, but the 20 mm high foam has higher heat transfer performances. Therefore, the foam

finned surface efficiency of the 20 mm high foam (Cu-10-6.7) is more than double than that of the 40 mm high foam (Cu-10-6.5), due to its lower equivalent fin.

In the case of 40 PPI foams, the 40 mm foam sample and the 20 mm foam sample show the same overall heat transfer coefficient. Again, these two foams present almost the same porosity and, thus, similar value of surface area per unit of volume: this means that the 40 mm high foam has double heat transfer area than the 20 mm high one. Since the two specimens show the same overall heat transfer coefficient, the foam finned surface efficiency of the 20 mm is some double than that of the 40 mm high foam sample.

1.8.2 Pressure drop comparisons

The following analysis of the experimental results aims to highlight the effects of each geometrical parameter, i.e. number of pores per linear inch (PPI), porosity, and foam core height, on the hydraulic performance of such materials.

Effect of the pore density

Figure 1.38 compares the hydraulic performance of the four copper foams each with a different number of pores per inch (5, 10, 20, and 40 PPI) but almost constant porosity ($\varepsilon = 0.933 - 0.934$) and the same foam core height (H=20 mm). As it appears, the pressure gradient increases as the number of pores per linear inch increases from 5 to 40 PPI. Cu-40-6.6 sample presents the highest pressure gradients, whereas the Cu-10-6.7 and Cu-5-6.7 show similar pressure gradient expecially at low velocities. Increasing the air mass velocity, the 5 PPI shows somewhat lower pressure drop when compared with the 10 PPI sample with the same porosity.

Effect of the porosity

Figure 1.39 compares the hydraulic performance of the four copper foams each with different porosity (ε=0.905 and 0.933) but the same pore density (10 PPI) and the same foam core height (H=20 mm). As it appear from the figure, when the pore density is kept constant, the pressure gradient slightly decreases as the porosity decreases. This results where also found in Mancin et al. [11] for aluminum foam samples with different foam core heights.

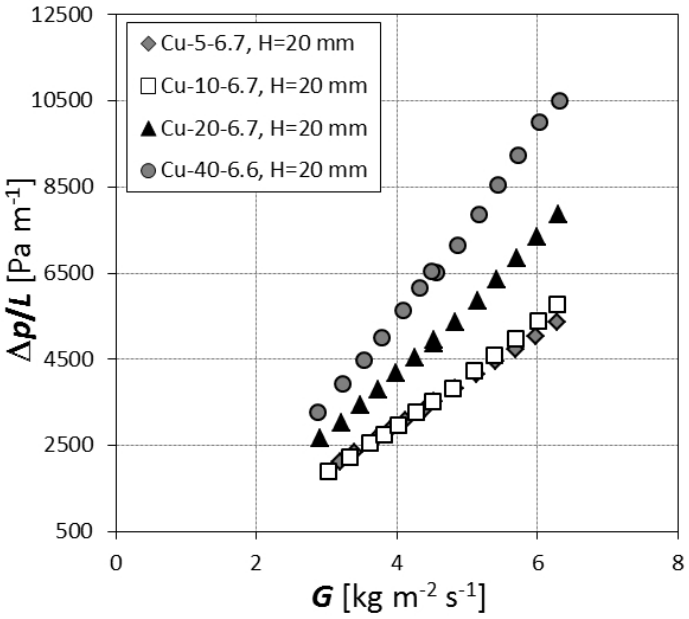

Figure 1.38: Pore density effects at constant porosity ($\varepsilon = 0.93$) and foam height ($H = 20$ mm) on the pressure gradient plotted against the mass velocity.

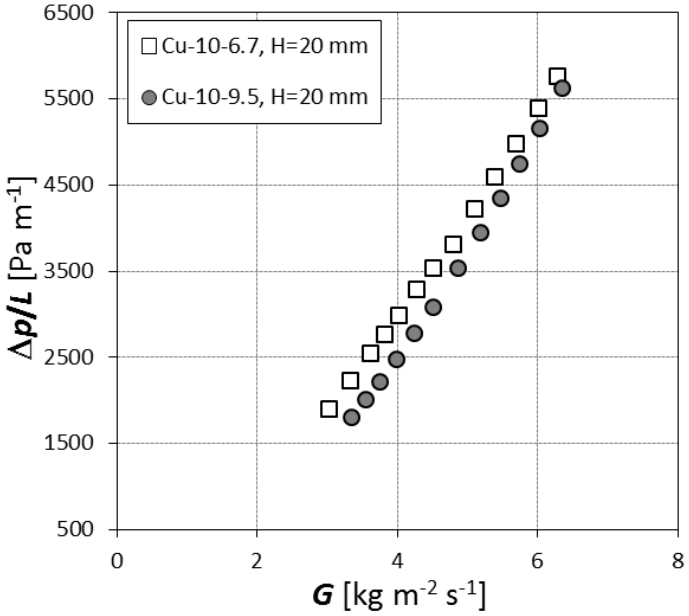

Figure 1.39: Porosity effects at constant pore density (10 PPI) and foam height ($H = 20$ mm) on the pressure gradient plotted against the mass velocity.

1.8.3 Overall thermal performance comparisons

The overall heat transfer coefficient is often used to compare performances of different enhanced surfaces. Further information about the effective heat transfer performance of the foam samples can be provided by the interstitial heat transfer coefficient, defined in equation 1.7 as:

$$\alpha^* = \alpha \cdot \Omega^* = \frac{HTC^*}{1 + a_{sv} \cdot H} \tag{1.7}$$

This interstitial heat transfer coefficient α^* provides more thorough comparisons between enhanced surfaces. Anyway, in case of foams, it is not possible to distinguish the effect of α from Ω^*. Figure 1.40 compares the interstitial heat transfer coefficients

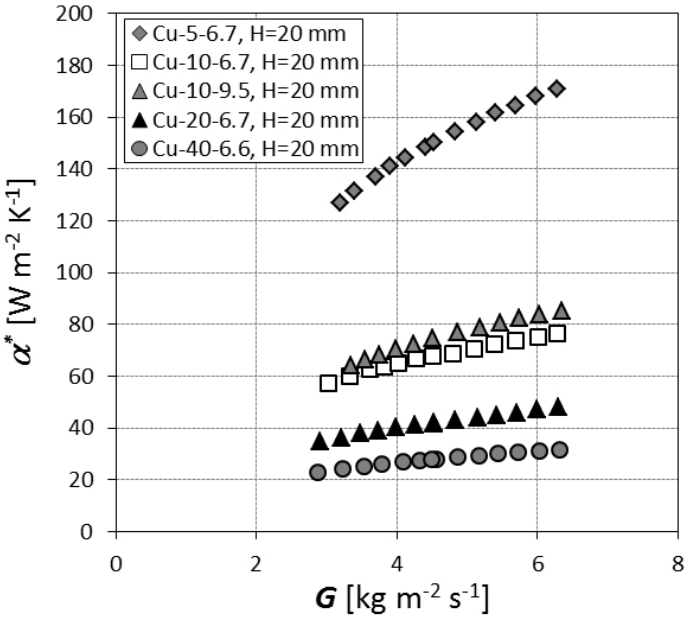

Figure 1.40: Interstitial heat transfer coefficient for the 20 mm high copper foams plotted against the mass velocity.

for the tested 20 mm high copper foams as a function of the mass velocity. Generally speaking, the interstitial heat transfer performance decreases as the number of pores per inch increases and, at constant pore density (10 PPI), Cu-10-9.5 shows higher interstitial heat transfer coefficients than those of Cu-10-6.7.

Cu-5-6.7 exhibits 5.5 times higher interstitial heat transfer coefficients than those

measured for Cu-40-6.6. It should be noted that the interstitial heat transfer coefficients for Cu-10-9.5, which are the highest values between 10, 20, and 40 PPI samples, remain two times lower than those measured for Cu-5-6.7. This experimental evidence can be explained when considering the geometrical characteristics of the five 20 mm foam samples reported in table 1.1. The foam Cu-5-6.7 presents the thickest and longest fibers and the least number of pores per linear inch. This means that the equivalent fin for the Cu-5-6.7 sample, which starts from the heated base and ends at the top plate, consists of the shortest and thickest fin among the five samples. Therefore, this equivalent fin would present the highest finned foam surface efficiency. According to the results plotted in figure 1.40, Cu-5-6.7 presents a foam structure which promotes higher heat transfer augmentation when compared to the other samples. The results clearly show that the pore density has a more significant effect on the interstitial heat transfer coefficient than porosity. Similar considerations can be drawn for the 40 mm high samples.

Comparing global and interstitial heat transfer coefficients (figure 1.35, 1.36, and 1.40), it appears that the surface area plays an important role on the overall performance of the foam. In particular, Cu-10-9.5, which shows lower interstitial heat transfer coefficients than Cu-5-6.7, exhibits the highest overall heat transfer coefficients. This can be explained considering that Cu-10-9.5 has a surface area some 2.8 times than that of Cu-5-6.7. Therefore, the optimal foam configuration, considering porosity, pore density, and volume, has to be sought comparing both the interstitial and the overall heat transfer performance of the foam, at constant pressure drop.

The tested foams were compared by means of the interstitial heat transfer coefficient and the pumping power (P) per area density (a_{sv}) which is defined as:

$$\frac{P}{a_{sv}} = \frac{\Delta p \cdot \dot{V}}{A_{tot}} \cdot V = \frac{\Delta p \cdot \dot{V}}{a_{sv}} \tag{1.49}$$

Therefore, using the pressure drop and geometrical database collected, it is possible to calculate this experimental parameter. The results of these calculations are reported in figure 1.41 for the 20 mm high copper foams. At constant pumping power per area density, the heat transfer performance of the copper foams decreases as the pore density (i.e. PPI) increases, whereas, for a selected copper foam, the

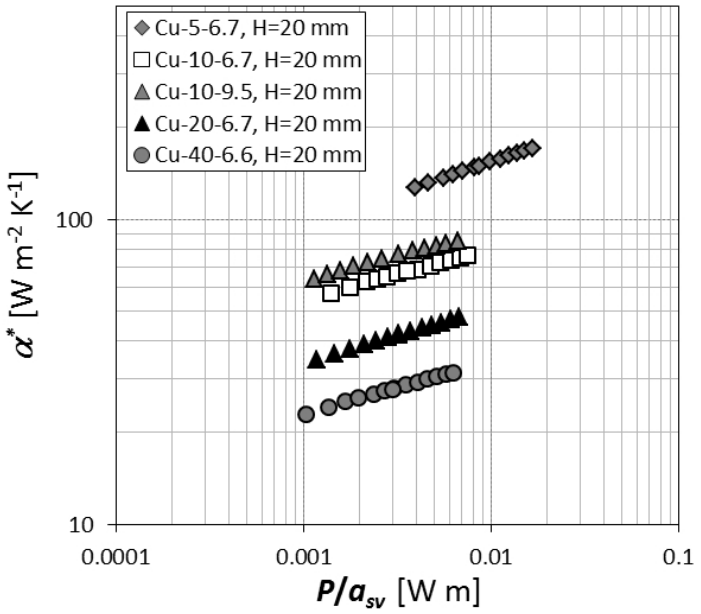

Figure 1.41: Interstitial heat transfer coefficient for the 20 mm high copper foams plotted against the pumping power per area density.

interstitial heat transfer coefficient α^* increases as the pumping power per area density increases. From the analysis of the diagram, Cu-5-6.5 shows again the highest interstitial heat transfer coefficient over the entire range of investigated operating conditions. For instance at a constant value of 0.003 W m of pumping power per area density, Cu-5-6.7 exhibits an interstitial heat transfer coefficient α^* around 130 W m^{-2} K^{-1} while for Cu-10-9.5 it is around 75 W m^{-2} K^{-1}, for Cu-20-6.7 and Cu-40-6.6 are equal to 40 W m^{-2} K^{-1} and for 30 W m^{-2} K^{-1}, respectively.

Finally, the wall temperature is a meaningful parameter because it is representative of the temperature of the electronic device attached to the spreader. The mean air temperature has been calculated at a constant inlet air temperature of 25 °C, as reported in equations 1.8-1.11. Figure 1.42 plots the calculated mean wall temperature for the tested 20 mm high copper foams as a function of the pumping power per area density. As it appears, the mean wall temperature monotically decreases as the pumping power per area density increases. This comparison shows the superior heat transfer capabilities of Cu-10-9.5 sample, which keeps the wall at the lowest temperature level across the range of operative conditions. At constant pumping

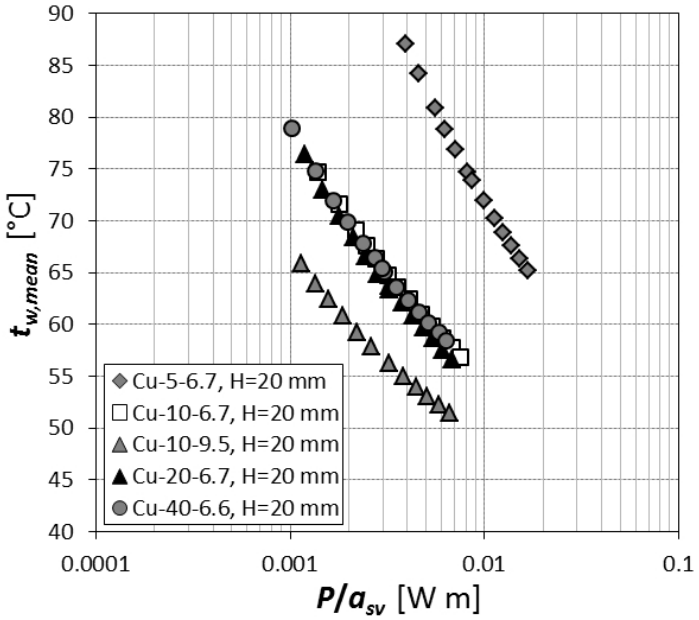

Figure 1.42: Mean wall temperature for the 20 mm high copper foams plotted against the pumping power per area density.

power per area density, the 5 PPI copper foam (Cu-5-6.7) exhibits higher mean wall temperatures than those of the other three samples: Cu-10-6.7, Cu-20-6.7, and Cu-40-6.6.

1.9 Heat transfer prediction models

1.9.1 Model of Ghosh [24]

Assuming a simple cubic structure of the foam, Ghosh [24] took into account the heat conduction through ligaments of the foams in conjugation with convective heat flow over the struts in all directions, as reported in figure 1.43. The foam can so be imagined as a bunch of several independent x-struts with projections along y and z directions. The protrusions along y and z direction are of length $d_p/2$. The strut

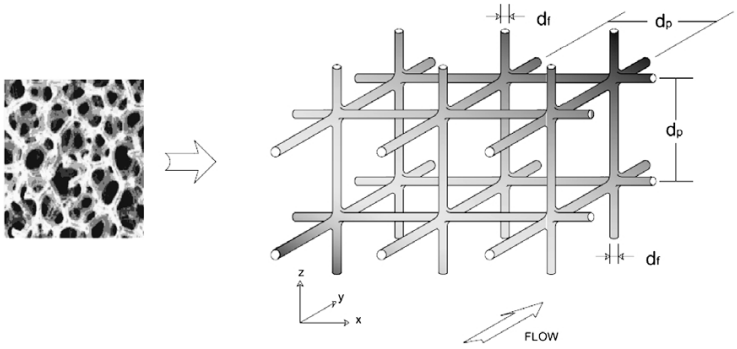

Figure 1.43: Simple cubic representation of porous foam [24].

diameter d_f can be related to the pore size D_p as [25]:

$$\frac{d_f}{d_p} = 2\sqrt{\frac{1-\varepsilon}{3\pi}}\frac{1}{G} \tag{1.50}$$

where

$$G = 1 - e^{-(1-\varepsilon)/0.04} \tag{1.51}$$

The heat transfer occurring across z and y is given by:

$$q_z = q_y = \sqrt{hPk_fA_c}(T_x - T_\infty)\left[\frac{\cosh(m\ d_p) - 1}{\sinh(md_p)}\right] = hPd_p(T_x - T_\infty)\eta_{1/2} \tag{1.52}$$

where h is the heat transfer coefficient, P the perimeter of the strut, k_f the thermal conductivity of the foam material, A_c the cross sectional area of strut, T_∞ the fluid stream temperature, and

$$\eta_{1/2} = \frac{\tanh m(d_p/2)}{m(d_p/2)} \tag{1.53}$$

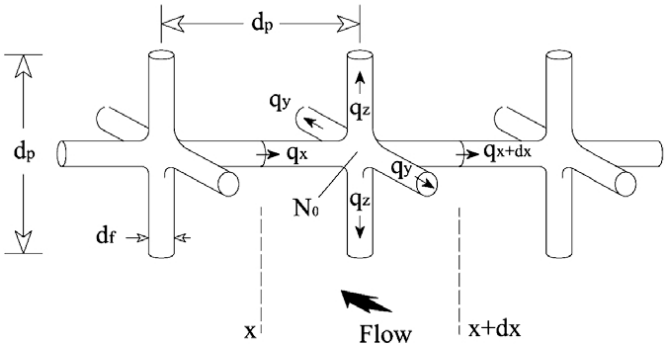

Figure 1.44: Differential element for deriving governing foam equation [24].

$$P = \pi d_f \tag{1.54}$$

$$A_c = \frac{\pi d_f^2}{4} \tag{1.55}$$

$$m = \sqrt{\frac{4h}{k_f d_f}} \tag{1.56}$$

where $\eta_{1/2}$ is the efficiency of half strut. Applying an energy balance at the nodal point N_0 in figure 1.44, the governing differential equation for the temperature difference (θ) between the solid and the convective fluid can be written as:

$$\frac{\mathrm{d}q_x}{\mathrm{d}x} + hP(T_x - T_\infty)(1 + 4\eta_{1/2}) = 0 \tag{1.57}$$

Substituting $q_x = -k_f A_c \frac{\mathrm{d}T_x}{\mathrm{d}x}$ and putting $\theta = T_x - T_\infty$:

$$\frac{\mathrm{d}^2\theta}{\mathrm{d}x^2} - M^2\theta = 0 \tag{1.58}$$

where

$$M = \sqrt{\frac{hP}{k_f A_c}(1 + 4\eta_{1/2})} = m\sqrt{1 + 4\eta_{1/2}} \tag{1.59}$$

With adiabatic boundary conditions at the top, the efficiency of the foam η_f can be expressed with the following equation:

$$\eta_f = \frac{\tanh(ML)}{ML} \tag{1.60}$$

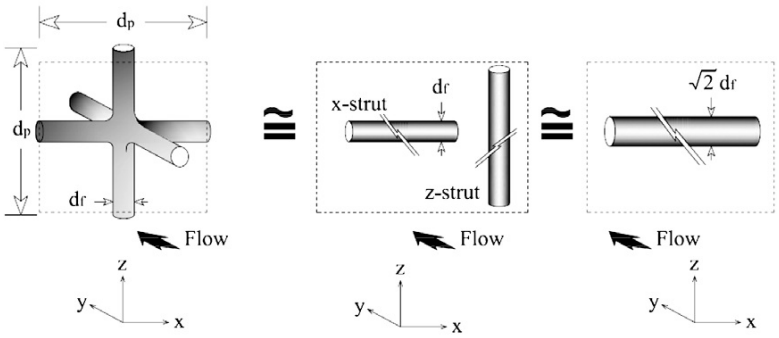

Figure 1.45: Increase in the effective strut diameter [24].

where L is the length of the foam.

If the fluid flow is occurring along the y-direction (see figure 1.45), the x- and z-struts are at right angle to the direction of flow, whereas the y-strut is parallel to the fluid flow. Thus it can be imagined that there is an inflated single tube at right angle to its paths, which takes into account the x- and z-struts, which are not distinguishable by the fluid, and the resulting single-strut becomes $\sqrt{2}d_f$. If h_{tube} is the heat transfer coefficient for a single tube, the interstitial heat transfer coefficient in open cell foams can be defined as:

$$h = \frac{\sqrt{2}h_{tube}}{1 + 4\eta_{1/2}} \tag{1.61}$$

Ghosh [24] suggested to use

$$\mathrm{Nu_{tube}} = \frac{h_{tube} \cdot d_f}{\lambda_{air}} = 0.8\,\mathrm{Re}^{0.8}\,\mathrm{Pr}^{0.33} \tag{1.62}$$

as reported in [23].

Figure 1.46 reports a comparison between experimental and calculated overall heat transfer coefficient. As it appears, this model is able to satisfactory estimate only the values of the 20 PPI foam sample, whereas it underestimate of about 70% the values of the 5 PPI foams.

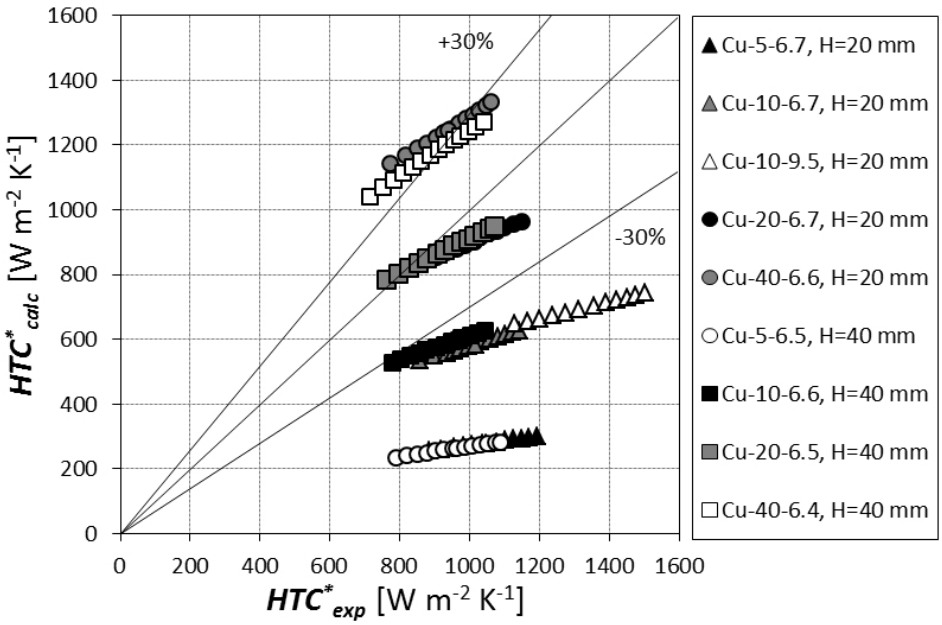

Figure 1.46: Comparison between experimental and calculated overall heat transfer coefficient with the correlation of [24].

1.9.2 Model of Mancin et al. [10]

Starting from a database of experimental values of overall heat transfer coefficients carried out during air forced convection through aluminum foams, Mancin et al. [10] proposed a simplified scheme for overall foam finned surface efficiency and heat transfer coefficient calculations. The overall heat transfer coefficient HTC^* can be calculated with the following expression:

$$HTC^* = \alpha \cdot a_{sv} \cdot H \cdot \Omega^* = \alpha \cdot a_{sv} \cdot H \cdot \left(\frac{1 + \Omega \cdot a_{sv} \cdot H}{1 + a_{sv} \cdot H} \right) \tag{1.63}$$

with

$$m = \left(\frac{4 \cdot \alpha}{\lambda_{mat} \cdot t} \right)^{0.5} \tag{1.64}$$

For all the foams except the 5 PPI one:

$$\alpha = \frac{\lambda_{air}}{t} \cdot 0.02 \cdot \mathrm{Re}^{0.9}\, \mathrm{Pr}^{0.33} \tag{1.65}$$

and for the 5 PPI foams:

$$\alpha = \frac{\lambda_{air}}{t} \cdot 0.058 \cdot \mathrm{Re}^{0.75}\,\mathrm{Pr}^{0.33} \tag{1.66}$$

The Reynolds number and the Prandtl number are defined as:

$$\mathrm{Re} = \frac{G \cdot t}{\mu_{air} \cdot \varepsilon} \qquad \mathrm{Pr} = \frac{\mu_{air} \cdot c_{p,air}}{\lambda_{air}} \tag{1.67}$$

where G is the air mass velocity, and λ_{air}, μ_{air}, and $c_{p,air}$ are the air conductivity, dynamic viscosity and specific heat at constant pressure calculated at the mean values of temperature and pressure. The equivalent fin length L can be calculated as:

$$L = 6.6 \cdot H \cdot \mathrm{PPI}^{0.99} \cdot (0.0254 - t \cdot \mathrm{PPI}) \tag{1.68}$$

where L, H, and t are expressed in meters and PPI in pores per linear inch.

Figures 1.47 reports a comparison between experimental and calculated overall heat transfer coefficient. Experimental data were measured by Mancin et al. [10] during air forced convection through aluminum foams: the experimental values are well estimated, with a relative deviation of 2.3%, an absolute deviation of 12.0%, and a standard deviation of 13.3%.

Figure 1.48 shows a comparison between experimental and calculated overall heat transfer coefficient for the copper foams under investigation. Even though the correlation works well for aluminum foams, it tends to underestimate the experimental values of the copper samples with a relative deviation of -25.0%, an absolute deviation of 25.4%, and a standard deviation of 11.4%.

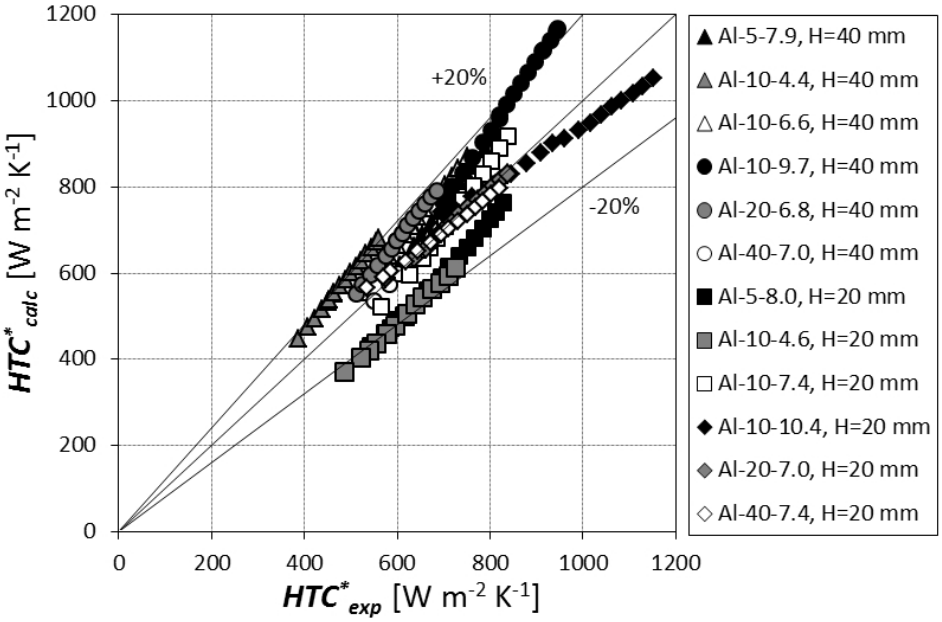

Figure 1.47: Comparison between experimental and calculated overall heat transfer coefficient with the correlation of Mancin et al. [10] for aluminum foams tested in [10].

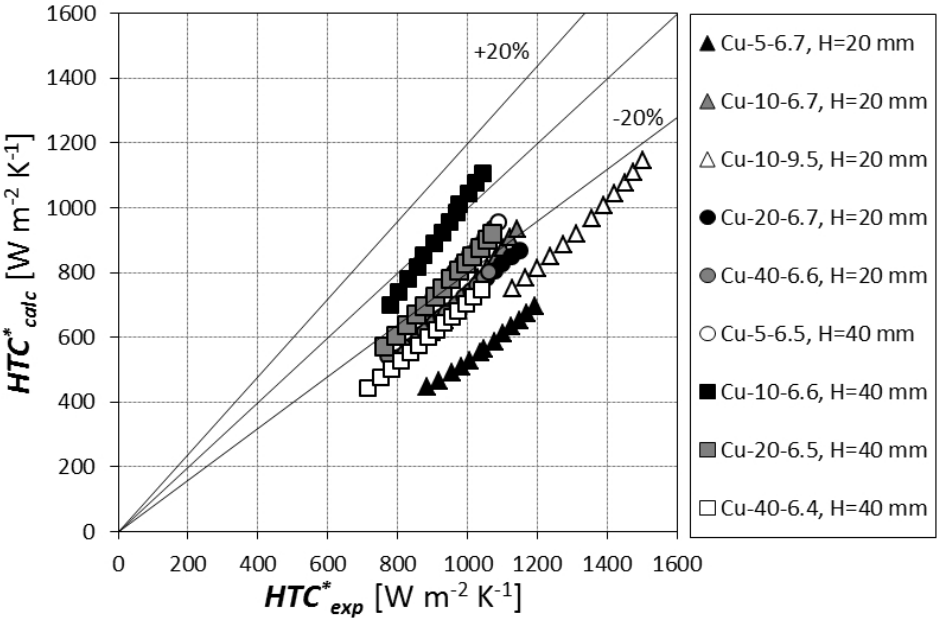

Figure 1.48: Comparison between experimental and calculated overall heat transfer coefficient with the correlation of Mancin et al. [10] for copper foams.

1.9.3 A new heat transfer model

The experimental results have permitted to understand the effects of different parameters: foam core height, porosity, number of pores per linear inch, and material, on the thermal and hydraulic behavior of such materials during air forced convection. On the basis of a large experimental database, including also previous results on aluminum foams [10], a new correlation was developed for the estimation of the heat transfer behavior. The heat transfer coefficient defined in equation 1.7 can be modeled as follows:

$$\alpha = 0.418 \cdot \mathrm{Re}^{0.53} \cdot \mathrm{Pr}^{0.33} \cdot \frac{\lambda_{air}}{t} \tag{1.69}$$

The Reynolds number (30<Re<200) and the Prandtl number (Pr=0.3) are defined as in equation 1.67. The foam finned surface efficiency can be calculated with:

$$\Omega^* = \frac{1 + \Omega \cdot a_{sv} \cdot H}{1 + a_{sv} \cdot H} = \frac{1 + \dfrac{\tanh(m \cdot L)}{m \cdot L}}{1 + a_{sv} \cdot H} \tag{1.70}$$

and the two parameters m and L were regressed using the experimental database:

$$m = \left(\frac{4 \cdot \alpha}{t \cdot \lambda_{mat}}\right)^{0.5} \cdot \left(\frac{\lambda_{mat}}{\lambda_{air}}\right)^{-0.52} \tag{1.71}$$

$$L = 1055 \cdot H^{1.18} \cdot \mathrm{PPI} \cdot (0.0254 - t \cdot \mathrm{PPI})^{0.66} \tag{1.72}$$

where α is the heat transfer coefficient calculated using equation 1.69, λ_{mat} is the thermal conductivity of the material, being 210 W m^{-1} K^{-1} for aluminum and 390 W m^{-1} K^{-1} for copper.

As reported in figure 1.49, the comparison between the suggested new model and the experimental database shows good agreement both for copper foams and for aluminum foams: the relative deviation is 1.4%, the absolute deviation 6.5%, and the standard deviation 5.1%.

This proposed model can be used to simulate the heat transfer behavior of metal foams as a function of the different geometrical characteristics and under different operating conditions. Table 1.5 reports the main geometrical parameters of the simulated metal foams.

Considering figure 1.50a, the foam finned surface efficiency is plotted against the

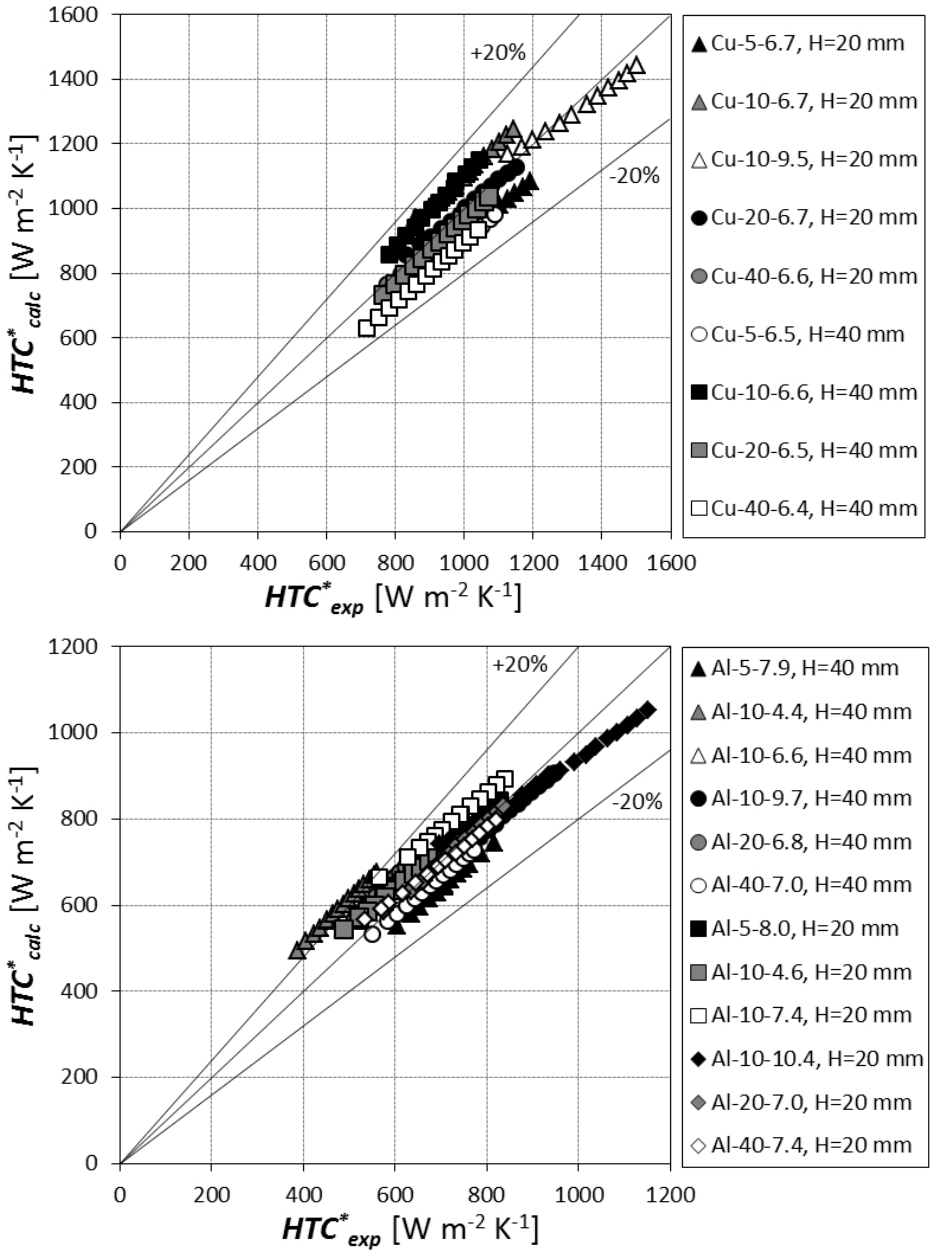

Figure 1.49: Comparison between calculated and experimental overall heat transfer coefficient for copper and aluminum foams with the new proposed equation.

foam height, as a function of the air mass velocity, for 5 PPI copper and aluminum foams, with a constant porosity of 0.93. It clearly appears that the foam finned surface efficiency decreases as the foam height increases. At a constant foam height,

Table 1.5: Geometrical parameters of the simulated metal foams.

PPI [in^{-1}]	ε [-]	t [mm]	a_{sv} m^{-1}
5	0.93	0.50	300
10	0.90	0.55	850
10	0.93	0.45	700
10	0.96	0.35	550
20	0.93	0.30	1150
40	0.93	0.25	1700

the foam finned surface efficiency decreases as the air mass velocity increases. Globally, the foam finned efficiency of the copper foams is greater than that of aluminum foams.

Figure 1.50b presents the effects of the pore density and of the foam height on the foam finned surface efficiency. In particular, keeping constant the porosity equal to 0.93, it appears that the foam finned surface efficiency decreases when increasing both the number of pores per inch and the foam height. The decreasing is much more evident as the pore density increases; at 20 mm of foam height, the efficiency of the 5 PPI foam is around Ω^*=0.57, that of 10 PPI is Ω^*0.33, Ω^*=0.15 for 20 PPI foam, and Ω^*=0.09 for 40 PPI foam. This diagram permits to understand what previously highlighted during the analysis of figure 1.37, where the 40 PPI copper foam with 20 mm and 40 mm high foam core height show almost the same overall heat transfer coefficient. This behavior has been explained considering that the foam efficiency of the 40 mm high sample is half than that of 20 mm high sample. The foam finned surface efficiency profile plotted in figure 1.50b for 40 PPI copper samples confirms that at H=40 mm the foam finned surface efficiency is half than that at H=20 mm.

The effects of the porosity on the foam finned surface efficiency are also shown in figure 1.50b, where three different copper foams with 10 PPI and a porosity from 0.90 and 0.96 are simulated. The foam finned surface efficiency decreases as the porosity increases.

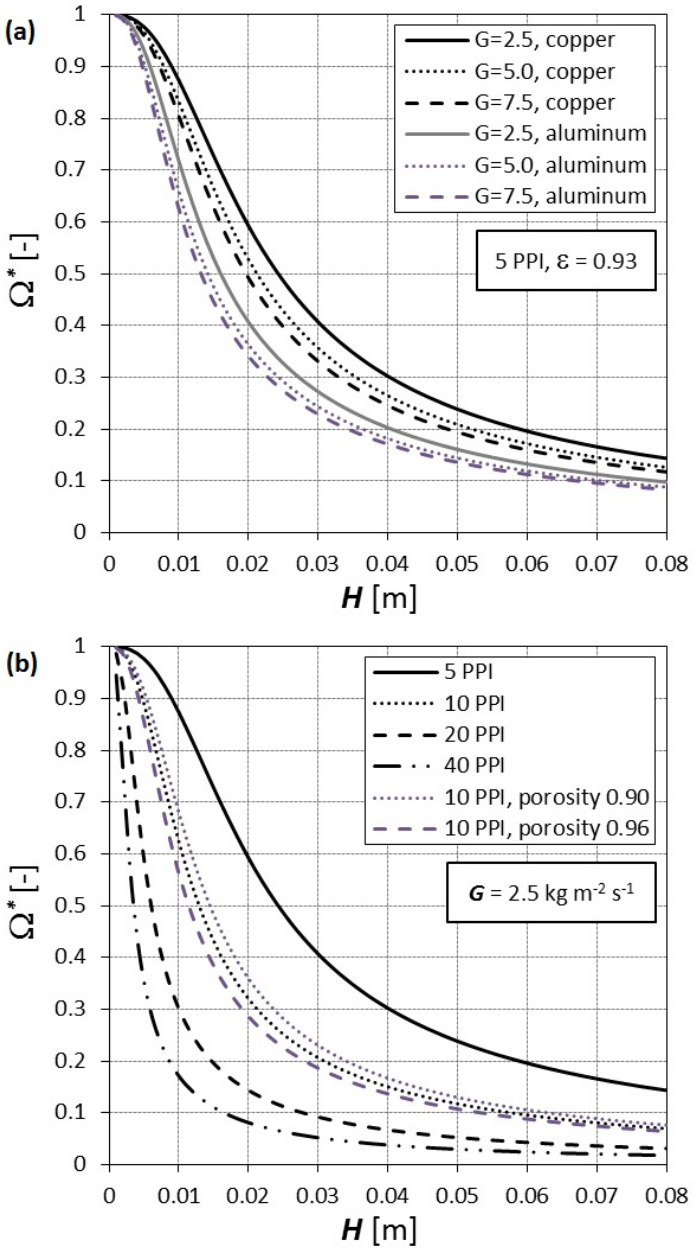

Figure 1.50: Foam finned surface efficiency plotted against the foam height. (a) Effect of material and air mass velocity. (b) Effect of the pore density and porosity at constant air mass velocity. G is expressed in [kg m^{-2} s^{-1}].

1.10 Pressure drop prediction models

1.10.1 Model of Mancin et al. [11]

Pressure gradient in the foams can be calculated with the following equation:

$$\left(\frac{\mathrm{d}p}{\mathrm{d}z}\right) = \frac{2 \cdot F \cdot G^2}{D_h \cdot \rho} \tag{1.73}$$

where the mass velocity G is defined as the ratio between the air mass flow rate and S, which is the cross section area of the empty channel, as:

$$G = \rho \cdot u = \frac{\dot{m}}{S} \tag{1.74}$$

The factor F is expressed as a function of porosity ε, of the number of pores per linear inch (PPI), and of the Reynolds number Re as:

$$F = \frac{1.765 \cdot \mathrm{Re}^{-0.1014} \cdot \varepsilon^2}{PPI^{0.6}} \tag{1.75}$$

where

$$\mathrm{Re} = \frac{D_h \cdot G}{\mu \cdot \varepsilon} \tag{1.76}$$

and the characteristic length D_h is given by:

$$D_h = \frac{4 \cdot \left(\frac{0.0254}{PPI} - t\right) \cdot l}{\left(\frac{0.0254}{PPI} - t + l\right) \cdot 2} \tag{1.77}$$

A comparison between predictions of the above equation and experimental pressure gradients is given in figure 1.51. As it appears, the model is able to predict the experimental values within ±20%, with a relative deviation of -4.1%, an absolute deviation of 11.2%, and a standard deviation of 9.4%.

Since fiber thickness and fiber length are not always available, the characteristic length D_h can also be calculated as:

$$D_h = 0.0122 \cdot PPI^{-0.849} \tag{1.78}$$

A comparison between predictions of the above equation and experimental pressure gradients is given in figure 1.52. As it appears, the model is able to predict the experimental values within ±20%, with a relative deviation of -0.4%, an absolute deviation of 9.2%, and a standard deviation of 10.5%.

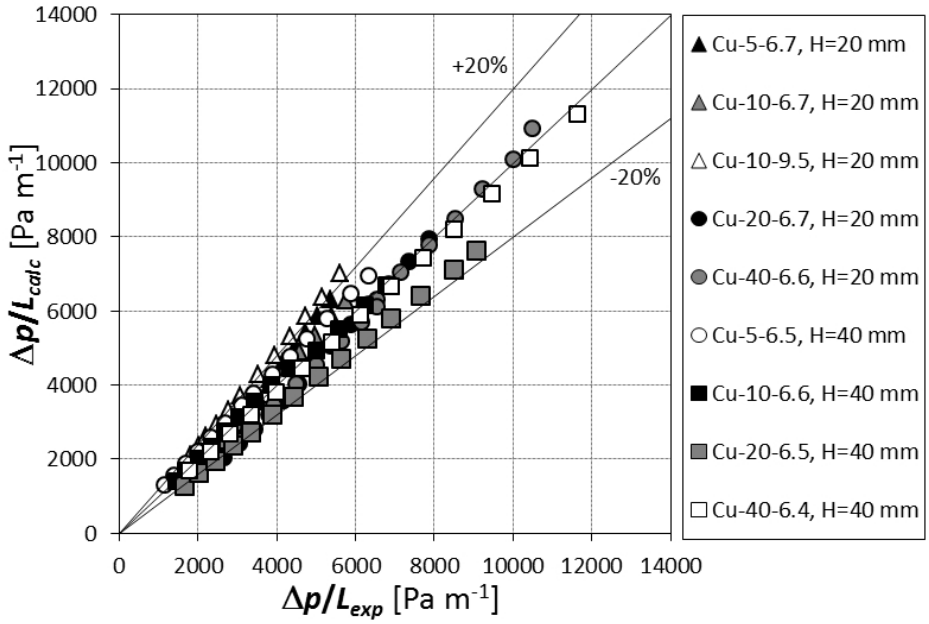

Figure 1.51: Comparison between experimental and empirical pressure gradient values suggested by the model of Mancin et al. [11] with the hydraulic diameter of equation 1.77.

1.10.2 Models of Paek et al. [26], Beavers and Sparrow [27], Hamaguchi et al. [28], and Vafai and Tien [29]

Paek et al. [26], Beavers and Sparrow [27], Hamaguchi et al. [28], and Vafai and Tien [29] calculate a friction factor F_K as a function of the experimental permeability values, as:

$$F_K = \frac{(\,\mathrm{d}p/\,\mathrm{d}z)\cdot\sqrt{K}}{\rho\cdot u^2} \tag{1.79}$$

The authors suggested to estimate F_K with the following equation:

$$F_K = \frac{1}{\mathrm{Re}_K} + z = \frac{\mu}{\rho\cdot u\cdot\sqrt{K}} + z \tag{1.80}$$

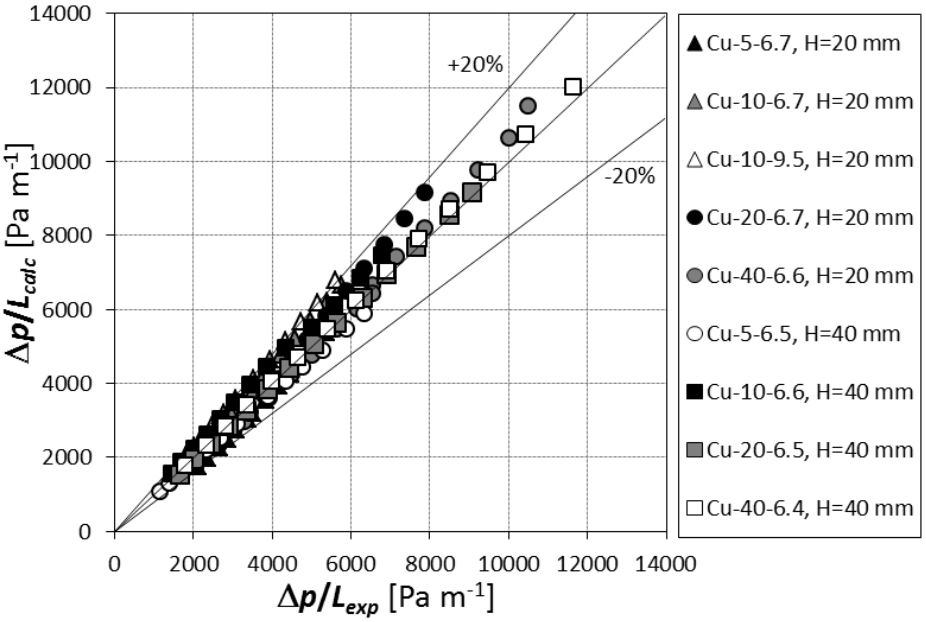

Figure 1.52: Comparison between experimental and empirical pressure gradient values suggested by the model of Mancin et al. [11] with the hydraulic diameter of equation 1.78.

This value tends to the inertia coefficient f when the velocity u tends to infinite. The values of z are: 0.105 for Paek et al. [26], 0.074 for Beavers and Sparrow [27], 0.076 for Hamaguchi et al. [28], and 0.057 for Vafai and Tien [29]. Figures 1.53-1.56 report comparisons between the experimental results and the values predicted by the correlations. As it appears, no one is suitable for all the tested copper foams.

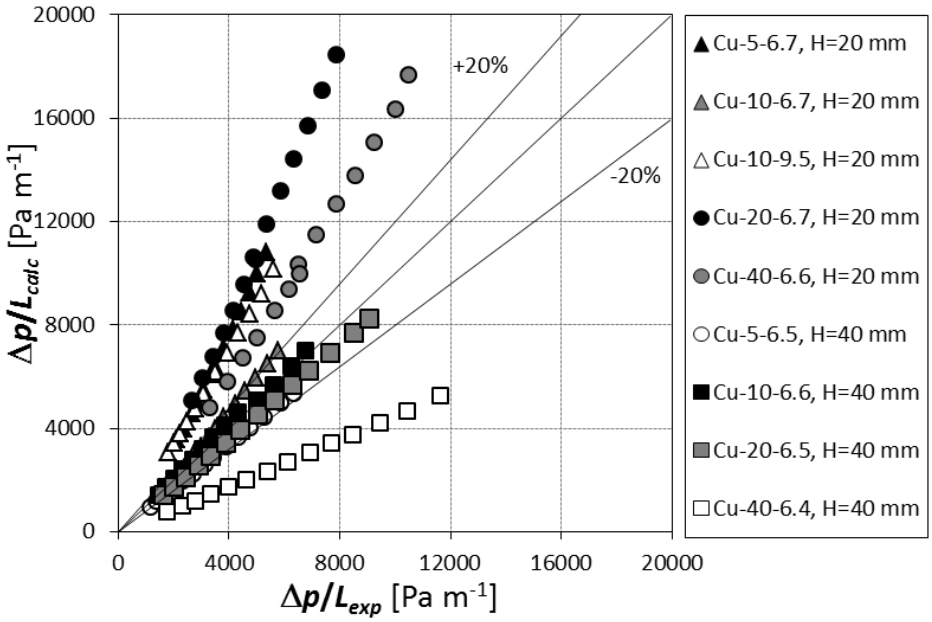

Figure 1.53: Comparison between experimental and empirical pressure gradient values suggested by the model of Paek et al. [26].

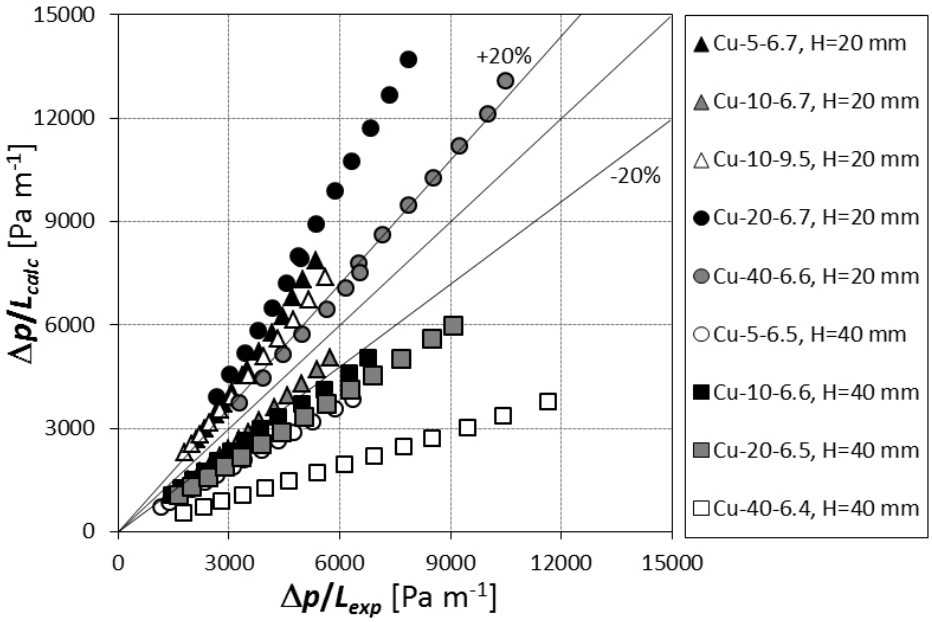

Figure 1.54: Comparison between experimental and empirical pressure gradient values suggested by the model of Beavers and Sparrow [27].

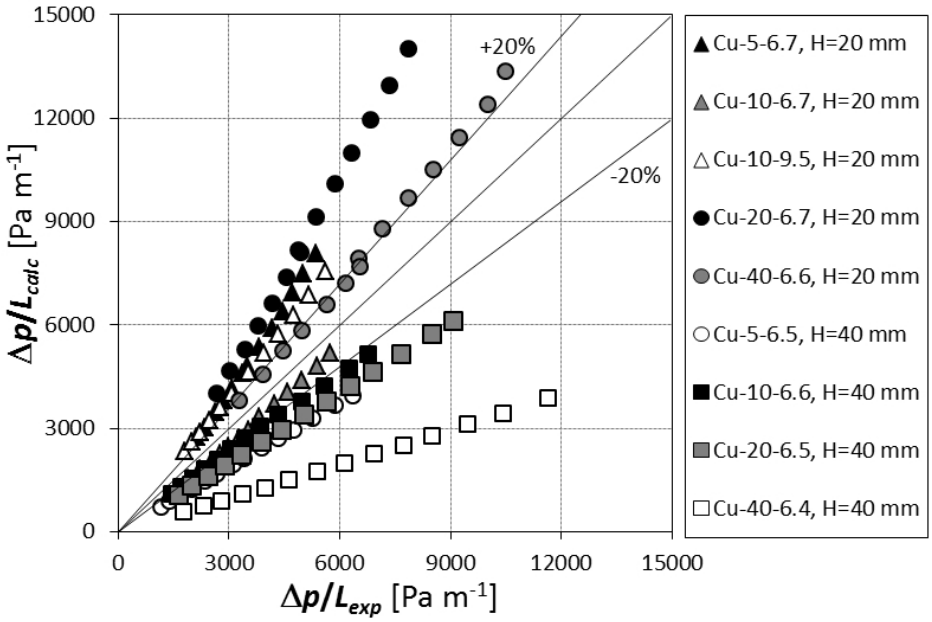

Figure 1.55: Comparison between experimental and empirical pressure gradient values suggested by the model of Hamaguchi et al. [28].

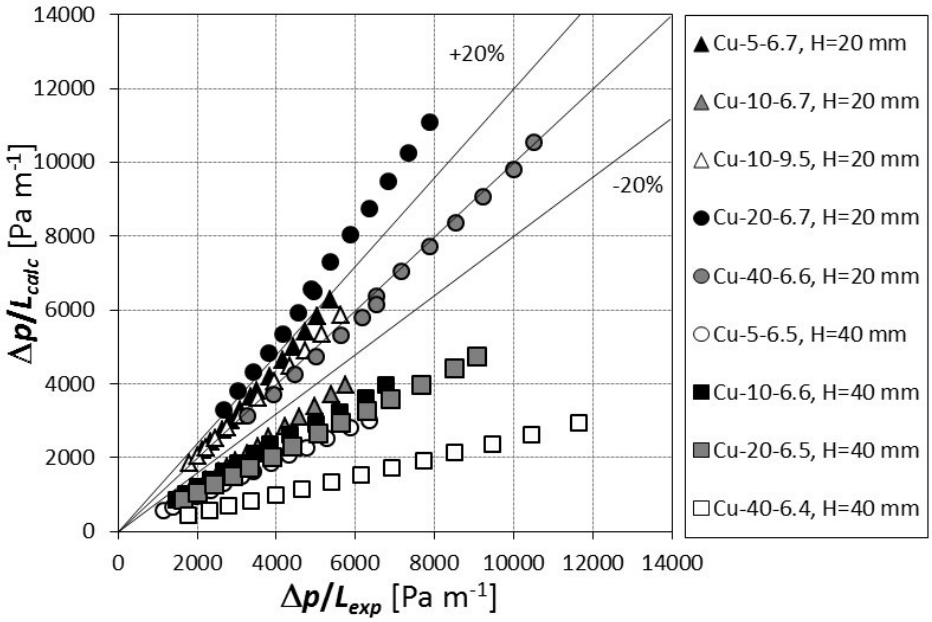

Figure 1.56: Comparison between experimental and empirical pressure gradient values suggested by the model of Vafai and Tien [29].

1.10.3 Models of Dukhan and Patel [31] and of Lacroix et al.[32]

Ergun's equation [30] has been successfully employed in the literature to predict the pressure drop of granular media. Ergun's equation for an uncompressible fluid, through a rigid and homogeneous porous medium is given by:

$$\frac{\Delta p}{L} = E_1 \frac{\mu \cdot (1-\varepsilon)^2 \cdot u}{\varepsilon^3 \cdot d_p^2} + E_2 \frac{\rho \cdot (1-\varepsilon) \cdot u^2}{\varepsilon^3 \cdot d_p} \tag{1.81}$$

where E_1 and E_2 are Ergun's constants, and d_p is the mean particle diameter of the granular medium. The major problem in the foam pressure drop estimation is to reliably define structural properties of the cellular medium to replace the equivalent particle diameter (d_p).

Dukhan and Patel [31] proposed that the equivalent particle diameter for porous metal is the reciprocal of the surface area per unit of volume, a_{sv}. Thus equation 1.81 becomes:

$$\frac{\Delta p}{L} = E_1 \frac{\mu \cdot (1-\varepsilon)^2 \cdot u}{\varepsilon^3 \cdot (1/a_{sv})^2} + E_2 \frac{\rho \cdot (1-\varepsilon) \cdot u^2}{\varepsilon^3 \cdot (1/a_{sv})} \tag{1.82}$$

with $E_1 = 150$ and $E_2 = 1.75$. The comparison between experimental and predicted pressure gradients is given in figure 1.57. This model tends to underestimate all the experimental pressure gradients. Only the values of pressure gradient for the foam Cu-10-9.5 are well estimated.

Lacroix et al. [32] suggested to use $1.5 \times t$ as d_p in equation 1.81. Thus:

$$\frac{\Delta p}{L} = E_1 \frac{\mu \cdot (1-\varepsilon)^2 \cdot u}{\varepsilon^3 \cdot (1.5 \cdot t)^2} + E_2 \frac{\rho \cdot (1-\varepsilon) \cdot u^2}{\varepsilon^3 \cdot (1.5 \cdot t)} \tag{1.83}$$

with $E_1 = 150$ and $E_2 = 1.75$. The comparison between experimental and predicted pressure gradients is given in figure 1.58. Generally speaking, this correlation well predicts the pressure gradient values, with a mean relative deviation of 9.5%, and an absolute deviation of 18.3%. It is interesting to highlight that the only one foam whose pressure gradients are not well estimated (Cu-10-9.5), is the foam well predicted by Dukhan and Patel [31].

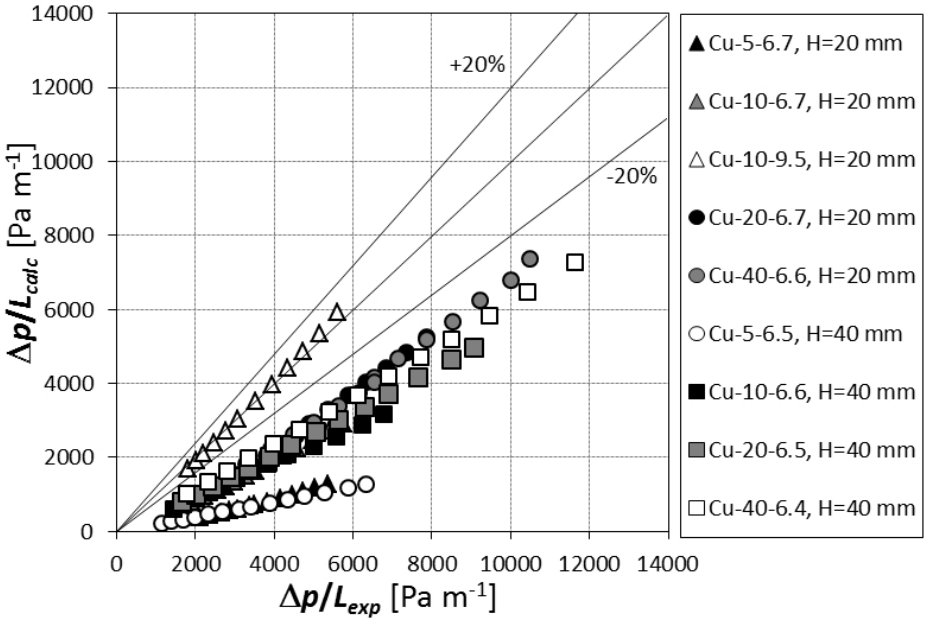

Figure 1.57: Comparison between experimental and empirical pressure gradient values suggested by the model of Dukhan and Patel [31].

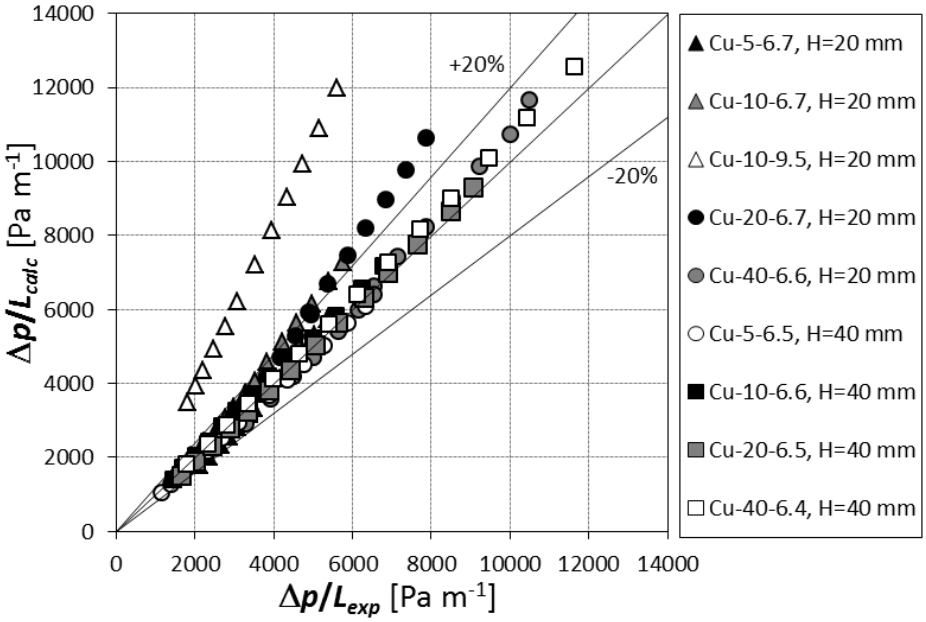

Figure 1.58: Comparison between experimental and empirical pressure gradient values suggested by the model of Lacroix et al. [32].

Chapter 2

Numerical analysis of the air forced convection through extended surfaces

2.1 Introduction

Air represents the safest and cheapest natural working fluid for thermal management applications. Many technologies such as plain and louvered fins, pin fins, offset strip fins and wire screens have been developed and studied both analytically and experimentally in the past decades to increase the heat transfer area density of heat sinks without losing the necessary compactness. Due to their simplicity and reliability, finned surfaces are among the most commonly used to cool electronic equipments. With the available modern numerical techniques, simulations are widely used to design and characterize new heat sinks, without the necessity of experimental set up and thus with relative lower costs. CFD models are a useful tool to predict heat transfer and fluid flow performance of heat sinks and heat exchangers: once the numerical results have been validated with the experimental ones, an optimization design can lead to the best geometrical configuration.

One of the pioneeristic works about turbulent heat transfer and fluid flow in longitudinal fin arrays has been carried out by Kadle and Sparrow [33]. In their

analytical-numerical work, a conjugate problem was solved, which encompassed turbulent flow and heat transfer in the air stream and heat conduction in the fins and in the base plate. The turbulence model and the numerical scheme were shown to be valid by comparisons with heat transfer data measured by the authors and with friction factors from the open literature.

Morega and Bejan [34] showed that the hot spot temperature of a finned module can be decreased by allowing the plate fin thickness and height to increase in the flow direction. They reached these conclusions by using two numerical models: a two-dimensional model, in which they uncoupled the fin conduction from the external convection by assuming the trend of the heat transfer coefficient along the longitudinal direction, and a three-dimensional problem of conjugate fin conduction and external convection. They found that the two-dimensional model breaks down when the inclination of the crest of the fin becomes excessive.

Teertstra et al [35] proposed an analytical model to predict the average heat transfer rate for forced convection cooled plate fin heat sinks based on a combination of the two limiting cases: fully developed and developing flow in a parallel plate channel. Measurements were performed for an air cooled, high aspect ratio, heat sink prototype and the model was found to be in excellent agreement with the experimental results.

CFD tools permit to check wether or not a complex geometry is better than a simpler one and they also allow to study the best geometrical configuration. Shwaish et al. [36] presented a numerical study on temperature distribution, local and global heat transfer coefficient, Nusselt number and pressure drop for serrated plate fin heat sinks. The computations yielded the optimal design of plate fin heat sinks, and also showed that the serration of the plate fin is not always a beneficial option: the baseline serrated plate fin can be replaced by a smooth surface (no-serration) plate fin that has the same thermal performance and it is less expensive to manufacture and to maintain.

Mon and Gross [37] investigated the effects of fin spacing on four-row annular-finned tube bundles in staggered and in-line arrangements by a three-dimensional numerical study. According to the flow visualization results, the boundary layer developments and the horseshoes vortices between the fins are found to be substantially dependent on the spacing to height ratio and Reynolds number. The heat

transfer and pressure drop results for various fin pitches were also presented.

Malapure et al. [38] numerically studied the fluid flow and heat transfer over louvered fins and flat tube in compact heat exchangers. Simulations were performed for different geometries with varying louver pitch, louver angle, fin pitch and tube pitch for different Reynolds numbers. The results were compared with experimental values and good agreement was observed. It was also found that both Stanton number and friction factor decrease when increasing fin pitch, and for each configuration an optimal louver angle exists, when heat transfer coefficient is maximum.

Zhu and Li [39] investigated flow and heat transfer in complete three-dimensional geometries of plain fin, strip offset fin, perforated fin, and wavy fin, in which the fin thickness, thermal entry effect, and the end effect were taken into account. The validity of the simulation models was verified by comparing the computed results of the strip offset fin with both the corresponding experimental data and three empirical correlations from literature. The effects of the offset fins in the strip fin, holes in the perforated fin, and corrugated walls in the wavy fin on the flow and heat transfer were investigated.

Yang and Peng [40] numerically studied a pin fin heat sink with a un-uniform fin height with confined impingement cooling. Different un-uniform fin height configurations were considered finding that an adequate design could decrease the junction temperature and increase the thermal performance of the heat sink.

Galvis et al. [41] developed a numerical tool to study different pin fin geometries for micro heat exchangers finding that these geometries can enhance the overall thermal performance when compared to parallel smooth plates case.

Kanaris et al. [42] suggested a general method for the optimization of a plate heat exchanger with ondulated surfaces. A previously validated CFD code was employed to predict the heat transfer rate and pressure drop in this heat sink. An objective function that linearly combines heat transfer augmentation with friction losses, using a weighting factor that accounts for the cost of energy, was employed for the optimization procedure.

Tari and Yalcin [43] analyzed a notebook computer thermal management system using a commercial computational fluid dynamic software package. The active and passive paths that are used for heat dissipation are examined for different steady-state operating conditions. Based on the analysis results and observations, a new

component arrangement considering passive paths and using the back side of the liquid crystal display screen was proposed.

Dong et al. [44] conducted three-dimensional numerical simulations and an experimental investigation of air flow and heat transfer characteristics over wavy fin heat exchangers. The authors implemented the $k - \varepsilon$ model to analyze the air flow through this extended surface in the range of Reynolds number between 1000 to 5000 finding that this model was the most suitable to predict the experimental results.

Rao et al. [45] compared the experimental and numerical results on the flow friction and heat transfer of a pin fin-dimple channel and a pin fin channel. The comparison showed that, compared to the pin fin channel, the pin fin-dimple channel has further improved convective heat transfer performance by about 8.0%, whereas lowered the flow friction by about 18.0%. In addition, fully three-dimensional and steady-state numerical computation were done to investigate the physical details about the flow and heat transfer in pin fin and pin fin-dimple channels. The numerical results provided the same trends as experimentally observed but they underpredict the heat transfer enhancement and flow friction reduction capability of the pin fin-dimple channel.

Peng et al. [46] compared the results obtained from numerical simulations and the experimental measurements relative to a fin-plate thermosyphon for high heat dissipation electronic devices. The authors analyzed the effect of fin pitch, fin thickness and fin type at the air side at different air velocities. The numerical model showed good agreement with the experimental results.

Finally, Yuan et al. [47] conducted an interesting analysis on the thermal hydraulic performance of flat pin fin heat sinks adopting the $k - \varepsilon$ model to describe the turbulent air flow. The Reynolds number ranged from 3500 to 8000 and different geometrical configurations were studied. The developed heat sinks were able to dissipate up to 60 W, keeping the junction temperature below 360 K.

The following analysis shows a simple and reliable tool to systematically study the air forced convection through different enhanced surfaces for electronic thermal management applications.

2.2 Problem description

2.2.1 Numerical model

The baseline aluminum heat sinks, which are a rectangular finned extended surface and a pin finned surface, attached to a 2.5 mm high base plate, are shown in figure 2.1, where w indicates the width of the finned surface, l the length of the sample, b the base plate height, H the height of the fins, p the pitch, t the fin thickness, S the longitudinal pin pitch, and T the transversal pin pitch of the pins. All the simulated plain fin surfaces are characterized by the same overall dimensions, which are 100 mm in width and 100 mm in length, whereas the pin fin surfaces have the same number of pins (30) both in the streamwise and in the spanwise direction: according to Short et al. [48, 49], this arrangement guarantees a fully development of the flow in all the pin surface configurations.

Due to their symmetry, only a single channel of the finned surfaces has been simulated (see figure 2.1). The fluid domain (air with constant thermophysical properties) starts 50 mm before the solid domain (finned surface) and ends 50 mm after the solid domain. In order to find the most suitable lengths of the inlet and outlet channels, which have been considered of the same length for simplicity, three

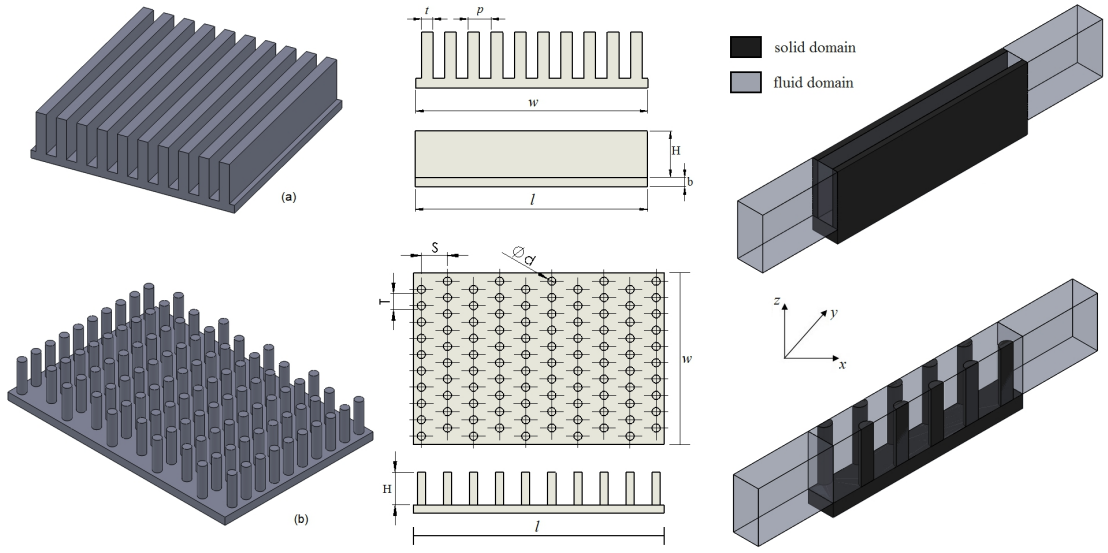

Figure 2.1: Geometries, dimensions, and simulated channels: (a) plain fin heat sink, (b) pin fin heat sink.

different lengths: 25, 50, and 100 mm have been studied for a specific case as a function of the inlet air velocity. The computed values of pressure drop have been considered as reference parameter to compare the configurations; for the investigated operating conditions, passing from 25 mm to 50 mm (for both inlet and outlet ducts), the difference in pressure drop values are around 4%, while from 50 mm to 100 mm the difference becomes lower than 0.2%. On the basis of these results, 50 mm long inlet and outlet ducts have been chosen. Figure 2.1 also shows the view of the simulated domains. For the fluid-dynamic analysis, the boundary conditions are:

- symmetry on the lateral sides of both the solid domain and fluid domain;
- constant longitudinal velocity u_y at the inlet of the fluid domain ($u_x = u_z = 0$);
- no slip conditions at the wall interface between the solid and the fluid domain, at the top of the fluid domain, and at the bottom of the inlet and outlet fluid domain.

For the thermal analysis, the boundary conditions are:

- symmetry on the lateral sides of both the solid domain and the fluid domain;
- temperature at the inlet of the fluid domain (25 °C);
- heat flux at the bottom of the solid domain (domain base) (25 kW m^{-2});
- adiabatic conditions at the top of the solid domain (top of the fins);
- adiabatic conditions at the top of all the fluid domain and at the base of the fluid domain in the inlet and outlet duct.

Several sensitivity mesh analyses have been carried out on different configurations of both plain fins and pin fins. For instance, in the case of plain fin surfaces, considering a fin configuration where the fin height is 10 mm, fin thickness is 4 mm, and fin pitch is 8.3 mm, three meshes have been tested with approximately: 41000, 227000, and 508000 elements. The deviations on the pressure drop and on the heat transfer coefficient between the first and the second mesh were -5.1% and -3.5%, respectively, while the deviations between the second and the third were -1.0% and -0.7%, respectively. In the case of fin pin surfaces, considering a configuration with

a pin diameter of 2.5 mm, a dimensionless pin height (H/d) of 4.0, a streamwise (S/d) and transverse (T/d) direction dimensionless pin spacing of 2.4 and 3.2, respectively, three meshes have been tested with approximately: 50000, 262000, and 527000 elements. In this case, the deviations on pressure drop and on the heat transfer coefficient between the first and the second mesh are -7.2% and -4.3%, respectively, whereas the deviations between the second and the third are -1.2% and -1.1%, respectively. Therefore, the second kind of mesh with intermediate number of elements has been selected being the appropriate trade-off between the accuracy of the numerical results and the computational efforts. Moreover, the mesh in the domains has been created by imposing a maximum size of the mesh elements, with a finer mesh at the interface between solid and fluid regions.

Conjugate problems, which included turbulent flow and heat transfer in air stream and heat conduction in the fins and in the base plate, were solved by using the commercial software COMSOL Multiphysics 3.5a [50]. The $k-\varepsilon$ model has been selected to study the air forced convection in turbulent regime inside extended surfaces. Recently, other authors, as reported in the introduction, have successfully implemented the $k-\varepsilon$ model to simulate air flow through fin surfaces, among them Dong et al. [44], who conducted three-dimensional numerical simulation and experimental investigation of air flow and heat transfer characteristics over wavy fin heat exchangers. The authors implemented the $k-\varepsilon$ model to analyze the air flow through this extended surface in the range of Reynolds number from 1000 to 5000 finding that this model was the most suitable to predict the experimental results. Yuan et al. [47] conducted an interesting analysis on the thermal hydraulic performance of plate pin fin heat sinks adopting the $k-\varepsilon$ model to describe the turbulent air flow. In their simulations, the Reynolds number ranged between 3500 and 8000. Therefore, the turbulent three-dimensional Navier-Stokes equations have been solved numerically combined with the continuity equation and the energy equation. An eddy viscosity model was used to account for the effects of turbulence. The flow is assumed to be three-dimensional, steady-state and incompressible, with constant fluid thermophysical properties calculated at the mean values of air temperature and pressure.

Continuity equation:

$$\nabla \cdot \mathbf{U} = 0 \tag{2.1}$$

RANS equations:

$$\rho\mathbf{U}\cdot\nabla\mathbf{U}+\nabla\cdot\Big(\underline{\rho\mathbf{u'}\otimes\mathbf{u'}}\Big)=-\nabla P+\nabla\cdot\mu\Big(\nabla\mathbf{U}+(\nabla\mathbf{U})^T\Big) \tag{2.2}$$

Eddy viscosity closure:

$$\rho\Big(\underline{\mathbf{u'}\otimes\mathbf{u'}}\Big)=\frac{2}{3}\rho k-\mu_t\Big(\nabla\mathbf{U}+(\nabla\mathbf{U})^T\Big) \tag{2.3}$$

Transport equation for k:

$$-\nabla\Big[\Big(\mu+\frac{\mu_t}{\sigma_k}\Big)\nabla k\Big]+\rho\mathbf{U}\cdot\nabla k=\frac{1}{2}\mu_t\Big(\nabla\mathbf{U}+(\nabla\mathbf{U})^T\Big)^2-\rho\varepsilon \tag{2.4}$$

Transport equation for ε:

$$-\nabla\Big[\Big(\mu+\frac{\mu_t}{\sigma_\varepsilon}\Big)\nabla\varepsilon\Big]+\rho\mathbf{U}\cdot\nabla\varepsilon=\frac{1}{2}C_{\varepsilon1}\frac{\varepsilon}{k}\mu_t\Big(\nabla\mathbf{U}+(\nabla\mathbf{U})^T\Big)^2-\rho C_{\varepsilon2}\frac{\varepsilon^2}{k} \tag{2.5}$$

where

$$\mu_t=\rho C_\mu\frac{k^2}{\varepsilon} \tag{2.6}$$

and the empirical constants are given by the following values: $C_{\varepsilon1}$=1.44, $C_{\varepsilon2}$=1.92, C_μ=0.09, σ_k=1.0, and σ_ε=1.3.

2.2.2 Data reduction

For both the experimental and numerical data points, the heat balance between the imposed heat flux at the base of the surface and the air side heat flow rate has to be verified:

$$P_{EL}=\dot{m}_{air}\cdot c_{p,air}\cdot(t_{air,out}-t_{air,in}) \tag{2.7}$$

where P_{EL} is the heat flow rate calculated from the constant value of the heat flux, 25 kW m^{-2}, $\dot{m}_{air}$ is the air mass flow rate, $c_{p,air}$ is the air mean specific heat at constant pressure, $t_{air,out}$ and $t_{air,in}$ are the outlet and inlet air temperatures, respectively. For the experimental results, the difference between the two sides of equation 2.7 was always lower than ±5%. Considering the numerical results, the difference was always lower than ±1%.

The product between the heat transfer coefficient α and the finned surface efficiency Ω^*, termed overall heat transfer coefficient α^*, is defined as:

$$\alpha^* = \alpha \cdot \Omega^* = \frac{P_{EL}}{A_{tot} \cdot \Delta t_{ml}} \tag{2.8}$$

where A_{tot} is the total heat transfer area of the finned surface and Δt_{ml} is the logarithmic mean temperature difference between the air and the surface:

$$\Delta t_{ml} = \frac{(t_{w,out} - t_{w,out}) - (t_{w,in} - t_{w,in})}{\ln \dfrac{t_{w,out} - t_{w,out}}{t_{w,in} - t_{w,in}}} \tag{2.9}$$

where $t_{w,out}$ and $t_{w,in}$ are the temperatures of the base of the specimen at the outlet and at the inlet sections, respectively.

According to the fin theory [23], the finned surface efficiency Ω^* can be calculated as:

$$\Omega^* = 1 - \frac{A_a}{A_{tot}}(1 - \Omega) \tag{2.10}$$

where A_a is the fin surface area and Ω the fin efficiency, which, assuming adiabatic conditions at the top of the fins, can be expressed as:

$$\Omega = \frac{\tanh(m \cdot H)}{m \cdot H} \tag{2.11}$$

with:

$$\text{for plain fin surfaces} \qquad m = \sqrt{\frac{2 \cdot \alpha}{\lambda \cdot t}} \tag{2.12}$$

$$\text{for pin fin surfaces} \qquad m = \sqrt{\frac{4 \cdot \alpha}{\lambda \cdot d}} \tag{2.13}$$

The finned surface efficiency Ω^* and the heat transfer coefficient can be calculated using an iterative procedure from equations 2.8-2.13.

2.2.3 Experimental results and model validation

The numerical tools need to be validated in order to assess their reliability and applicability to solve and predict the thermal fluid dynamic behaviour of different

enhanced surfaces. For this reason, the numerical model developed in this work has to be compared against the experimental heat transfer and pressure drop results obtained during experiments on a reference trapezoidal finned surface [51]. A picture of the tested specimen is reported in figure 2.2. The finned surface is made in

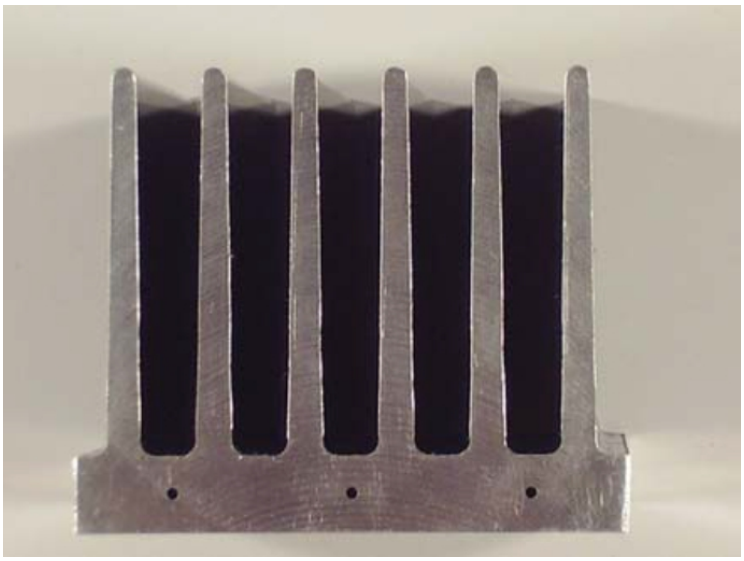

Figure 2.2: Picture of the reference finned surface.

aluminum and consists of six trapezoidal fins attached to a rectangular base of $70 \times 100 \times 12$ mm. Each fin has a base width of 5 mm, a top width of 3 mm, and it is 48 mm high. This enhanced surface has been previously tested by Cavallini et al. [51] in the experimental set up described in chapter 1. The experiments were carried out by varying the air mass flow rate from 0.010 kg s^{-1} to 0.026 kg s^{-1} and two different heat fluxes were investigated: 21.4 kW m^{-2} (i.e. 150 W) and 25.0 kW m^{-2} (i.e. 175 W). The experimental results are proposed in terms of: heat transfer coefficient, maximum measured wall temperature, and pressure drop. From the error propagation analysis, it can be pointed out that the heat transfer coefficient has an uncertainty of $\pm 2.0\%$; the wall temperatures were measured by means of calibrated T-type thermocouples with an accuracy of ± 0.05 K, while the pressure drop measured by means of differential pressure transducer with an accuracy of ± 0.275 Pa.

Figure 2.3 reports the experimental overall heat transfer coefficient calculated using equation 2.8 plotted against the air mass flow rate as a function of the imposed

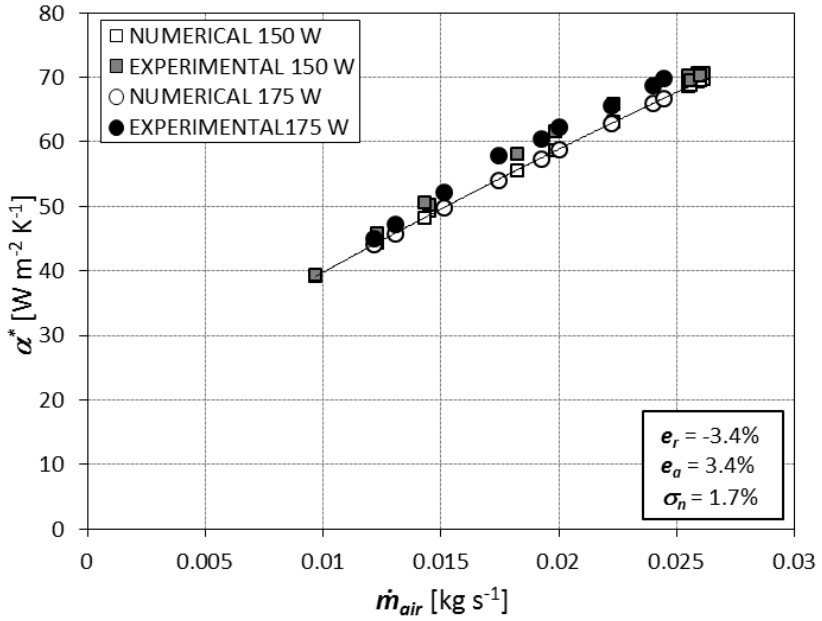

Figure 2.3: Experimental and numerical overall heat transfer coefficient against air mass flow rate for the reference finned surface.

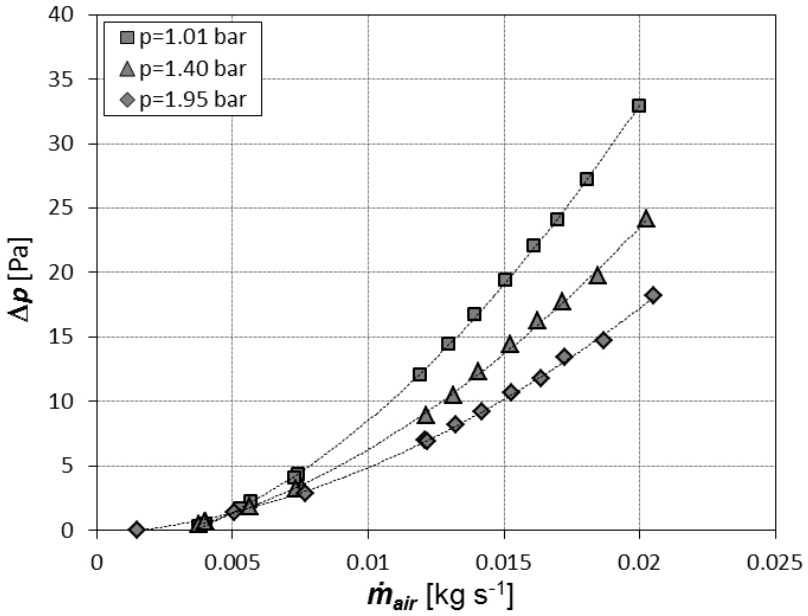

Figure 2.4: Experimental values of pressure drop against air mass flow rate at different air pressure levels for the reference finned surface.

heat flux. It can be noticed that the overall heat transfer coefficient increases as the air mass flow rate increases and it does not depend on the imposed heat flux.

Figure 2.4 shows the pressure drop measurements collected at different air pressure levels: 1.01 bar, 1.40 bar, and 1.95 bar, as a function of the air mass flow rate. The diagram clearly highlights the effect of the air mass flow rate on the pressure drops. At constant air flow rate, the pressure drop increases as the inlet air pressure decreases; this can be explained considering that the air properties change with temperature and pressure; in particular, varying pressure from 1.01 bar (ambient conditions) to 1.95 bar, air density doubles. At constant mass flow rate and cross sectional area, the mass velocity G, defined as the ratio of these two parameter, remains constant as well; therefore, since frictional pressure drop is a function of the ratio between air mass velocity and density, it increases as the air pressure decreases (i.e. the air density decreases).

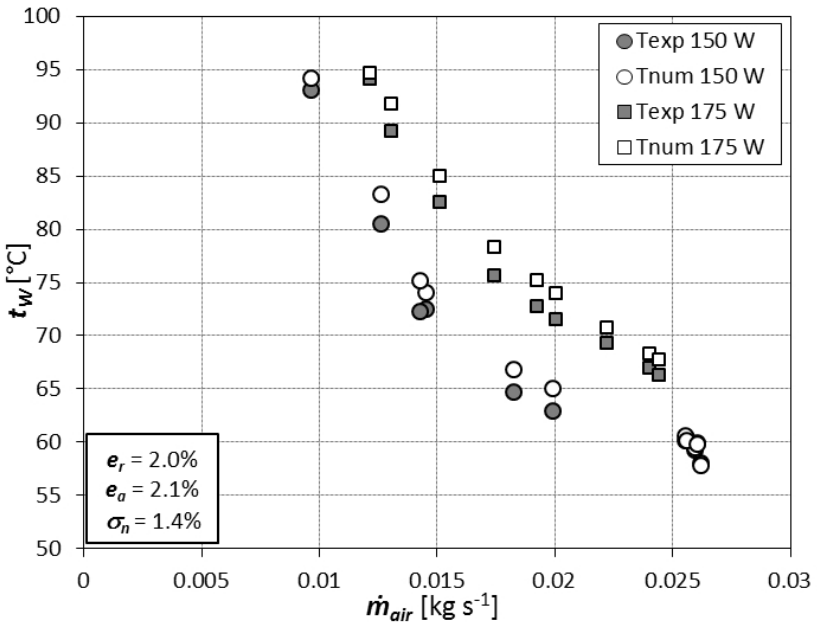

Figure 2.5: Experimental and numerical wall temperatures against air mass flow rate at two different heat flow rates (150 W and 175 W) for the reference finned surface.

Finally, figure 2.5 reports the measured values of the wall temperatures against the air mass flow rate as a function of the imposed heat flux. As expected, the wall temperature decreases as the air mass flow rate increases and, at constant mass flow

rate, higher the heat flux, higher the wall temperature.

Considering the numerical model, the finned surface has been simulated as a solid body with constant thermal conductivity λ of 175 W m^{-1} K^{-1}, whereas the fluid domain consists of air with constant thermophysical properties, such as density, viscosity, thermal conductivity and specific heat at constant pressure, calculated at the mean values of temperature and pressure. During the experimental measurements, the mean air temperature varied between 23 °C and 32 °C, whereas the mean pressure varied between 1.0 bar and 2.7 bar.

The reference surface presents a trapezoidal fin shape with a base angle of 88.8°, thus a study on the effect of the fin shape on both the heat transfer and fluid flow behaviours was carried out by comparing the trapezoidal and rectangular configurations. The numerical results obtained in three different operating test conditions (density = 2.474 kg m^{-3} and air velocity = 1.256 m s^{-1}, density = 3.013 kg m^{-3} and air velocity = 1.378 m s^{-1}, and density = 2.198 kg m^{-3} and air velocity = 2.171 m s^{-1}) show that both the Nusselt number and friction factor differ less than 1.8%, which can be considered lower than the experimental uncertainty. For these reasons, the simplified rectangular fin shape has been selected for the successive simulations.

Figure 2.3 also compares the numerical and experimental overall heat transfer coefficients for the reference finned surface. As it can be observed, the numerical results are in good agreement with the experimental measurements; in particular, the numerical ones tend to slightly underestimate the experimental values, with a relative deviation of -3.4% and a standard deviations of 1.7%. In figure 2.5 the numerical results of wall temperature are compared against the measured values, in this case the numerical tool slightly overestimates the experimental temperatures of about 1-2 K. Globally, it is proved that the numerical model is able to predict the thermal bahaviour of the reference finned surface.

Furthermore, a comparison between experimental and numerical values of pressure drop is given in figure 2.6. The numerical results show a good agreement for experimental pressure drop higher than 20 Pa, with a deviation lower than 4 Pa. At lower pressure drop, even if the deviations are lower than 2 Pa, the predictions worsen: this might be also due to the low accuracy of the experimental measurements in these working conditions because the relative uncertainty of the measurement increases as the absolute value of the pressure drop decreases. The

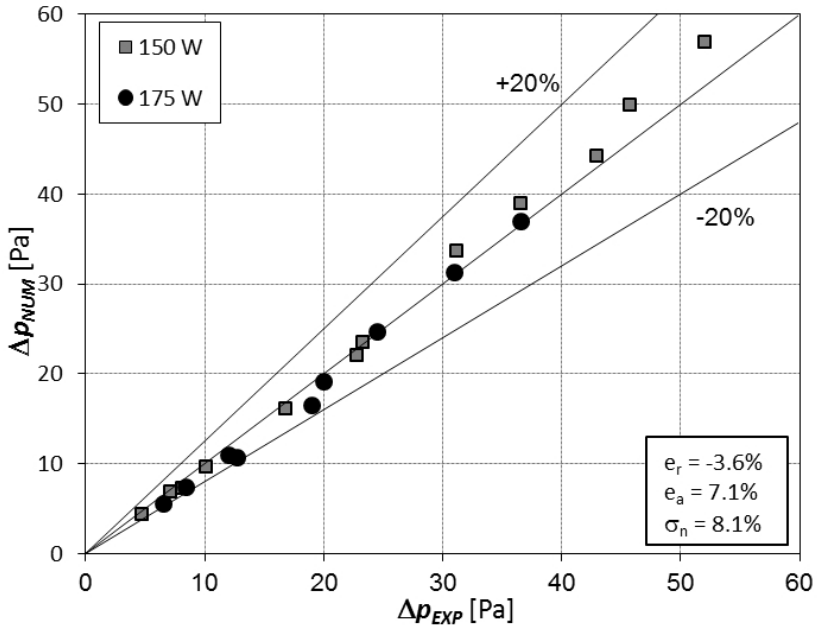

Figure 2.6: Numerical versus experimental pressure drop for the reference finned surface.

relative, absolute, and standard deviations between the experimental and numerical pressure drop results are: -3.6%, 7.1%, and 8.1%, respectively.

Finally, we can state that the numerical results show good agreement with the experimental ones, confirming the suitability of the simulation tool to predict the thermal and hydraulic behaviour of finned surfaces. The $k-\varepsilon$ turbulence model is demonstrated to be suitable to simulate the reference finned surface in the Reynolds number between 3000 and 9000. The Reynolds number is defined as:

$$\mathrm{Re} = \frac{\rho_{air} \cdot u_{max} \cdot D_h}{\mu_{air}} \tag{2.14}$$

where ρ_{air} and μ_{air} are the density and the dynamic viscosity of the air, calculated at the mean values of temperatures and pressures, u_{max} is the maximum air velocity referred to the minimum cross sectional area, D_h is the hydraulic diameter. As suggested by Kays and London [52], the hydraulic diameter is defined as:

$$D_h = \frac{4 \times V_{flow}}{A_w} \tag{2.15}$$

where V_{flow} is flow volume and A_w the wetted area. In case of plain fin surfaces, the equation can be simplified as:

$$D_h = \frac{4 \times V_{flow}}{A_w} = \frac{2 \cdot H \cdot (p - t)}{H + p - t} \tag{2.16}$$

2.3 Enhanced surface simulations

2.3.1 Plain fin surfaces

The above comparison between the experimental and numerical results for the reference finned surface showed the reliability of the simulation tool to predict the heat transfer and fluid flow performance of finned surfaces. A systematic study of the effects of different geometrical parameters on the heat transfer and fluid flow behaviour of plain finned surfaces was implemented. Keeping constant the base area of the heat sink of the finned surface, the number of fins (i.e. fin pitch), fin thickness, and fin height have been varied as listed in table 2.1. The fin pitch is calculated

Table 2.1: Geometrical and hydraulic characteristics of the simulated plain finned and pin fin surfaces.

Surface	Parameter	Range
Plain fin	t/H [-]	0.1-0.6
	p/H [-]	0.33-1.11
	Re [-]	2700-10100
Pin fin	S/d	1.8-3.0
	T/d	2.5-3.0
	H/d	3.0-7.0
	Re	1000-4200

as the ratio between the width of the heat sink and the number of fins. Three different air frontal velocities (5.0, 7.5, and 10.0 m s^{-1}) have been investigated, thus 108 simulations have been performed. The geometrical parameters coupled with the selected air velocities ensure that the flow can always be considered turbulent (Re>2700). The validation previously proposed and the works by Dong et al. [44] and Yuan et al. [47] proved the suitability of the $k - \varepsilon$ turbulent model to simulate

the air forced convection through plain finned surfaces. For this reason, this model has been implemented to extend the numerical database. Table 2.1 reports also the range of Reynolds number investigated.

Figures 2.7-2.10 show some numerical results, which help to understand how each parameter affects the heat transfer and fluid flow behaviour of the plain finned surfaces during air forced convection. Figure 2.7 reports two diagrams where the effects of the number of fins, of the air frontal velocity, and of the fin thickness are explored. Considering the top diagram, it plots the heat transfer coefficient against the air frontal velocity as a function of the number of fins, at constant fin height and fin thickness. As expected, the heat transfer coefficient increases as the air velocity increases and also when increasing the number of fins. The bottom diagram shows the effects of the fin thickness at constant velocity of 5.0 m s^{-1}. For a given fin pitch (i.e. number of fins), the heat transfer coefficient increases as the fin thickens.

Figure 2.8 reports the computed values of pressure drop in two diagrams aiming at highlighting the effects of the fin pitch (top) and of the fin thickness (bottom). Considering the top diagram, the pressure drop increases as the velocity increases and, at constant frontal velocity, higher the number of fins, higher the pressure drops. The second diagrams shows that the pressure drops increase as the fin thickens.

These conclusions can be easily explained looking at the computed velocity fields at the inlet of the finned surface displayed in figure 2.9. Again, data at 5 m s^{-1} are presented in two separate pictures: the top one reports the effects of the fin pitch (i.e. number of fins) at constant fin thickness, while the bottom one shows the effects of the fin thickness at constant fin pitch. It clearly appears that, keeping constant the fin thickness, as the fin pitch decreases the free channel narrows, the velocity increases and, thus, the heat transfer coefficient and the pressure drop increases (figure 2.9 top). Similar considerations can be drawn from the velocity fields plotted at constant fin pitch (figure 2.9 bottom), when increasing the fin thickness the magnitude of the velocity increases and both the heat transfer coefficient and pressure drop increase.

Equation 2.8 defines the overall heat transfer coefficient α^* as the product between the heat transfer coefficient α and the extended surface efficiency Ω^*; the diagram reported in figure 2.10 plots these two parameters against the frontal air velocity as a function of the fin height. First of all, the fin height does not affect

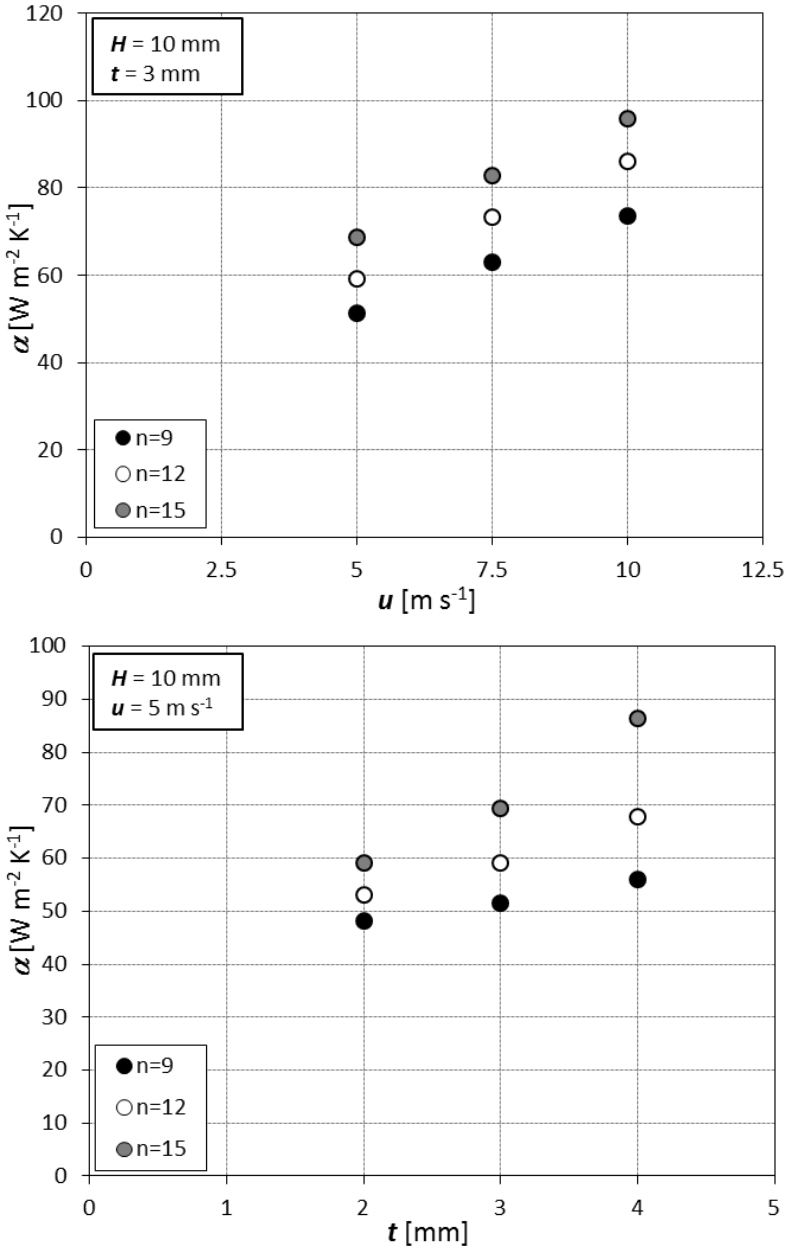

Figure 2.7: Heat transfer coefficient, for plain finned surfaces, plotted against the air frontal velocity (top) and fin thickness (bottom) as a function of the number of fins.

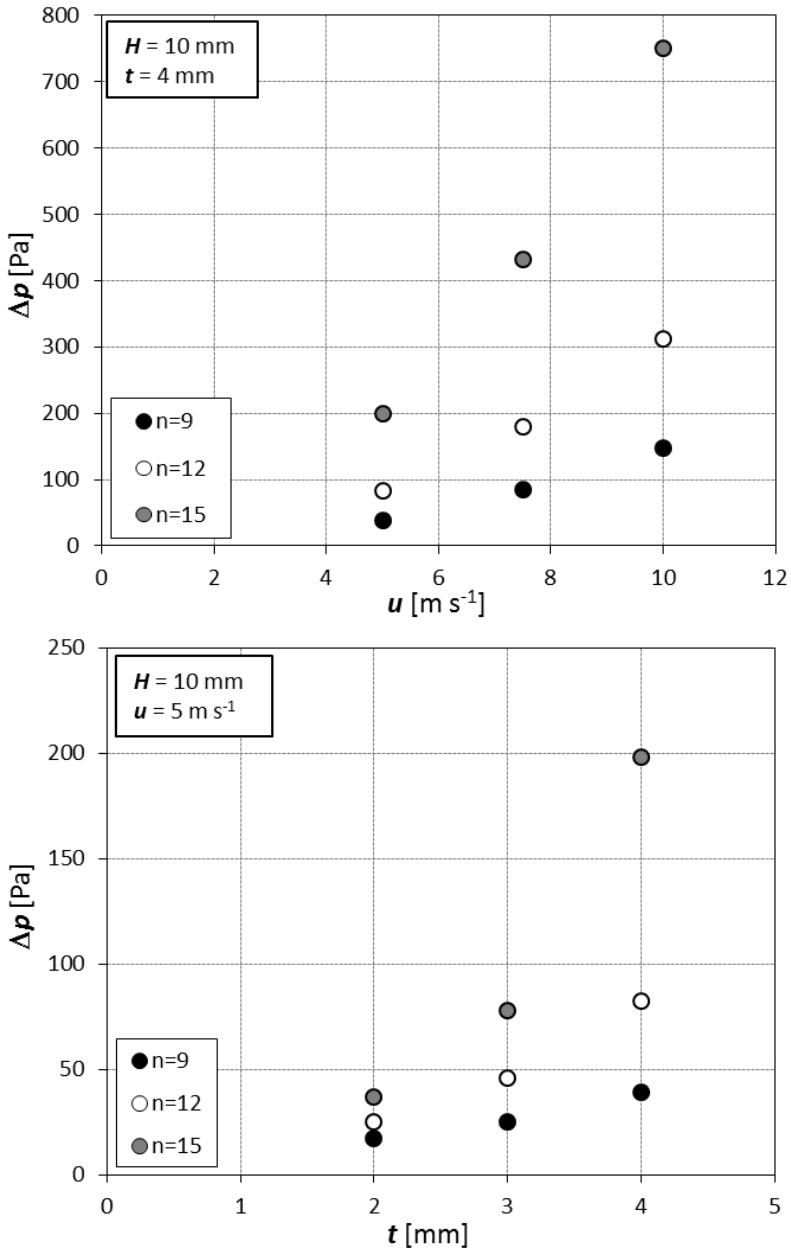

Figure 2.8: Pressure drop, for plain finned surfaces, plotted against the air frontal velocity (top) and fin thickness (bottom) as a function of the number of fins.

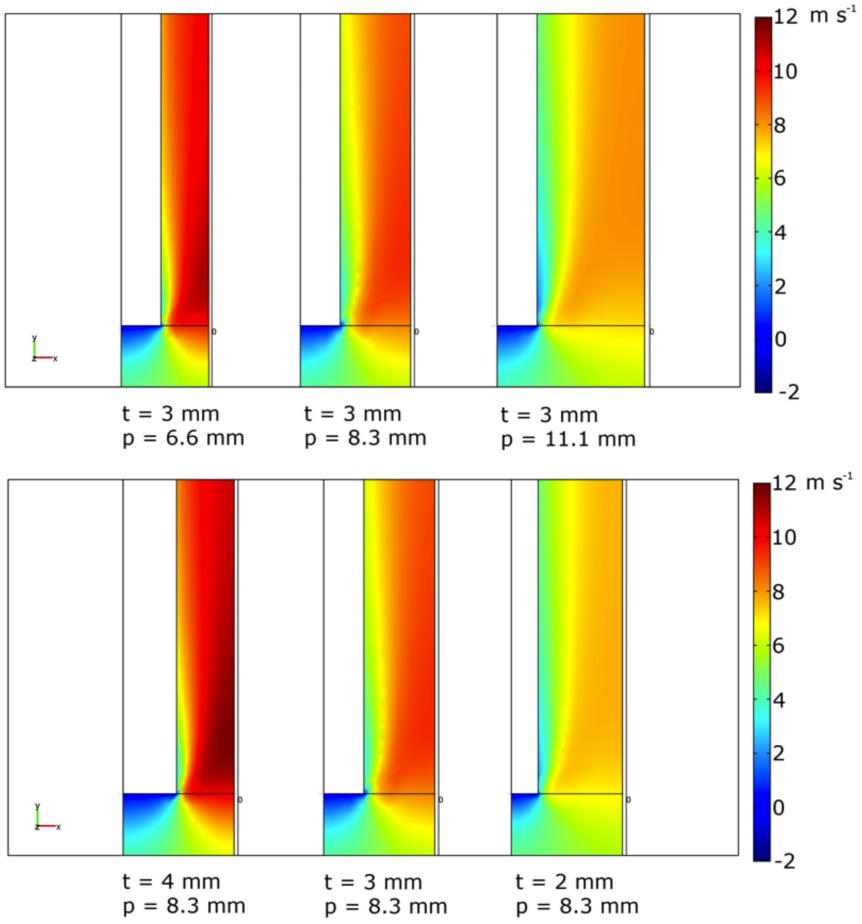

Figure 2.9: Computed velocity fields at the inlet of the finned surfaces: effect of fin pitch (top) and effect of fin thickness (bottom).

the heat transfer coefficient since the computed values at 10, 15, and 20 mm are the same at constant frontal air velocity, fin thickness, and number of fins. The Nusselt number and the heat transfer coefficient α in fact depend on mass velocity, hydraulic diameter, thermophysical properties. It depends on dimensionless Reynolds number and Prandtl number and, if the flow is not fully developed, it is also a function of the ratio fin length to hydraulic diameter. The numerical simulations have been run at constant air frontal velocity; therefore, at almost constant Reynolds number, Prandtl number, and fin length, the heat transfer coefficient α cannot vary of a remarkable amount with the fin height. The finned surface efficiency is more affected by the fin height, according to the classical fin theory [23]: when increasing the fin

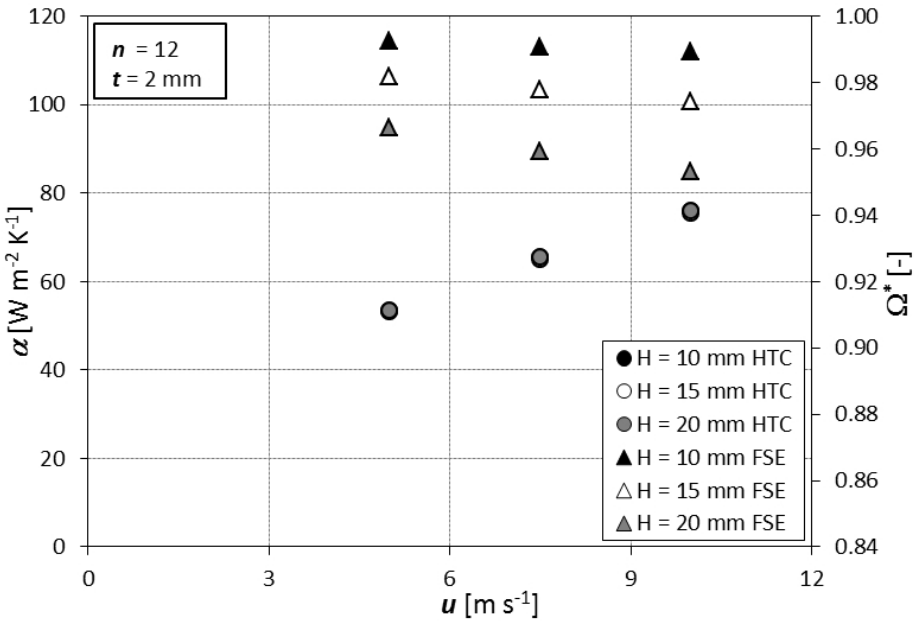

Figure 2.10: Effect of fin height on the heat transfer coefficient and on the surface efficiency as a function of the air frontal velocity (HTC = heat transfer coefficient, FSE = finned surface efficiency.

height and the air velocity, the finned surface efficiency Ω^* decreases. The values of the finned surface efficiency Ω^* are always greater than 95%: this is due to the high thermal conductivity of the material of the fins (aluminum alloy with a thermal conductivity of 175 W m^{-1} K^{-1}) and to the fin geometrical characteristics. Globally, the overall heat transfer coefficient decreases as the fin height increases. Finally, as an outcome of this analysis, it is clear that the plain finned surface which shows the best heat transfer performance also exhibits the highest pressure drop.

2.3.2 Pin fin surfaces

The numerical analysis has been extended to another enhanced surface widely used in electronic cooling applications; several staggered pin fin surfaces have been studied. A reported in table 2.1, a systematic study has also been carried out in this case by varying the streamwise and spanwise spacing values of the pins, the pin diameter, and the pin height. For each configuration, three different frontal air velocities (5.0,

7.5, and 10.0 m s^{-1} have been simulated. The geometrical characteristics on operating conditions have been chosen in order to ensure that the flow can be considered turbulent. In the present simulations, 30 pins were considered in the streamwise direction, which guarantee the fully development of the flow, as suggested by Short et al. [48, 49]. According to the same authors, the transitional Reynolds number can be considered equal to 1000, therefore, the turbulent $k - \varepsilon$ model has been implemented in the case of pin fin geometry too.

The numerical model has been applied to the case of pin fin surfaces, and more than 60 simulations have been run; figures 2.11-2.13 report a selection of the results, which permits to highlight the effects of the investigated parameters on the heat transfer and fluid flow behaviours during air forced convection in turbulent flow. Figure 2.11 explores the effects of the streamwise spacing ratio for a pin surface (2.5 mm of pin diameter and 10 mm of pin height) on the heat transfer coefficient (top) and on the pressure drop (bottom) at constant spanwise pin spacing ratio of 3.2. As expected, the heat transfer coefficient increases as the velocity increases; the contribution of the streamwise direction dimensionless spacing on the heat transfer coefficient is weak since, for a given frontal velocity, the heat transfer coefficient is almost the same when the streamwise spacing ratio passes from $S/d = 3.0$ to $S/d = 2.4$, but when it decreases to $S/d = 1.8$ the heat transfer coefficient slightly decreases. With regards to the pressure drop, it increases as the air frontal velocity increases and as the streamwise pin spacing decreases. These results can be explained observing the top picture of figure 2.13. At air frontal velocity of 5.0 m s^{-1} and at $S/d = 3.0$ and $S/d = 2.4$, the air is forced to follow a tortuous path when flowing through the pins; this promotes the heat transfer process, whereas when the S/d is equal to 1.8, even if the local air velocity is high, the air passes in a privileged passage between the pins. This may explain why the pressure drop increases as the S/d decreases while the heat transfer coefficient is only weakly affected by this parameter.

The effects of the spanwise pin spacing on the heat transfer and fluid flow behaviours for a pin fin surface with pin diameter equal to 2.5 mm, a pin height of 10 mm, and a streamwise pin spacing ratio of 2.4 are shown in figure 2.12. Both the heat transfer coefficient and the pressure drop increase as the spanwise pin spacing decreases and as the air velocity increases; in particular, decreasing T/d from 4.8

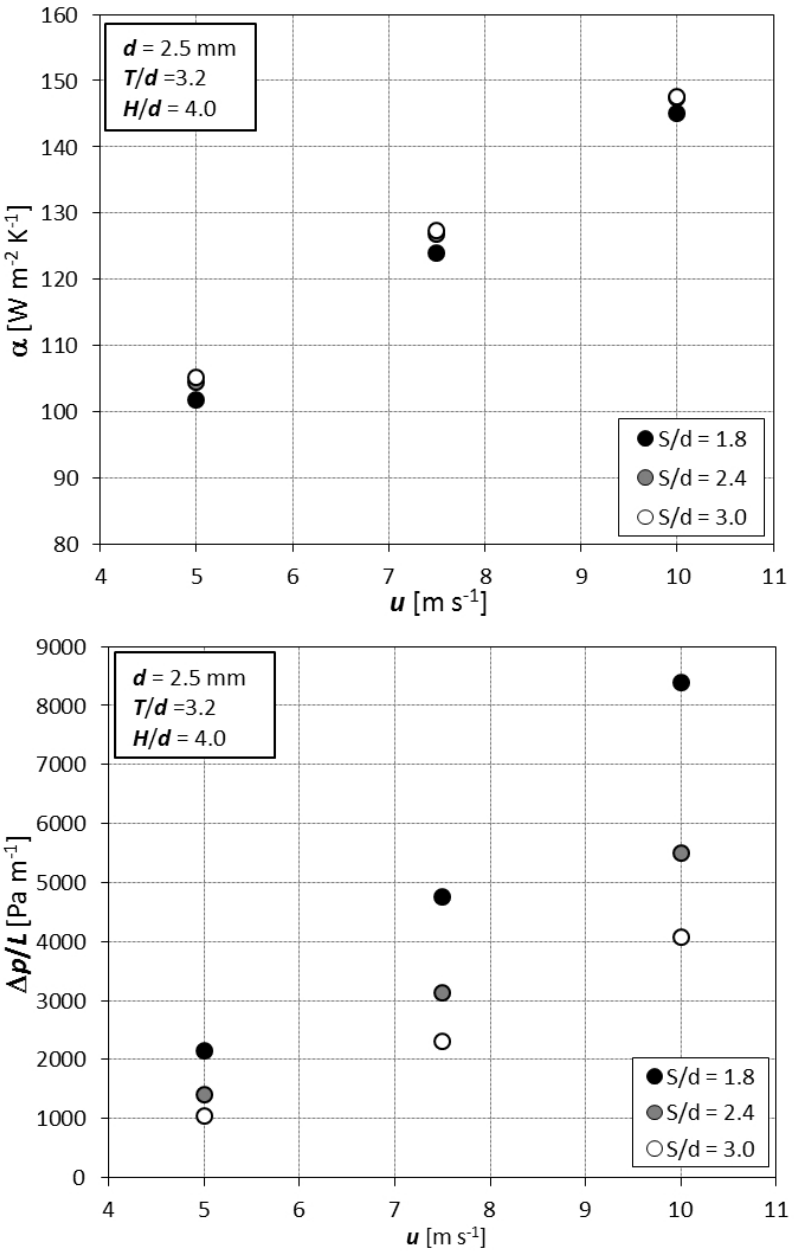

Figure 2.11: Effects of the streamwise spacing ratio on: heat transfer coefficient (top) and on pressure drop (bottom), for the pin fin surfaces, plotted against the air frontal velocity.

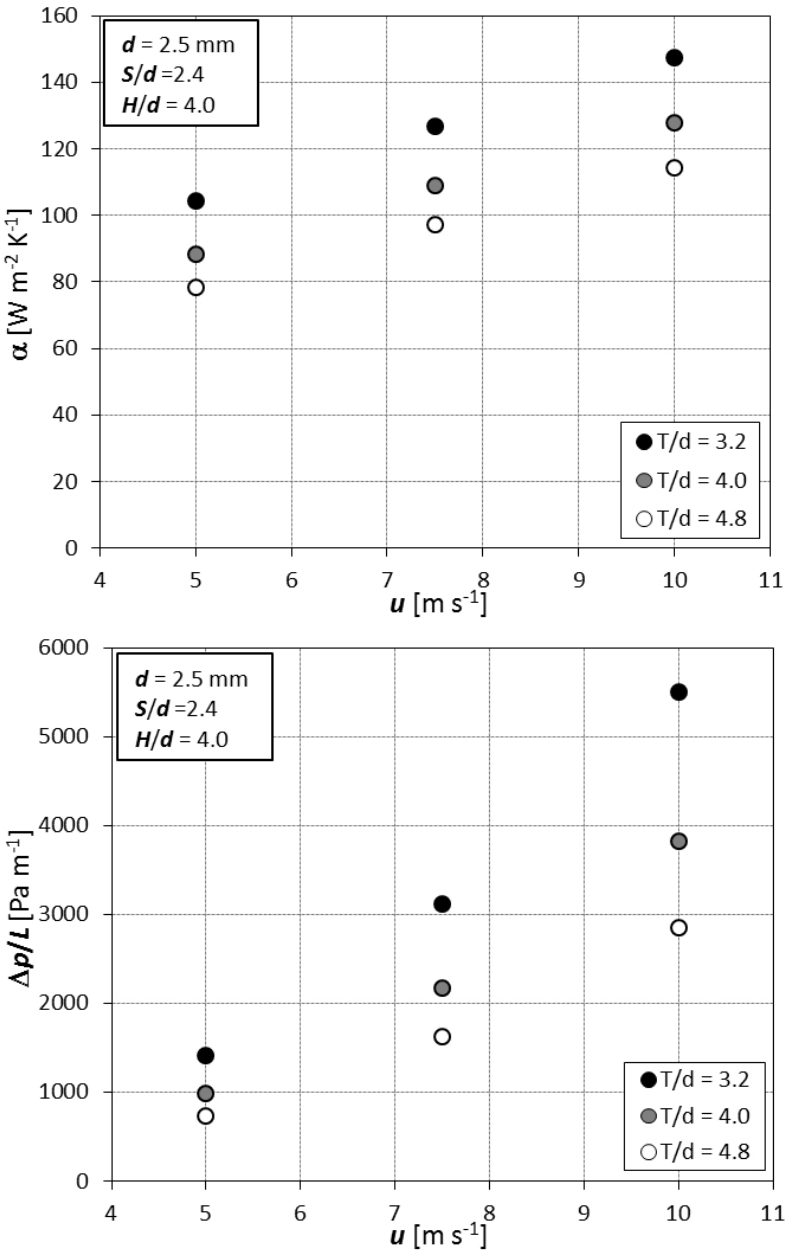

Figure 2.12: Effects of the spanwise spacing ratio on: heat transfer coefficient (top) and on pressure drop (bottom), for the pin fin surfaces, plotted against the air frontal velocity.

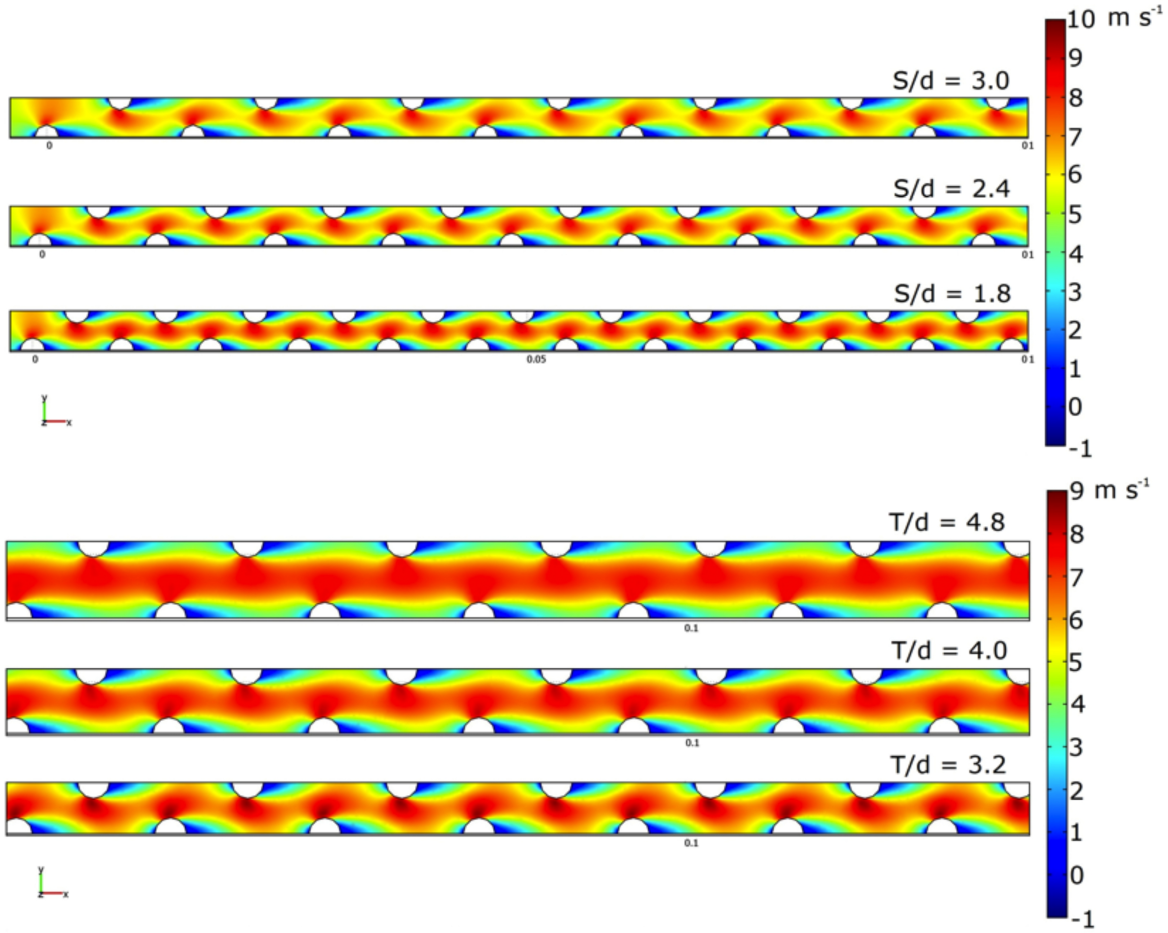

Figure 2.13: Computed longitudinal velocity fields for different pin fin surfaces: effects of the streamwise spacing ratio (top) and effects of the spanwise spacing ratio (bottom).

to 3.2 leads to a 1.33 times higher heat transfer coefficient. The computed velocity fields at constant inlet air velocity of 5.0 m s^{-1}, reported in the bottom picture of figure 2.13, help to explain these results. As the spanwise pin spacing ratio decreases from T/d=4.8 to T/d=3.2, the maximum air velocity increases and the air is forced to follow a tortuous path around the pins, this permits to enhance the turbulence and to promote the heat transfer process but, on the other hand, it also increases the frictional pressure losses.

According to the numerical results, the finned surface efficiency Ω^* assumes high values for all the simulated geometrical configurations: this is due to the high thermal conductivity of the heat sink material (aluminum alloy) and to the geometrical

characteristics. From the fin efficiency theory, the efficiency of the finned surface increases when decreasing the H/d ratio (to which shorter fin heights correspond), and when increasing the T/d ratio (to which a lower heat transfer coefficient corresponds).

2.4 Heat transfer and fluid flow modeling

Thermal and hydraulic behaviours of the different simulated plain fin and pin fin surfaces have been compared against predictions of different models selected from the open literature. Furthermore, for each extended surface, two new correlations are suggested and validated using the numerical results.

2.4.1 Plain fin surfaces

The heat transfer coefficient can be expressed as a function of two dimensionless parameters: Nusselt number and Colburn j-factor, defined as:

$$\mathrm{Nu} = \frac{\alpha \cdot D_h}{\lambda_{air}} \tag{2.17}$$

$$j = \frac{\mathrm{Nu}}{\mathrm{Re} \cdot \mathrm{Pr}^{0.33}} \tag{2.18}$$

with the Reynolds number defined in equation 2.14 and the Prandtl number defined as:

$$\mathrm{Pr} = \frac{c_{p,air} \cdot \mu_{air}}{\lambda_{air}} \tag{2.19}$$

where λ_{air} and $c_{p,air}$ are the thermal conductivity and specific heat at constant pressure of the air calculated at the mean values of temperature and pressure.

The pressure drop can be considered as the sum of three contributions: contraction and expansion losses at the inlet and at the outlet of the extended surfaces, and core friction losses. Thus, the total pressure losses, neglecting momentum pressure variations, can be expressed as:

$$\Delta p_{tot} = \Delta p_c + \Delta p_e + \Delta p = \frac{1}{2}\rho \cdot u_{max}^2 \cdot \left[K_c + K_e + 4 \cdot f \cdot \frac{L}{D_h}\right] \tag{2.20}$$

where L is the length of the finned surface and K_c and K_e are the contraction and the expansion coefficients, as suggested by Kays and London [52] for turbulent flow regime, whereas f is the core friction factor. The contraction and expansion coefficients at different Reynolds number, for a multiple-tube flat-duct heat exchanger core with abrupt-contraction entrance and abrupt-expansion exit, can be interpolated using the following equations, for laminar and turbulent flow regimes, at different Reynolds number: 2000, 10000, and infinite:

$$K_c = a \cdot \sigma^2 + b \cdot \sigma + c \tag{2.21}$$

$$K_e = a \cdot \sigma^2 + b \cdot \sigma + c \tag{2.22}$$

where σ is the core free-flow to frontal-area ratio. Table 2.2 lists a, b, and c coefficients of equations 2.21 and 2.22.

Table 2.2: Values of the coefficients of equations 2.21 and 2.22.

Reynolds number	a	b	c
K_c			
Laminar	-0.440	0.039	0.797
2000	-0.424	0.022	0.490
10000	-0.420	0.018	0.461
>10000	-0.424	0.021	0.400
K_e			
Laminar	1.012	-2.409	1.000
2000	1.013	-2.099	0.998
10000	0.973	-2.031	0.991
>10000	1.015	-2.011	0.999

Basing their analysis on Engineering Sciences Data Unit (ESDU) recommendations [53] and on Churchill correlations [54], Polley and Abu-Khader [55] suggested two empirical correlations for the estimation of the Nusselt number and core friction factor for laminar, transitional, and turbulent flow regimes. The model tends to underestimate both the thermal and the hydraulic behaviour of the simulated plain finned surfaces. The relative, absolute, and standard deviations on the Nusselt number are: -11.3%, 11.5%, and 5.4%, respectively, whereas for the core friction

factor are: -33.6%, 33.6%, and 5.7%, respectively.

Wu et al. [56] developed a correlation for a wide range of Reynolds numbers, which is able to predict the core friction factor and the Nusselt number for a plain fin heat sink for electronic cooling applications. They obtained a general friction factor correlation for rectangular-duct flow over laminar, transitional, and turbulent flow regimes; the asymptotic solution is given using the correlation developed by Shah and London [57] for the laminar flow and the correlation by Zhi-Qing [58] for the turbulent flow. They proposed an asymptotic solution for the Nusselt number using a modified Muzychka and Yovanovich [59] correlation for laminar flow and Gnielinki [60] correlation for turbulent flow. This correlation is less accurate than that of Polley and Abu-Khader [55] for the estimation of the Nusselt number, whereas it is more accurate for the prediction of the core friction factor. The relative, absolute, and standard deviations on the Nusselt number are: -11.3%, 14.5%, and 13.7%, respectively, whereas on the core friction factor are: -8.2%, 8.3%, and 6.3%.

Two new correlations for the prediction of the thermal and hydraulic behaviour of rectangular finned surfaces are here presented. They are obtained interpolating the numerical results and they are valid in the geometrical and hydraulic ranges previously reported. As described by Shah and Sekulic [61], the hydrodynamic entrance length and the thermal entrance length for turbulent duct flow are typically complied between $8 \leq L_{th}/D_h \leq 15$. The L_{th}/D_h ratio for the simulated geometrical configurations, and also for the reference finned surface, ranges between 8 and 25, thus an hydrodynamic and a thermal entrance lengths have to be considered since developing flow occurs.

The Colburn j-factor defined in equation 2.18 and the friction factor defined in equation 2.20 can be calculated with the following correlations:

$$j = 0.609 \cdot \left(\frac{t}{H}\right)^{-0.011} \cdot \left(\frac{p}{H}\right)^{-0.071} \cdot \mathrm{Re}^{-0.493} \cdot \left(\frac{L}{D_h}\right)^{-0.298} \tag{2.23}$$

$$f = 0.059 \cdot \left(\frac{t}{H}\right)^{0.118} \cdot \left(\frac{p}{H}\right)^{-0.253} \cdot \mathrm{Re}^{-0.117} \cdot \left(\frac{L}{D_h}\right)^{-0.147} \tag{2.24}$$

where the Reynolds number is calculated according to equation 2.14. In almost all electronic cooling application, the length L is not sufficient to allow to full development of both the thermal and hydraulic boundary layer. The L/D_h ratio that

appears in equations 2.23 and 2.24 takes into account the hydrodynamic and thermal entry effects. As it can be noticed from figures 2.14 and 2.15, these two correlations are accurate: the numerical Colburn j-factors are estimated with a relative deviation of -0.1%, an absolute deviation of 0.9%, and a standard deviation of 1.2%, with almost all the points within ±3%; the numerical core friction factors are estimated with a relative deviation of 0.1%, an absolute deviation of 1.9%, and a standard deviation of 2.5%, with all the points within ±8%.

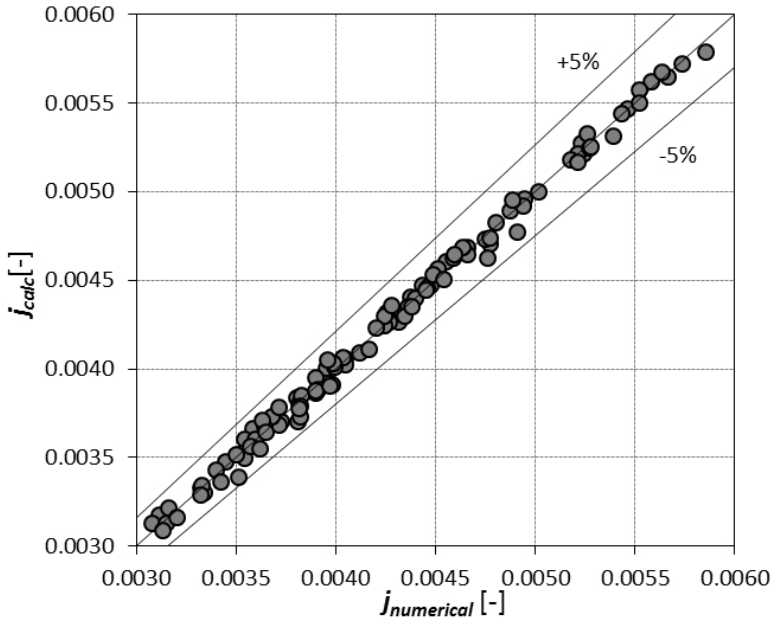

Figure 2.14: Calculated versus numerical Colburn j-factor for the proposed new correlation for plain fin surfaces.

Table 2.3 compares the relative, absolute, and standard deviations of the selected and proposed equations.

2.4.2 Pin fin surfaces

Thermal and hydraulic behaviours of the different simulated pin fin surfaces have been compared against the prediction of Short et al. [48, 49]. Short et al. [48, 49] conducted an experimental program over a wide range of geometric configurations and Reynolds numbers with staggered pin fin sections producing heat transfer and pressure drop data for streamwise spacing ratio S/d from 1.8 to 3.2, transverse

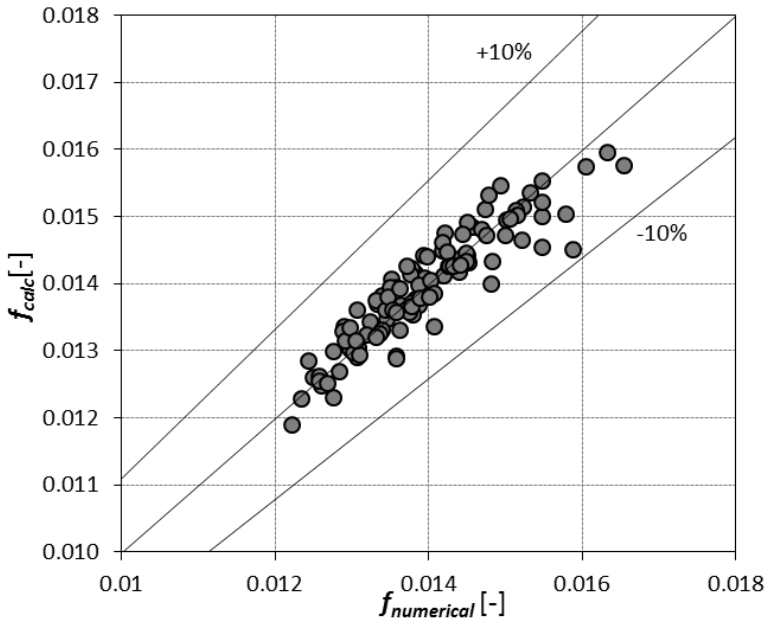

Figure 2.15: Calculated versus numerical core friction factor for the proposed new correlation for plain fin surfaces.

spacing ratio T/d from 2.0 to 6.4, and pin length ratio H/d from 1.9 to 7.2. Empirical correlations are now presented both for the Colburn j-factor and for the apparent friction factor f_{app} as a function of spacing ratios, pin length, and Reynolds number, where the hydraulic diameter is now replaced by the pin diameter d as a reference dimension. The apparent friction factor, which includes also the entry and exit losses, can be calculated as:

$$f_{app} = \frac{\Delta p \cdot D_h}{2 \cdot \rho_{air} \cdot L \cdot u_{max}^2} \tag{2.25}$$

Short et al. [48, 49] correlation tends to underestimate the numerical values: for the Colburn j-factor, the relative deviation is -19.2%, the absolute deviation 20.2%, and the standard deviation 12.3%, whereas for the friction factor the relative deviation is -26.9%, the absolute deviation 26.9%, and the standard deviation 4.4%.

The numerical results have been interpolated and the exponents of the correlations of Short et al. [48, 49] have been recalculated. Thus, the heat transfer and fluid dynamic performance of a pin fin surface in forced convection in turbulent

flow regime can be expressed with the Colburn j-factor and the apparent friction factor calculated using the following two expressions, valid for the geometrical and hydraulic ranges reported in table 2.1:

$$j = 0.327 \cdot \left(\frac{S}{d}\right)^{0.037} \cdot \left(\frac{T}{d}\right)^{-0.397} \cdot \left(\frac{H}{d}\right)^{0.201} \cdot \mathrm{Re_d}^{-0.45} \tag{2.26}$$

$$f_{app} = 0.227 \cdot \left(\frac{S}{d}\right)^{-1.307} \cdot \left(\frac{T}{d}\right)^{-0.692} \cdot \left(\frac{H}{d}\right)^{0.107} \cdot \mathrm{Re_d}^{-0.04} \tag{2.27}$$

where $\mathrm{Re_d}$ is the Reynolds number based on the pin diameter d and maximum air velocity. As it appears from figures 2.16 and 2.17, the two new correlations predict

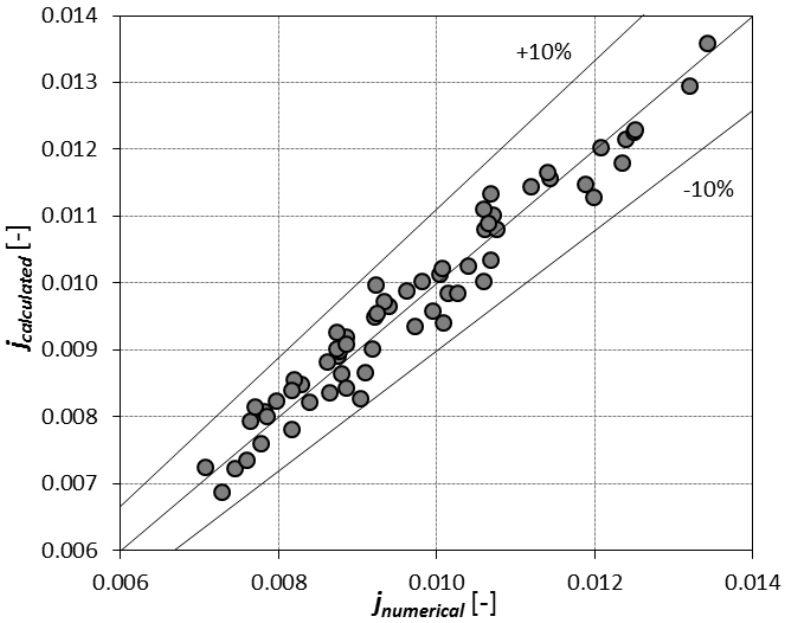

Figure 2.16: Calculated versus numerical Colburn j-factor for the proposed new correlation for pin fin surfaces.

the numerical values with good accuracy: the Colburn j-factor is predicted with a relative deviation of 0.1%, an absolute deviation of 3.3%, and a standard deviation of 3.7% and all the deviations are within ±8%; the apparent friction factors are estimated with a relative deviation of 0.2%, an absolute deviation of 4.9%, and a standard deviation of 6.1% and all the numerical points are predicted within ±14%. Table 2.3 compares the relative, absolute, and standard deviations of the presents models and those proposed by Short et al. [48, 49].

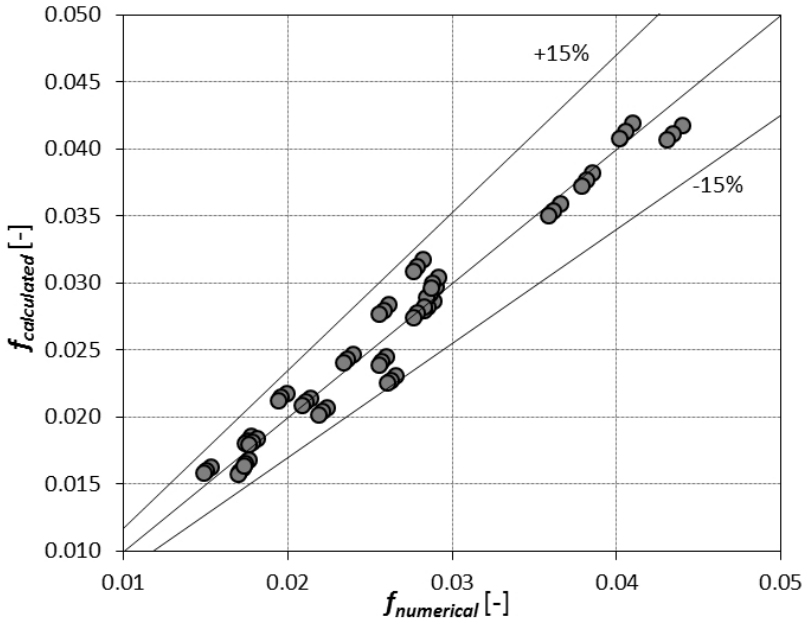

Figure 2.17: Calculated versus numerical apparent friction factor for the proposed new correlation for pin fin surfaces.

Table 2.3: Deviations between correlations and numerical results.

Surface	Parameter	Correlation	e_r [%]	e_a [%]	σ_N [%]
Plain fin	Nu	Polley and Abu-Khader [55]	-11.3	11.5	5.4
		Wu et al. [56]	-11.3	14.5	13.7
		Present model	-0.1	0.9	1.2
	f	Polley and Abu-Khader [55]	-33.6	33.6	5.7
		Wu et al. [56]	-8.2	8.3	6.3
		Present model	-0.1	1.9	2.5
Pin fin	j	Short et al. [49]	-19.2	20.2	12.3
		Present model	0.1	3.3	3.7
	f	Short et al. [48]	-26.9	26.9	4.4
		Present model	0.2	4.9	6.1

2.5 Optimal finned configurations

The proposed equations can be used to optimize the geometrical configuration of a heat sink for a given application. Therefore, in this section, a study on the best heat sink configuration is proposed for two case studies: a plain fin surface for a civil application and a plain fin surface for aeronautical applications. Obviously, the maximum allowable pressure drop for the two different applications can be much different: 50 Pa in civil case and 200 Pa in aeronautical case. Also the maximum wall temperature is different: 80 °C and 100 °C, for civil and aeronautical applications, respectively. Two objective functions have been maximized for each optimization: the product $\Omega^* \cdot \alpha \cdot A_{tot}$, which guarantees the minimum wall temperature, and the ratio $\Omega^* \cdot \alpha \cdot A_{tot}/W$, where W represents the weight of the finned heat sink. The last objective function, useful for aeronautical applications, guarantees to comply the thermal and hydraulic constraints with the lowest weight solution.

From the analysis of equations 2.23 and 2.24, it is clear that for a maximum allowable pressure drop, the optimal finned heat sink configuration depends on the air frontal velocity; therefore, the best geometrical arrangements have been found at three different velocities: 2.5 m s^{-1}, 5.0 m s^{-1}, and 7.5 m s^{-1}. External dimensions of the heat sink are input parameters in the optimization procedure; thus, a surface length of 100 mm, width of 100 mm, and a fin height of 20 mm have been chosen. An heat flux of 25 kW m^{-2} was considered. The thermal behaviour has been predicted with equation 2.23, whereas the hydraulic behaviour, which takes into account pressure losses due to friction and entrance and exit pressure drops, with equations 2.20-2.24. The contraction and expansion coefficient that appear in equation 2.20 have been calculated with equations 2.21 and 2.22.

The optimization results for the two different applications are summarized in tables 2.4 and 2.5, where the optimal number of fins, n (and thus the fin pitch, which is calculated as the ratio between the width of the heat sink and the number of fins) and the optimal fin thickness are reported.

Similar trends can be observed for both stationary and aeronautical applications: when the product $\Omega^* \cdot \alpha \cdot A_{tot}$ is maximized, an increase of the air frontal velocity leads to a thinner fins (from 3.7 mm to 1.8 mm in civil field, from 4.5 mm to 3.0 mm for aeronautical field), whereas the number of fins remains almost constant (18 fins).

Table 2.4: Geometrical parameters for the highest-performance finned surface for different air frontal velocities for stationary applications (maximum allowable pressure drop 50 Pa, maximum allowable wall temperature 80 °C).

Air frontal velocity	Objetive function	n	t
2.5 m s^{-1}	$\Omega^* \cdot \alpha \cdot A_{tot}$	18	3.7 mm
5.0 m s^{-1}		18	2.6 mm
7.5 m s^{-1}		17	1.8 mm
2.5 m s^{-1}	$\Omega^* \cdot \alpha \cdot A_{tot}/W$	18	1.4 mm
5.0 m s^{-1}		16	1.3 mm
7.5 m s^{-1}		14	1.3 mm

Table 2.5: Geometrical parameters for the highest-performance finned surface for different air frontal velocities for aeronautical applications (maximum allowable pressure drop 200 Pa, maximum allowable wall temperature 100 °C).

Air frontal velocity	Objetive function	n	t
2.5 m s^{-1}	$\Omega^* \cdot \alpha \cdot A_{tot}$	18	4.5 mm
5.0 m s^{-1}		18	3.7 mm
7.5 m s^{-1}		18	3.0 mm
2.5 m s^{-1}	$\Omega^* \cdot \alpha \cdot A_{tot}/W$	18	0.9 mm
5.0 m s^{-1}		13	1.1 mm
7.5 m s^{-1}		11	1.2 mm

On the contrary, when it is maximized $\Omega^* \cdot \alpha \cdot A_{tot}/W$, when increasing the air frontal velocity, the fin thickness remains almost constant (on average thickness of 1.4 mm for stationary applications and an average value of 1.1 mm for aeronautical applications) and the fin number decreases: from 18 to 13 fins in stationary field and from 18 to 11 fins in aeronautical field.

Considering $\Omega^* \cdot \alpha \cdot A_{tot}$ as the objective function for both applications, at the same frontal air velocity, the number of fins is the same, whereas the fin thickness is always higher for the aeronautical application. On the contrary, by considering the ratio $\Omega^* \cdot \alpha \cdot A_{tot}/W$ as objective function, at the same frontal air velocity, both the fin number and the fin thickness are lower for aeronautical applications.

Chapter 3

Numerical analysis of the air forced convection through metal foams

3.1 Introduction

Traditional approaches of modeling fluid and thermal transport through metal foams approximate stochastic foams as periodic porous materials. Different ways to model the structure of such materials can be found in the open literature. The discussion about how to model the structure of a foam started in the last years of the nineteenth century, when lord Kelvin asked: "How space would be partitioned into cells of equal volume with the least area of surface between them, i.e. what is the most efficient bubble foam [62]?" He proposed a foam based on the bitruncated cubic honeycomb, leading to a tetrakaidecahedron, which is called Kelvin structure. This solid is formed by the truncated octahedron, which is a solid with 14 faces (6 square faces and 8 hexagonal faces) and it is represented in figure 3.1.

The Kelvin structure was widely believed as solution of the Kelvin structure for more than 100 years. More recently, Phelan et al. [63], using a computer software for minimization of surface area, Surface Evolver [64], identified a unit cell of even lower surface area per unit of volume than that of the Kelvin structure. This unit cell is made up of six 14-sided cells (with 12 pentagonal and 2 hexagonal faces) and two

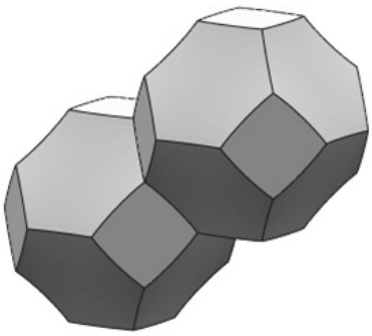

Figure 3.1: Example of a tetrakaidecahedron.

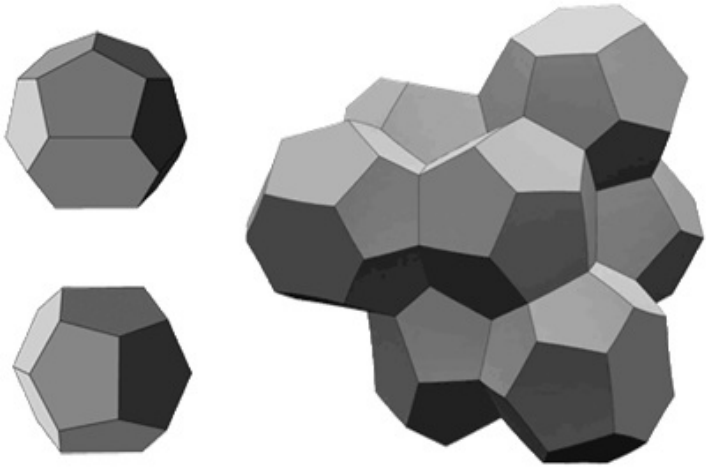

Figure 3.2: Example of the Weaire-Phelan structure.

pentagonal dodecahedra, all of equal volume. This structure, called Weaire-Phelan structure, is shown in figure 3.2. Both the Kelvin structure and the Weaire-Phelan structure are "dry" foams, meaning that the porosity is very close to 100% and the foam is basically a set of films, which is seen in reality when soap foam is observed.

Boomsma et al. [65] modeled the fluid flow through porous media with periodic unit cells using the energy minimization tool, Surface Evolver [64]. Starting from the Weaire-Phelan structure, they increased the fluid fraction during the foaming process with a procedure called "wetting". The wetting process was accomplished with a foam-wetting command in Surface Evolver [64], obtaining a porosity of approximately 0.96. The geometry was then imported into an unstructured mesh flow

solver to solve the fluid flow through the fluid domain. The pressure drop numerical data of the flow through the cellular unit were then compared against experimental data. The pressure drop values predicted by the simulations were consistently 25% lower than the values obtained in the experiments on a similar foam and under identical flow conditions.

Surface Evolver [64] was also used by Kopanidis et al. [66], who modeled the structure of two different aluminum foams, the first having 10 PPI and a porosity of 0.97, and the second with 40 PPI and a porosity of 0.97. These foams were then meshed with tetrahedral elements, and the conjugate flow and temperature fields were obtained by solution of the Navier-Stokes and energy equations for the two different foams under various flow and temperature conditions.

Bai and Chung [67] evaluated the pressure drop in metal foams using a unit-cell CFD model. The model is based on a structure of sphere-centered open-cell tetrakaidecahedron: a tetrakaidecahedron is generated first by cutting off the six corners of a regular octahedron. Then generating a sphere at the center of the tetrakaidecahedron and subtracting the sphere from it yields the sphere-centered Kelvin structure shown in figure 3.3. They considered two type of cells: an interior

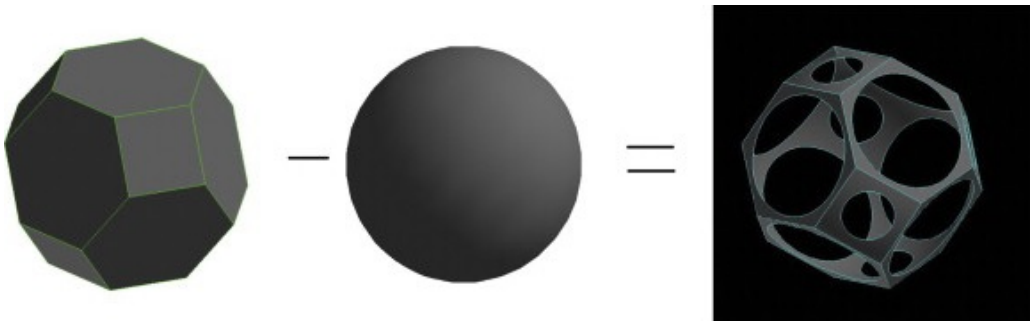

Figure 3.3: Geometrical creation of a sphere-centered open-cell tetrakaidecahedron [67].

cell and a boundary cell, to take into account also the effect of the wall friction on the total pressure drop. Simulations investigated the pressure drop of a 10 PPI foam with a porosity of 0.97. Experimental data of Leong and Jin [68] were compared with the simulations results. The current direct numerical simulation method predicted the pressure drops very well compared to the experimental values since only the simulation results at 1 m s^{-1} inlet velocity were somewhat higher. The wall cell experienced an approximately 5% higher pressure drop because of the

no-slip condition at the wall and the larger velocity gradient near the wall.

Another work based on the tetrakaidecahedron structure is that of Wu et al. [69], who numerically studied the convective heat transfer inside ceramic foams. They used a periodical structure formed by packed tetrakaidecahedra to represent the real ceramic matrix. By adding a face-blend structure and adjusting the curvature of the blend faces and the mean diameter of struts, the real porosity of the tetrakaidekahedral model can be adjusted. Based on the numerical simulation results, they developed a correlation for the volumetric local convective heat transfer coefficient between air and the ceramic foams. The correlation results were compared against experimental data from the literature, and the comparison showed good agreement.

Horneber et al. [70] presented 3D numerical simulations of structured open-cell foams based on the tetrakaidecahedron geometry. The velocity and pressure fields for a single cell with varied surface roughness and the whole reactor with the same pore size were calculated. The friction factor for the whole reactor was found to be smaller than the one for a single cell. A single unit cell was chosen to study the effect of the surface roughness. When the roughness increases, the Euler number was found to increase, and it became more and more independent on the Reynolds number.

A simpler way to model the structure of a foam is that proposed by Yu et al. [71]. They used a unit-cube model based on interconnected sphere-centered cubes, where the interconnected spheres represent the fluid or void space, by subtracting a sphere from a cube. An example of this geometry can be seen in figure 3.4. The unit-cube model was used to derive all the geometric parameters required to calculate the

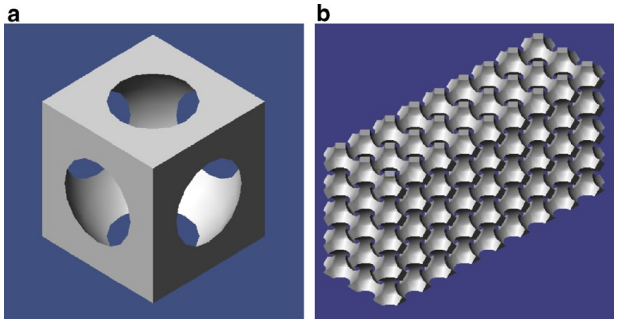

Figure 3.4: Single unit-cube cell with spherical voids (a) and interconnection of pores (b) [71].

heat transfer and flow through the porous foam. They derived an expression for the effective thermal conductivity, which gave good predictions compared against experimental values from the open literature. When combined with existing expressions for the pore-level Nusselt number, the proposed model also yielded reasonable predictions of the internal convective heat transfer. Estimations of the fluid pressure drop were shown to be well described using the Darcy-Forchheimer law; however, further exploration is required to understand how the permeability and Forchheimer coefficients vary as a function of porosity and pore diameter. This geometrical model was later used by Karimian and Straatman [72], who performed numerical simulations to study the hydraulic and thermal behavior of such materials.

Krishnan et al. [73] conducted direct numerical simulations of thermal transport in open-cell metal foams using different periodic unit-cell geometries. The shape of the pore was assumed to be spherical and spheres of equal volume were arranged according to the following three lattice structures: Body Centred Cubic (BCC), Face Centered Cubic (FCC), and A15. The periodic unit-cell geometry is obtained by subtracting the unit-cell cube from the spheres at the various Lattice points. The resulting geometries are shown in figure 3.5. The BCC, FCC, and A15 were found to predict friction factor and Nusselt number values which are in good agreement with available experimental and semianalytical results. The BCC and A15 models also predicted thermal conductivity reasonably well, whereas the FCC model predictions for effective thermal conductivity showed greater deviations from the available measurements.

Annapragada et al. [74] proposed a computational methodology to describe the fluid transport in compressed open-cell metal foams. They considered the same geometrical model of Krishnan et al. [73]. Since Krishnan et al. [73] showed that the BCC and A15 models were most capable of representing the flow characteristics of foams, and since the A15 structure yielded good predictions for both structural deformation and fluid flow, the A15 model was chosen for prediction of the convective flow characteristics of compressed foams. Predictions of permeability as a function of compression using the A15 model have been validated against experimental results by Dawson et al. [75]. Once validated, they used this model to predict permeability, friction factor, Nusselt number and effective thermal conductivity of aluminum foams, highlighting the effect of the compression on these parameters.

There has been a growing interest in the use of X-ray microtomography for a variety of applications such as material characterization and reverse engineering. For example, Fiedler et al. [76] numerically identified and repaired defects produced in the manufacturing of an open-cell metal foam. Finite element calculations were performed based on microcomputed tomography data of samples. The effective Young's modulus and 0.2% offset yield strength were calculated, so that it was possible to identify weakness within the material. Defected structures were digitally repaired locally and the calculations repeated in order to highlight the change in the material properties.

Microcomputed tomography images may also be employed as the starting point of a CFD analysis. Metal foams are inherently stochastic; thus unit-cell based models only approximate the true microstructure and fail to capture the intricate details of fluid flow and heat transfer in such media. Recent advancements in computing architecture have led to increased processor speeds and memory, which enable tomography scans to be employed for mesh generation and subsequent, detailed fluid-thermal performance analysis of random porous materials such as metal foams.

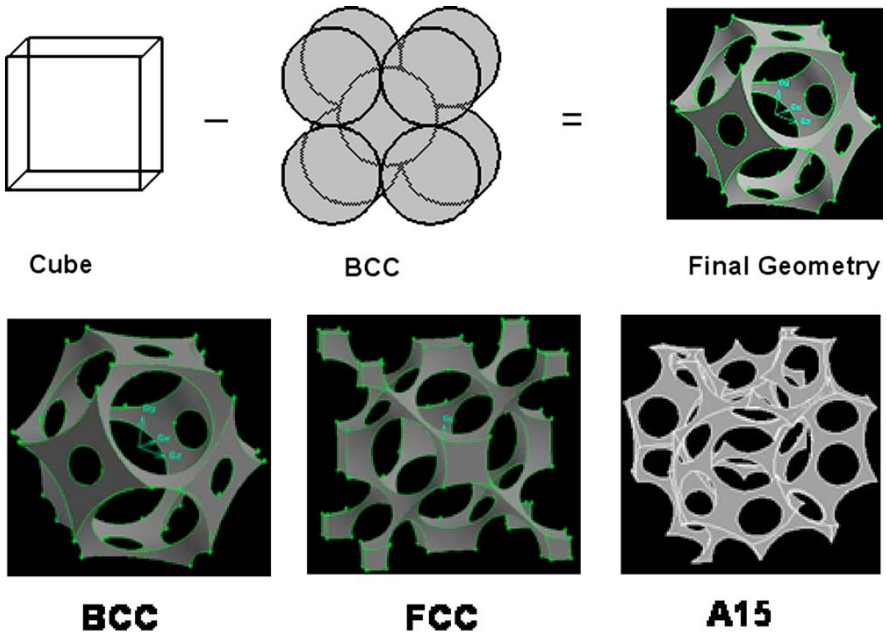

Figure 3.5: Construction and images of the created models for the BCC, FCC, and A15 models [73].

Bodla et al. [77] investigated important heat transfer characteristics of aluminum foams with different pore densities through computed tomography scanning at 20 micron of resolution. They considered three aluminum foams with 10, 20, and 40 PPI and a porosity in the range 0.91-0.93. The effective thermal conductivity was found to be a strong function of the porosity, whereas it was a much weaker function of the number of pores per linear inch. Tortuosity computations indicated that the foams were essentially isotropic. Permeability analysis for the Darcy flow regime established the inverse dependence of permeability on pore size. Numerical friction factors and heat transfer coefficient were compared against values predicted by correlations from the open literature, and a good match was found.

Mendes et al. [78] numerically predicted the effective thermal conductivity of open cell foams over the complete range of thermal conductivity ratios of fluid and solid phases lower than unity. The predictions were obtained using a Finite Volume Method, where both regular cellular structures and real open cell foam structures were systematically analyzed. Kelvin and cubic cells were considered as regular structures. Real structures were taken from samples of metal and ceramic foams with different porosities and comparable characteristic pore dimension. The true geometries were obtained by 3D CT-scan images.

3.2 Methodology

X-rays are a form of the electromagnetic radiation. Most X-rays have a wavelength in the range of 0.01 to 10 nanometers, corresponding to frequencies in the range 30 petahertz to 30 exahertz (3×10^{16} Hz to 3×10^{19} Hz) and energies in the range 100 eV to 100 keV. German physicist Wilhelm Röntgen is usually credited as the discoverer of X-rays in 1895, because he was the first to systematically study them, though he is not the first to have observed their effects. Röntgen discovered its medical use when he made a picture of his wife's hand on a photographic plate formed due to X-rays. The photograph of his wife's hand was the first ever photograph of a human body part using X-rays.

X-ray computed tomography (X-ray CT) is a technology that uses computer-processed X-rays to produce tomographic images (virtual 'slices') of specific areas of the scanned object, allowing the user to see what is inside it without cutting it.

The different absorptivity of the object under scanning leads to brighter or darker images: a brighter image is the result of a denser object, which does not let X-rays pass, and vice versa. This technique is widely used in medical fields, for scanning of specific areas of the body, for example for tumor or crack bones detection. The two dimensional images can be combined to produce a three-dimensional image, and may thus be employed for diagnostic or therapeutic purposes in various medical disciplines.

During the 1970s, computed tomography applications spread to industrial problems. Industrial CT scanning is now used in many areas for a variety of applications such as internal inspection of components for flaw detection, failure analysis, metrology, reverse engineering, and material characterization.

In this study, the computed tomography technique is employed for scanning the 40 mm high copper foams whose experimental results were discussed in Chapter 1. For the sake of clarity, the major geometrical characteristics of the tested foams are reported in table 3.1.

Table 3.1: Major geometrical characteristics of the scanned copper foams.

Sample	PPI [in^{-1}]	Porosity [-]	H [mm]	a_{sv} [m^{-1}]	t [mm]	l [mm]
Cu-5-6.5	5	0.935	0.02	292	0.495	1.890
Cu-10-6.6	10	0.934	0.02	692	0.432	1.739
Cu-20-6.5	20	0.935	0.02	1134	0.320	1.402
Cu-40-6.4	40	0.936	0.02	1511	0.244	0.999

All of these foams are manufactured in a sandwich-like arrangement, where the foam core height is brazed between two 10 mm thick copper plates. Experimental specimens were 100 mm long and wide, and 40 mm high. Owing to a trade-off between scan resolution and size of the sample being scanned, smaller samples were used in the scanning and subsequent numerical analysis. For this purpose, square specimens with an edge of approximately 15 mm were cut from the original copper samples by means of electro-erosion. This cutting technique avoids damage to the fiber ligaments, and hence the structure is scanned without introducing any defects. The cut foams, shown in figure 3.6, were scanned with a commercial X-rays μ-CT scanner at a resolution of 20 μm, with the axis along the longer direction, i.e. along

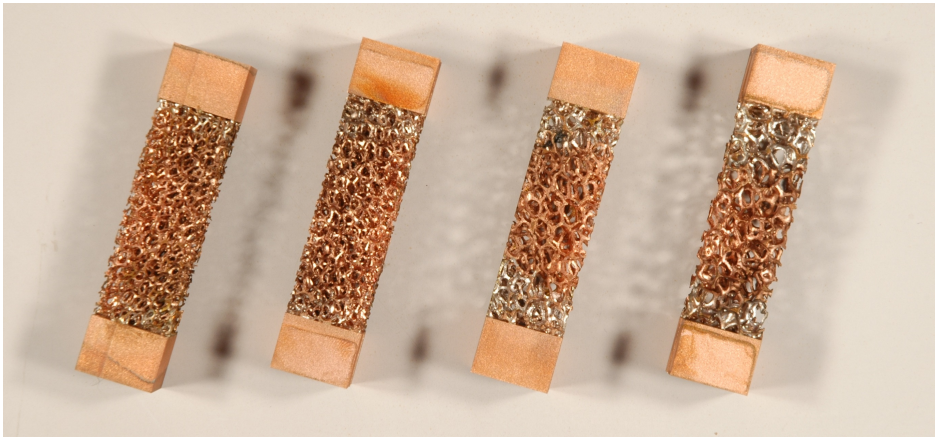

Figure 3.6: Copper foam slabs (40, 20, 10, and 5 PPI, respectively).

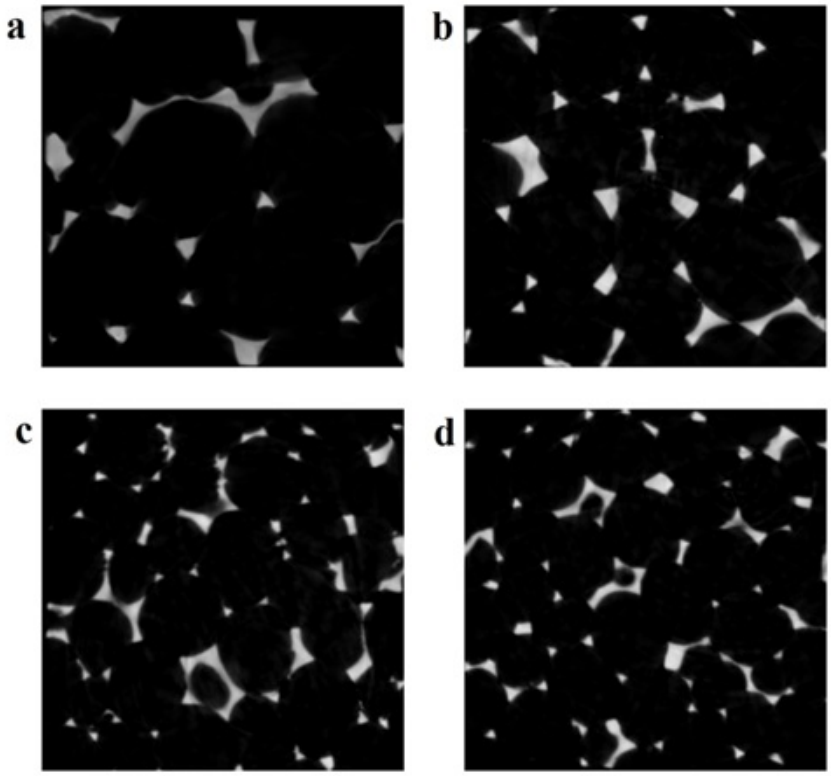

Figure 3.7: Representative two-dimensional scan images, shown for: (a) 5 PPI, (b) 10 PPI, (c) 20 PPI, and (d) 40 PPI, respectively.

the height of the foams. This resolution was chosen to enable all the microstructural details of the individual pores and ligaments to be captured.

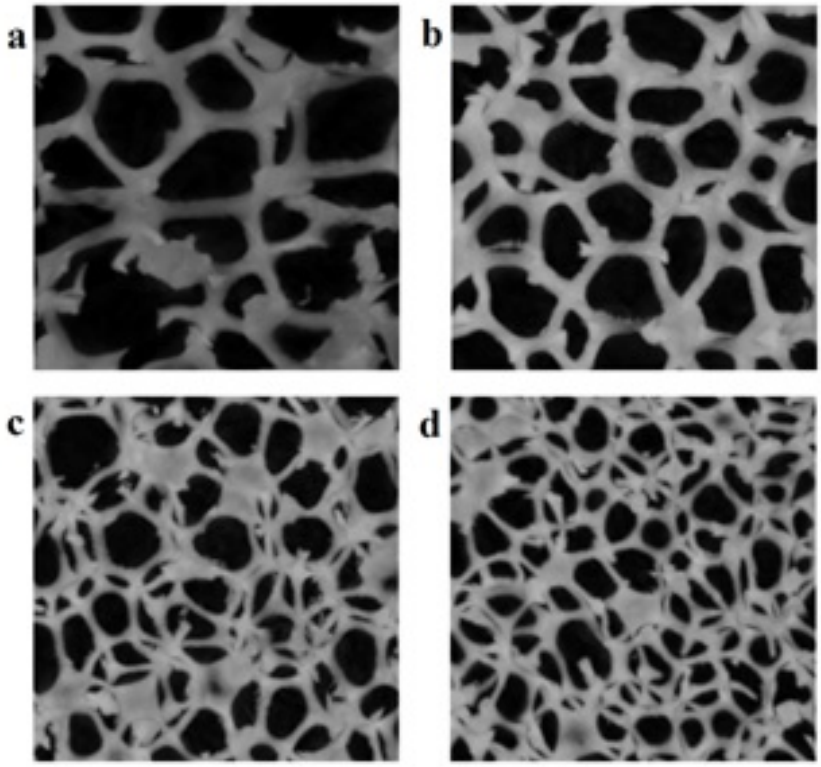

Figure 3.8: Examples of reconstructed foams. Images correspond to: (a) 5 PPI, (b) 10 PPI, (c) 20 PPI, and (d) 40 PPI, respectively.

The image processing was performed using the commercial software Simpleware [79] employing the ScaIP module, which permits operations such as filtering, noise removal, region identification, and three-dimensional reconstruction. It also permits exporting the 3D images for CAD or mesh generation. In figure 3.7, examples of the scan images are shown for the 5, 10, 20, and 40 PPI copper foams, respectively. As it appears from these scans, the strut cross sections seem to be triangular. The demarcation between the solid phase and the fluid phase is not crisp: metal absorbs X-rays leading to brighter zones, whereas air let X-rays pass, leading to darker zones. Thus, the identification of the two distinct regions (fluid and solid) is based on a threshold value. Appropriate greyscale values are identified so as to match the porosities of the reconstructed foams with those provided by the manufacturer. Further, floodfill segmentation was also performed to retain the connected ligaments, while discarding the unconnected loose ones.

At this point, since a large number of pixels would increase both the number of mesh elements and the demand on memory, a down-sampling operation was performed, such that the resolution of images is slightly lowered but the geometry is still well-represented. Representative reconstructions of the foam samples are shown in figure 3.7. According to the measurements reported in table 3.1 and as can be seen from figure 3.8, the pores become smaller and the ligaments shorter and thinner as the number of pores per linear inch of the sample increases.

The foam region in the brazed regions adjacent to the copper plates at the bottom and top (see figure 3.6) was difficult to reconstruct as the presence of the copper plate created considerable noise in the scanned images. As a result, it was not possible to reconstruct the entire height of the scanned samples (40 mm). The typical reconstructed sample height was roughly 30 mm, omitting 5 mm of interface region on either sides. However, this height is sufficient for fluid flow computations, as will be explained in the following section.

3.3 Numerical model

The reconstructed three-dimensional foams are input to the ScanFE module in Simpleware [79] for generating finite-volume meshes. Meshing the entire scanned volume would place a significant demand on memory during mesh generation. Further, the meshes thus produced would need huge computational resources for numerical analysis of fluid flow and heat transfer. Therefore, only smaller regions were employed for mesh generation. The length of the sample in the flow direction was 100 mm in the experiments, leading to fully developed flow. To ensure similar, fully developed flow conditions in the numerical simulations, the foam must have an adequate number of pores in the flow direction. A sensitivity analysis was carried out in order to determine the number of pores that is necessary for attaining fully developed flow. Preliminary simulations were run on the 40 PPI sample with fluid domains having the same boundary conditions and fluid properties but different number of pores along the flow direction. Domains consisting of 5, 10, and 20 pores in the flow direction were considered, and the difference in the pressure gradient determined. It was observed that the difference between the 10 pores and the 5 pores sized domains was -15.7% in pressure gradient, whereas between the 20 pores and 10 pores sized

domains, the difference was only -3.2%. A domain size of approximately 10 pores in the flow direction is therefore deemed sufficient for the flow to attain fully developed conditions for the flow speeds considered for the 10, 20, and 40 PPI samples. However, for the 5 PPI copper foam, only 6 pores were present in the flow direction as the maximum height that was possible to reconstruct was only 30 mm, as described in the previous section.

At a constant minimum mesh element size, and considering domains with 10 pores along the flow direction, the number of mesh elements directly depends on the number of pores per linear inch of the foam; the number of mesh elements increases when linear porosity decreases because the pore dimension increases, and vice-versa. To reduce the overall mesh count, mixed tetrahedral and hexahedral elements were employed during meshing. A typical mesh volume is represented in figure 3.9. Table 3.2 presents the size of the meshed domain along with the number of elements present in the meshed volume.

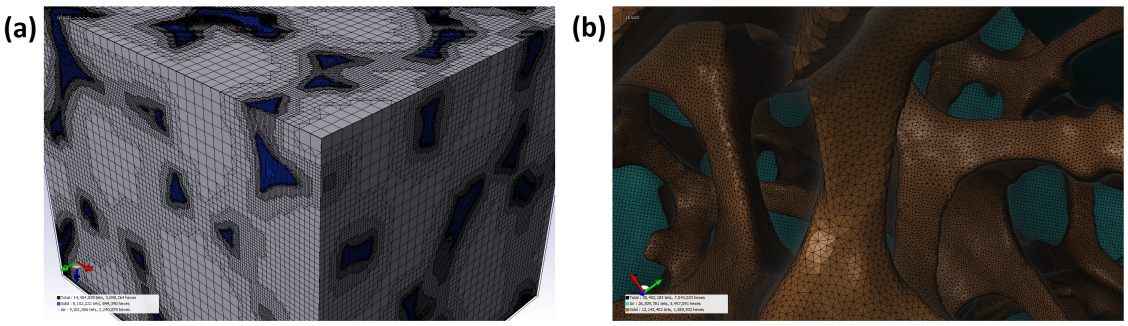

Figure 3.9: Global (a) and internal (b) view of a typical mesh.

Table 3.2: Domain sizes and number of mesh elements in a typical volume employed for analysis.

Sample	Domain Size [mm × mm × mm]	Mesh Elements [-]
Cu-5-6.5	9.92 × 9.92 × 29.96	27 million
Cu-10-6.6	5.96 × 5.96 × 25.36	10 million
Cu-20-6.5	4.40 × 4.40 × 12.76	5 million
Cu-40-6.4	4.48 × 4.48 × 6.34	3 million

Considering a pore diameter of 5.08, 2.54, 1.27, and 0.635 mm for the 5, 10, 20, and 40 PPI foam, respectively, 10 pores are included along the flow direction for all the samples, except for the 5 PPI sample for which 6 pores are included. The meshes are created with the ScanFE module of Simpleware [79] as noted previously. The continuity, momentum and energy equations for a laminar steady-state incompressible flow are given by:

$$\frac{\partial}{\partial x_i}\rho u_i = 0 \tag{3.1}$$

$$\frac{\partial}{\partial x_i}\left(\rho u_j u_i\right) = -\frac{\partial p}{\partial x_i} + \frac{\partial}{\partial x_i}\left(\mu \frac{\partial u_i}{\partial x_j}\right) \tag{3.2}$$

$$\frac{\partial}{\partial x_i}\left(\rho u_i c_p T\right) = \frac{\partial}{\partial x_i}\left(\lambda \frac{\partial T}{\partial x_i}\right) \tag{3.3}$$

where u represents the air velocity in the i or j direction, ρ the density of fluid, μ the dynamic viscosity, c_p the specific heat at constant pressure, T the temperature and λ the thermal conductivity. The governing equations are solved using the finite-volume commercial software ANSYS Fluent [80], using a first-order upwind difference scheme for flow and energy calculations. The SIMPLE scheme is employed for pressure-velocity coupling, and the flow field is deemed converged when the absolute value of all the residuals falls below 1.0×10^{-6} for the flow calculation, and below 1.0×10^{-7} for the thermal calculations.

The boundary conditions employed in the present work are shown schematically

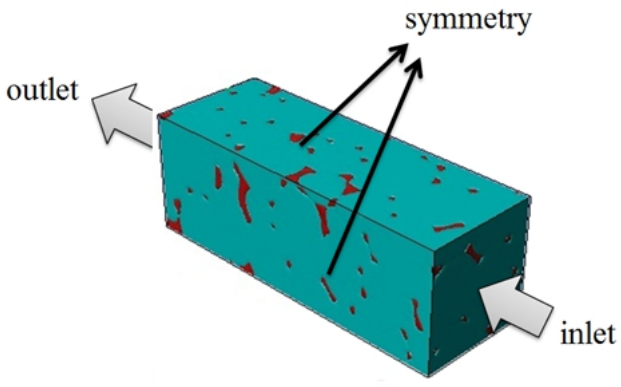

Figure 3.10: Boundary conditions employed in the present study.

in figure 3.10. Here, the solid zone is highlighted in red, while the fluid zone is shown in blue. The boundary conditions are also detailed below:

- velocity-inlet boundary condition and temperature at the inlet of the fluid domain;
- pressure-outlet boundary condition with zero gauge pressure at the outlet of the fluid domain;
- symmetry boundary condition on the lateral sides of the domain; and
- wall with no slip boundary condition and constant heat flux at the interface between the solid and fluid domains.

The flow is assumed to be three-dimensional, steady-state and incompressible, and the working fluid is air, with constant fluid properties calculated at the mean values of air temperature and pressure as reported in chapter 1. Further, fluid flow and heat transfer simulations were only performed in the laminar regime, with Reynolds numbers (based on the superficial velocity and on the square root of permeability [77] as the characteristic length) in the range of 62 - 215. The following section presents the details of the results obtained, as well as a comparison against experiments and empirical correlations.

3.4 Numerical results

The experimental velocities and air properties described in chapter 1 are taken as input parameters for the numerical simulations, to enable a direct comparison. A superficial velocity range from 2.5 to 5 m s^{-1} is explored in the numerical study, with the air being at ambient pressure as in the experiments. For each sample, 6 different velocities are investigated, and the resulting numerical pressure gradients and interstitial heat transfer coefficient are discussed and compared against previously obtained experimental results.

Pore-scale simulations permit to study the real fluid flow and heat transfer in detail. Figures 3.11a and 3.11b present the streamlines and velocity field, and the temperature field, respectively, for the 10 PPI sample with an air inlet velocity of

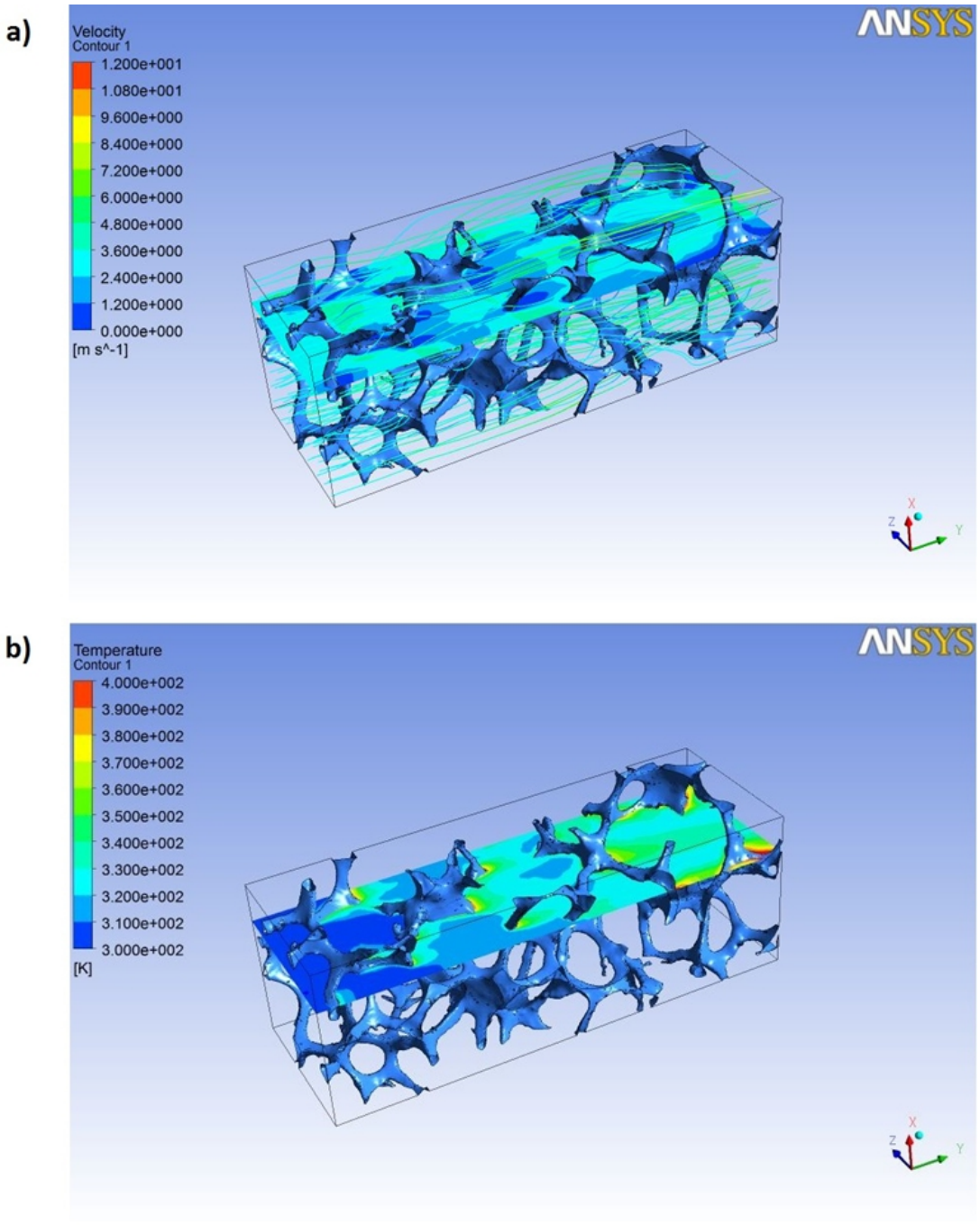

Figure 3.11: Streamlines, velocity and temperature field with an inlet velocity of 2.5 m s^{-1} for the 10 PPI foam sample.

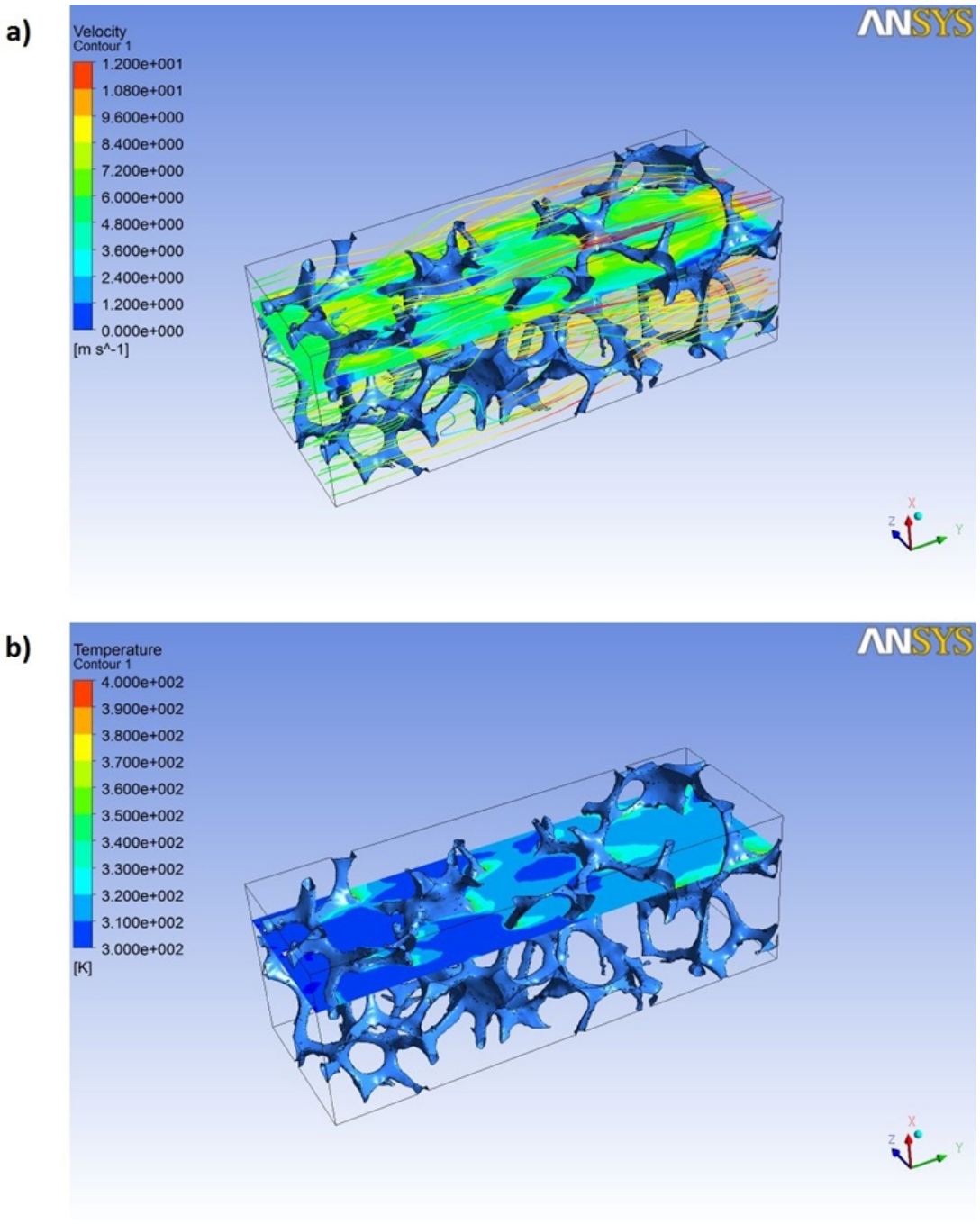

Figure 3.12: Streamlines, velocity and temperature field with an inlet velocity of 5.0 m s^{-1} for the 10 PPI foam sample.

2.5 m s^{-1} and an inlet air temperature of 300 K. As it appears, the metal foam structure creates turbulence and, as a result, the fluid is well mixed, remaining at a temperature lower than 340 K on average. As expected, the fluid is heated along the flow direction. Shadow zones with very low air velocities are present near the trailing edge of the ligaments, with a consequent high temperature; anyway, these are delimited zones, and the temperature falls down again in a small volume, thanks to the high mixing of the fluid. This demonstrates the effectiveness of such material in creating highly mixed zones that enhance the heat transfer.

The velocity and temperature fields for the same sample with an inlet velocity of about 5.0 m s^{-1} are reported in figure 3.12. As expected, higher velocity gradients appear, with subsequent higher pressure drop. Zones with very low velocities are still present near the trailing edge of the ligaments. The resulting temperature is lower than the former case.

In figure 3.13, the numerical pressure gradients for the 4 copper foams are plotted against the pore velocity. It is observed that the pressure gradient has an almost quadratic dependence on velocity in the range of the tested working conditions, in accordance with the Darcy-Forchheimer equation. At any velocity, the samples with the smallest pore sizes (or largest PPI) demonstrated the highest pressure drop and vice-versa, as expected. Similar observations may also be made from the experimental results shown in chapter 1.

Figure 3.14 compares pressure gradients from the numerical simulations against data from experiments performed at similar velocities. The pressure gradient results for the four copper foams are seen to match the experimental values very well, globally with a mean relative and absolute deviation of -3.8% and 5.4%, respectively. Relative, absolute, and standard deviations between the numerical and experimental results for each foam are summarized in table 3.3.

The thermal simulations are performed by imposing a constant heat flux q at the interface between the solid and fluid region. Thus, it is possible to calculate the numerical interstitial heat transfer coefficient $\alpha_{numerical}$ defined as:

$$\alpha_{numerical} = \frac{q}{\bar{T}_{wall} - \bar{T}_{air}} \tag{3.4}$$

where $\bar{T}_{wall}$ and $\bar{T}_{air}$ are the mean wall temperature and the mean air temperature,

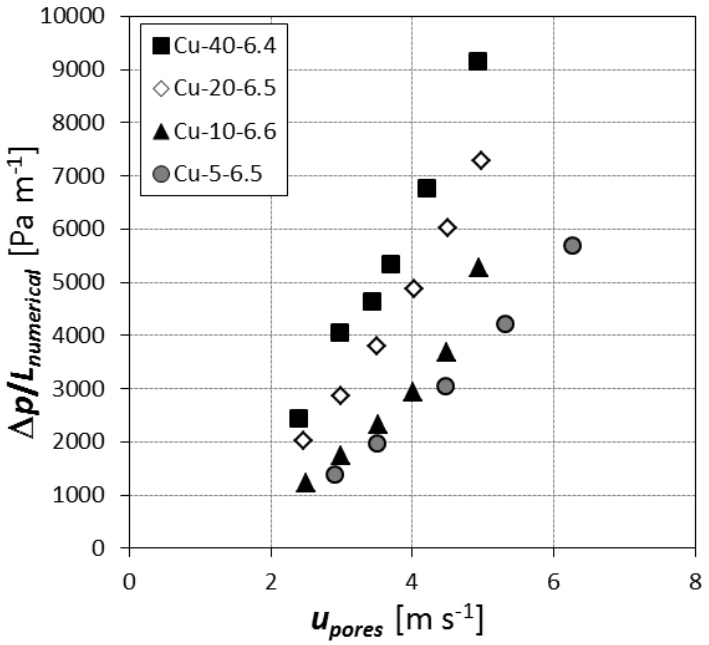

Figure 3.13: Numerical pressure gradient plotted against the pores velocity.

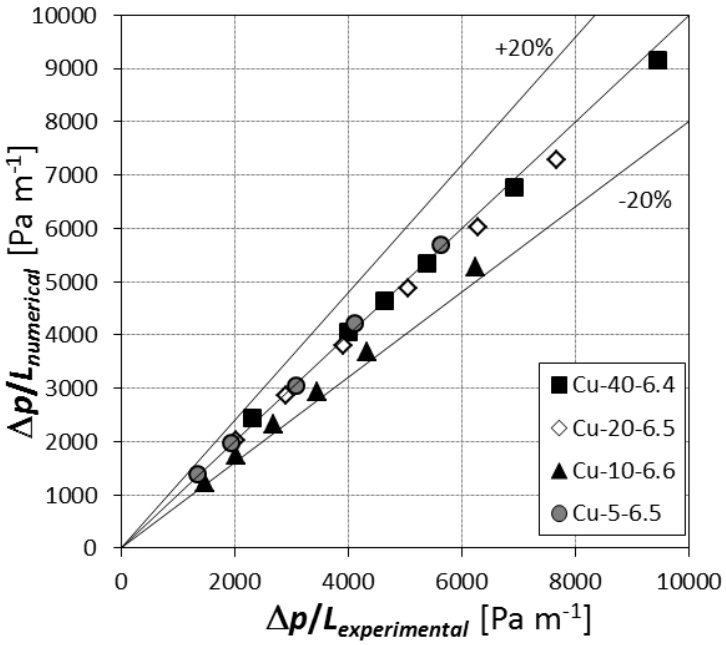

Figure 3.14: Comparison between numerical and experimental pressure gradients.

Table 3.3: Difference between numerically computed and experimental pressure gradients, shown for the four copper foams considered.

Sample	e_{rel} [%]	e_{abs} [%]	σ_N [%]
Cu-5-6.5	2.1	2.2	1.9
Cu-10-6.6	-14.6	14.6	0.6
Cu-20-6.5	-2.7	2.8	1.6
Cu-40-6.4	-0.4	2.4	1.9

respectively. Since q is applied to the total surface area, α refers to the overall heat transfer area.

In paragraph 1.9.3 a new model to estimate the thermal performances of metal foams has been proposed. This model permits to calculate both the interstitial heat transfer coefficient and the foam finned surface efficiency.

Figure 3.15 highlights the trend of the numerical heat transfer coefficient and of the foam finned surface efficiency against the pores velocity. Ω^* is calculated using equations 1.70-1.72 with $\alpha_{numerical}$ as interstitial heat transfer coefficient, and with a foam core height H of 40 mm, which is the height of the original specimens under investigation. As it can be observed, the interstitial heat transfer coefficient increases with the pores velocity and with the number of pores per linear inch, and it is higher for the foam sample with the largest number of pores per inch. Nevertheless, the 40 PPI sample has the lowest efficiency, since it has the thinnest ligaments and the highest heat transfer coefficient. The foam finned surface efficiency has the opposite trend of the interstitial heat transfer coefficient: Ω^* decreases when the pores velocity increases and when the number of pores per linear inch increases.

The comparison between numerical interstitial heat transfer coefficient and the values predicted by the correlation of equation 1.69 is reported in figure 3.16. A good match can be found between numerical and empirical values, on average with a relative deviation of 1.6%, an absolute deviation of 9.5%, and a standard deviation of 2.7%. Figure 3.17 presents a comparison between the experimental and numerical product $\alpha \cdot \Omega^*$, where $\alpha_{numerical}$ is used as interstitial heat transfer coefficient in equation 1.71 for the calculation of Ω^*: globally, the mean relative, absolute and standard deviations are: -2.1%, 5.5%, and 4.8%, respectively. The deviations for

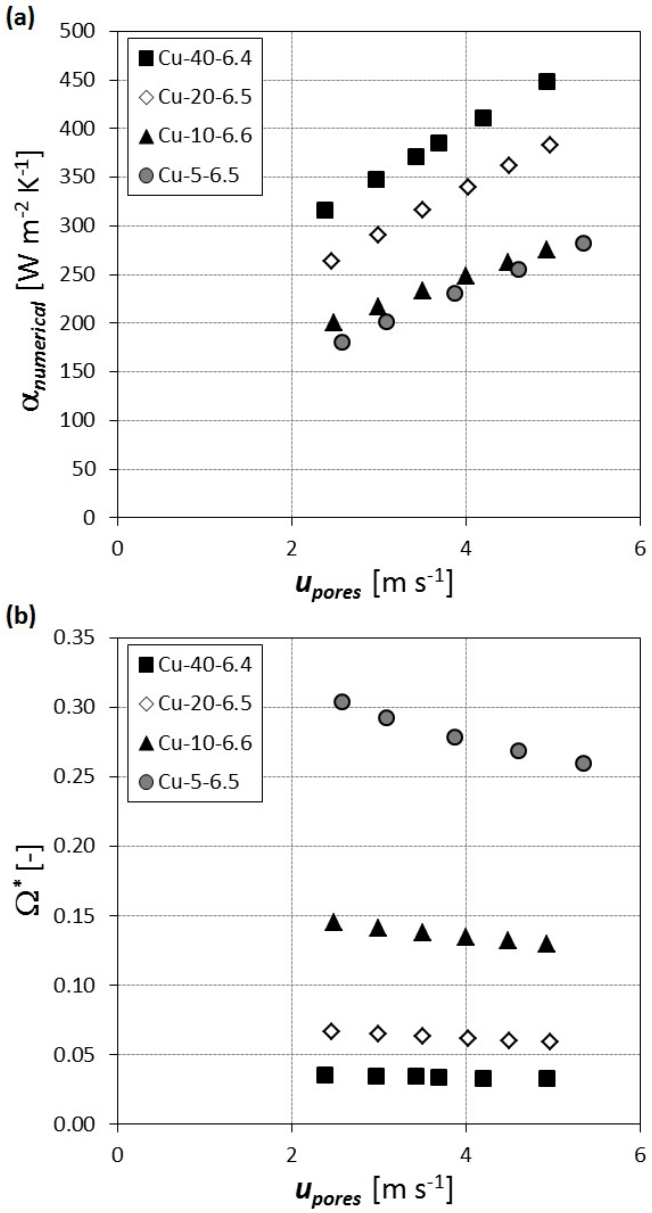

Figure 3.15: Numerical interstitial heat transfer coefficient (a) and foam finned surface efficiency (b) plotted against the pores velocity.

each sample are reported in table 3.4.

These results validate the numerical hydraulic and thermal approach employed in the present study and demonstrate the utility of the employed approach in computing detailed flow physics directly at the pore scale.

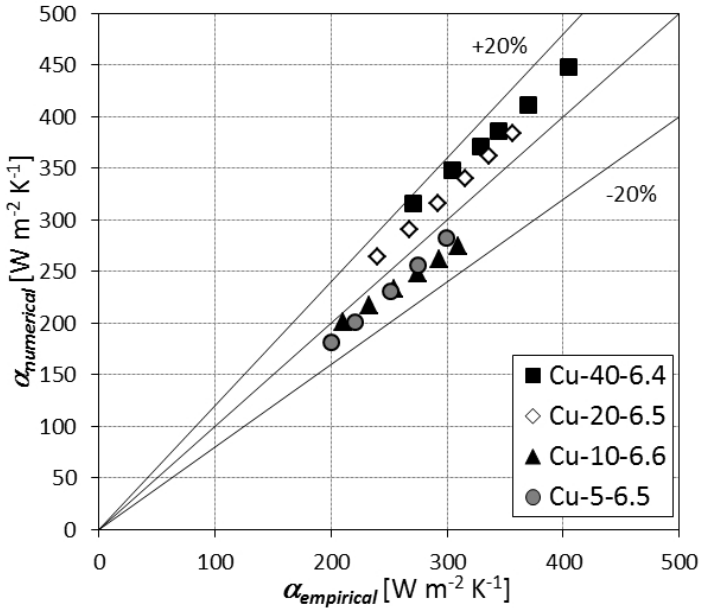

Figure 3.16: Comparison between numerical and empirical interstitial heat transfer coefficients.

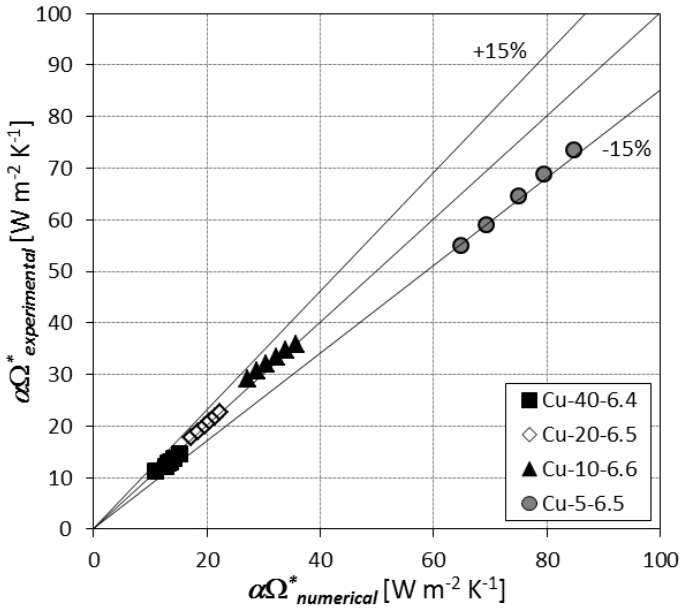

Figure 3.17: Comparison between numerical and experimental values of the product between interstitial heat transfer coefficient and foam finned surface efficiency.

Table 3.4: Difference between numerically computed and empirical/experimental values of α and $\alpha \cdot \Omega^*$.

Parameter	Sample	e_{rel} [%]	e_{abs}[%]	σ_N [%]
α	Cu-5-6.5	-7.7	7.7	1.4
α	Cu-10-6.6	-8.6	8.6	2.2
α	Cu-20-6.5	8.2	8.2	0.8
α	Cu-40-6.4	13.0	13.0	2.1
$\alpha \cdot \Omega^*$	Cu-5-6.5	-14.0	14.0	0.8
$\alpha \cdot \Omega^*$	Cu-10-6.6	4.0	4.0	2.4
$\alpha \cdot \Omega^*$	Cu-20-6.5	1.8	1.8	0.3
$\alpha \cdot \Omega^*$	Cu-40-6.4	-2.3	3.6	2.8

Chapter 4

Development of a new experimental setup for the study of the flow boiling

In this chapter, the development of a new experimental setup for the study of the flow boiling phenomenon inside microstructured surfaces is presented. The first part regards the basic theory on two-phase flow and flow boiling, which will help to understand the mechanisms that control the phenomenon. Then, the state of the art is discussed, focusing the attention to the experimental facilities that employ microstructured surfaces which are able to augment the heat transfer. Finally, the new experimental facility, built at the Department of Industrial Engineering of the University of Padova is introduced, along with calibration tests.

4.1 Introduction

4.1.1 Flow patterns

The hydrodynamic and thermal behaviour of two-phase flow, such as pressure drop, void fraction, velocity distribution, and heat transfer coefficient, varies with the observed flow pattern (or regime).

Figure 4.1 shows the flow pattern in an horizontal tube. Flow patterns that can be distinguished are here described.

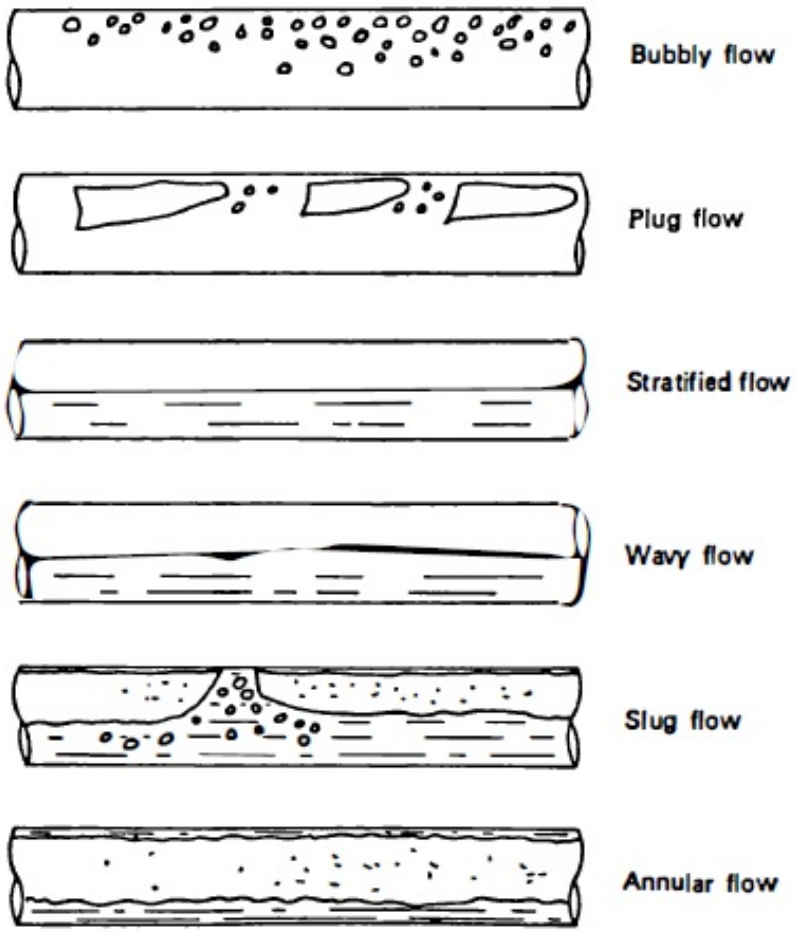

Figure 4.1: Flow patterns in an horizontal tube, from Tong and Tang [81].

Bubbly flow In bubbly flow, the vapour phase is moving as isolated bubbles in a liquid stream. This flow pattern occurs at low void fractions.

Plug flow Plug flow consists of elongated vapour bubbles.

Stratified flow Stratified flow occurs when the two phases are moving separately. This patterns occurs only at very low liquid and vapour velocities.

Wavy flow When the vapour velocity increases, the interface between liquid and vapour phase becomes disturbed by waves traveling in the flow direction.

Slug flow A further increase in vapour velocity causes the waves at the interface to reach the top wall of the tube.

Annular flow A further increase in the vapour velocity leads to the formation of a gas core with a liquid film around the inner surface of the tube.

An accurate analysis of regime transitions with flow in horizontal pipes was carried out by Taitel and Dukler [82]. They proposed a map which was successfully compared with a large amount of experimental data. Figure 4.2 shows this gener-

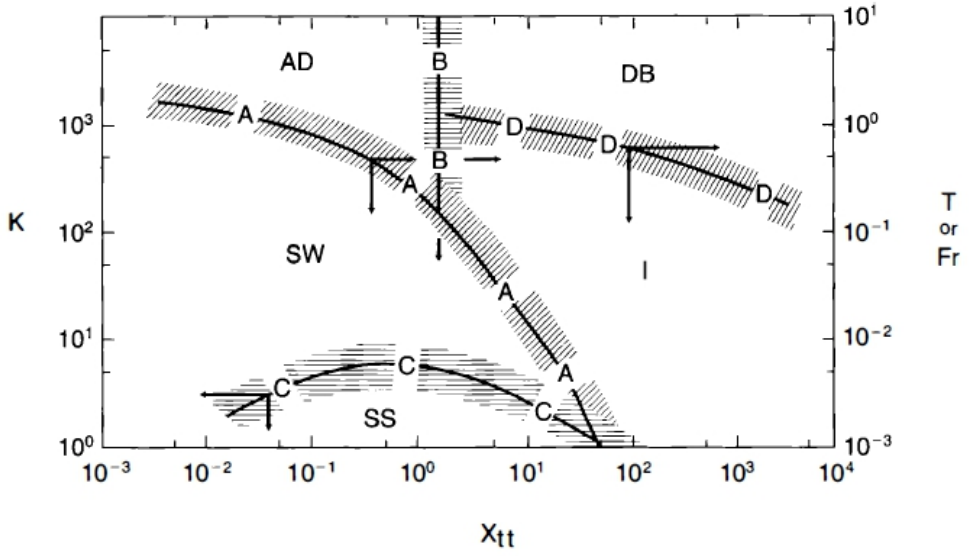

Figure 4.2: Flow regime map, from Taitel and Dukler [81].

alized map, and it makes use of different coordinates for the different transitions. These functions are defined as follow:

$$\mathrm{Fr} = \left(\frac{\rho_V}{\rho_L - \rho_V}\right)^{1/2} \left[\frac{V_{SV}}{(dg\cos\theta)^{1/2}}\right] \tag{4.1}$$

$$K = \left[\frac{\rho_V V_{SV}^2 V_{SL} \rho_L}{(\rho_L - \rho_V) g \mu_L \cos\theta}\right]^{1/2} \tag{4.2}$$

$$T = \left[\frac{(\,\mathrm{d}p/\,\mathrm{d}z)_L}{(\rho_L - \rho_V) g \cos\theta}\right]^{1/2} \tag{4.3}$$

$$X_{tt} = \frac{(\,\mathrm{d}p/\,\mathrm{d}z)_L}{(\,\mathrm{d}p/\,\mathrm{d}z)_V} = \left(\frac{\rho_V}{\rho_L}\right)^{0.5} \left(\frac{\mu_L}{\mu_V}\right)^{0.1} \left(\frac{1-x}{x}\right)^{0.9} \tag{4.4}$$

where ρ_V and ρ_L are the vapour and liquid densities, V_{SV} and V_{SL} the vapour and liquid superficial velocities, μ_V and μ_L the vapour and liquid dynamic viscosities,

and θ the slope angle of the channel. $(\mathrm{d}p/\mathrm{d}z)_L$ and $(\mathrm{d}p/\mathrm{d}z)_V$ are pressure drops calculated as if the liquid or the vapour were the sole flow in the channel.

4.1.2 Flow boiling

Regions of heat transfer

Boiling is the heat transfer mechanism which involves the phase change process from the liquid phase to the vapor phase. There are two basic types of boiling: pool boiling and flow boiling. Pool boiling is boiling that happens when the heating surface is submerged in a pool of liquid, whereas the flow boiling is the boiling that happens in a flowing stream of fluid.

To explain the various regimes that are encountered in flow boiling, let us consider the upward flow of a liquid in vertical channel with heated walls. Figure 4.3 shows the various flow patterns encountered over the length of the vertical tube.

At first, the liquid temperature is lower than its saturation temperature. Whilst the liquid is being heated up to the saturation temperature and the wall temperature remains below that necessary for nucleation, the process of heat transfer is "single phase convective heat transfer" to the liquid phase (region A).

At some point along the tube, the conditions adjacent to the wall are such that the formation of vapour from nucleation sites can occur. Initially, the vapour formation takes place even in presence of subcooled liquid and this heat transfer mechanism is called "subcooled nucleate boiling". In this region, the wall temperature remains essentially constant few degrees above the saturation temperature, while the mean bulk fluid temperature is increasing its temperature up to the saturation temperature. The transition from regions B to C, i.e. from subcooled nucleate boiling to "saturated nucleate boiling", happens when the liquid reaches the saturation temperature (x=0). Anyway, subcooled liquid can persist in the liquid core, as shown in figure, until the liquid mixed temperature reaches the saturation temperature.

As the quality increases, a fundamental transition in the mechanism of heat transfer takes place: the process of "boiling" is replaced by the process of "evaporation". This transition is preceded by a change in the flow patterns, from bubbly or slug flow (regions C and D) to annular flow (regions E and F). Close to this transition point, the formation of vapour at wall sites may cease, and further vapour

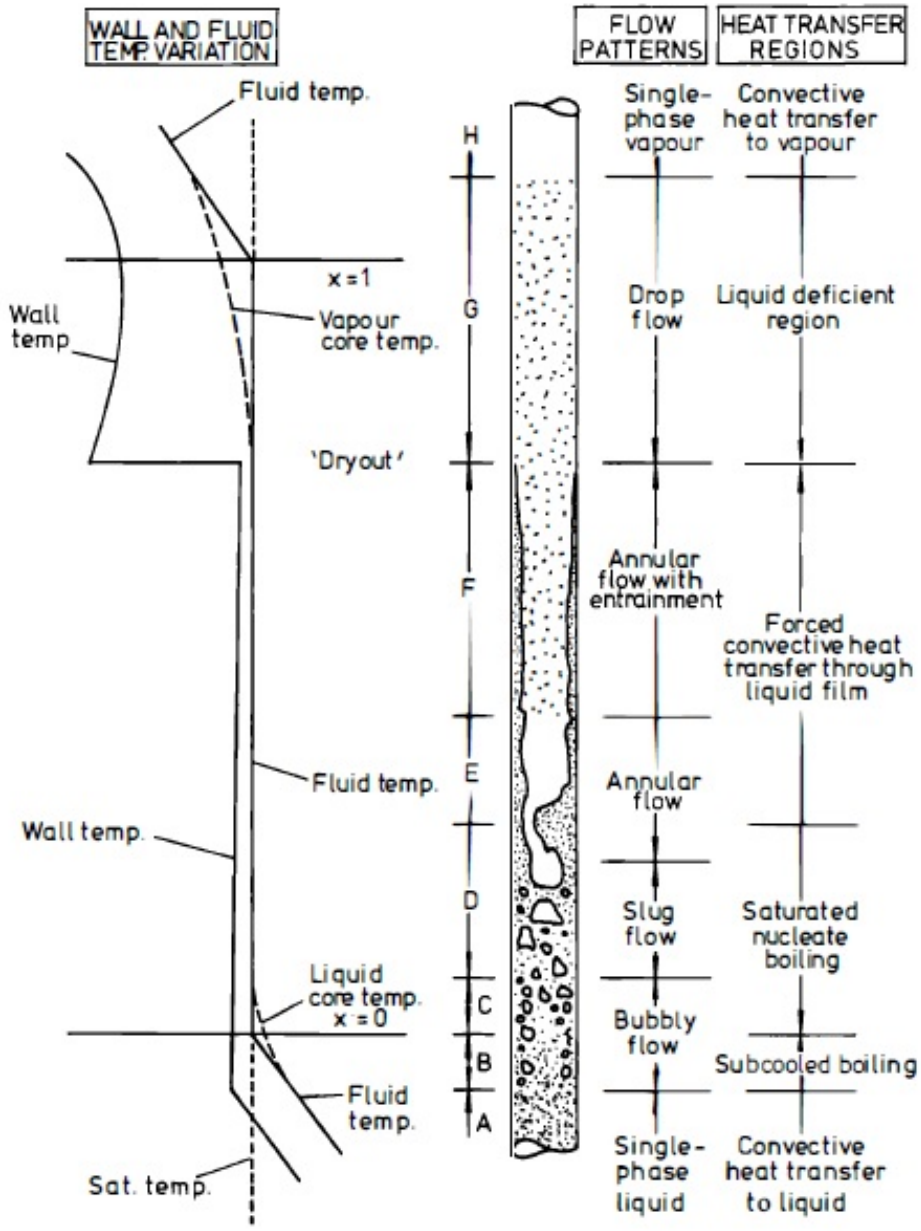

Figure 4.3: Regions of heat transfer in convective boiling, from Collier and Thome [83].

formation will be a result of evaporation at the liquid film - vapour core interface. Increasing velocities in the vapour core will cause entrainment of liquid in the vapour core (region F). The region is referred to as “two-phase forced convection region” of heat transfer. In this region, the wall temperature slightly diminishes.

As the vapour quality increases, the liquid thickness at the tube wall thins, until at some critical value of vapour quality the complete evaporation of the liquid occurs: this transition is called "dryout", and it is accomplished by a sudden rise of the wall temperature.The area between the dryout point and the transition to dry saturated vapour (region H) is called "liquid deficient region" (region G).

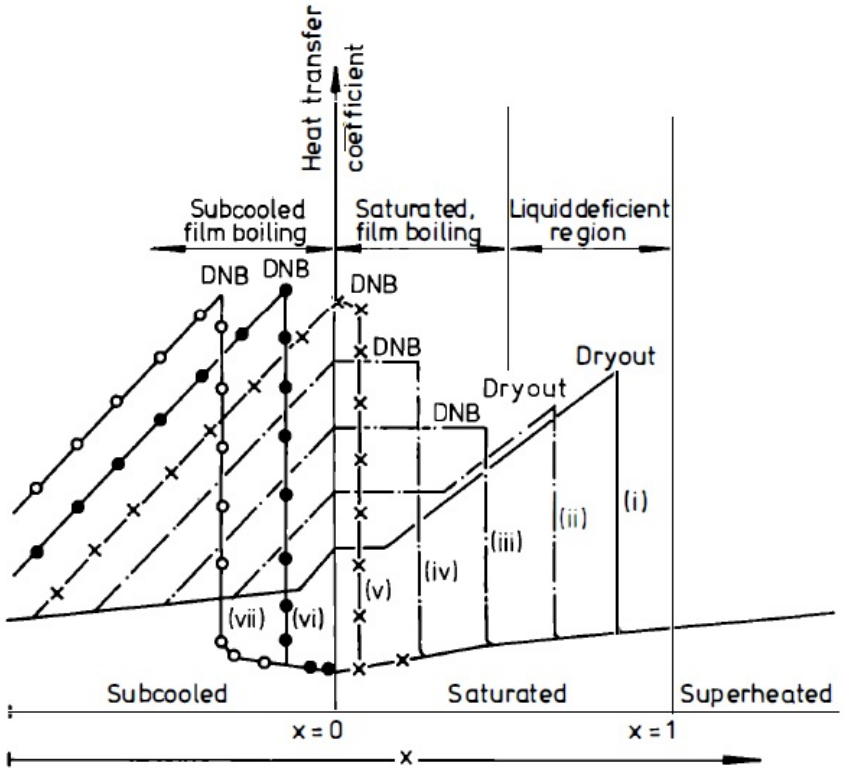

Figure 4.4: Variation of the heat transfer coefficient with vapour quality with increasing heat flux, from Collier and Thome [83].

The variation of the heat transfer coefficient is reported in figure 4.4. The local heat transfer coefficient can be defined as the ratio between the heat flux and the temperature difference between wall and fluid. In the "single phase convective heat transfer region", the heat transfer coefficient is almost constant, and thus the temperature difference between wall and fluid remains constant. In the "subcooled nucleate boiling region", the wall temperature is almost constant, thus the temperature difference decreases with a relative increase of the heat transfer coefficient, up

to a vapour quality x=0. In the "saturated nucleate region" the temperature difference is constant, and consequently the heat transfer coefficient remains constant. Because of the reducing liquid film thickness in the "two-phase forced convection region", the heat transfer coefficient increases with increasing vapour quality, up to "dryout", when the heat transfer coefficient suddenly drops, with consequent increase of the wall temperature. In the "liquid deficient region" the heat transfer coefficient slightly increases with vapour quality. Finally, in the "single-phase vapour region" the heat transfer coefficient is that corresponding to a single-phase vapour flow. The trend of the heat transfer coefficient along the length of the tube follows curve i of figure 4.4.

The above analysis is valid for a relatively low heat transfer. For a higher heat flux (curve ii), the subcooled boiling starts sooner, the heat transfer coefficient in the nucleate region is higher, but it is unaffected in the two-phase forced convection, and the dryout occurs at lower vapour quality. A further increase of heat flux (curve iii) leads the subcooled boiling to start sooner, the heat transfer coefficient in the nucleate boiling region is again higher. As the vapour quality increases, before the two-phase forced convection is initiated and while bubbles formation is still occurring, the "departure from nucleate boiling (DNB)" occurs. Further increases of the heat flux (curves iv and v) cause DNB to occur earlier. At really high heat fluxes (curves vi and vii), DNB occurs in the subcooled region.

Saturated nucleate flow boiling

Saturated nucleate flow boiling covers regions C and D, where nucleate boiling is occurring at the wall and where the flow pattern is typically bubbly, slug, or low vapour quality annular flow. In this region, the two well known mechanisms of the flow boiling exists: nucleate boiling and two-phase forced convection, and up today it is not possible to separate these two contributes.

Chen [84] proposed an equation which covers both the saturated nucleate boiling region and the two-phase forced convection region, assuming that both these two contributions occur at some degree. The two-phase heat transfer coefficient (h_{tp}) can be considered as:

$$h_{tp} = h_{NB} + h_{fc} \tag{4.5}$$

where h_{NB} and h_{fc} are contributions due to nucleate boiling and forced convection, respectively. For the convection component, h_{fc}, Chen suggested:

$$h_{fc} = 0.023\,\mathrm{Re_{tp}}^{0.8}\,\mathrm{Pr_{tp}}^{0.4}\left(\frac{k_{tp}}{D}\right) \tag{4.6}$$

where $\mathrm{Re_{tp}}$, $\mathrm{Pr_{tp}}$, and k_{tp}, are the Reynolds number, Prandtl number, and thermal conductivity of the two-phase flow. Since heat is transferred through a liquid film in annular or dispersed flow, Chen proposed to use the liquid thermal conductivity k_L instead of k_{tp}. Since the value of Prandtl number for liquid and vapour are usually of the same magnitude, $\mathrm{Pr_L}$ can be used for $\mathrm{Pr_{tp}}$. A parameter F is defined such that:

$$F = \left[\frac{\mathrm{Re_{tp}}}{\mathrm{Re_L}}\right]^{0.8} = \left[\frac{\mathrm{Re}_{tp}}{G(1-x)D/\mu_L}\right]^{0.8} \tag{4.7}$$

and thus h_{fc} bocomes:

$$h_{fc} = 0.023F\left[\frac{G(1-x)D}{\mu_L}\right]^{0.8}\left[\frac{\mu_L c_{p,L}}{k_L}\right]\left(\frac{k_L}{D}\right) = Fh_L \tag{4.8}$$

where F may be expected to be a function of the Martinelli factor X_{tt}, since it is a flow parameter only.

For the evaluation of the nucleate boiling component h_{NB}, Forster and Zuber's [85] analysis with pool boiling was used. However, the actual superheat is not constant across the boundary layer, but it falls down. Thus, the mean superheat of the fluid, ΔT_0, in which bubbles grows, is lower than the wall superheat ΔT_{sat}, defined as the difference between the wall temperature and the fluid saturation temperature. Thus:

$$h_{NB} = 0.00122\left[\frac{k_L^{0.79} c_{p,L}^{0.45}\,\rho_L^{0.49}}{\sigma^{0.5}\mu_L^{0.29} h_{lv}^{0.24}\rho_V^{0.24}}\right]\Delta T_0^{0.24}\Delta p_0^{0.75} \tag{4.9}$$

where h_{lv} is the latent heat of vaporization. The ratio between the mean superheat ΔT_0 and the wall superheat ΔT_{sat} is defined by Chen as a convective boiling suppression factor S and, using also the Clausius-Clapeyron equation:

$$S = \left(\frac{\Delta T_0}{\Delta T_{sat}}\right)^{0.99} = \left(\frac{\Delta T_0}{\Delta T_{sat}}\right)^{0.24}\left(\frac{\Delta T_0}{\Delta p_{sat}}\right)^{0.75} \tag{4.10}$$

and thus equation 4.9 becomes:

$$h_{NB} = 0.00122S\left[\frac{k_L^{0.79}c_{p,L}^{0.45}\rho_L^{0.49}}{\sigma^{0.5}\mu_L^{0.29}h_{lv}^{0.24}\rho_G^{0.24}}\right]\Delta T_{sat}^{0.24}\Delta p_{sat}^{0.75} \tag{4.11}$$

The value of S ranges between 0 and 1. In this model, the two functions F and S were empirically determined. Generally speaking, F increases with increasing values of the reciprocal Martinelli parameter indicating that the effective turbulence associated with two-phase flow increases with increasing vapor fraction. The suppression factor, S, approaches unity at low values of the two-phase Reynolds number and decreases asymptotically to zero at high values of the two-phase Reynolds number. These results are reasonable in indicating that at low flow rates and low vapour fraction the boiling mechanism plays a relatively important part, whereas at high flow rates and high vapour fraction, the boiling is suppressed and the convective heat transfer mechanism becomes increasingly important.

Later different equations have been proposed by many authors, but the basic idea of the two concurrent mechanisms (nucleate boiling and two-phase forced convection) persists. More recent correlations are based on a general power law, in which nucleate boiling and convective mechanisms are combined together to obtain the two-phase heat transfer coefficient h_{tp}:

$$h_{tp} = \left[(h_{NB})^n + (h_{fc})^n\right]^{1/n} \tag{4.12}$$

4.2 State of the art on the flow boiling through enhanced heat transfer surfaces

Boiling is the heat transfer mechanism with the highest heat transfer coefficients, thus it can be used to spread high fluxes to maintain the wall temperature at low values with compact heat sinks. Moreover, new surfaces with microporous coatings, Carbon Nano Tubes (CNTs) coatings, or microstuctured surfaces are now available to enhance the boiling phenomenon. Nevertheless, a lot of work is still needed to deeply understand the boiling mechanism in such surfaces, where a huge number of variables (among those heat flux, saturation temperature, flow pattern, gravity,

subcooling, wall surface, and others) are linked together and play important and crucial roles. In this section, the state of the art of the flow boiling through enhanced surfaces is presented, with particular attention to the experimental facility and experimental results.

4.2.1 Carbon Nano Tubes

A Carbon Nanotube is a tube-shaped material, made of carbon, having a diameter measuring on the nanometer scale. Typical outer diameters range from 1 to 100 nm and length from 1 to 50 μm. They exist in single-walled (SWCNT) or multi-walled (MWCNT) forms. SWCNTs are made from single graphene sheet with hexagonally arranged groups of carbon atoms, whereas MWCNTs have multiple co-axial graphene sheets. Due to their extremely high thermal conductivity, higher than 3000 W m^{-1} K^{-1}, they can be used for thermal management applications.

Khanikar et al. [86] performed experiments to assess the heat transfer enhancement benefits of coating the bottom wall of a shallow rectangular micro-channel with carbon nanotubes. They used water as working fluid. The main components of the test module are shown in figure 4.5a. The housing is made in G-7 Fiberglass Plastic, and it was machined to house an inlet and an outlet plenum to ensure uniform

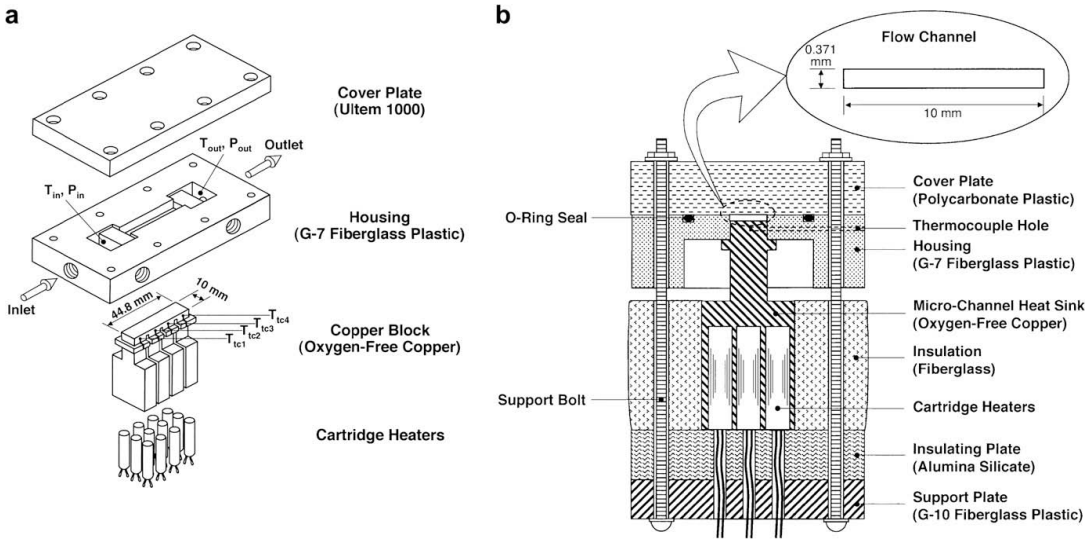

Figure 4.5: (a) Main components and (b) sectional assembly view of the test module [86].

flow distribution in the flow channel. A copper block with CNTs-coated surface is inserted upwards through the central cavity of the G-7 housing and, as shown in figure 4.5b, a single 10 mm wide, 0.371 mm high, and 44.8 mm long microchannel is formed. Twelve cartridges heaters are inserted in holes in the underside of the copper block to supply heat to the surface. Four K-type thermocouples are inserted in the copper block under a short distance below the heated surface.

Figure 4.6 depicts a schematic of the flow loop. A gear pump supplies the water from the loop's reservoir into a filter, followed by one of two parallel rotameters, and two plate-type heat exchangers before entering the test module. Water from a constant temperature bath is circulated through the two heat exchangers to control the test module's inlet temperature. Control valves situated both upstream and downstream of the test module are used to set the desired test module's outlet pressure as well as to minimize flow or pressure oscillations in the test module. A third heat exchanger is situated downstream of the test module to remove the heat supplied by the test module and the pump.

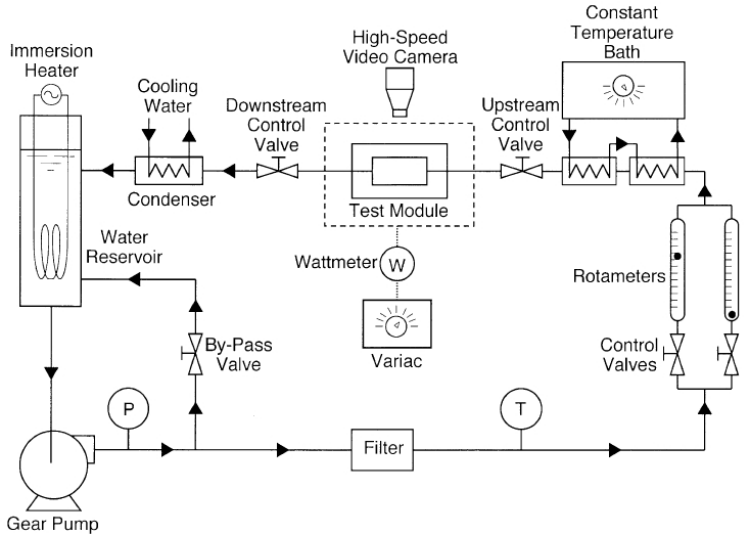

Figure 4.6: Schematic of the flow loop [86].

To understand the enhancement benefits of CNTs, thermal results with CNTs coating were compared with a bare surface in the same operating conditions. The study was supported by flow visualization using a high-speed video camera. The bare and CNTs-coated surfaces present similarities in the boiling behavior. Critical

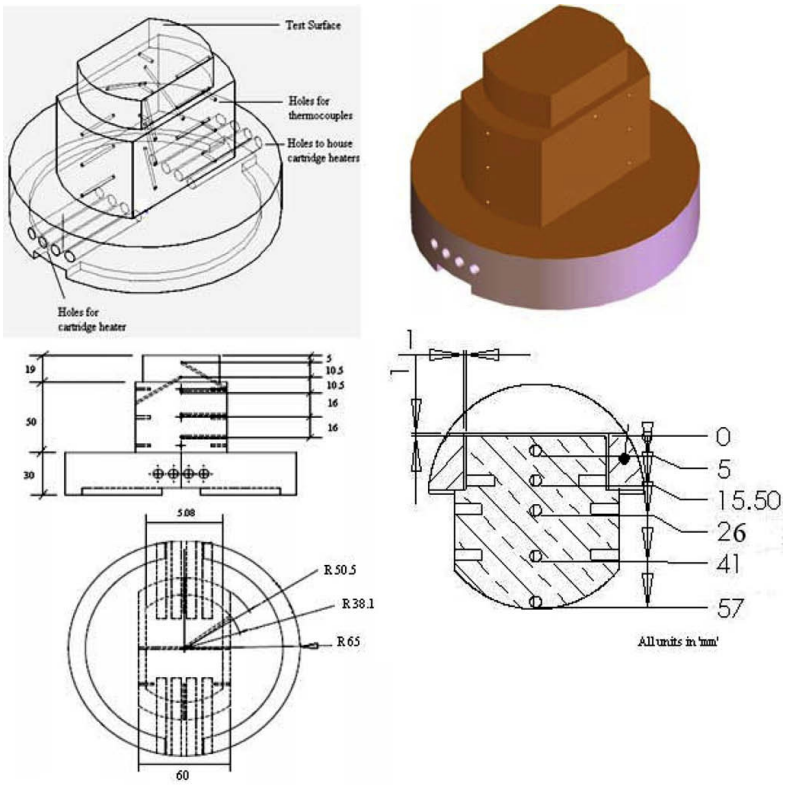

Figure 4.7: Schematic of the heater apparatus [87].

heat flux results were found to be quite repeatable for the bare surface, whereas it is degraded following repeated tests for the CNTs surface, especially at high mass velocities. SEM images revealed significant changes to the morphology of the CNTs-surface with repeated tests.

Singh et al. [87] studied the flow boiling heat transfer over a horizontal heater with carbon nanotube coatings. The horizontal heater consisted of either a bare silicon wafer or a silicon wafer coated with multi walled carbon nanotubes. The test section consists of a rectangular chamber housing the heater apparatus. The test section configuration was realized utilizing a rectangular macro-channel of a square cross section of 10 cm $\times$ 10 cm and the length of the test section in the flow direction is 20 cm. The heater apparatus was placed at the bottom of the channel on which a silicon wafer (bare or coated with CNTs) was mounted. In figure 4.7 a schematic of the heater apparatus is shown. The test section is made of aluminum and acetyl frames, and the top and two sides were fitted with glass windows to permit the direct

visualization of the flow boiling phenomenon. The copper block was heated using eight cartridges, able to supply a total flow rate of 6 kW. K-type thermocouples were inserted in different locations in the copper block, to enable heat flux calculations. Additional thermocouples were placed inside the test section to monitor the liquid temperature, the temperature of the ambient and the glass windows.

Flow boiling experiments were performed with de-ionized water at 60 °C and 40 řC of subcooling and at two different mass fluxes: 18 and 25 kW m^{-2}. Compared to the bare silicon wafer, the flow boiling heat transfer coefficient was found to be 30-80% higher, and the enhancement levels were higher at lower flow rates and lower values of subcoolings. In addition, the onset of boiling incipience was found to occur at lower values of heater temperature for the CNTs coating compared to that of bare silicon wafer.

4.2.2 Microporous coatings

Microporous coatings are another interesting method for enhancing the flow boiling mechanism. They consists of particles of few micron of diameter, which are deposited over a surface, leading to a coating thickness up to 1000 μm.

Sun et al. [88] investigated the enhancement of microporous surfaces in water subcooled flow boiling in a small channel. The coatings were produced by sintering spherical copper particles on the bottom surface of the channel. The experimental setup is shown in figure 4.8. It is a closed loop, where the working fluid was preheated in the preheating section to set the inlet temperature at the test section. The flow rate is controlled by a needle valve. Condenser A was used to condense the working fluid prior to reach the pump. The outlet pressure was maintained at 103.3 kPa. The test section was formed by bolting together a top plate and a support plate, as shown in figure 4.9. A 15 mm thick transparent polycarbonate plastic plate served as top plate. After the assembly, the rectangular channel was 10 mm wide, 1.28 mm high, and the heated length was 150 mm. A 0.03 mm thick Nickel-Chrome serpentine was used as heating element. Five T-type thermocouples were used to measure the fluid temperature: two were positioned at the inlet and outlet for fluid inlet and outlet temperature, and the other three were horizontally inserted in the copper plate for wall temperature measurement. Different microporous coatings

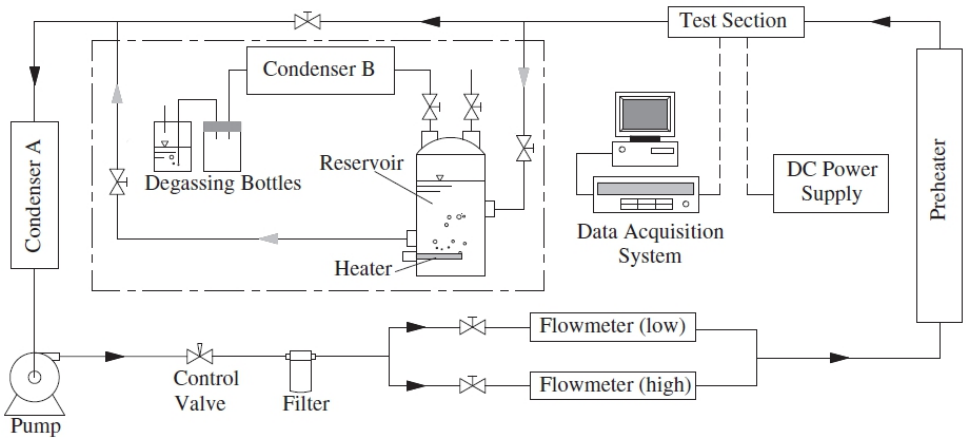

Figure 4.8: Flow boiling test loop [88].

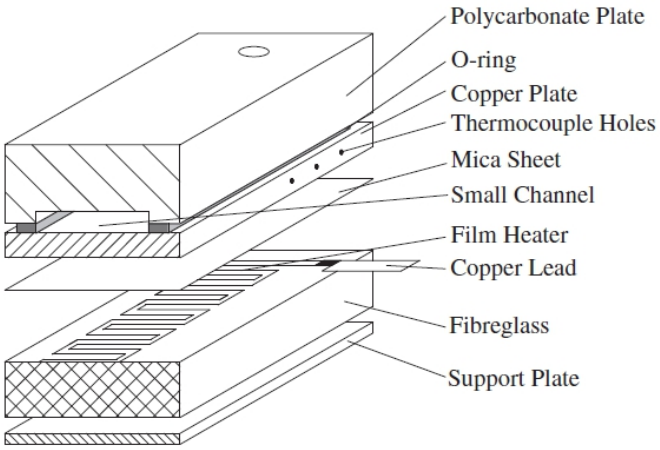

Figure 4.9: Test section assembly [88].

were tested, having particle diameter from 35 to 240 μm, and thickness from 100 to 673 μm.

Microporous coatings were found to enhance bubble confinement, leading to high heat transfer coefficient at low vapour quality. This enhancement became less apparent as the fluid mass flux was raised. Compared to heat transfer coefficients estimated by correlations for macroscale channels, the experimental values with the microporous coating were more than double. Under the tested experimental conditions, the optimum porous structure for flow boiling enhancement was obtained using a particle diameter of 120 μm with a coating thickness of 237 μm. i.e. two

layers of coating. Compared to a smooth surface, the optimum coating gave a 5.9 K (62%) lower wall superheat, a 121% higher heat transfer coefficient in the subcooled region, and a 178% higher heat transfer coefficient in the saturated region at a mass velocity of 100 kg m^{-2} s^{-1} and a subcooling of 50 K. In addition, higher inlet subcooling produced higher heat transfer coefficient enhancement in subcooled flow boiling. As subcooling increased from 30 to 70 K, the enhancement increased from 84% to 173%. In saturated regime, a 178% and 202% enhancement was observed, and was independent from subcooling increment.

Rayney et al. [89] experimentally studied the FC-72 subcooled flow boiling of two 1 cm^2 copper surfaces, one plain and one microporous coated. Experiments were performed for fluid velocities ranging from 0.5 to 4 m s^{-1} and subcooling levels from 4 to 20 K. The test loop is similar to the previous one. An heat exchanger after the test section was used to cool the fluid, and the desired temperature at the inlet of the section was controlled by using a preheater. The flow channel is 12.7 mm $\times$ 12.7 mm square cross section and it is 552 mm long. The two different tested copper surfaces were flush-mounted into this channel. The heating element consisted of thin tantalum and titanium nitride films. The plain surface nucleate boiling heat transfer performance was significantly affected by the fluid velocity up to 5 m s^{-1} and by subcooling up to 4 K. The microporous surface was significantly affected by fluid subcooling at low heat fluxes for the lowest velocity tested (0.5 m s^{-1}), whereas this behavior disappears with increased velocity and/or heat flux. For heat fluxes higher than 50 W cm^{-2}, the slope of the nucleate boiling curve for the microporous surface was found to be lower than that of the plain surface. In addition, the enhancement of critical heat flux provided by the microporous coating over the plain surface increases with increased fluid subcooling; however, compared to the plain surface, the enhancement effectiveness of the coating decreases linearly with increased velocity.

4.2.3 Microstructured surfaces

Microstructured surfaces can promote bubble nucleation, reduce onset of nucleate boiling, augment two-phase mixing, enhance critical heat flux, thus they can be an efficient way to enhance the flow boiling phenomenon.

Kuo and Peles [90] suggested a microchannel device as shown in figure 4.10: it consists of five parallel 10 mm long, 200 μm wide, 253 μm deep microchannels, spaced 200 μm apart, and each sidewall encompasses an array of 100 reentrant cavities spaced 100 μm apart. A 20 μm wide and 400 μm long orifice is installed at the entrance of each channel to suppress flow instabilities. Three thermistors 10 μm wide and 300 μm long are located 3400 μm, 6700 μm, and 10000 μm downstream the channel inlet. On the top of the thermistor layer, a 1 μm silicon oxide layer is deposited for electrical insulation. A heater is then formed on the top of the oxide layer to deliver the heating power and it also served as thermistor to measure the average temperature of the entire microchannel area. This device was micromachined on a silicon wafer. They used water as working fluid, with mass velocities ranging

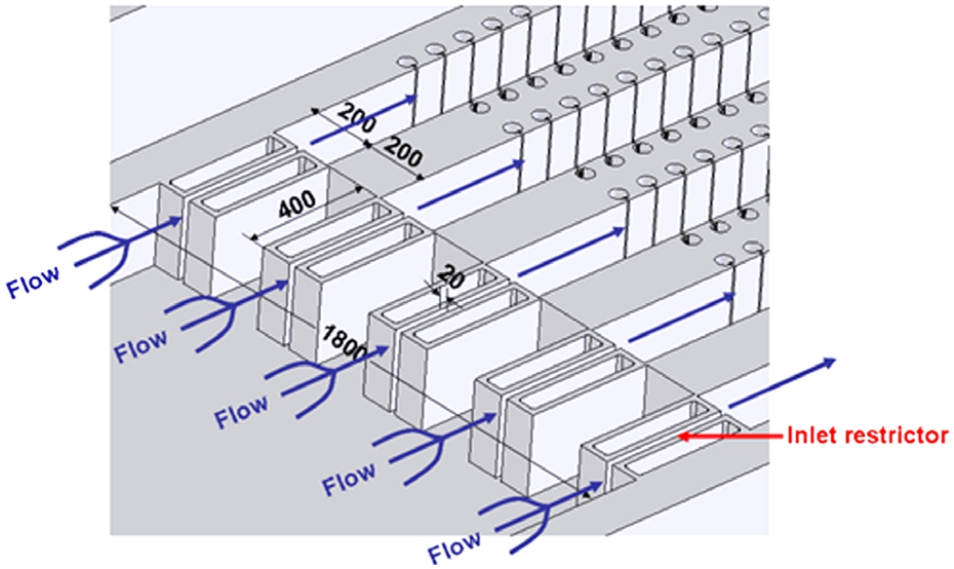

Figure 4.10: Particular of the microchannel device [90].

between 83 and 303 kg m^{-2} s^{-1}, and heat fluxes up to 643 W cm^{-2}. In addition, they performed experiments on a plain microchannel, in order to verify the improved performance of the microstructured one.

The microchannel with reentrant cavities showed an intensified nucleation activity with a better uniformity of nucleation site distribution. Flow patterns in microchannel with reentrant cavities were similar to those of a plain microchannel. Significant reductions in the wall superheat required to initiate boiling were

measured with the enhanced surface microchannel compared to the plain-wall microchannel. The bubble nucleation process in the structured surface microchannel was much more consistent and reproducible than in the plain channel. Combined with the increased nucleation activity, this enhanced consistency and reproducibility suppressed flow oscillations and assisted in the enhancement of the critical heat flux in the reentrant cavity microchannel.

One of the few works about flow boiling in metal foams in that of Zhao et al. [91]. They experimentally investigated the R134a flow boiling inside metal foam filled tubes. The experimental apparatus consists of a gear pump, mass flow meters (one for low flows and another one for high flow), a preheater, a test section, and three chillers: one for subcooling the refrigerant before the flow meters and the other two for condensing the refrigerant, an electrically heated refrigerant reservoir, and an electric power system in the test section. The preheater was used to control the vapour quality at the inlet of the test section. The required system pressure can be adjusted by controlling the heating system in the refrigerant reservoir. The tested copper foam filled tubes were 150 mm long with an inner diameter of 26 mm. T-type thermocouples were attached to the outer surface of tube, as shown in figure 4.11 at three locations (50 mm, 75 mm, and 100 mm) along the flow direction to monitor the temperature variation along the tube. The test tubes are heated by a direct current surface heater, which provides controlled and uniform heat fluxes on the surface of the tube.

The pressure drops were found to increase with vapour quality and mass flow

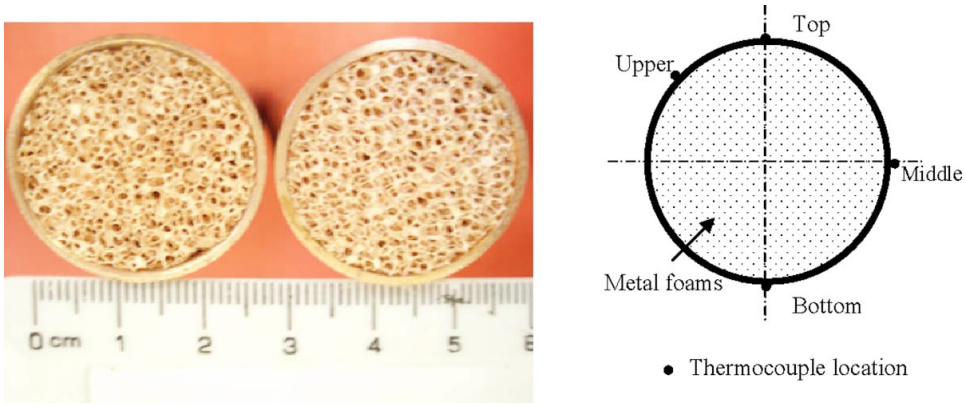

Figure 4.11: Foam filled tube [91].

rates. Pore density has a strong effect on the hydraulic behavior: pressure drop was double by reducing the cell size from 20 PPI to 40 PPI. Flow patterns were judged by the wall temperature fluctuations. The flow patterns that occurred inside the metal-foam tubes should be the stratified or slug wavy flow for low mass flow rates and the annular flow for high mass flow rates as the vapor quality rises. The heat transfer coefficient behavior was found to be highly dependent on vapour quality and mass flux: for lower mass flow rates, the heat transfer coefficient becomes smaller with the increase in the vapor quality, while the reverse situation holds for higher mass flow rates. Compared to a plain tube, a metal foam filled tube has approximately three times heat transfer coefficient. However, heat transfer coefficient could be higher with a better contact between foam and tube.

4.3 Development of the test section

The test section is the part of the facility where the phenomenon of the flow boiling though metal foams is studied. It houses metal foams, which are 200 mm long, 10 mm wide, and 5 mm high, and are brazed over a plate which is 200 mm long, 10 mm wide, and 10 mm high. An example of a metal foam with such characteristics is shown in figure 4.12. Thus, housing such metal foams is one of the constraints for the new test section.

Figure 4.12: Example of a metal foam.

An inner diameter of 10 mm has been chosen for the tube connected to the test section. Two plenums, one at the inlet and another at the outlet, are needed. According to the other works from the open literature, a parallelepiped plenum has to be developed, in order to find the combination of length, width, and height that guarantees the most uniform velocity distribution at the inlet of the rectangular channel. The geometrical variables of the plenum are reported in figure 4.13. A CFD analysis was carried out in order to find the most suitable dimensions of plenums. Plenum geometrical parameters considered for numerical simulations are reported in table 4.1.

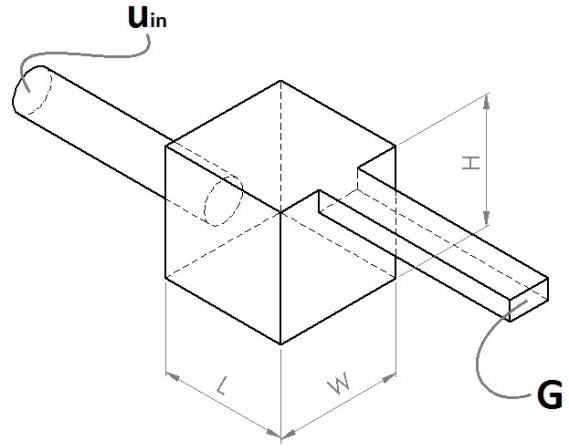

Figure 4.13: Geometrical dimensions of plenum.

Table 4.1: Geometrical parameters of plenums for the numerical simulations.

H [mm]	W [mm]	L [mm]
30	60	40
30	60	30
30	60	20
30	50	40
30	50	30
30	50	20
30	40	40

to next page —

— from previous page

H [mm]	W [mm]	L [mm]
30	40	30
30	40	20
30	30	40
30	30	30
30	30	20
40	60	40
40	60	30
40	60	20
40	50	40
40	50	30
40	50	20
40	40	40
40	40	30
40	40	20
40	30	40
40	30	30
40	30	20

R134a at a pressure of 10 bar and at a temperature of 25 °C is considered as working fluid for numerical simulations. In these operative conditions, thermophysical properties are the following:

- density: 1209 kg m^{-3};
- dynamic viscosity: 196×10^{-6} Pa s.

For the numerical study, the inner round tube has a length of 50 mm and the rectangular channel of 200 mm. The boundary conditions are here summarized:

- velocity-inlet boundary condition at the inlet of the fluid domain, i.e. at the inlet of the round tube;

- pressure-outlet boundary condition with zero gauge pressure at the outlet of the fluid domain, i.e. at the outlet of the rectangular channel.

A maximum mass velocity of 800 kg m^{-2} s^{-1} in the rectangular channel was considered for the numerical simulations, to which an inlet velocity of 0.42 m s^{-1} corresponds. Reynolds number in these operative conditions is 27186. Therefore, the $k - \varepsilon$ model was used to solve the fluid flow for each configuration shown in figure 4.13 using the commercial software COMSOL Multiphysics 3.5a [50].

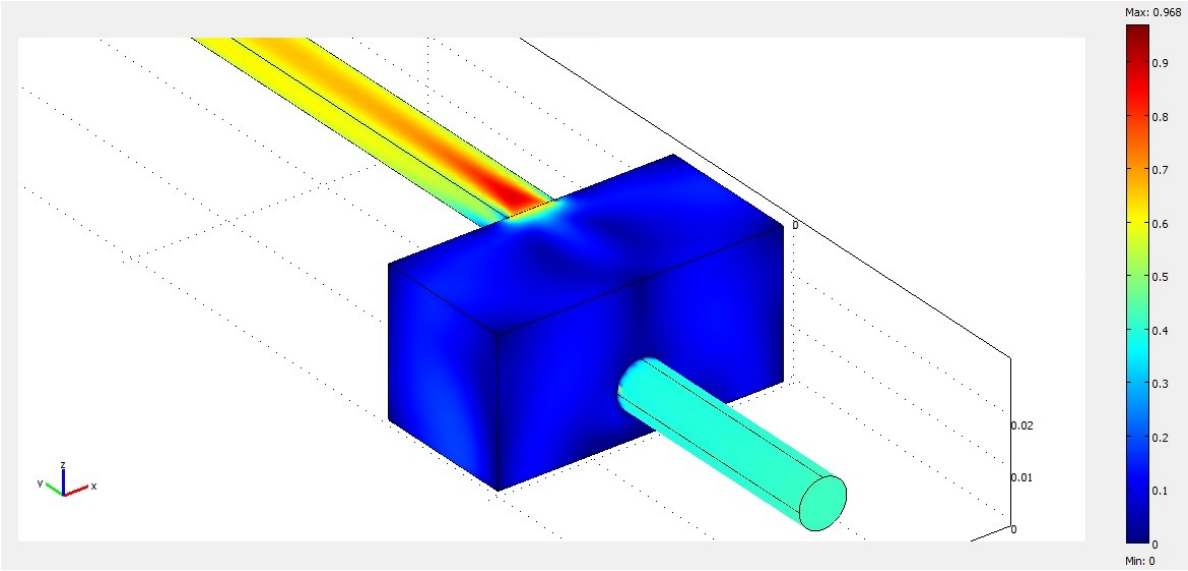

Figure 4.14: Example of the flow field inside a plenum with the following dimensions: length $L = 30$ mm, width $W = 60$ mm, and height $H = 30$ mm.

Figure 4.14 shows an example of the velocity field inside a plenum with the following geometrical characteristics: length $L = 30$ mm, width $W = 60$ mm, and height $H = 30$ mm. The fluid at constant inlet velocity (0.42 m s^{-1}) enters into the plenum where it spreads in all the directions, lowering its velocity. The fluid is accelerated in the top part at the inlet of the rectangular channel, as shown in the figure. Fluid needs a certain length to uniform its velocity in the rectangular channel, and the main purpose of these numerical simulations is to find the geometrical configuration of the plenum that minimize this length.

Velocity profiles along the center line of the rectangular are considered in order to find the plenum configuration that uniforms the fluid velocity in the shortest

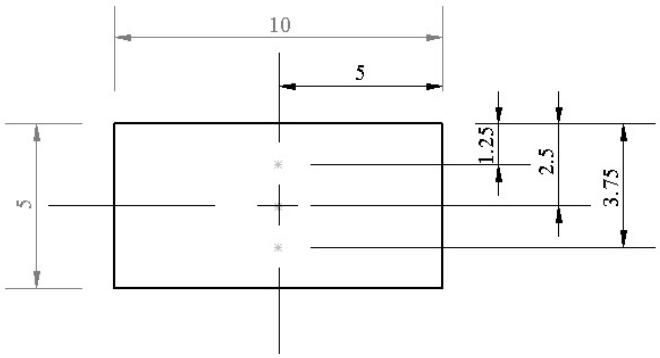

Figure 4.15: Example of a simulated fluid domain.

length. Velocities are evaluated at three different y-locations, as shown in figure 4.15.

Figures 4.16-4.18 show the effect of the plenum height on the velocity profile at constant width of 30 mm and constant height of 30 mm. The peak of velocity is few millimeters far from the inlet of the rectangular, and the velocity peak is higher near the bottom wall of the channel. Plenum with a height of 30 mm needs a shorter

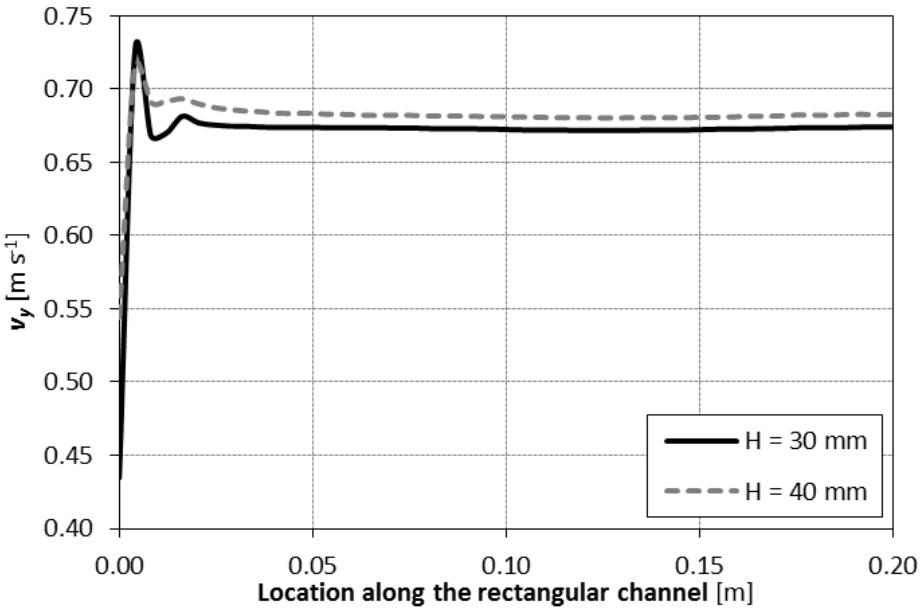

Figure 4.16: Effect of the plenum height on the velocity profile for plenums with a width of 30 mm and a length of 30 mm at a location 1.25 mm far from the top of the channel.

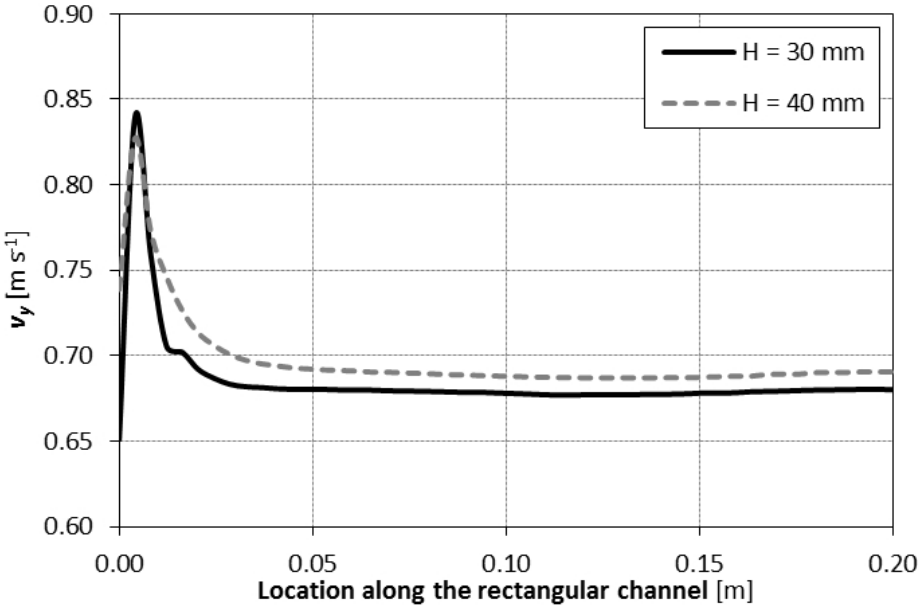

Figure 4.17: Effect of the plenum height on the velocity profile for plenums with a width of 30 mm and a length of 30 mm at a location 2.50 mm far from the top of the channel.

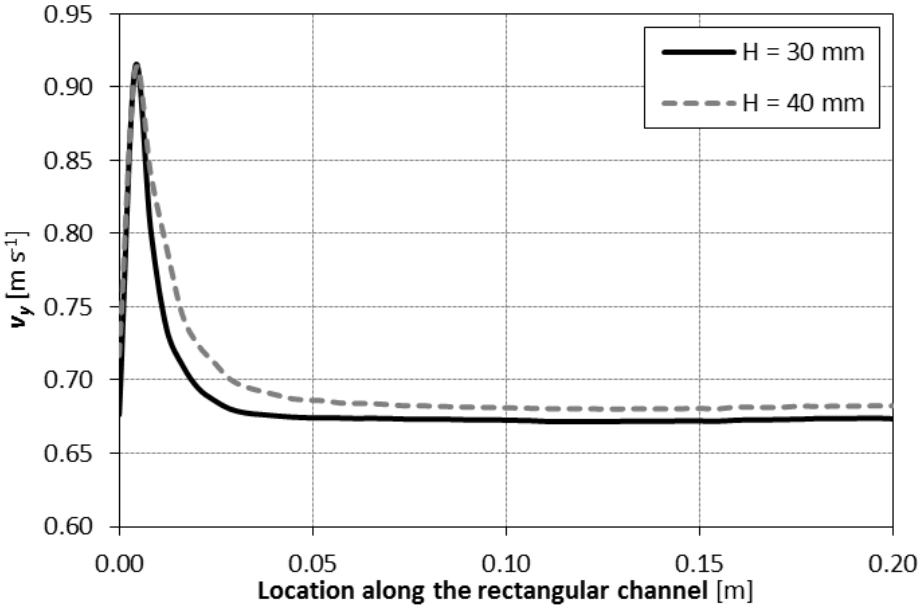

Figure 4.18: Effect of the plenum height on the velocity profile for plenums with a width of 30 mm and a length of 30 mm at a location 3.75 mm far from the top of the channel.

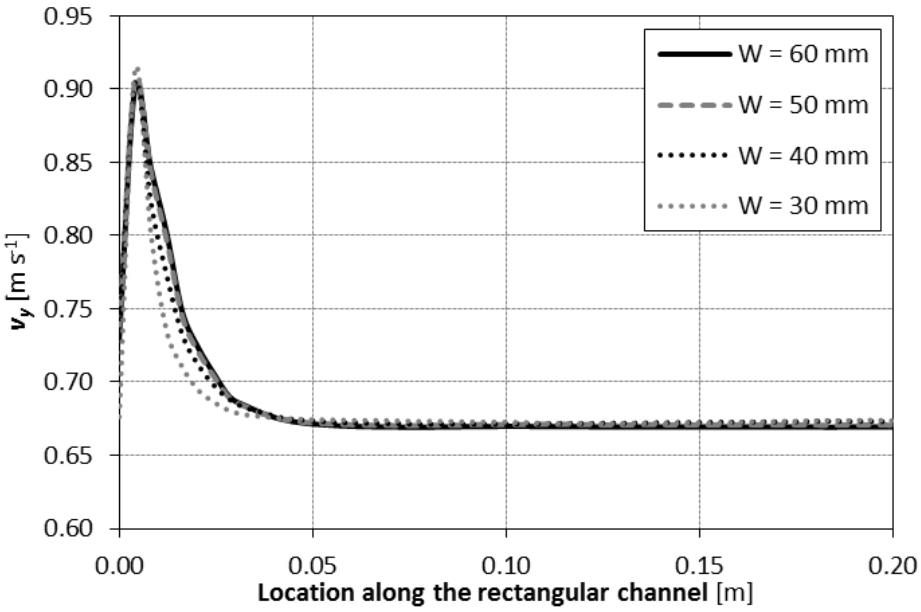

Figure 4.19: Effect of the plenum width on the velocity profile for plenums with a height of 30 mm and a length of 30 mm at a location 3.75 mm far from the top of the channel.

length to have a uniform velocity profile, as it appears from figures 4.17 and 4.18. Similar conclusions can be drawn for the other combinations of width and length. Therefore, plenums with a height of 30 mm perform better than those with a height of 40 mm in these conditions.

Figure 4.19 shows the effect of the plenum width on the velocity profile at constant height of 30 mm and constant length of 30 mm. Plenum with a width of 30 mm needs a slightly shorter length to have a uniform velocity profile than the others cases. Similar conclusions can be drawn for the other combinations of width and length.

In the end, figure 4.20 shows the effect of the plenum length on the velocity profile at constant height of 30 mm and constant width of 30 mm. No appreciable differences can be observed between different lengths.

From this numerical analysis, the geometrical characteristics of the plenum that uniform the fluid velocity in the shortest region are the following:

- length $L = 30$ mm;
- width $W = 30$ mm; and

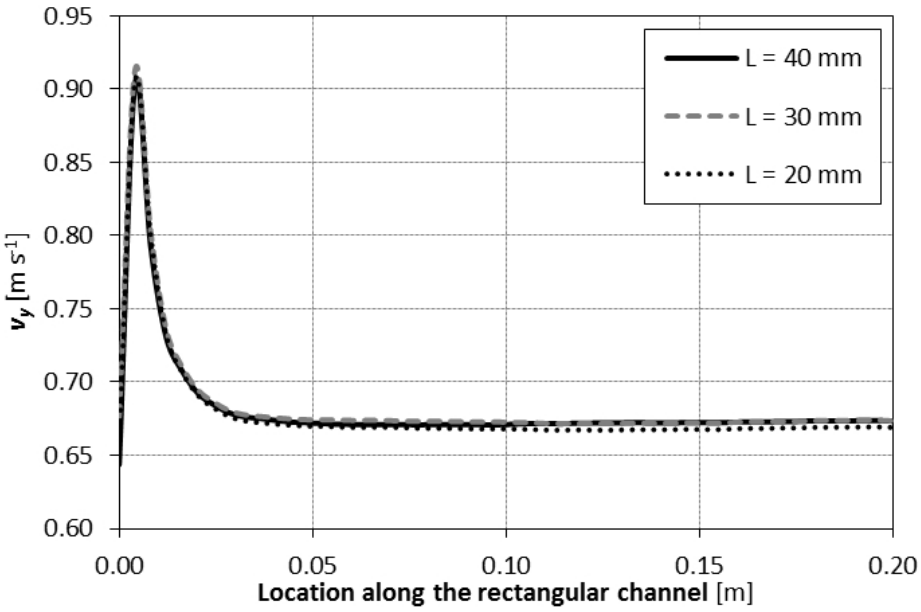

Figure 4.20: Effect of the plenum length on the velocity profile for plenums with a height of 30 mm and a width of 30 mm at a location 3.75 mm far from the top of the channel.

- height $H = 30$ mm.

Furthermore, a total length of 300 mm is chosen for the rectangular channel, in order to house the 200 mm long foams, giving 50 mm from the inlet of the rectangular channel to the foam to achieve a uniform flow distribution, and 50 mm from the end of the foam to the exit of the rectangular channel.

The plenums and rectangular channel are machined from a parallelepiped with the following dimensions: length of 440 mm, width of 130 mm, and height of 50 mm. The material of this parallelepiped should have interesting thermal properties, such as a low thermal conductivity and a high working temperature. Misoglass1 was chosen as material: it is a glass mat and special epoxy resin laminate, suitable for continuous operating temperature at 220 °C. The main characteristics are reported in table 4.2.

A 3D drawing of the test section is shown in figure 4.21, where inlet and outlet plenums are highlighted. Two holes were drilled in correspondence with inlet and outlet plenum, in order to locate thermocouples to measure inlet and outlet refrigerant temperatures. Other two symmetrical holes (not visible in figure) were

Table 4.2: Misoglass properties.

Property	Value
Compressive strength ⊥ at 20 °C	45000 N cm^{-2}
Modulus of elasticity	1800000 N cm^{-2}
Dielectric strength at 90° C	13 kV mm
Flexural strength at 20° C	36000 N cm^{-2}
Tensile stress at 20° C	28000 N cm^{-2}
Continuous operating temperature	220 °C
Maximum operating temperature	280 °C
Thermal conductivity	0.35 W m^{-1} K^{-1}
Coefficient of expansion	15×10^{-6} K^{-1}

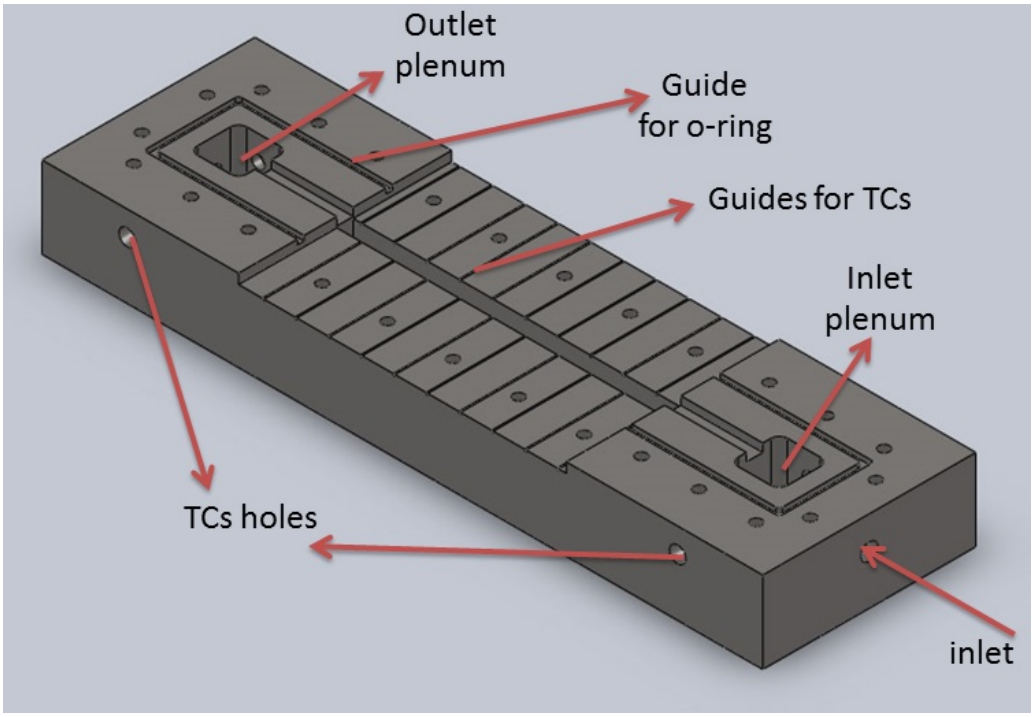

Figure 4.21: 3D view of the test section.

drilled on the other side, in order to locate the pressure ports to measure inlet and outlet refrigerant pressure. In figure twenty grooves are also visible in the central part, to house thermocouples that will be inserted in the sample to monitor the wall temperature distribution. These parts are covered by two masks, shown in figure 4.22, which are glued to the base block with an epoxy resin. A guide (see figure 4.21

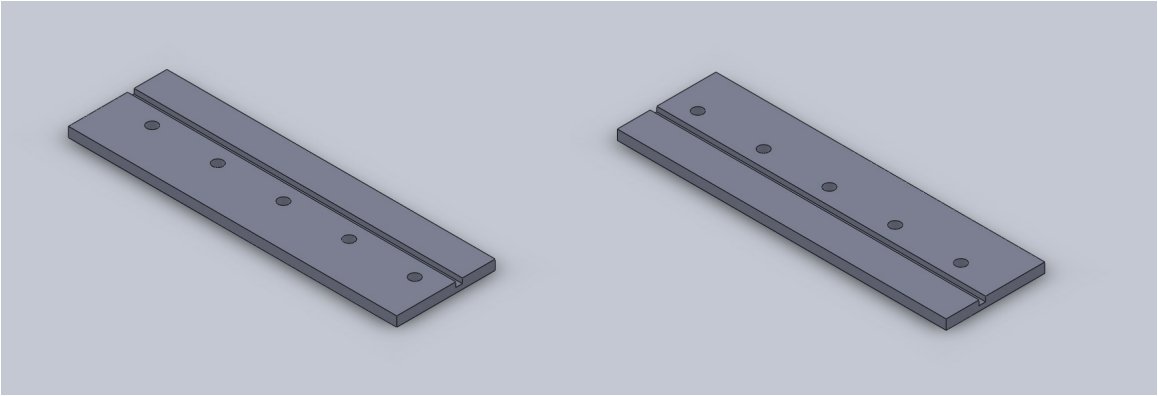

Figure 4.22: Drawing of the two masks.

is milled on the top of the section body, to accomplish the sealing using an EPDM O-ring.

A heater is used to supply the heat flow rate needed to vaporize the refrigerant. A guide is milled in a copper plate, which is 7 mm high, 10 mm wide, and 200 mm long, and a Nichel-Chrome wire resistance is inserted inside this guide. The electric heater is inserted in the core region of the rectangular channel of the test section. Two holes were drilled on the bottom side of the test section in order to accomplish the electric connection for the wire resistance.

A tempered glass is positioned over the section block, it is 19 mm thick, 398 mm long, and 69 mm wide, with a radius of curvature of 10 mm at the angles. Two 15 mm thick stainless steel plates are located on the top and on the bottom of the assembled test section and they are bolted together. The top plate has a central window, which permits to directly visualize the flow boiling phenomenon occurring inside the foam. A view of the test section with all the components is given in figure 4.23.

4.4 Development of the new setup

4.4.1 General description

The new experimental setup consists of four main loops: the refrigerant loop, the hot water loop for the evaporator, the cold water loop for the pre-condenser, and

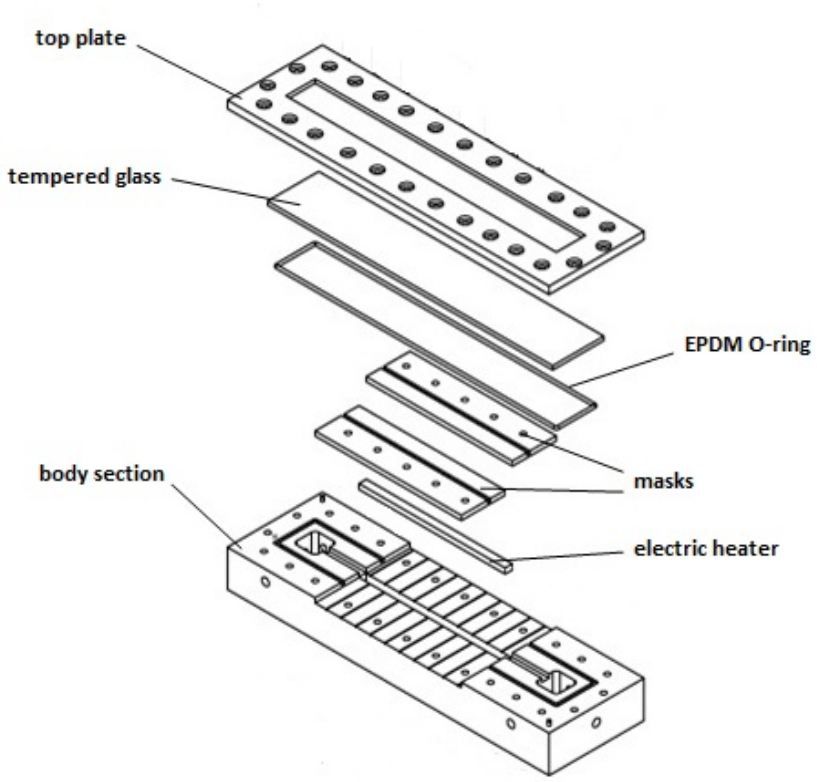

Figure 4.23: Components of the test section.

the sink water loop for the post-condenser.

A schematic and a picture of the refrigerant loop are shown in figures 4.24 and 4.25, respectively. In the refrigerant loop the refrigerant is pumped through the circuit by means of a magnetically coupled gear pump, it is vaporized and superheated in a brazed plate heat exchanger fed with hot water. Superheated vapour then partially condenses in a pre-condenser fed with cold water to achieve the set quality at the inlet of the test section. The refrigerant enters the test section at a known mass velocity and vapour quality and then it is vaporized by means of the calibrated Nichel-Chrome wire resistance. The fluid leaves the test section and enters in a post-condensers, which is a brazed plate heat exchanger, where it is fully condensed and subcooled. The subcooled liquid passes through a drier filter and then is sent back to the evaporator by the pump. A damper connected to the compressed air line operates as pressure regulator to control the saturation condition in the refrigerant loop.

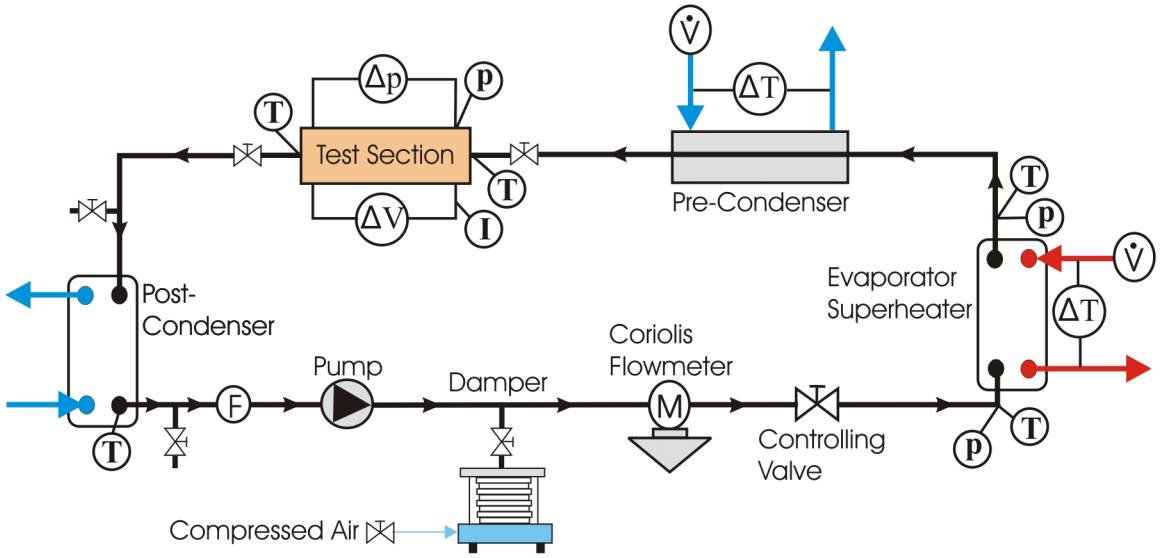

Figure 4.24: Schematic of the refrigerant loop.

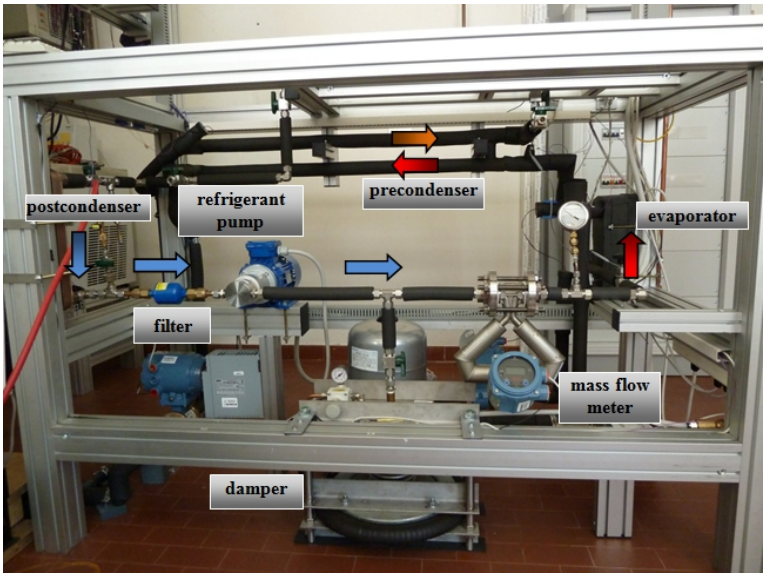

Figure 4.25: Picture of the refrigerant loop.

Figure 4.26 shows a picture of the hot water loop. This loop is designed to supply the hot water needed to the evaporator in the refrigerant loop in order to vaporize and superheat the refrigerant. The water is pumped by a multi-stage pump. Before reaching the plate heat exchanger, water is sent to an electric boiler, which provides the necessary heat flow rate. Two mixers are installed in the hot loop, down- and

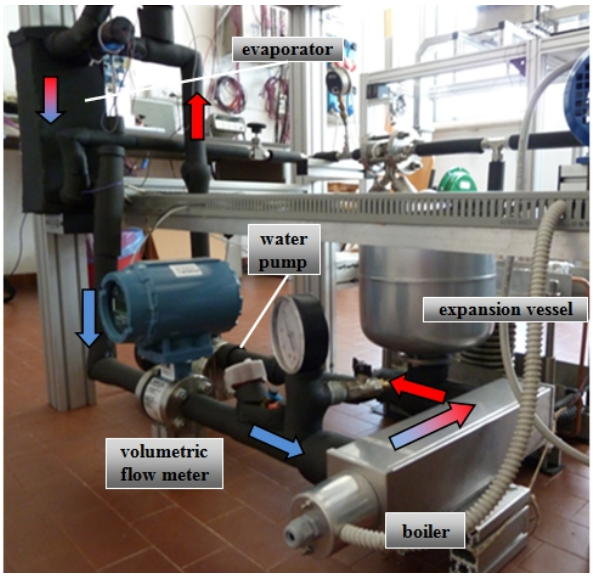

Figure 4.26: Picture of the hot water loop.

upstream of the evaporator, and each one can locate a temperature probe to house a thermocouple to measure the water temperature. In addition, a magnetic effect flow meter is installed between the plate heat exchanger and the boiler. The water flow rate can be adjusted with a controlling valve. An expansion vessel can contain water density variations.

A picture of the cold water loop is shown in figure 4.27. The refrigerant coming from the evaporator is partially condensed in a pre-condenser, which is a tube-in-tube heat exchanger, where the refrigerant flows in the inner tube, whereas cold water in the outer tube. The inlet water temperature at the pre-condenser can be controlled with a stabilized chiller. A controlling valve is installed in the cold loop, therefore it is possible to control both the flow rate and the temperature of the water, to achieve the desired vapour quality at the inlet of the pre-condenser. An expansion vessel is also present to contain any water density variations. Similarly to the hot water loop, mixers with temperature probes are installed down- and upstream of the pre-condenser, to house thermocouples to measure the water temperature at the inlet and outlet of the heat exchanger.

The post-condenser is shown in figure 4.28. It is another brazed plate heat exchanger, where the refrigerant flows in counter-current with water. No controlling

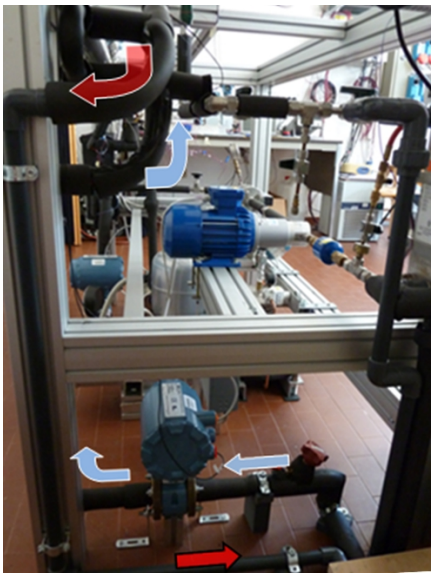

Figure 4.27: Picture of the cold water loop.

Figure 4.28: Picture of the sink water loop.

valve is needed, since its main purpose is just to condense and subcool the refrigerant before it reaches the pump. A thermocouple is located downstream of the heat exchanger, so that it is possible to verify the thermodynamic state of the refrigerant. Sink water temperature is usually between 15 °C and 18 °C.

4.4.2 The refrigerant loop

The refrigerant pump

A pump is needed in the refrigerant loop to overcome the pressure drop in the curves in the loop, in the heat exchangers (evaporator, pre-condenser, and post-condenser), in the test section, in the filter, and in the mass flow meter. An oil-free pump was chosen, in order to avoid any traces of oil in the refrigerant loop, because the main purpose of the setup is to study the flow of pure refrigerants. Thus a magnetically coupled gear pump was selected. In this kind of pumps, the motor is coupled to the pump by magnetic couplings rather than by a direct mechanical shaft. The pump works via a drive magnet, driving the pump rotor, which is magnetically coupled to the primary shaft driven by the motor. They have no direct connection between the motor shaft and the impeller, so no lubricant is needed. A MICROPUMP GC M25 series magnetically coupled gear pump was selected, with a CANTONI 4 poles 3-phase AC driver. A picture of the pump is shown in figure 4.29.

Figure 4.29: Picture of the magnetically coupled gear pump.

The pump is mounted over an aluminum chassis, in the lowest part of the facility, at the same height of the exit of the post-condenser. Thus, the pump will elaborate liquid, avoiding also any cavitation problems. The main characteristics of the pump are reported in table 4.3. The pump specifications in terms of curve characteristic is given in figure 4.30.

Table 4.3: Properties of the magnetically coupled pump.

Property	Value
Displacement	1.82 mL/rev
Max Flow	2640 mL/min
Max Differential Pressure	8.2 bar
Viscosity Range	0.2 to 1500 cP
Max Speed	4000 rpm
Rotation (facing motor shaft)	Clockwise
Weight	1.7 kg
Ports	3/8-18 (F) NPT Side Ports
Driven Magnet	Ferrite

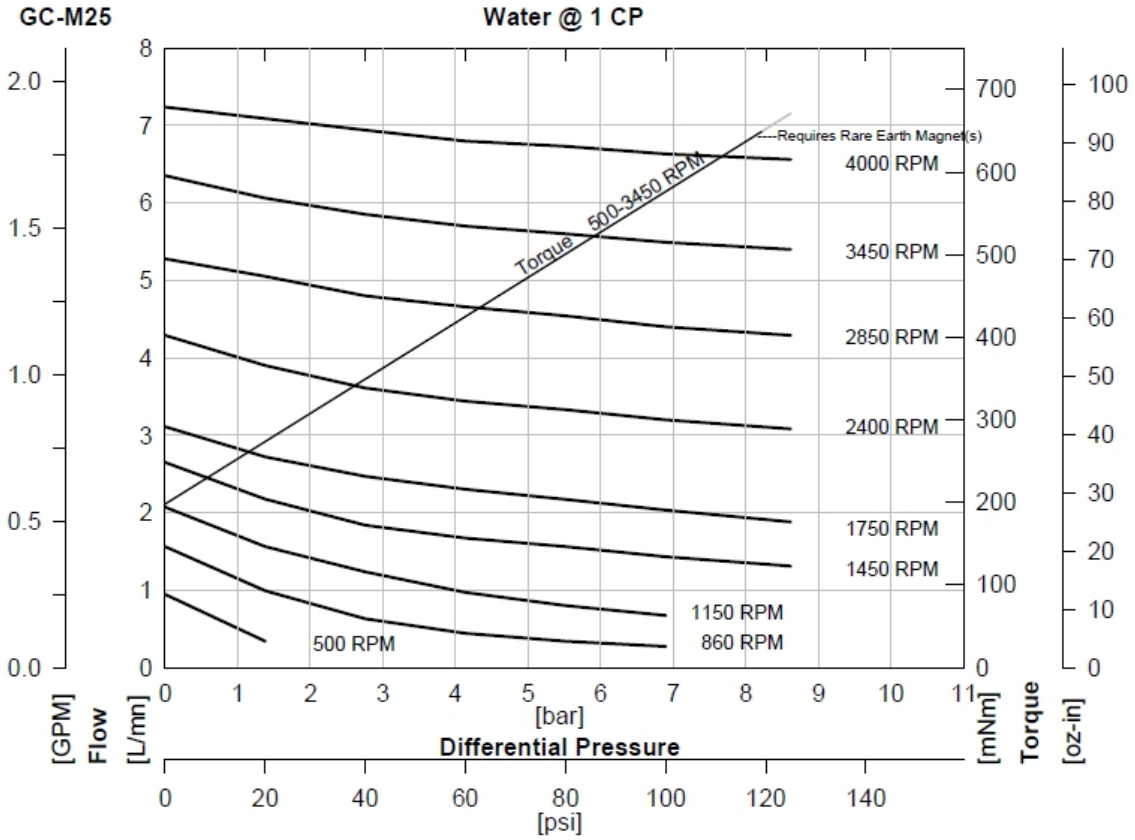

Figure 4.30: Characteristic curve of the magnetically coupled gear pump.

An inverter is coupled with the driver, in order to control its speed, and so the refrigerant mass flow rate. Mass flow rate can also be adjusted with a controlling valve, installed between the mass flowmeter and the evaporator in the refrigerant loop. The inverter is installed near the pump, in such a way that its electromagnetic field does not create interference with other signals.

The filter

A dehydrating filter with molecular sieves is installed between the exit of the post-condenser and the pump. It is a "Castel" filter, 4303 series. Its main purpose is to remove any traces of impurity that may be produced throughout the circuit, to protect the integrity of the pump, and it also adsorbs humidity that could be present inside the facility. The main characteristics are reported in table 4.4. A refrigerant charge port is installed upstream of the filter, along with two ON-OFF valves.

Table 4.4: Properties of the filter.

Property	Value
Filtering surface	47 cm^2
Ports	3/8"
Absorbing capacity at 25 °C	4 g of H_2O
Dehydration charge at 25 °C	4 kg of fluid
Maximum working pressure	45 bar
Range working temperature	-40 °C ÷ 80 °C

Figure 4.31: Picture of the filter and of the refrigerant charge port.

The damper

The refrigerant loop is connected to a pressure damper, which is used to control the pressure of the system, and thus the saturation conditions in the test section. A picture of the damper is shown in figure 4.32. It is connected to the compressed air

Figure 4.32: Picture of the damper.

line. An air pressure regulator is located at the inlet of the damper, and it permits to control the pressure inside an air chamber, shown on the bottom of the figure. The pressure of this chamber exerts a force on a circular plate located over the top of the chamber. This force is balanced by the pressure of the refrigerant, which exerts its force on the top of the circular plate. Since the section where the compressed air applies its force is larger than that of the refrigerant, the air pressure is lower than that of the refrigerant. Therefore, it is possible to control the refrigerant pressure by adjusting the air pressure inside the chamber.

The Coriolis effect mass flow meter

A Coriolis effect mass flow meter is installed between the pump and the evaporator, in the liquid line. It permits to directly measure the mass flow rate flowing in the main loop. A picture of the Coriolis effect mass flow meter is shown in figure 4.33

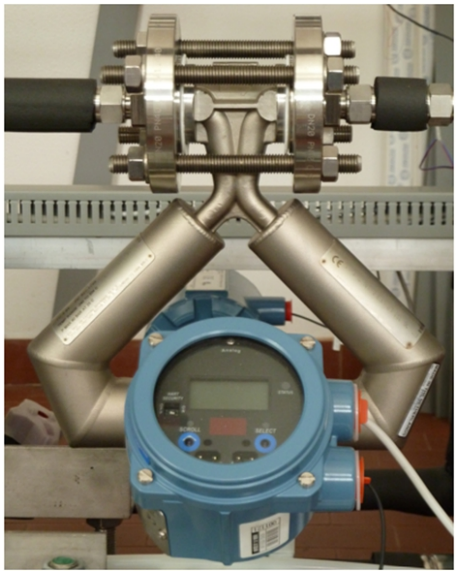

Figure 4.33: Picture of the Coriolis effect mass flow meter.

A Micro Motion Coriolis effect mass flow meter (2400S series) was installed, supplied by EMERSON. It is installed between two flanges, in the liquide line. As a practical application of the Coriolis effect, the Coriolis mass flow meter operating principle involves an induced vibration of the flow tube through which the fluid passes. The vibration provides the rotating reference frame which gives rise to the Coriolis effect. While specific methods vary according to the design of the flow meter, sensors monitor and analyze changes in frequency, phase shift, and amplitude of the vibrating flow tubes. The changes observed represent the mass flow rate and density of the fluid. The measuring tubes are forced to oscillate producing a sine wave. At zero flow, the two tubes vibrate in phase with each other. When flow is introduced, the Coriolis forces cause the tubes to twist resulting in a phase shift, as shown in figure 4.34. The time difference between the waves is measured and is directly proportional to the mass flow rate.The temperature range of operating conditions is shown in figure 4.35. Since the flowmeter operates at 20-30 °C and the working temperature is approximately 20-40 °C, no special recommendations are needed. In addition, the flowmeter has a maximum working pressure of 40 bar, with a maximum mass flow rate of 400 kg h^{-1}. Table 4.5 reports the measurement characteristics under various flow conditions. At nominal flow rate, the instruments

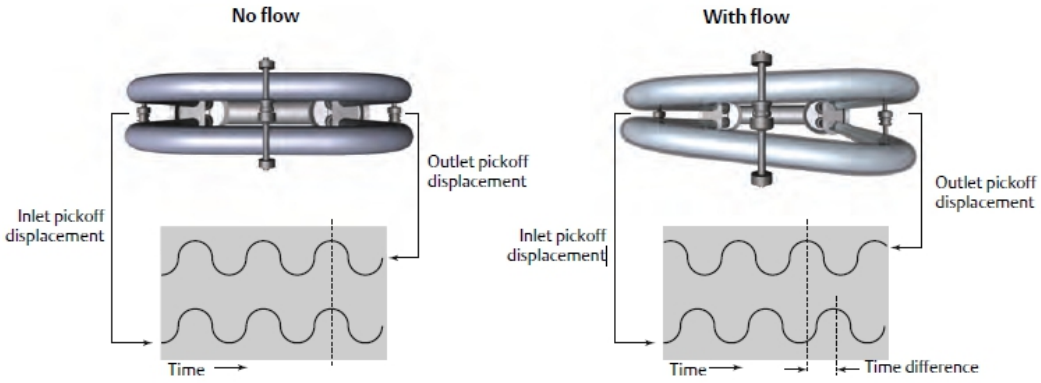

Figure 4.34: Operation principle of the Coriolis effect mass flow meter [92].

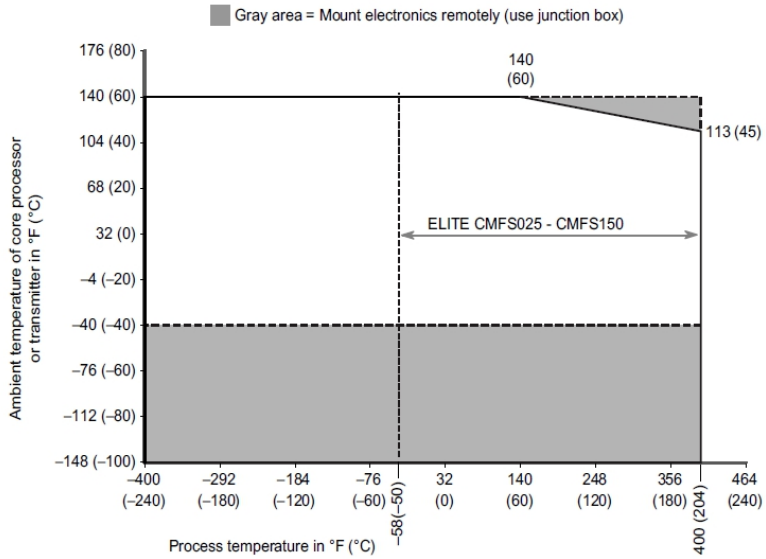

Figure 4.35: Temperature range of operating conditions for the Coriolis effect mass flow meter.

has an accuracy of ±0.1%. The calibration certificate of the mass flow meter is reported in figure 4.36.

Table 4.5: Measurement characteristics under various flow conditions for the Coriolis effect mass flow meter.

Turndown from nominal flow rate	500:1	100:1	20:1	10:1	2:1
Accuracy [%]	1.25	0.25	0.1	0.1	0.1

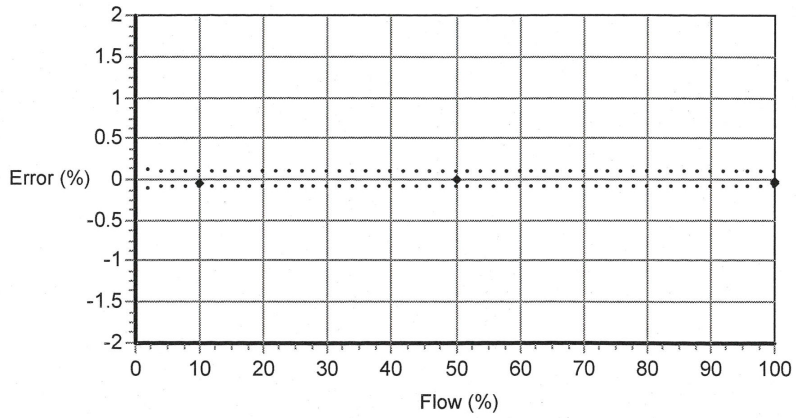

Flow (%)	Flow Rate (kg/min)	Meter Total (kg)	Reference Total (kg)	Error (%)	Specification (±%)
100.0	18.1437	18.22988	18.23791	-0.044	0.100
10.0	1.81437	1.801821	1.8025	-0.038	0.100
50.0	9.07185	9.269012	9.269166	-0.002	0.100
100.0	18.1437	18.23593	18.24158	-0.031	0.100

Figure 4.36: Mass flow meter calibration certificate.

The evaporator

A brazed plate heat exchanger is installed as evaporator. It is fed with hot water, supplied in the hot water loop, and it vaporizes and superheats the refrigerant coming from the Coriolis effect mass flow meter, before reaching the pre-condenser. It is supplied by WTT-GEA, it has four frontal 3/4" ports, and it is made in AISI 316 stainless steel, with 99.9% pure copper as filler material for brazing. The maximum working temperature is 195 °C, the maximum working pressure 30 bar, whereas it was tested at 39 bar. It is able to supply a variable heat flow rate up to approximately 5 kW. Two mixers are installed in the water side, and they also include a temperature probe to house a thermocouple. The heat exchanger is insulated with Armaflex. Technical specifications and pictures of the evaporated are shown in figures 4.37 and 4.38, respectively.

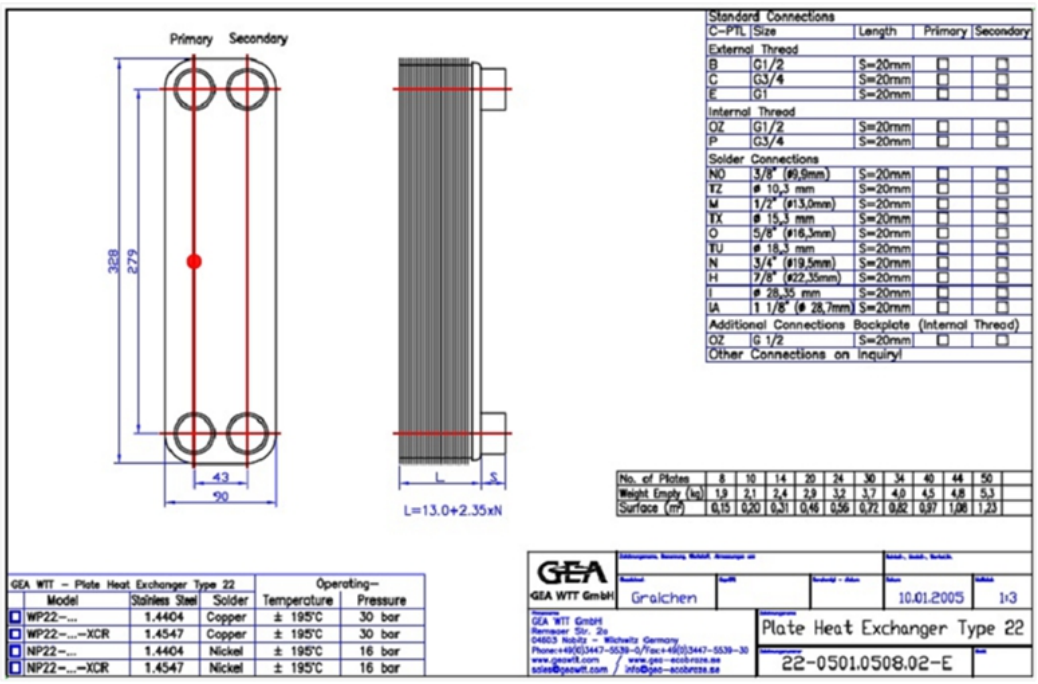

Figure 4.37: Technical specifications of the evaporator.

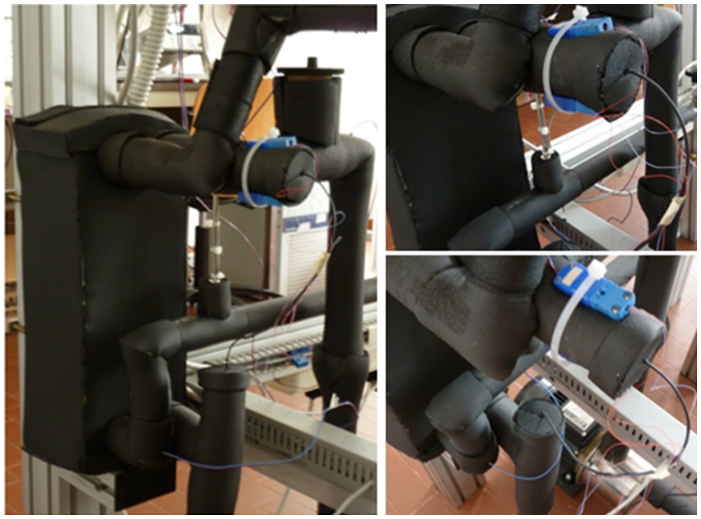

Figure 4.38: Pictures of the evaporator.

The pre-condenser

The pre-condenser is installed between the evaporator and the test section. The vapour coming from the evaporator is partially condensed in the pre-condenser, up

to the desired vapour quality, thus it is possible to control the vapour quality at the inlet of the test section. The connection between the exit of the pre-condenser and the inlet of the test section should be as short as possible.

The pre-condenser is a home-made tube-in-tube heat exchanger, with a U-shape, where the refrigerant flows in the inner tube, whereas the water in the outer tube, in countercurrent respect to the refrigerant. This configuration permits also to reduce the size of the heat exchanger. A schematic and a picture of the pre-condenser are shown in figures 4.39 and 4.40. This heat exchanger is made in brass (external tube) and in copper (internal tube), and is externally insulated with Armaflex. The internal tube has an inner and outer diameter of 10 mm and 12 mm, respectively, and it is 1200 mm long, whereas the external tube has an inner and outer diameter of 18 mm and 30 mm, and it is 1150 mm long. The curvature of the inner tube has a radius of 50 mm.

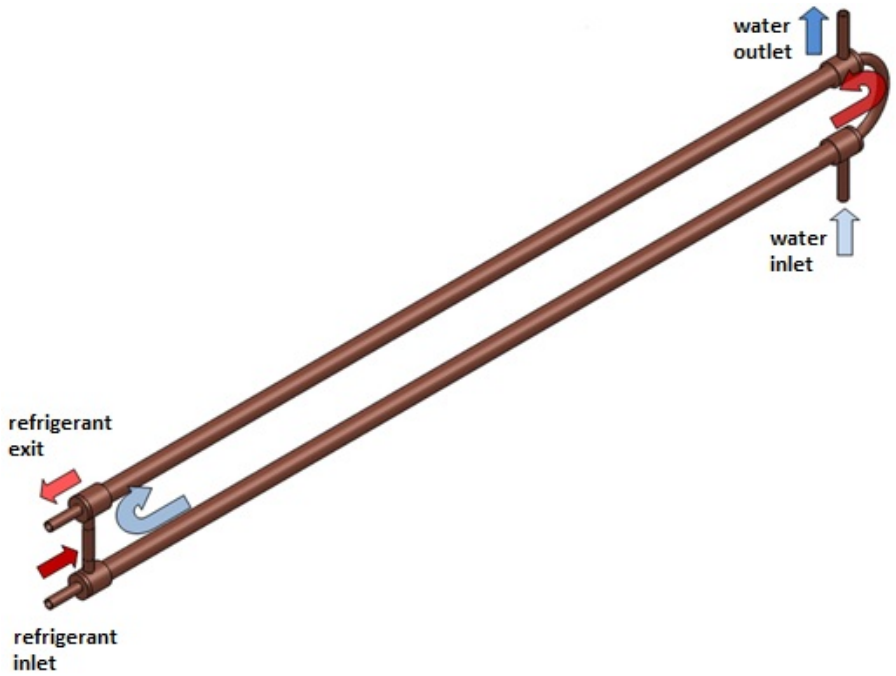

Figure 4.39: Schematic of the pre-condenser.

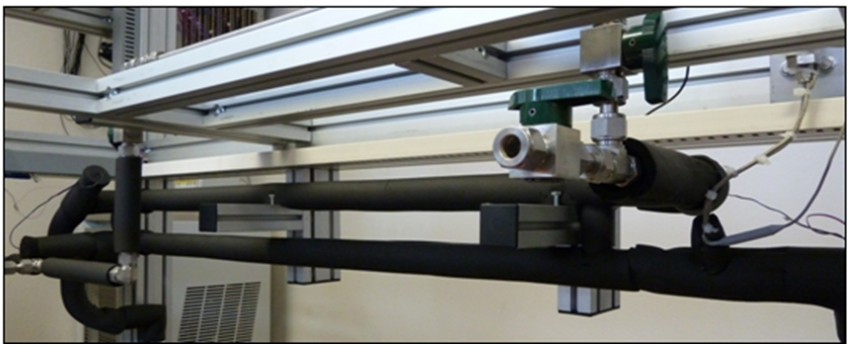

Figure 4.40: Picture of the pre-condenser.

The electric heater and the power supplier

An electric heater is used as heating element at the base of the sample. A guide was milled in a 7 mm high, 10 mm wide, and 200 mm long copper plate, to house a Nichel-Chrome wire resistance. The wire is sheathed in a thermal-shrink tubing, immersed in thermal grease inside the groove, which is covered with a 1 mm thick aluminum plate.

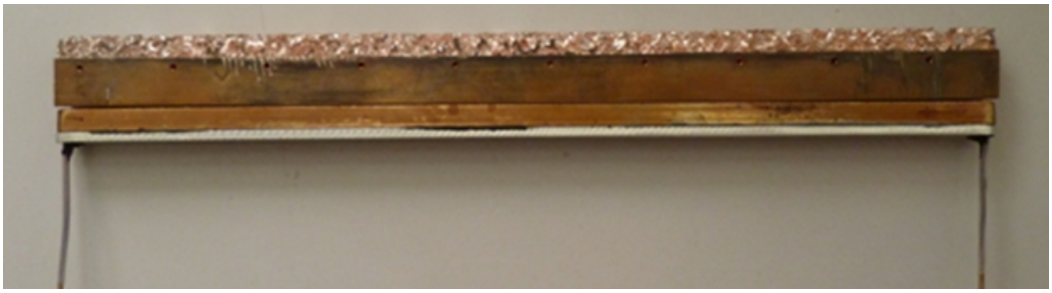

Figure 4.41: Picture of the electric heater.

The electric wire is connected to a power supplier, ALN series by CEA. It is able to supply an electric power up to 900 W. A calibrated reference resistance (shunt) is used for current measurement. The accuracy of the reference resistance is ±0.03%. Thus, with two accurate EDP measurements it is possible to know the effective power supplied to the test sample by applying the following equation:

$$P_{EL} = V_R \cdot I = V_R \cdot \frac{V_S}{R_S} \tag{4.13}$$

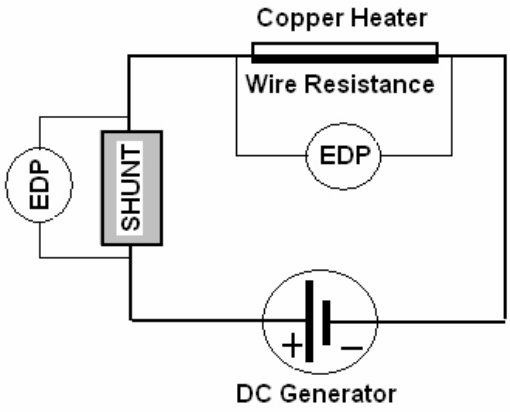

Figure 4.42: Schematic of the electrical difference potential measurements.

where the subscripts R and S refer to the wire resistance and to the shunt, respectively. Applying the error analysis it appears that the electric power uncertainty is always lower than $\pm 0.15\%$ of the reading.

The pressure transducers

Three absolute pressure transducers were installed in the refrigerant loop: one at the inlet of the evaporator, one at the outlet of the evaporator, and another one at the inlet of the test section. A differential pressure transducer is also installed across the test section, in order to measure the pressure drop across the sample under investigation. A picture of the pressure transducers is shown in figure 4.43. These instruments are supplied by Rosemount.

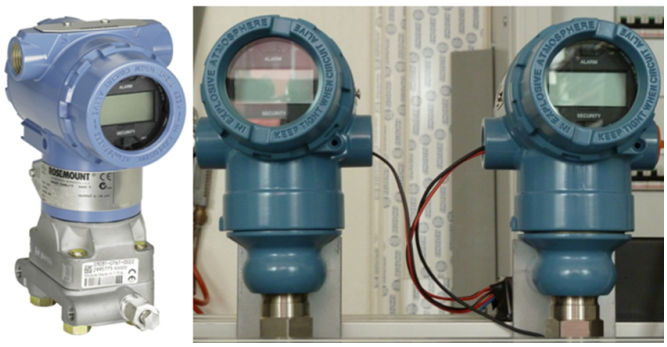

Figure 4.43: Picture of the mounted pressure transducers.

The absolute pressure transducers have a full scale of 30 bar, 4-20 mA with digital signal based on HART protocol as output, 1/2 - 14 NPT female as process connection, the isolating diaphragm is made in 316L stainless steel. These absolute pressure transducers have an accuracy of 0.065% of the full scale.

The differential pressure transducer has a full scale of 1 bar, 4-20 mA with digital signal based on HART protocol as output, 1/4 - 18 NPT female as process connection, the isolating diaphragm is made in 316L stainless steel. This differential pressure transducer has an accuracy of 0.025% of the full scale. Its certificate of calibration is reported in figure 4.44.

% of Range	Applied Pressure	Requested Pressure	Output (Analog)	% Span Error	Pass/Fail
100,00	1000,00 MBAR	1,0000 BAR	20,0004 (mA)	0,0025	PASS
80,00	800,00 MBAR	0,8000 BAR	16,8010 (mA)	0,0063	PASS
60,00	600,00 MBAR	0,6000 BAR	13,6018 (mA)	0,0112	PASS
40,00	400,00 MBAR	0,4000 BAR	10,4026 (mA)	0,0163	PASS
20,00	200,00 MBAR	0,2000 BAR	7,2036 (mA)	0,0225	PASS
0,00	0,00 MBAR	0,0000 BAR	3,9996 (mA)	-0,0025	PASS

Figure 4.44: Certificate of calibration of the differential pressure transducer.

4.4.3 The how water loop

The electric boiler and the power regulator

The water flowing in the hot water is heated up by an electric boiler, able to supply a heat flow rate up to approximately 5 kW. It is made in stainless steel, and it houses three electric resistances. Each of these resistances can be independently controlled. Electric power is modularly supplied to the boiler, thus it is possible to supply to the hot water a variable heat flow rate up to 5 kW: two magnetothermic switches (on-off control) have been installed and connected to two of the electric resistances, and a power regulator is connected to the third resistance. The power regulator (425 A model) is supplied by Eurotherm. For instance, to supply a heat flow rate of 0.8 kW, the two magnetothermic switches are turned off, and only the power regulator is turned on; whereas to supply 3.0 kW, one of the magnetothermic switches is turned on, the other one is turned off, and the power regulator is turned on.

The 425 A model is a thyristor unit for electrical power control. It is composed of two thyristors mounted in antiparallel for control of a load connected to an AC electrical supply.

The power regulator can automatically control the supplied electric power, its action is based on the temperature value measured by a thermocouple inserted at the water inlet of the evaporator. A temperature value is set on a digital display, and the regulator modulates the electric power supplied to the resistance in order to reach and maintain the desired temperature within ±0.1 K.

The limit control thermostat

A thermostat ("JUMO eTRON T" model) is installed, in order to maintain the water temperature inside the boiler within safety limits, i.e. below its boiling temperature. This thermostat acts as a switch, and it opens the circuit of the electric resistances in case of water overheating. It is connected to a thermocouple inserted into the electric boiler.

The expansion vessel

An expansion vessel is mounted downstream of the electric boiler. It is pre-charged at a pressure of about 2.5 bar, and it compensates for thermal expansion of the water, due to water heating in the boiler. It is supplied by "CIMM", and it has the following characteristics:

- volume: 8 L;
- diameter: 220 mm;
- height: 305 mm;
- working temperature range: -10 °C ÷ 100 °C;
- membrane material: butyl rubber.

The water pump

The water is moved by a pump through the hot water loop. It is a multi-stage pump, supplied by OSIP, MC 80 model. It has the following characteristics:

- speed: 2800 rpm;
- input power: 0.6 kW;
- maximum flow rate: 98 L/min;
- maximum head: 37 m H_2O;
- material: AISI 304 stainless steel.

The mixers

Two mixers were installed upstream and downstream of the evaporator in the hot water loop. They have a double function: they mix the water, in order to avoid any temperature non-uniformities, and they also house a thermocouple probe. A schematic of the mixers is shown in figure 4.45.

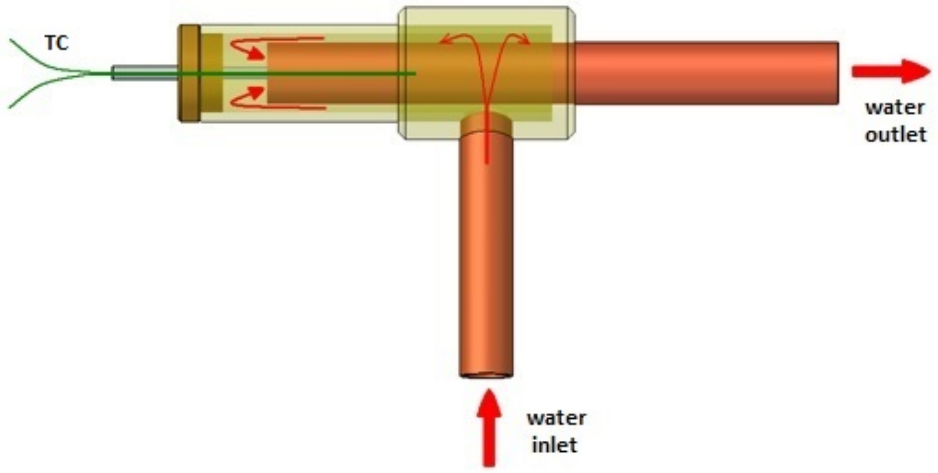

Figure 4.45: Schematic of a water mixer.

The water is highly mixed between the inlet and the outlet of the mixer, due to the tortuous flow pattern. The inlet and outlet tubes of the mixer have an inner diameter of 10 mm, and they are made in copper. The outer tube that creates the hollow space with the inner tube is made in brass. The temperature probe is shown in figure 4.45 on the left side of the mixer, and it consists of a stainless steel thin tube (3 mm diameter), inserted in the mixer.

The volumetric flowmeter

The principle of operation of magnetic flowmeters is based on the Faraday's law, which states that the voltage induced across any conductor moving through a magnetic field is proportional to the velocity of that conductor. The water (conductor), which is flowing into the tube, moves through the magnetic field created by the transmitter. Thus, the signal voltage measured by the instruments is proportional to the fluid velocity, i.e. to the fluid flow rate.

A Rosemount 8700 series magnetic flowmeter is installed in the hot water loop. According to the specifications, the sensor is installed more than five straight pipe diameters upstream and two pipe diameters downstream are respected. Figure 4.46 shows a picture of the flowmeter along with installation specifications.

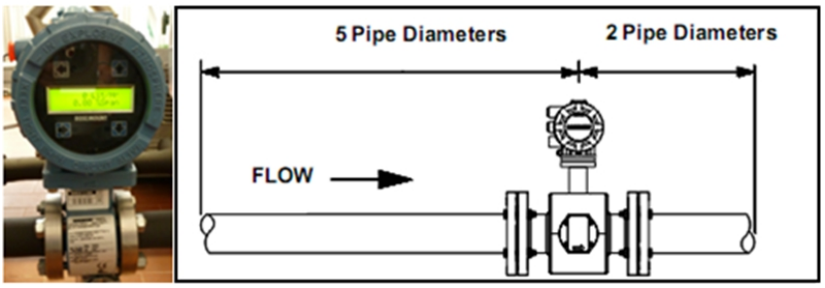

Figure 4.46: Picture of the magnetic flowmeter and installation specifications.

This instrument has a fulls scale of 800 L/h with an accuracy of 0.25% of the reading, with a 4-20 mA digital electronics (HART protocol) as output. It is installed between a flow control valve and the boiler.

4.4.4 The cold water loop

The chiller

A stabilized water chiller is installed in the cold water loop, to control the water side heat transfer at the pre-condenser. It is able to supply a water flow rate at a stable temperature (within ± 0.1 °C) at the inlet of the pre-condenser. This temperature can be manually set. The installed chiller is supplied by AIR CONTROL, ROCK 4W model. The chiller has a modulation system of the cooling capacity, with a minimum water temperature of 5 °C.

It has a water cooled brazed plate condenser, and a brazed plate evaporator. A first PID thermoregulator controls the water temperature at the outlet of the evaporator. The refrigerated water is stored in a 12 L tank, from which the water is pumped to the pre-condenser. Before reaching the pre-condenser, the water passes through an electric resistance for a better temperature control. This resistance is controlled by a second PID thermoregulator. Thus, two setpoint temperature values have to be set: the first one for the water temperature at the outlet of the evaporator, and the second one for the water temperature to be sent to the pre-condenser. The setpoint temperature of the second PID thermoregulator should be at least 2 K higher than that of the first one, since the second one acts on a thermal resistance.

The main characteristics of the chiller are here reported:

- electric power input: 13.5 kW;
- nominal cooling capacity at evap. 7.2 °C, cond. 54.2 °C: 8.07 kW;
- cooling capacity at evap. -5 °C, cond. 40 °C: 5.52 kW;
- compressor: MTZ 50;
- refrigerant: R134a;
- refrigerant charge: 3 kg;
- thermal resistance input: 9 kW;
- pump flow rate: 1000 - 4200 L/h;
- pump electric power input: 0.55 kW;
- pump head: 18 - 37 m H_2O;
- pump speed: 2900 rpm.

The mixers

Two mixers were installed upstream and downstream of the pre-condenser in the cold water loop. They have a double function: they mix the water, in order to avoid any temperature non-uniformities, and they also house a probe to insert a thermocouple. They are identical to those installed in the hot water loop.

The volumetric flowmeter

A magnetic flowmeter is installed in the cold water loop between the chiller and the inlet of the pre-condenser. Similarly to that in the hot water loop, a Rosemount 8700 series magnetic flowmeter is mounted, with a full scale of 650 L/h and an accuracy of 0.25%, with a 4-20 mA digital electronics (HART protocol) as output.

4.4.5 The data acquisition system

A National Instrument CompactDAQ is used as data acquisition system. More precisely, NI CompactDAQ 9178 8-Slot USB Chassis with 5 NI-9213 modules, a NI-9208, and a NI-9219 was chosen.

The NI cDAQ-9178 (shown in figure 4.47) is an 8-slot NI CompactDAQ USB chassis designed for small, portable, mixed-measurement test systems. It can be combine with up to eight NI C Series I/O modules for a custom analog input, analog output, digital I/O, and counter/timer measurement system.

Figure 4.47: Picture of the NI cDAQ-9178 chassis.

The NI-9213 is a high-density thermocouple module. It has also a cold-junction compensation, but it was chosen to use an ice-point reference (KAYE K170 model) as 0 °C reference for thermocouples for a better accuracy. It has 16 channels with a sample rate up to 1200 S/s at a resolution of 24 bit. It has an operative range of ±22 mA.

The NI-9208 current input module has 16 channels of ±21 mA input with

50/60 Hz rejection for noise rejection. Signals coming from flowmeter and pressure transducers are connected to this module. It has 16 channels with a sample rate up to 500 S/s at a resolution of 24 bit.

The NI-9219 is a 4 channels universal module. Different measurement types can be selectable on each of the four channels. Measurement ranges differ for each type of measurement and include up to ±60 V for voltage and ±25 mA for current. The signals of the current and voltage applied to electric heater are connected to this module. These modules are shown in figure 4.48.

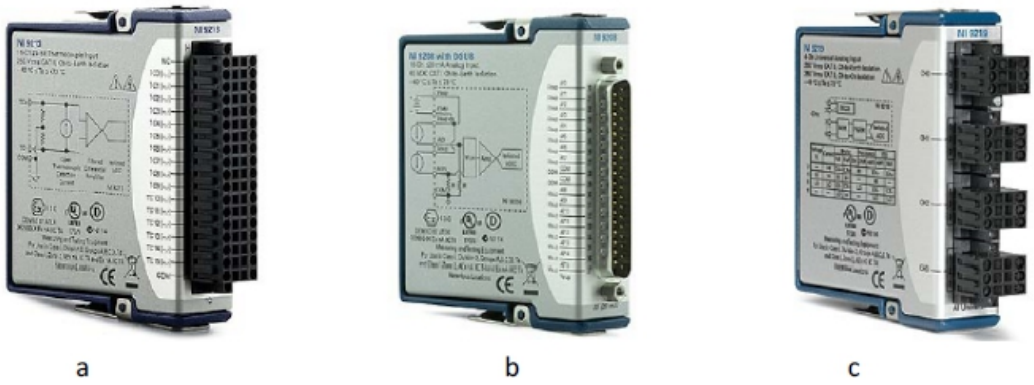

Figure 4.48: Picture of the NI moduled: NI 9213 (a), NI 9208 (b), and NI 9219 (c).

The USB port of the NI cDAQ-9178 is connected to a personal computer, and signals are elaborated using the commercial software LabVIEW 11 [93]. The LabVIEW [93] code permits to monitor all the thermophysical parameters of the facility, and it is also interfaced with Refprop 9.1 [94] to calculate thermodynamic properties such as the inlet quality in the the test section. The description of channels connected to the data acquisition system is reported in table 4.6. Operative parameters are also saved in tabular format for the further data reduction.

Table 4.6: Description of the channel connected to data acquisition system.

Module	Module channel	Kaye channel	Description
NI-9213 slot 2	9	26	water temperature at inlet of pre-condenser
	10	27	water temperature at outlet of pre-condenser
	11	28	water temperature at inlet of evaporator
	12	29	water temperature at outlet of evaporator

to next page —

— from previous page

Module	Module channel	Kaye channel	Description
	13	30	refrigerant temperature at outlet of post-condenser
	14	31	refrigerant temperature at inlet of evaporator
	15	32	refrigerant temperature at outlet of evaporator
NI-9213 slot 3	0	33	refrigerant temperature at outlet of pre-condenser
	1	34	refrigerant temperature at inlet of test section
	2	35	refrigerant temperature at outlet of test section
	3	36	wall temperature
	4	37	wall temperature
	5	38	wall temperature
	6	39	wall temperature
	7	40	wall temperature
	8	41	wall temperature
	9	42	wall temperature
	10	43	wall temperature
	11	44	wall temperature
	12	45	wall temperature
	13	46	wall temperature
	14	47	wall temperature
	15	48	wall temperature
NI-9213 slot 4	0	49	wall temperature
	1	50	wall temperature
	2	51	wall temperature
	3	52	wall temperature
	4	53	wall temperature
	5	54	wall temperature
	6	55	wall temperature
NI-9213 slot 5	11	-	water temperature at outlet of pre-condenser (with thermopile)
	12	-	water temperature at outlet of evaporator (with thermopile)
NI-9208 slot 1	0	-	refrigerant mass flow rate
	1	-	water flow rate at evaporator
	2	-	water flow rate at pre-condenser
	3	-	refrigerant pressure at outlet of evaporator
	4	-	refrigerant pressure at inlet of evaporator
	5	-	refrigerant pressure drop at test section
	6	-	refrigerant pressure at inlet of test section
NI-9219 slot 1	0	-	voltage at electric heater
	1	-	current at electric heater

4.5 Data reduction and uncertainty analysis

4.5.1 Evaporator

The subcooled liquid is pumped to the evaporator where it is vaporized and superheated. The refrigerant flows into the evaporator in counter current with hot water, supplied in the hot water loop. The refrigerant temperature is measured at both inlet and outlet of the heat exchanger ($t_{ref,eva,in}$ and $t_{ref,eva,out}$, respectively), and the pressure is also measured at inlet and outlet of the heat exchanger ($p_{ref,eva,in}$ and $p_{ref,eva,out}$, respectively). Thus, the heat flow rate ($q_{ref,eva}$) exchanged in the evaporator can be calculated from the refrigerant side as:

$$q_{ref,eva} = \dot{m}_{ref} \cdot (h_{ref,eva,out} - h_{ref,eva,in}) \tag{4.14}$$

From the water side, the water temperature is measured at both inlet and outlet of the heat exchanger by means of two T-type thermocouples ($t_{w,eva,in}$ and $t_{w,eva,out}$, respectively), and in addition a thermopile measures the water temperature difference ($\Delta t_{w,eva}$). Thermocouples have an uncertainty of ±0.05 K, whereas the thermopile has an uncertainty of (±0.03 K). Thus, the heat flow rate exchanged in the evaporator can be calculated from the water side using either thermocouples or thermopile ($q_{w,eva,tc}$ or $q_{w,eva,tp}$) as:

$$q_{w,eva,tc} = \dot{m}_{w,eva} \cdot c_{p,w} \cdot (t_{w,eva,in} - t_{w,eva,out}) \tag{4.15}$$

$$q_{w,eva,tp} = \dot{m}_{w,eva} \cdot c_{p,w} \cdot \Delta t_{w,eva} \tag{4.16}$$

Deriving equation 4.14, the sensitivity terms are:

$$\frac{\partial q_{ref,eva}}{\partial \dot{m}_{ref}} = h_{ref,eva,out} - h_{ref,eva,in} \tag{4.17}$$

$$\frac{\partial q_{ref,eva}}{\partial h_{ref,eva,out}} = \dot{m}_{ref} \tag{4.18}$$

$$\frac{\partial q_{ref,eva}}{\partial h_{ref,eva,in}} = -\dot{m}_{ref} \tag{4.19}$$

Thus, the experimental uncertainty on heat flow rate exchanged at the evaporator from the refrigerant side can be estimated with the following equation:

$$i_{q_{ref,eva}} = \sqrt{\left(\frac{\partial q_{ref,eva}}{\partial \dot{m}_{ref}} i_{\dot{m}}\right)^2 + \left(\frac{\partial q_{ref,eva}}{\partial h_{ref,eva,out}} i_{h_{ref,eva,out}}\right)^2 + \left(\frac{\partial q_{ref,eva}}{\partial h_{ref,eva,in}} i_{h_{ref,eva,in}}\right)^2} \tag{4.20}$$

Deriving equation 4.15, the sensitivity terms are:

$$\frac{\partial q_{w,eva,tc}}{\partial \dot{m}_{w,eva}} = c_{p,w} \cdot t_{w,eva,out} - t_{w,eva,in} \tag{4.21}$$

$$\frac{\partial q_{w,eva,tc}}{\partial c_{p,w}} = m_{w,eva} \cdot (t_{w,eva,out} - t_{w,eva,in}) \tag{4.22}$$

$$\frac{\partial q_{w,eva,tc}}{\partial t_{w,in}} = \dot{m}_{w,eva} \cdot c_{p,w} \tag{4.23}$$

$$\frac{\partial q_{w,eva,tc}}{\partial t_{w,out}} = -\dot{m}_{w,eva} \cdot c_{p,w} \tag{4.24}$$

Thus, the experimental uncertainty on heat flow rate exchanged at the evaporator from the water side using the thermocouples can be estimated with the following equation:

$$i_{q_{w,tc,eva}} = \sqrt{\left(\frac{\partial q_{w,eva,tc}}{\partial \dot{m}_{w,eva}} i_{\dot{m}_{w,eva}}\right)^2 + \left(\frac{\partial q_{w,eva,tc}}{\partial c_{p,w}} i_{c_{p,w}}\right)^2 + \left(\frac{\partial q_{w,eva,tc}}{\partial t_{w,in}} i_{t_{w,in}}\right)^2 + \left(\frac{\partial q_{w,eva,tc}}{\partial t_{w,out}} i_{t_{w,out}}\right)^2} \tag{4.25}$$

Deriving equation 4.16, the sensitivity terms are:

$$\frac{\partial q_{w,eva,tp}}{\partial \dot{m}_{w,eva}} = c_{p,w} \cdot \Delta t_{w,eva} \tag{4.26}$$

$$\frac{\partial q_{w,eva,tp}}{\partial c_{p,w}} = m_{w,eva} \cdot \Delta t_{w,eva} \tag{4.27}$$

$$\frac{\partial q_{w,eva,tp}}{\partial \Delta t_{w,eva}} = \dot{m}_{w,eva} \cdot c_{p,w} \tag{4.28}$$

Thus, the experimental uncertainty on heat flow rate exchanged at the evaporator from the water side using the thermopile can be estimated with the following

equation:

$$i_{q_{w,tp,eva}} = \sqrt{\left(\frac{\partial q_{w,eva,tp}}{\partial \dot{m}_{w,eva}} i_{\dot{m}_{w,eva}}\right)^2 + \left(\frac{\partial q_{w,eva,tp}}{\partial c_{p,w}} i_{c_{p,w}}\right)^2 + \left(\frac{\partial q_{w,eva,tp}}{\partial \Delta t_{w,eva}} i_{\Delta t_{w,eva}}\right)^2} \quad (4.29)$$

4.5.2 Pre-condenser

Only in the testing phase of the experimental setup, the superheated vapour coming from the evaporator is condensed and subcooled in the pre-condenser. The refrigerant temperature is measured at the outlet of the pre-condenser ($t_{ref,pc,out}$), whereas its inlet temperature is assumed to be the temperature at the outlet of the evaporator ($t_{ref,pc,in} = t_{ref,eva,out}$). The pressure is measured at the outlet of the pre-condenser ($p_{ref,pc,out}$), whereas its inlet pressure is assumed to be the pressure at the outlet of the evaporator ($p_{ref,pc,in} = p_{ref,eva,out}$). Thus, the heat flow rate ($q_{ref,eva}$) exchanged in the pre-condenser can be calculated from the refrigerant side as:

$$q_{ref,pc} = \dot{m}_{ref} \cdot (h_{ref,pc,in} - h_{ref,pc,out}) \quad (4.30)$$

From the water side, the water temperature is measured at both inlet and outlet of the heat exchanger by means of two T-type thermocouples ($t_{w,pc,in}$ and $t_{w,pc,out}$, respectively), and in addition a thermopile measures the water temperature difference ($\Delta t_{w,pc}$). Thermocouples have an uncertainty of ±0.05 K, whereas the thermopile has an uncertainty of (±0.03 K). Thus, the heat flow rate exchanged in the pre-condenser can be calculated from the water side using either thermocouples or thermopile ($q_{w,pc,tc}$ or $q_{w,pc,tp}$) as:

$$q_{w,pc,tc} = \dot{m}_{w,pc} \cdot c_{p,w} \cdot (t_{w,pc,out} - t_{w,pc,in}) \quad (4.31)$$

$$q_{w,pc,tp} = \dot{m}_{w,pc} \cdot c_{p,w} \cdot \Delta t_{w,pc} \quad (4.32)$$

Deriving equation 4.30, the sensitivity terms are:

$$\frac{\partial q_{ref,pc}}{\partial \dot{m}_{ref,pc}} = h_{ref,pc,in} - h_{ref,pc,out} \quad (4.33)$$

$$\frac{\partial q_{ref,pc}}{\partial h_{ref,pc,in}} = \dot{m}_{ref,pc} \tag{4.34}$$

$$\frac{\partial q_{ref,pc}}{\partial h_{ref,pc,out}} = -\dot{m}_{ref,pc} \tag{4.35}$$

Thus, the experimental uncertainty on heat flow rate exchanged at the pre-condenser from the refrigerant side can be estimated with the following equation:

$$i_{q_{ref,pc}} = \sqrt{\left(\frac{\partial q_{ref,pc}}{\partial \dot{m}_{ref,pc}} i_{\dot{m}}\right)^2 + \left(\frac{\partial q_{ref,pc}}{\partial h_{ref,pc,in}} i_{h_{ref,pc,in}}\right)^2 + \left(\frac{\partial q_{ref,pc}}{\partial h_{ref,pc,out}} i_{h_{ref,pc,out}}\right)^2} \tag{4.36}$$

Deriving equation 4.31, the sensitivity terms are:

$$\frac{\partial q_{w,pc,tc}}{\partial \dot{m}_{w,pc}} = c_{p,w} \cdot t_{w,pc,in} - t_{w,pc,out} \tag{4.37}$$

$$\frac{\partial q_{w,pc,tc}}{\partial c_{p,w}} = m_{w,pc} \cdot t_{w,pc,in} - t_{w,pc,out} \tag{4.38}$$

$$\frac{\partial q_{w,pc,tc}}{\partial t_{w,out}} = \dot{m}_{w,pc} \cdot c_{p,w} \tag{4.39}$$

$$\frac{\partial q_{w,pc,tc}}{\partial t_{w,in}} = -\dot{m}_{w,pc} \cdot c_{p,w} \tag{4.40}$$

Thus, the experimental uncertainty on heat flow rate exchanged at the pre-condenser from the water side using the thermocouples can be estimated with the following equation:

$$i_{q_{w,pc,tc}} = \sqrt{\left(\frac{\partial q_{w,pc,tc}}{\partial \dot{m}_{w,pc}} i_{\dot{m}_{w,pc}}\right)^2 + \left(\frac{\partial q_{w,pc,tc}}{\partial c_{p,w}} i_{c_{p,w}}\right)^2 + \left(\frac{\partial q_{w,pc,tc}}{\partial t_{w,out}} i_{t_{w,out}}\right)^2 + \left(\frac{\partial q_{w,pc,tc}}{\partial t_{w,in}} i_{t_{w,in}}\right)^2} \tag{4.41}$$

Deriving equation 4.32, the sensitivity terms are:

$$\frac{\partial q_{w,pc,tp}}{\partial \dot{m}_{w,pc}} = c_{p,w} \cdot \Delta t_{w,pc} \tag{4.42}$$

$$\frac{\partial q_{w,pc,tp}}{\partial c_{p,w}} = m_{w,pc} \cdot \Delta t_{w,pc} \tag{4.43}$$

$$\frac{\partial q_{w,pc,tp}}{\partial \Delta t_{w,pc}} = \dot{m}_{w,pc} \cdot c_{p,w} \tag{4.44}$$

Thus, the experimental uncertainty on heat flow rate exchanged at the evaporator from the water side using the thermopile can be estimated with the following equation:

$$i_{q_{w,pc,tp}} = \sqrt{\left(\frac{\partial q_{w,pc,tp}}{\partial \dot{m}_{w,eva}} i_{\dot{m}_{w,pc}}\right)^2 + \left(\frac{\partial q_{w,pc,tp}}{\partial c_{p,w}} i_{c_{p,w}}\right)^2 + \left(\frac{\partial q_{w,pc,tp}}{\partial \Delta t_{w,pc}} i_{\Delta t_{w,pc}}\right)^2} \tag{4.45}$$

The mean and maximum uncertainties on the heat flow rates exchanged in the evaporator and in the pre-condenser are reported in table 4.7.

Table 4.7: Uncertainties on the heat flow rates exchanged in the evaporator and in the pre-condenser.

		i_{mean}	i_{max}
EVAPORATOR	$q_{w,eva,tc}$	2.9%	3.9%
	$q_{w,eva,tp}$	1.6%	2.0%
	$q_{ref,eva}$	2.3%	2.4%
PRE-CONDENSER	$q_{w,pc,tc}$	2.3%	4.8%
	$q_{w,pc,tp}$	1.3%	2.2%
	$q_{ref,pc}$	2.5%	2.7%

4.6 Calibration tests

Once the facility had been built, calibration tests were run in order to check the heat balances at the heat exchangers. Tests were run with the refrigerant R22 as working fluid, at a saturation temperature of 40 °C, with different refrigerant mass flow rate, different water mass flow rate at the evaporator, different water flow rate at the pre-condenser, and different subcoolings at the inlet of the pre-condenser. The test section was replaced with a straight tube, and attention was focused only to the evaporator and pre-condenser.

4.6.1 Evaporator

Calibration tests were run to check heat balance at the evaporator. The deviation on the heat balance is calculated as:

$$deviation = \frac{q_{ref,eva} - q_{w,eva}}{q_{w,eva}} \cdot 100 \ [\%] \tag{4.46}$$

In figures 4.49 and 4.50 deviations on the heat balance calculated with the thermocouples and with the thermopile, respectively, are shown. Q_w and m represent the water volumetric flow rate at the evaporator and the refrigerant mass flow rate, respectively. In figures the interval of the calculated uncertainty on the heat flow rate is also reported. These lines correspond to the maximum value of uncertainty between the heat flow rate exchanged on water side and on refrigerant side (see table 4.7). Considering the heat balance calculated with thermocouples, the deviation is outside from the uncertainty range only for the lowest refrigerant mass flow rate, whereas the deviation is within the range for all the other data points, with a mean deviation of 2.6%. The uncertainty is better with the thermopile on average, due

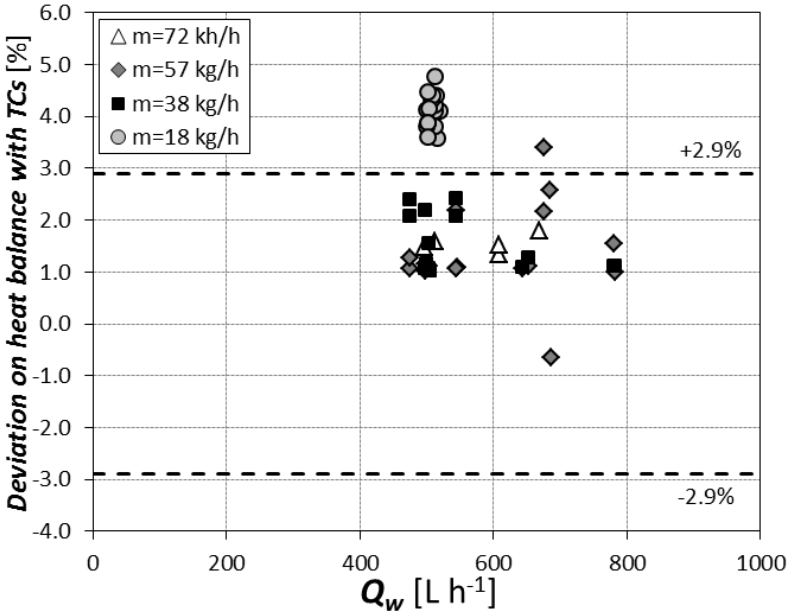

Figure 4.49: Deviation on the heat balance at the evaporator calculated with the thermocouples.

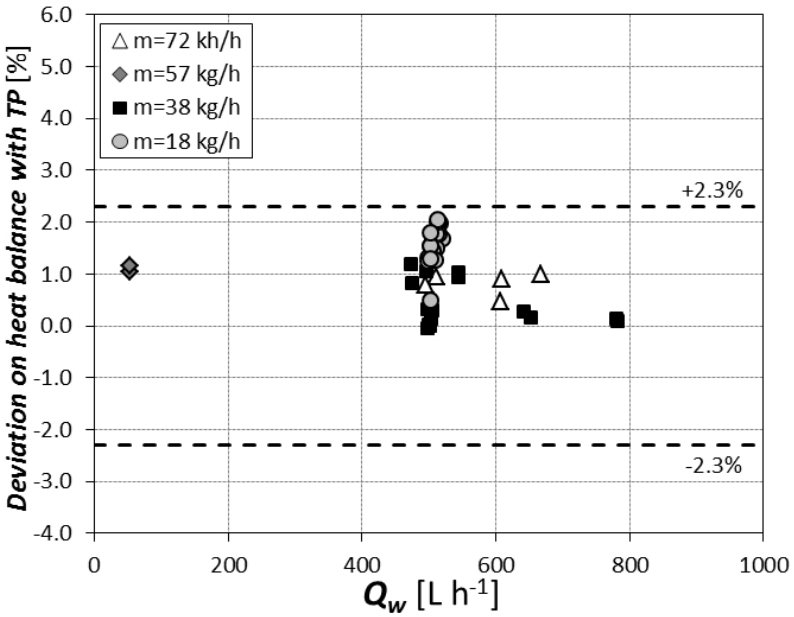

Figure 4.50: Deviation on the heat balance at the evaporator calculated with the thermopile.

to a higher accuracy than thermocouples, and all the data points are within the uncertainty range, with a mean deviation of 1.0%.

4.6.2 Pre-condenser

Calibration tests were run to check heat balance at the pre-condenser. The deviation on the heat balance is calculated as:

$$deviation = \frac{q_{ref,pc} - q_{w,pc}}{q_{w,pc}} \cdot 100\ [\%] \tag{4.47}$$

In figures 4.51 and 4.52 deviations on the heat balance calculated with the thermocouples and with the thermopile, respectively, are shown. Q_w and m represent the water volumetric flow rate at the pre-condenser and the refrigerant mass flow rate, respectively. The heat balance calculated with the thermopile (average value of -1.1%) is better than that with the thermocouples (-1.9%), even though there are some points completely outside from the uncertainty range. The reason can be addressed to the level of subcooling of the refrigerant at the outlet of the pre-condenser.

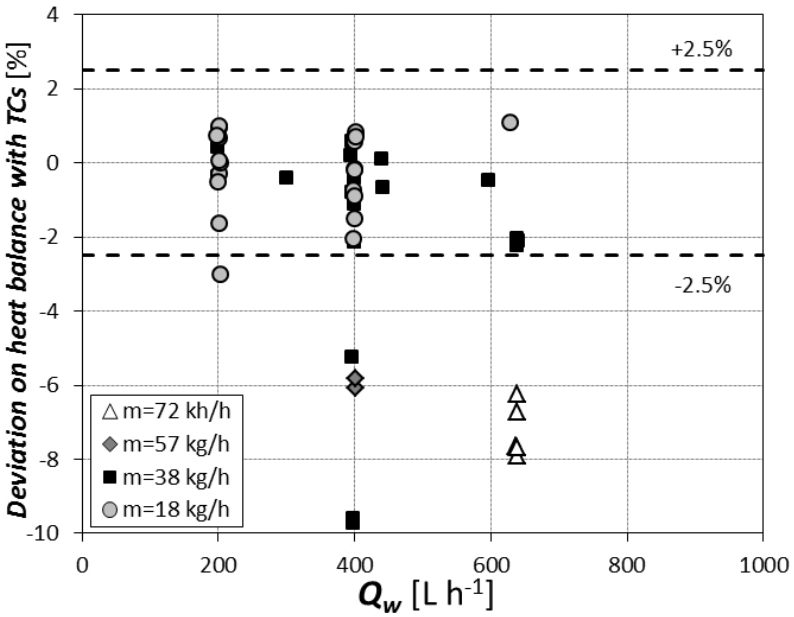

Figure 4.51: Deviation on the heat balance at the pre-condenser calculated with the thermocouples.

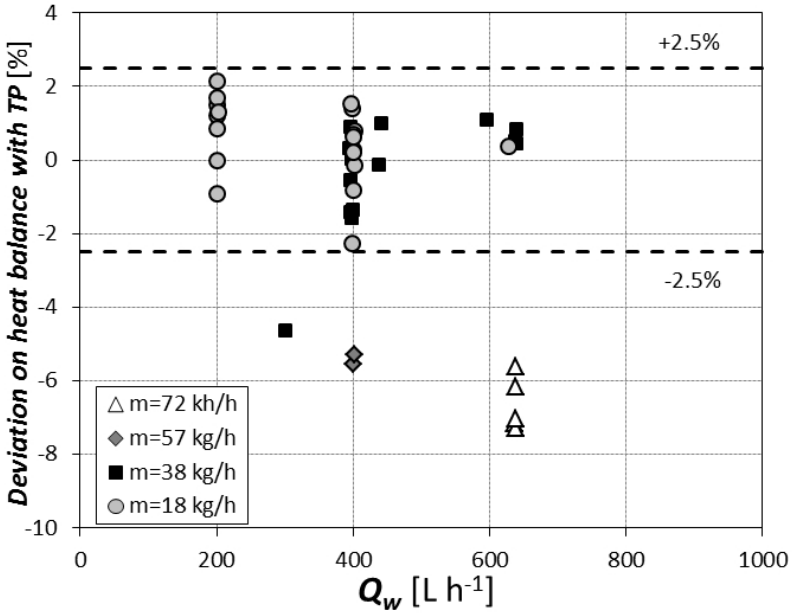

Figure 4.52: Deviation on the heat balance at the pre-condenser calculated with the thermopile.

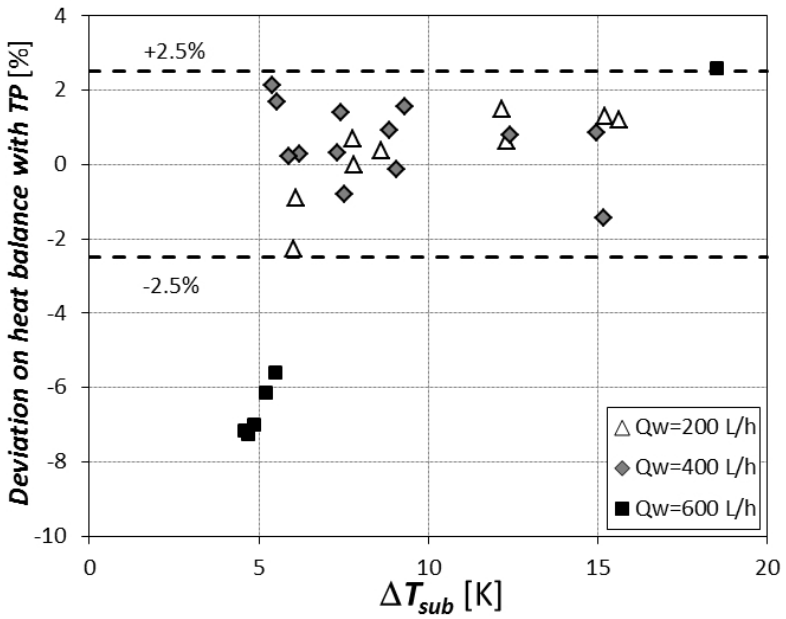

Figure 4.53: Deviation on the heat balance at the pre-condenser calculated with the thermocouples as a function of the level of subcooling.

The subcooling is defined as:

$$\Delta t_{sub} = t_{ref,sat} - t_{ref,pc,out} \tag{4.48}$$

where $t_{ref,sat}$ is the saturation temperature calculated from the value of pressure.

Figure 4.53 shows the deviations on the heat balance calculated with the thermopile as a function of the level of subcooling. As it appears, higher the subcooling level, lower the deviation on the heat balance. The deviation is within the uncertainty range at subcooling higher than 6 °C. Thus, a minimum subcooling of 6 °C is required for the single-phase liquid tests.

Chapter 5

Flow boiling inside a copper foam

5.1 State of the art

Boiling is the heat transfer mechanism with the highest heat transfer coefficients, thus it can be used to spread high fluxes to maintain the wall temperature at low values with compact heat sinks. Recently, there has been a growing interest from research groups on metal foams, but up today only few works involve boiling inside such materials. Among the few works, a greater number of researches can be found about pool boiling rather than flow boiling.

Xu et al. [95] investigated acetone pool boiling heat transfer of copper foams. They considered six different copper foams, with 30, 60, and 90 PPI, and porosities of 0.88 and 0.95, with a heating surface of 12 mm $\times$ 12 mm. The surface superheats were from -20 to 190 K, and the heat fluxes reached 140 W cm^{-2}. The 30 PPI and 60 PPI foams displayed periodic single bubble generation and departure pattern at low wall superheats; when superheats increased, they behaved periodic bubble coalescence and/or re-coalescence pattern. A "cage bubble" coming from the coalescence of miniature bubbles was observed. The 90 PPI foam induced coalescence of miniature bubbles at small surface superheats, with a periodic bubble coalescence pattern. At moderate or large surface superheats, vapour fragments were found to depart from the foam continuously. Three distinct heat transfer regions were identified: liquid natural convection and nucleate boiling heat transfer for all the foams, and a region of vapour resistance to vapour release for the 30 PPI and 60

PPI foams, whereas a region of capillary-assisted liquid towards cells for the 90 PPI foam. Therefore, the pore density was found to have a strong effect on the heat transfer: larger values of PPI have larger resistance to vapour release, lowering the heat transfer performance at small or moderate wall superheats, but larger values of PPI leads to larger capability of liquid suction at high superheats, thus increasing the heat transfer perfomance.

Ji et al. [96] experimentally studied the R134a pool boiling heat transfer of 12 foam-coated tubes at a saturation temperature of 6 °C. Three pore density values: 40, 80, and 130 PPI, two porosities values: 0.90 and 0.97, and two thicknesses: 1.6 mm and 2.5 mm were considered. The foam coating enhanced the pool boiling heat transfer especially at low and moderate heat fluxes less than 30 kW m^{-2}. Highly porous foam tubes with small thickness offered superior performance than tubes with low porosity and high thickness. However, at larger heat fluxes a sharp reduction in heat transfer coefficients was observed for high pore density tubes. Generally speaking, the porous foam structure served as an activated artificial nucleation site and effectively decreased the wall superheat at the onset of nucleate boiling. The highest heat transfer coefficient was showed by the 80 PPI foam with a porosity of 0.97 and a thickness of 1.6 mm, and lies in the intermediate position when compared with typical enhanced tubes.

Graphite foams as enhanced surfaces for pool boiling were studied by Pranoto et al. [97]. Block and fin evaporator structures of aspect ratios of 3.7 and 2.73 were tested with FC-72 and HFE-7000 dielectric liquids. The wall temperatures were measured and the boiling heat transfer coefficients were calculated to analyze the boiling performance. The wall temperatures of the block structure were about 8 and 10 °C lower than the fin structure for AR=3.70 and 2.73, respectively, and the average boiling heat transfer coefficients of the block structure were about 1.2-1.6 times higher than those of the fin structure for the tested heat flux level up to 112 W cm^{-2}. Boiling images were also captured by a high speed video camera. The much larger bubble density from the block structure supported the evidence that the fin structure reduces the number of nucleation sites and decreases the boiling performance. The use of FC-72 resulted in higher heat transfer coefficients compared with HFE-7000.

Xu and Zhao [98] investigated pool boiling heat transfer of open-celled metal

foams with V-shaped grooves. The foam materials were copper and nickel. The pore densities were 80 PPI, 100 PPI and 130 PPI, while the porosity and foam thickness remained the fixed values of 0.95 and 4 mm, respectively. A parametric study was performed by varying groove width and number. The results showed that the characteristics of the V-shaped grooves highly affected the pool boiling heat transfer of the foam surfaces with high pore densities. For the 100 PPI copper foam with the thickness of 4 mm, the optimal groove number maximally enhancing the pool boiling heat transfer was 2, whereas, for the 80 PPI copper foam, the optimal number was 3. At the pore density of 100 PPI, single-directional V-shaped groove enhancement effect on the pool boiling heat transfer of nickel foam was better than that of copper foam. Compared with single-directional V-shaped grooves, crossing V-shaped grooves can further improve pool boiling heat transfer performance and delay CHF of the copper foam with the high pore density, because the latter can further reduce bubble escaping resistance and uniformly utilize the foam capillary force.

Fewer works can be found about flow boiling through metal foams. Madani et al. [99] characterized the hydraulic performance of a channel filled with a metallic foam during n-pentane flow boiling, with a mass velocity lying between 4 and 49 $kg^{-2}\ s^{-1}$, and heat flux between 0 and 35 W cm^{-2}. They measured the static pressure at different locations along the test section, showing the effect of the acceleration of the fluid due to phase change, determining the boiling front. Experimental results also showed that the laws governing flow in a channel provided with metallic foams are very similar to those for a channel without foams. The heat transfer was studied by the same authors in [100], in which they analyzed the n-pentane upward flow boiling inside a 36 PPI copper foam with a porosity of 97%. The mass velocity ranged between 10 and 100 kg $m^{-2}\ s^{-1}$, and the heat flux between 0 and 25 W cm^{-2}. Thermal results were analyzed in terms of mean heat transfer coefficient and boiling curves for several mass velocities. Experimental results were also compared with values for a plain channel. The comparison revealed that the metallic foam enhances the heat transfer coefficient by a factor of 2 - 4 at low quality.

Hu et al. [101] experimentally analyzed the effect of tube diameter on pressure drop characteristics of refrigerant-oil mixture flow boiling in metal foam filled tubes. Experiments were carried out on tubes with an inner diameter of 7.9 mm, and the

analysis of the diameter effect was done based on experimental data of 7.9 mm tubes together with those of 13.8 mm and 26.0 mm from the literature. For metal foam filled tubes with an inner diameter of 7.9 mm, the presence of oil increased pressure drop by a maximum of 29% and 37% for 5 PPI and 10 PPI, respectively; the pressure drop increases by a maximum of 25% as PPI increases from 5 to 10, which is smaller than that for 13.8 mm. As the tube diameter decreases, the pressure drop in metal foam filled tubes decreases due to the presence of incomplete cells. A new correlation was proposed to estimate pressure drop of refrigerant-oil mixture flow boiling in metal foam filled tube, taking into account also the tube diameter.

5.2 Data reduction

The subcooled liquid is pumped to the boiler where it is vaporized and superheated (see figure 4.25); the refrigerant temperature and pressure are measured at both inlet and outlet of the heat exchanger. The vapour quality at the inlet of the test section depends on the refrigerant conditions at the inlet of the pre-condenser and on the heat flow rate exchanged in the tube-in-tube heat exchanger and obtained from a thermal balance on the cooling water side as given by:

$$q_{pc} = \dot{m}_{w,pc} \cdot c_{p,w} \cdot (t_{w,pc,out} - t_{w,pc,in}) = \dot{m}_{ref} \cdot (h_{vs} - h_{TS,in}) \tag{5.1}$$

where $\dot{m}_{w,pc}$ is the water mass flow rate at the pre-condenser, $c_{p,w}$ the water specific heat at constant pressure, $t_{w,pc,out}$ and $t_{w,pc,in}$ the water temperatures at the outlet and inlet of the pre-condenser, respectively. Considering the right-hand side of equation 5.1, $\dot{m}_{ref}$ is the refrigerant mass flow rate, while h_{vs} the enthalpy of the superheated gas at the inlet of the pre-condenser, and $h_{TS,in}$ the enthalpy of the refrigerant at the inlet of the test section. The vapour quality at the inlet of the test section (x_{in}) can be calculated from the heat balance, as:

$$x_{in} = \frac{h_{TS,in} - h_L}{h_V - h_L} \tag{5.2}$$

where h_L and h_V are the specific enthalpy of the saturated liquid and vapour, respectively, evaluated at the saturation pressure of the refrigerant measured at the

inlet of the test section. The electrical power supplied to the sample is indirectly measured by means of a calibrated reference resistance (shunt) and by the measurement of the effective EPD (Electrical Difference Potential) of the resistance wire inserted in the copper heater. The current can be calculated fron the Ohm's law.

Preliminary heat transfer measurements permitted to estimate the heat losses (q_{loss}) due to conduction through the test section as a function of the mean wall temperature. The tests were run under vacuum conditions by supplying the power needed to maintain the mean wall temperature from around 30 °C to more than 60 °C. The results of these calibration tests are shown in figure 5.1, where the heat lost through the test section is plotted against the mean wall temperature. As it clearly appears, the relationship is linear; in this way, the actual value of heat supplied to the sample can be evaluated.

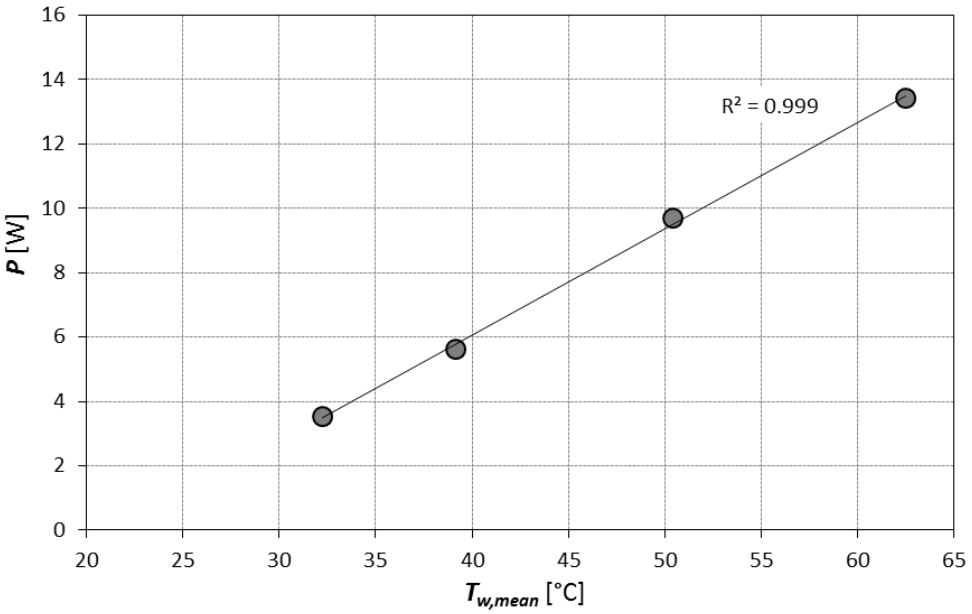

Figure 5.1: Estimated values of heat losses through the test section.

The heat losses through the test section are given by:

$$q_{loss}[W] = 0.3311 \cdot \bar{t}_{wall}[^{\circ}C] - 7.128 \tag{5.3}$$

where $\bar{t}_{wall}$ is the mean wall temperature; thus, the actual heat flow rate supplied

to the foam is given by:

$$q_{TS} = P_{EL} - q_{loss} = \Delta V \cdot I - q_{loss} \tag{5.4}$$

where P_{EL} is the electrical power supplied, ΔV is the electrical potential, and I is the current. It was estimated that the heat lost was always less than 3%. The specific enthalpy at the outlet of the test section can be calculated from the thermal balance applied to the test section:

$$h_{TS,out} = h_{TS,in} + \frac{q_{TS}}{\dot{m}_{ref}} \tag{5.5}$$

Then, vapour quality x_{out} is given by:

$$x_{out} = \frac{h_{TS,out} - h_L}{h_V - h_L} \tag{5.6}$$

In this case, the thermodynamic properties of the refrigerant are evaluated at the outlet saturation pressure. The two phase heat transfer coefficient HTC_{TP}, referred to the bare base area A_{base} can now be defined as:

$$HTC_{TP} = \frac{q_{TS}}{A_{base} \cdot (\bar{t}_{wall} - \bar{t}_{sat})} \tag{5.7}$$

where $\bar{t}_{wall}$ is the average value of the wall thermocouples, and $\bar{t}_{sat}$ the average value of the saturation temperatures obtained from the measured values of the pressure, as:

$$\bar{t}_{wall} = \frac{1}{20} \sum_{i=1}^{20} t_{wall,i} \tag{5.8}$$

$$\bar{t}_{sat} = \frac{t_{sat,in}(p_{sat,in}) + t_{sat,out}(p_{sat,out})}{2} \tag{5.9}$$

where $t_{wall,i}$ is the temperature measured by the i-th thermocouple, and $p_{sat,in}$ and $p_{sat,out}$ are the saturation pressure at the inlet and outlet of the test section, respectively. Thermodynamic and transport properties of the refrigerant are estimated from Refprop 9.1 [94].

In case of single phase heat transfer measurements, the heat transfer coefficient

HTC_{SP} is defined as:

$$HTC_{SP} = \frac{q_{TS}}{A_{base} \cdot \Delta T_{ml}} \tag{5.10}$$

where the logarithmic mean temperature difference can ba calculated as follows:

$$\Delta T_{ml} = \frac{(t_{wall,in} - t_{ref,in}) - (t_{wall,out} - t_{ref,out})}{\ln \dfrac{t_{wall,in} - t_{ref,in}}{t_{wall,out} - t_{ref,out}}} \tag{5.11}$$

5.3 Uncertainty analysis

5.3.1 Uncertainty on the heat flow rate exchanged in the pre-condenser

Deriving equation 5.1, the sensitivity terms to calculate the uncertainty on the heat flow rate exchanged at the pre-condenser on the water side are:

$$\frac{\partial q_{pc,w}}{\partial \dot{m}_w} = c_{p,w} \cdot \Delta T_{w,pc} \tag{5.12}$$

$$\frac{\partial q_{pc,w}}{\partial c_{p,w}} = \dot{m}_w \cdot \Delta T_{w,pc} \tag{5.13}$$

$$\frac{\partial q_{pc,w}}{\partial \Delta T_{w,pc}} = \dot{m}_w c_{p,w} \tag{5.14}$$

Therefore, the uncertainty ob the heat flow rate can be calculated using the following equation:

$$i_{q_{w,pc}} = \sqrt{\left(\frac{\partial q_{pc,w}}{\partial \dot{m}_w} i_{\dot{m}_{w,pc}}\right)^2 + \left(\frac{\partial q_{w,pc}}{\partial c_{p,w}} i_{c_{p,w}}\right)^2 + \left(\frac{\partial q_{w,pc}}{\partial \Delta t_{w,pc}} i_{\Delta t_{w,pc}}\right)^2} \tag{5.15}$$

5.3.2 Uncertainty on the inlet quality

From equation 5.1, the refrigerant enthalpy at the outlet of the pre-condenser can be estimated as:

$$h_{ref,pc,out} = h_{ref,pc,in} - \frac{q_{w,pc}}{\dot{m}_{ref}} \tag{5.16}$$

An uncertainty of ±1% of the value was considered for thermophysical properties calculated using Refprop 9.1 [94]. Since the tube portion between the outlet of the pre-condenser and the inlet of the test section is adiabatic, the enthalpy of the refrigerant at the outlet of the pre-condenser is equal to the enthalpy of the refrigerant at the inlet of the test section, i.e. $h_{ref,pc,out} = h_{ref,TS,in}$. Deriving equation 5.16, the sensitivity terms are:

$$\frac{\partial h_{ref,TS,in}}{\partial h_{ref,pc,in}} = 1 \tag{5.17}$$

$$\frac{\partial h_{ref,TS,in}}{\partial q_{w,pc}} = -\frac{1}{\dot{m}_{ref}} \tag{5.18}$$

$$\frac{\partial h_{ref,TS,in}}{\partial \dot{m}_{ref}} = \frac{q_{w,pc}}{\dot{m}_{ref}^2} \tag{5.19}$$

Thus, the uncertainty on the refrigerant enthalpy at the inlet of the test section can be estimated as:

$$i_{h_{ref,TS,in}} = \sqrt{\left(\frac{\partial h_{ref,TS,in}}{\partial h_{ref,pc,in}} i_{h_{ref,pc,in}}\right)^2 + \left(\frac{\partial h_{ref,TS,in}}{\partial q_{w,pc}} i_{q_{w,pc}}\right)^2 + \left(\frac{\partial h_{ref,TS,in}}{\partial \dot{m}_{ref}} i_{\dot{m}_{ref}}\right)^2} \tag{5.20}$$

Deriving equation 5.2, it is possible to calculate the following sensitivity terms:

$$\frac{\partial x_{in}}{\partial h_{ref,TS,in}} = \frac{1}{h_{LV}} \tag{5.21}$$

$$\frac{\partial x_{in}}{\partial h_L} = -\frac{1}{h_{LV}} \tag{5.22}$$

$$\frac{\partial x_{in}}{\partial h_{LV}} = -\frac{h_{in} - h_L}{h_{LV}^2} \tag{5.23}$$

Thus, the uncertainty on the inlet quality is given by:

$$i_{x_{in}} = \sqrt{\left(\frac{\partial x_{in}}{\partial h_{ref,TS,in}} i_{h_{ref,TS,in}}\right)^2 + \left(\frac{\partial x_{in}}{\partial h_L} i_{h_L}\right)^2 + \left(\frac{\partial x_{in}}{\partial h_{LV}} i_{h_{LV}}\right)^2} \tag{5.24}$$

5.3.3 Uncertainty on the mean vapour quality

Deriving equation 5.5:

$$\frac{\partial h_{ref,TS,out}}{\partial h_{ref,TS,in}} = 1 \tag{5.25}$$

$$\frac{\partial h_{ref,TS,out}}{\partial q_{TS}} = \frac{1}{\dot{m}_{ref}} \tag{5.26}$$

$$\frac{\partial h_{ref,TS,out}}{\partial \dot{m}_{ref}} = -\frac{q_{TS}}{\dot{m}_{ref}^2} \tag{5.27}$$

Therefore, the uncertainty on the refrigerant enthalpy at the outlet of the test section can be estimated as:

$$i_{h_{ref,TS,out}} = \sqrt{\left(\frac{\partial h_{ref,TS,out}}{\partial h_{ref,TS,in}} i_{h_{ref,TS,in}}\right)^2 + \left(\frac{\partial h_{ref,TS,out}}{\partial q_{TS}} i_{q_{TS}}\right)^2 + \left(\frac{\partial h_{ref,TS,out}}{\partial \dot{m}_{ref}} i_{\dot{m}_{ref}}\right)^2} \tag{5.28}$$

By the knowledge of the uncertainty on the refrigerant enthalpy at the outlet of the test section, it is possible to estimate the uncertainty on the outlet quality. Deriving equation 5.6:

$$\frac{\partial x_{out}}{\partial h_{ref,TS,out}} = \frac{1}{h_{LV}} \tag{5.29}$$

$$\frac{\partial x_{out}}{\partial h_L} = -\frac{1}{h_{LV}} \tag{5.30}$$

$$\frac{\partial x_{out}}{\partial h_{LV}} = -\frac{h_{out} - h_L}{h_{LV}^2} \tag{5.31}$$

Thus:

$$i_{x_{out}} = \sqrt{\left(\frac{\partial x_{out}}{\partial h_{ref,TS,out}} i_{h_{ref,TS,out}}\right)^2 + \left(\frac{\partial x_{out}}{\partial h_L} i_{h_L}\right)^2 + \left(\frac{\partial x_{out}}{\partial h_{LV}} i_{h_{LV}}\right)^2} \tag{5.32}$$

The mean vapour quality x_{mean} is calculated as the arithmetic average between inlet and outlet vapour quality:

$$x_{mean} = \frac{x_{in} + x_{out}}{2} \tag{5.33}$$

Deriving:

$$\frac{\partial x_{mean}}{\partial x_{in}} = \frac{\partial x_{mean}}{\partial x_{out}} = \frac{1}{2} \tag{5.34}$$

and so:

$$i_{x_{mean}} = \frac{1}{2}\sqrt{i_{x_{in}}^2 + i_{x_{out}}^2} \tag{5.35}$$

From the above analysis, the mean uncertainty on the mean vapour quality, calculated with the instruments accuracy reported in chapter 4 and considering an uncertainty of 1% for the values calculated with Refprop 9.1 [94], is 0.030.

5.3.4 Uncertainty on the two-phase heat transfer coefficient

Deriving equation 5.7:

$$\frac{\partial HTC_{TP}}{\partial q_{TS}} = \frac{1}{A_{base} \cdot (\bar{t}_{wall} - \bar{t}_{sat})} \tag{5.36}$$

$$\frac{\partial HTC_{TP}}{\partial A_{base}} = -\frac{q_{TS}}{A_{base}^2 \cdot (\bar{t}_{wall} - \bar{t}_{sat})} \tag{5.37}$$

$$\frac{\partial HTC_{TP}}{\partial \bar{t}_{wall}} = -\frac{q_{TS}}{A_{base} \cdot (\bar{t}_{wall} - \bar{t}_{sat})^2} \tag{5.38}$$

$$\frac{\partial HTC_{TP}}{\partial \bar{t}_{sat}} = \frac{q_{TS}}{A_{base} \cdot (\bar{t}_{wall} - \bar{t}_{sat})^2} \tag{5.39}$$

Thus, the uncertainty on the two-phase heat transfer coefficient can estimated as follows:

$$i_{HTC_{TP}} = \sqrt{\left(\frac{\partial HTC_{TP}}{\partial q_{TS}} i_{q_{TS}}\right)^2 + \left(\frac{\partial HTC_{TP}}{\partial A_{base}} i_{A_{base}}\right)^2 + \left(\frac{\partial HTC_{TP}}{\partial \bar{t}_{wall}} i_{\bar{t}_{wall}}\right)^2 + \left(\frac{\partial HTC_{TP}}{\partial \bar{t}_{sat}} i_{\bar{t}_{sat}}\right)^2} \tag{5.40}$$

The uncertainty on the mean wall temperature and on the mean saturation temperature can be calculated as:

$$i_{\bar{t}_{wall}} = \frac{\sqrt{20}}{20} \cdot i_{t_{wall,i}} \tag{5.41}$$

$$i_{\bar{t}_{sat}} = \frac{\sqrt{2}}{2} \cdot i_{t_{sat,i}} \tag{5.42}$$

From the above analysis, the mean uncertainty on the two-phase heat transfer coefficient, calculated with the instruments accuracy reported in chapter 4 and considering an uncertainty of 1% for the values calculated with Refprop 9.1 [94], is 4.0%.

5.3.5 Uncertainty on the single-phase heat transfer coefficient

Deriving equation 5.10:

$$\frac{\partial HTC_{SP}}{\partial q_{TS}} = \frac{1}{A_{base} \cdot \Delta T_{ml}} \tag{5.43}$$

$$\frac{\partial HTC_{SP}}{\partial A_{base}} = -\frac{q_{TS}}{A_{base}^2 \cdot \Delta T_{ml}} \tag{5.44}$$

$$\frac{\partial HTC_{SP}}{\partial \Delta T_{ml}} = -\frac{q_{TS}}{A_{base} \cdot \Delta T_{ml}^2} \tag{5.45}$$

Thus, the uncertainty on the single-phase heat transfer coefficient can estimated as follows:

$$i_{HTC_{SP}} = \sqrt{\left(\frac{\partial HTC_{SP}}{\partial q_{TS}} i_{q_{TS}}\right)^2 + \left(\frac{\partial HTC_{SP}}{\partial A_{base}} i_{A_{base}}\right)^2 + \left(\frac{\partial HTC_{SP}}{\partial \Delta T_{ml}} i_{\Delta T_{ml}}\right)^2} \tag{5.46}$$

The logarithmic mean difference temperature can be defined as:

$$\Delta T_{ml} = \frac{\Delta_2 - \Delta_1}{\ln \frac{\Delta_2}{\Delta_1}} \tag{5.47}$$

and in this case:

$$\Delta_1 = t_{wall,in} - t_{sat,in} \tag{5.48}$$

$$\Delta_2 = t_{wall,out} - t_{sat,out} \tag{5.49}$$

Deriving:

$$\frac{\partial \Delta_1}{\partial t_{wall,in}} = \frac{\partial \Delta_2}{\partial t_{wall,out}} = 1 \tag{5.50}$$

$$\frac{\partial \Delta_1}{\partial t_{sat,in}} = \frac{\partial \Delta_2}{\partial t_{sat,out}} = -1 \tag{5.51}$$

and thus the uncertainties on Δ_1 e Δ_2 can be estimated as:

$$i_{\Delta_1} = \sqrt{\left(\frac{\partial \Delta_1}{\partial t_{wall,in}} i_{t_{wall,in}}\right)^2 + \left(\frac{\partial \Delta_1}{\partial t_{sat,in}} i_{t_{sat,in}}\right)^2} \tag{5.52}$$

$$i_{\Delta_2} = \sqrt{\left(\frac{\partial \Delta_2}{\partial t_{wall,out}} i_{t_{wall,out}}\right)^2 + \left(\frac{\partial \Delta_2}{\partial t_{sat,out}} i_{t_{sat,out}}\right)^2} \tag{5.53}$$

The sensitivity terms of ΔT_{ml} are:

$$\frac{\partial \Delta T_{ml}}{\partial \Delta_1} = \frac{\left(\frac{\Delta_2 - \Delta_1}{\Delta_1}\right) - \ln \frac{\Delta_2}{\Delta_1}}{\left(\ln \frac{\Delta_2}{\Delta_1}\right)^2} \tag{5.54}$$

$$\frac{\partial \Delta T_{ml}}{\partial \Delta_2} = \frac{\left(\frac{\Delta_1 - \Delta_2}{\Delta_2}\right) + \ln \frac{\Delta_2}{\Delta_1}}{\left(\ln \frac{\Delta_2}{\Delta_1}\right)^2} \tag{5.55}$$

Therefore, the uncertainty on the logarithmic mean temperature difference can be estimated with:

$$i_{\Delta T_{ml}} = \sqrt{\left(\frac{\partial \Delta T_{ml}}{\partial \Delta_1} i_{\Delta_1}\right)^2 + \left(\frac{\partial \Delta T_{ml}}{\partial \Delta_2} i_{\Delta_2}\right)^2} \tag{5.56}$$

From the above analysis, the mean uncertainty on the single-phase heat transfer coefficient, calculated with the instruments accuracy reported in chapter 4 and considering an uncertainty of 1% for the values calculated with Refprop 9.1 [94], is 1.7%.

5.4 Experimental results

The experimental measurements were carried out keeping constant the saturation temperature at the inlet of the test section at 30 °C, which can be considered suitable for the case of electronic cooling as well as for other applications, such as: high temperature heat pumps, heat exchangers for chemical industry, etc. The tests investigated the effects of different parameters: refrigerant mass velocity from 50 to 200 kg m^{-2} s^{-1}, vapour quality from 0.20 to 0.95, and heat flux from 50 to 100 kW m^{-2} on the single-phase (liquid) and flow boiling of refrigerants inside a 5 PPI copper foam. Three different refrigerants were tested: HFC-134a, HFO-1234ze(E), and HFO-1234yf. Due to their low Global Warming Potential, R1234ze(E) (GWP=6) and R1234yf (GWP=4) are possible substitutes of R134a, whose GWP is 1300.

5.4.1 The copper foam

A picture of the tested metal foam is reported in figure 5.2, while table 5.1 lists its major characteristics, where a_{sv} represents the surface area per unit of volume. It is made by copper, it is 10 mm wide, 5 mm high, and 200 mm long, it has 5 PPI and a porosity ε of 0.93; it was brazed over a 200×10×10 mm of copper plate. As shown in figure 5.2, 20 holes (5 mm deep) were drilled under the foam-wall brazing surface to monitor the wall temperature distribution by locating as many calibrated T-type thermocouples. The top wall consists of a 19 mm high tempered glass positioned over the test section, in order to visualize and record the flow boiling mechanism occurring inside the sample.

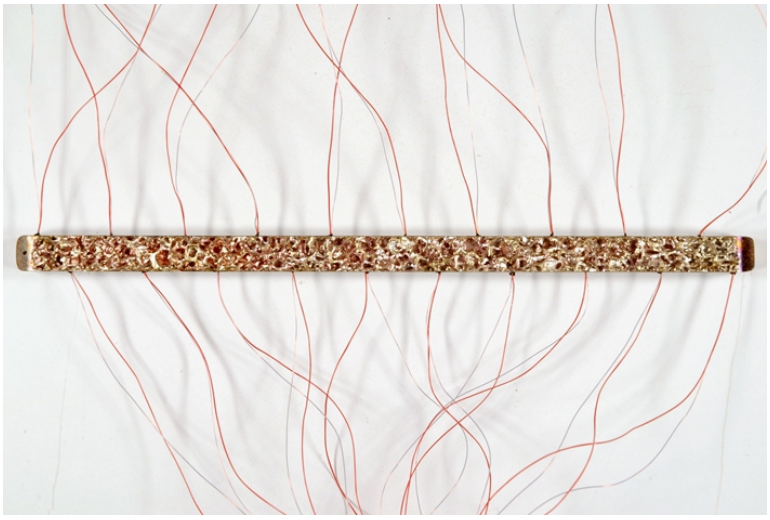

Figure 5.2: Top view of the 5 PPI copper foam sample equipped with 20 T-type thermocouples.

Table 5.1: Major geometrical characteristics of the copper foam sample.

Type	PPI [in^{-1}]	ε [-]	Fiber thickness [mm]	Fiber length [mm]	a_{sv} [m^2 m^{-3}]
Cu-5-7.0	5	0.93	0.588	2.049	310

5.4.2 R134a

Single-phase results

Figures 5.3 and 5.4 show the heat transfer coefficient and the pressure gradient values measured during single-phase liquid flow of R134a inside the tested foam sample. The measurements were carried out keeping the subcooling at the inlet of the test section at least greater than 15 °C, as compared to a saturation temperature of around 40 °C. Experimental measurements were also run at different subcoolings but no differences in the experimental results were found. The refrigerant mass velocity was varied between $G = 30$ kg m^{-2} s^{-1} and $G = 225$ kg m^{-2} s^{-1}. According to the results, both the heat transfer coefficient and the pressure gradient increase with the refrigerant mass flow rate. In particular, the heat transfer coefficient is around 4000 W m^{-2} K^{-1}, 5000 W m^{-2} K^{-1}, and 7100 W m^{-2} K^{-1} at 50 kg m^{-2} s^{-1}, 100 kg m^{-2} s^{-1}, and 200 kg m^{-2} s^{-1}, respectively. The pressure gradient is around 0.016 bar m^{-1}, 0.03 bar m^{-1}, and 0.10 bar m^{-1} at 50 kg m^{-2} s^{-1}, 100 kg m^{-2} s^{-1}, and 200 kg m^{-2} s^{-1}, respectively.

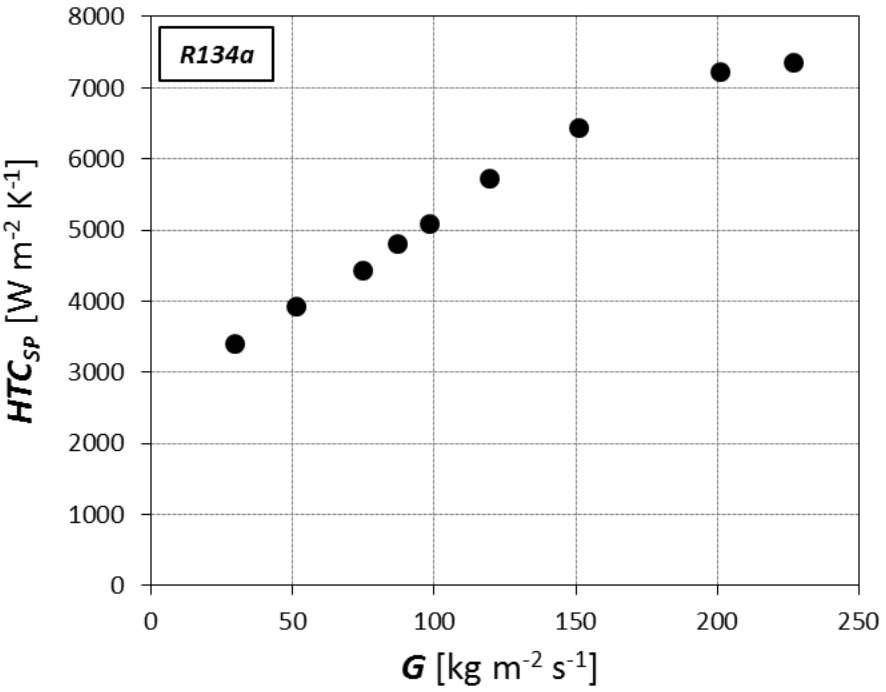

Figure 5.3: R134a single-phase heat transfer coefficient plotted against the mass velocity.

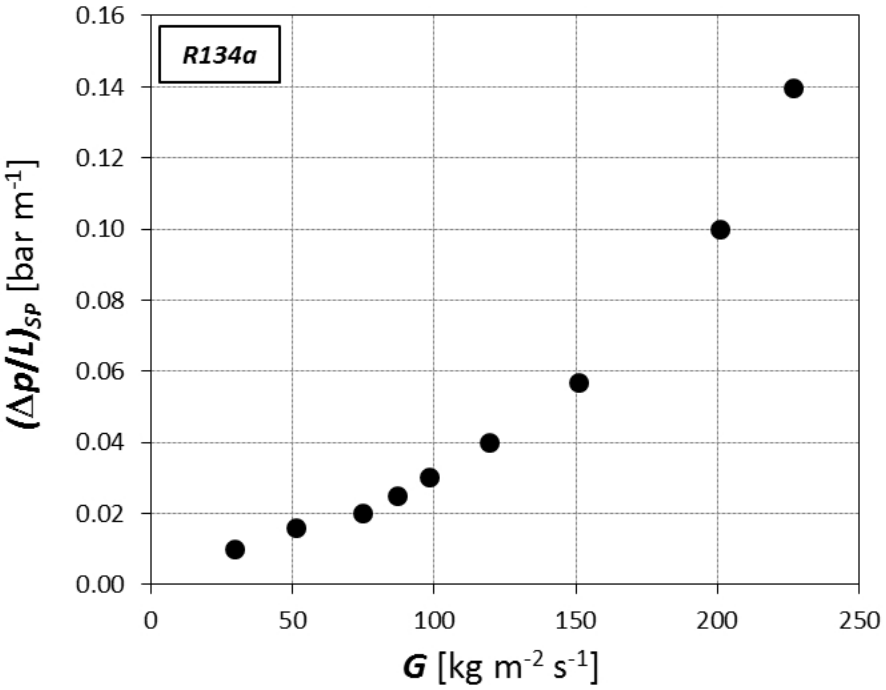

Figure 5.4: R134a single-phase pressure gradient plotted against the mass velocity.

Two-phase results

Figure 5.5 shows the effect of the refrigerant mass velocity on the two-phase flow boiling heat transfer coefficient at constant heat flux of 50 kW m^{-2}. Tests have also been run at 75 kg m^{-2} s^{-1} but the heat transfer coefficient felt over those measured at 100 kg m^{-2} s^{-1}, thus, for the sake of clarity, their graphical representation is avoided. First of all, at all the investigated mass velocities, the flow boiling heat transfer coefficient increases as the vapour quality increases up to around $x = 0.75 - 0.77$, then it suddenly decreases because the dryout phenomenon occurs. The apexes of the heat transfer coefficient curves highlight the vapour quality values at the onset of the dryout. The criterion selected for the determination of the value of the vapour quality at the onset of the dryout was taken according to that suggested by Wojtan et al. [102]. At low vapour quality, 50 and 100 kg m^{-2} s^{-1} exhibit similar heat transfer coefficients values; then, at higher vapour quality, the values measured at 100 kg m^{-2} s^{-1} are higher than those obtained at 50 kg m^{-2} s^{-1}. The effect of the mass flow rate is evident when mass velocity varies from 100 kg m^{-2} s^{-1}

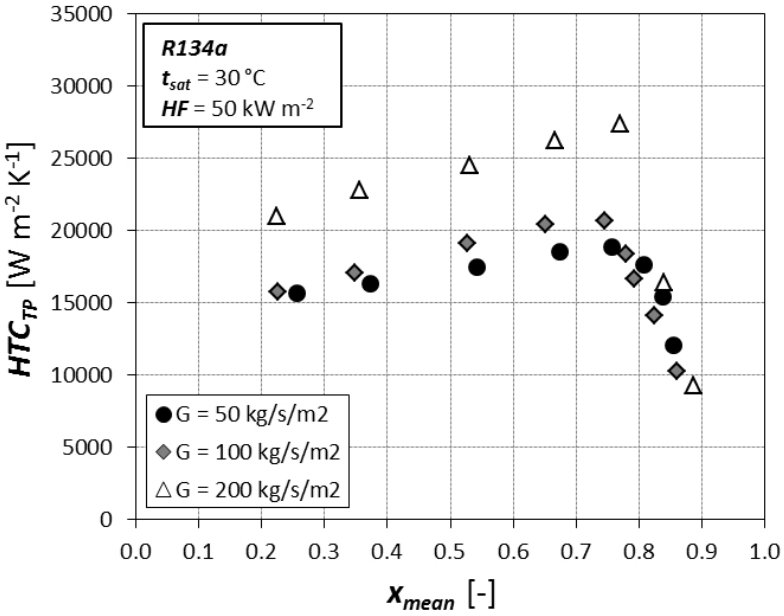

Figure 5.5: R134a two phase heat transfer coefficient as a function of the mean vapor quality at constant heat flux HF=50 kW m^{-2}.

to 200 kg m^{-2} s^{-1}: the heat transfer coefficient increases by about 30%. This behavior can be explained considering the stochastic structure of the metal foam, which enhances the mixing process during flow boiling, especially at high mass velocity. From these experimental results, it seems that nucleate boiling dominates the phase change process up to 100 kg m^{-2} s^{-1}; at higher mass velocity, forced convection starts to enhance the mixing capabilities of the metal foam and the heat transfer coefficient also increases. Moreover, at vapour quality greater than 0.75-0.77 with developed dryout phenomenon, all the mass fluxes are characterized by similar heat transfer coefficient values which exhibit the same slope of the trend profile.

The effects of the refrigerant mass flux on the heat transfer coefficient at constant heat flux of 100 kW m^{-2} are plotted in figure 5.6. As previously described, also in this case at all the investigated mass velocities, the flow boiling heat transfer coefficient increases with increasing vapour quality up to around $x = 0.66 - 0.72$, then it suddenly decreases because the dryout phenomenon occurs. In this case, the increase of the heat transfer coefficient with increasing vapour is less evident than the case at $HF = 50$ kW m^{-2}. It is worthy to underline that 50 kg m^{-2} s^{-1}

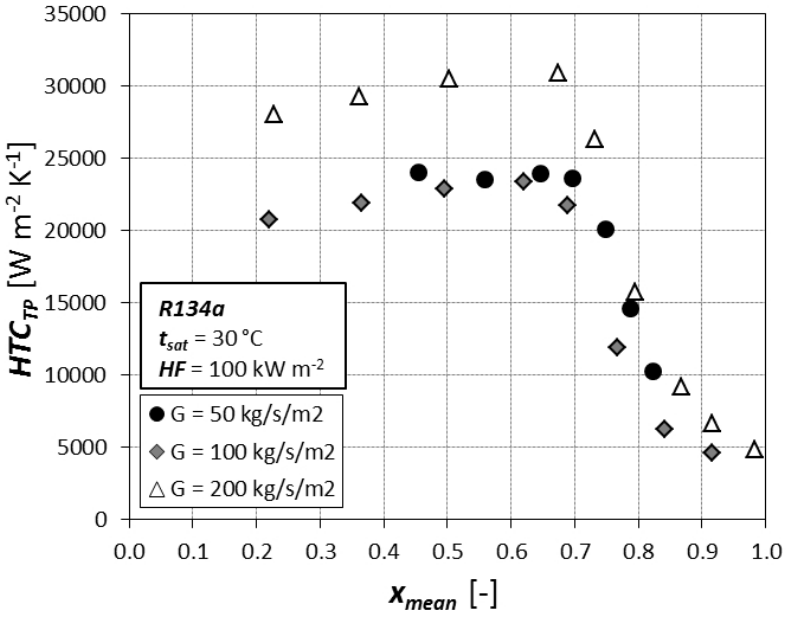

Figure 5.6: R134a two phase heat transfer coefficient as a function of the mean vapor quality at constant heat flux HF=100 kW m^{-2}.

and 100 kg m^{-2} s^{-1} exhibit similar values of heat transfer coefficient at all vapour qualities. The effect of the mass flow rate is again evident when mass velocity varies from 100 kg m^{-2} s^{-1} to 200 kg m^{-2} s^{-1}.

The two-phase flow pattern visualizations permit to explain this behaviour; three different images associated to videos recorded at different refrigerant mass velocity, keeping constant the heat flux at $HF = 100$ kW m^{-2} and inlet vapour quality of 0.5, are reported in figure 5.7. They permit to clarify the effects of the foam structure on the phase change process. The videos were recorded by means of a high speed B/W Phantom v9.1 video camera positioned on the top of the test section. Figure 5.7a shows the phase change process at $G = 50$ kg m^{-2} s^{-1}. At these operating conditions, the refrigerant does not fill the channel, it flows in a stratified-like flow, the nucleate boiling controls the vaporization process and the foam structure only helps in mixing the bubble nucleated on the surface avoiding any coalescence process. This analysis confirms what highlighted in figure 5.6, where the heat transfer coefficient is weakly affected by the vapour quality, especially for the refrigerant mass velocity of 50 kg m^{-2} s^{-1}. When increasing the refrigerant

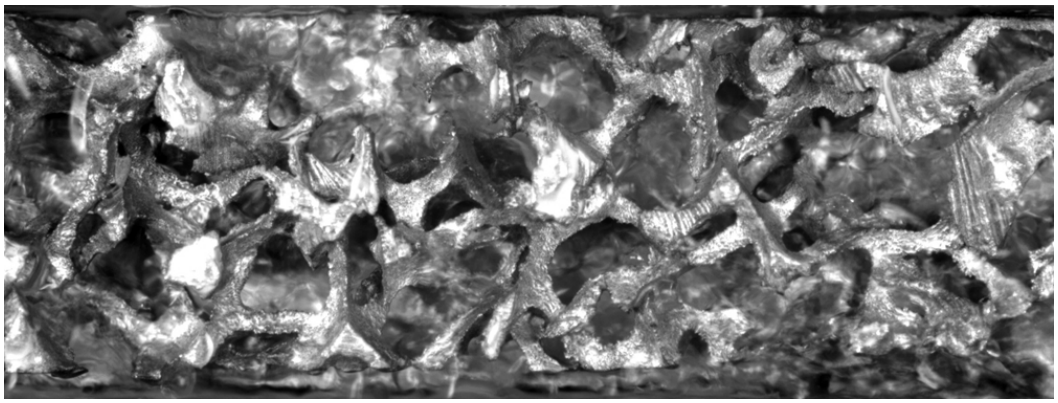

(a) G=50 kg m^{-2} s^{-1}; x=0.50; HF=100 kW m^{-2}

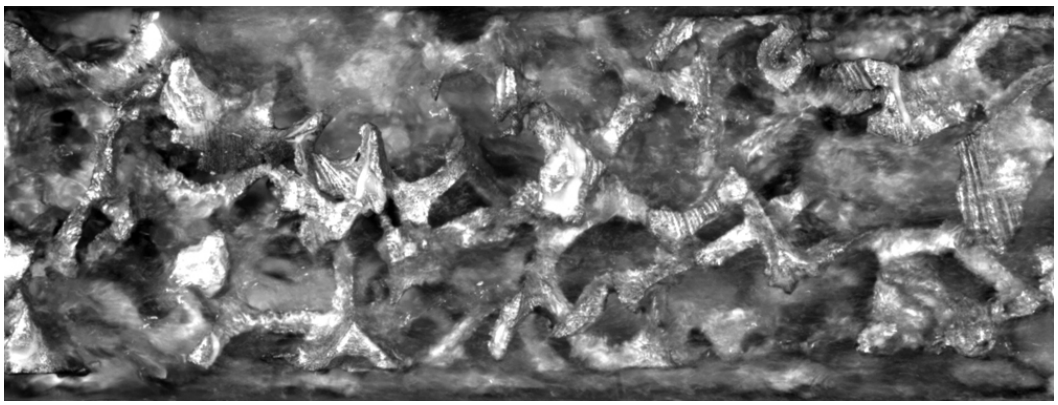

(b) G=100 kg m^{-2} s^{-1}; x=0.50; HF=100 kW m^{-2}

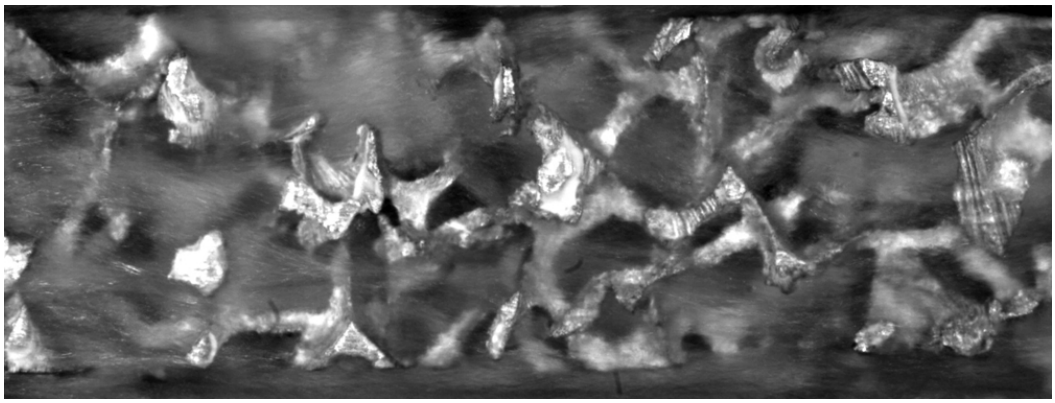

(c) G=200 kg m^{-2} s^{-1}; x=0.50; HF=100 kW m^{-2}

Figure 5.7: Effect of the refrigerant mass velocity on the two-phase flow of R134a at constant inlet vapour quality and heat flux.

mass velocity to $G = 100$ kg m^{-2} s^{-1} (figure 5.7b), even if the channel still remains not completely filled by the refrigerant, some liquid entrainment caused by the vapour shear through the foam fibers starts to be visible but it is no sufficient to overtake the nucleate boiling and the heat transfer coefficients remain almost the same measured at $G = 50$ kg m^{-2} s^{-1}, even if they increase with the vapour quality. The mixing effects of the foam structure associated to the high shear stress due to vapour velocity are clearly highlighted in the third image (figure 5.7c) taken at $G = 200$ kg m^{-2} s^{-1}. Liquid and vapour are highly mixed and the fluid streams are deviated by the fibers of the foam through a tortuous path; in this way the convective contribute is extremely enhanced and it actively participates to the phase change process.

Figure 5.8 shows the effect of the imposed heat flux on the two-phase heat transfer coefficient as a function of the mean vapour quality at a fixed mass velocity $G =$ 50 kg m^{-2} s^{-1}. At first sight, the heat transfer coefficient increases as the imposed heat flux increases. The heat transfer coefficient increases when increasing the mean vapour quality passing from 15000 W m^{-2} K^{-1} to around 20000 W m^{-2} K^{-1}, then it

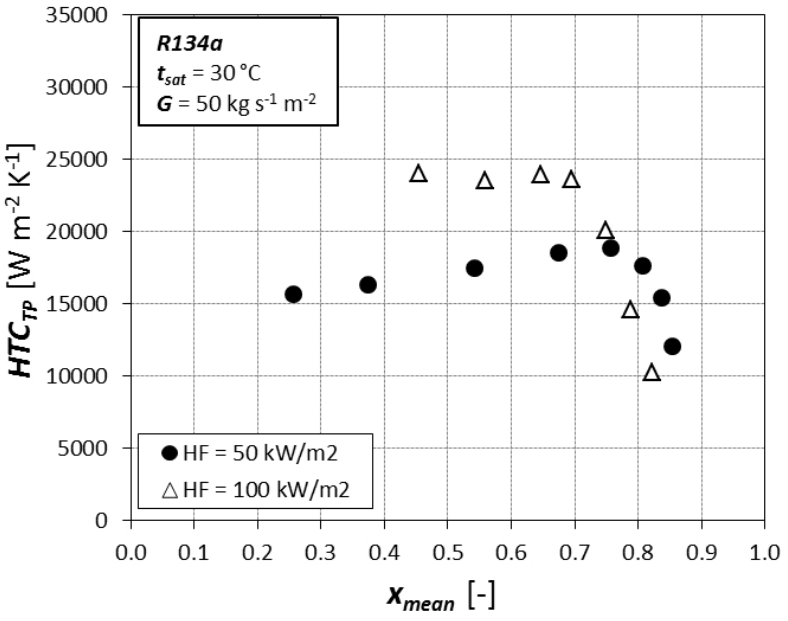

Figure 5.8: R134a two phase heat transfer coefficient as a function of the mean vapor quality at constant mass velocity G=50 kg m^{-2} s^{-1}.

suddenly decrease because the dryout phenomenon occurs. When increasing the heat flux to $HF = 100$ kW m^{-2}, the two-phase heat transfer coefficients are greater than those measured at $HF = 50$ kW m^{-2}, but their values are almost constant, around 24000 W m^{-2} K^{-1}, up to the vapour quality at the onset of the dryout, around 0.7, and then they decrease. Two different behaviours are clearly highlighted, which can be linked to the two major competitive heat transfer mechanisms that control the phase change process: nucleate boiling and two-phase forced convection. At $HF = 50$ kW m^{-2}, the heat transfer coefficient increases with the vapour quality, meaning that two-phase forced convection plays a non-negligible role in the phase change process. At $HF = 100$ kW m^{-2}, the heat transfer coefficient is almost constant; in this case the nucleate boiling seems to dominate the vaporization process.

A direct explanation of the heat transfer behaviour during the phase change phenomenon at $G = 50$ kg m^{-2} s^{-1} is given by two videos associated to the images reported in figure 5.9. The first image was taken at $HF = 50$ kW m^{-2}, and it appears that the two-phase mixture does not fill the entire channel and some small bubbles come out from the heated surface between the fibers. The nucleate boiling is enhanced at $HF = 100$ kW m^{-2}, when some big bubbles grow up between the fibers, and they are then broken up by the foam structure.

Figure 5.10 reports the results carried out at $G = 100$ kg m^{-2} s^{-1} as a function of the heat flux. Again, the heat transfer coefficient increases with both vapour quality and heat flux. For instance, at x_{mean}=0.50, the heat transfer coefficient is equal to around 19000 and 22900 W m^{-2} K^{-1} at 50 and 100 kW m^{-2}, respectively. In this case, the nucleate boiling and the two-phase forced convection mechanisms seem to be combined rather than competitive. As already shown, the vapur quality at the onset of dryout decreases as the imposed heat flux increases, passing from 0.76 to 0.67, when the heat flux goes from $HF = 50$ kW m^{-2} to $HF = 100$ kW m^{-2}.

Finally, the results proposed in figure 5.11, measured at $G = 200$ kg m^{-2} s^{-1}, confirm those highlighted at $G = 100$ kg m^{-2} s^{-1}; the heat transfer coefficient increases with both vapour quality and heat flux. The vapour quality at the onset of the dryout decreases as the heat flux increases passing from 0.77 to 0.70.

In summary, at $G = 50$ kg m^{-2} s^{-1} the two-phase heat transfer mechanisms, nucleate boiling and two-phase forced convection, seem to be competitive, while at higher mass velocities, their effects seem to be combined allowing a much more

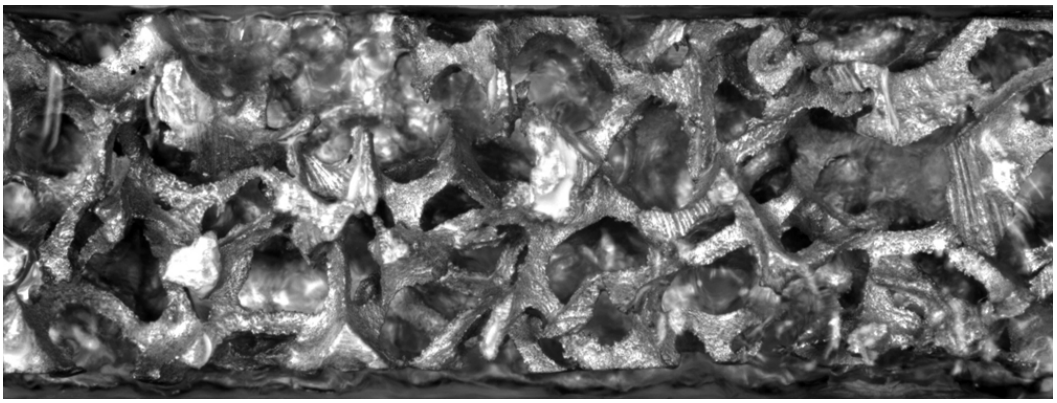

(a) G=50 kg m^{-2} s^{-1}; x=0.50; HF=50 kW m^{-2}

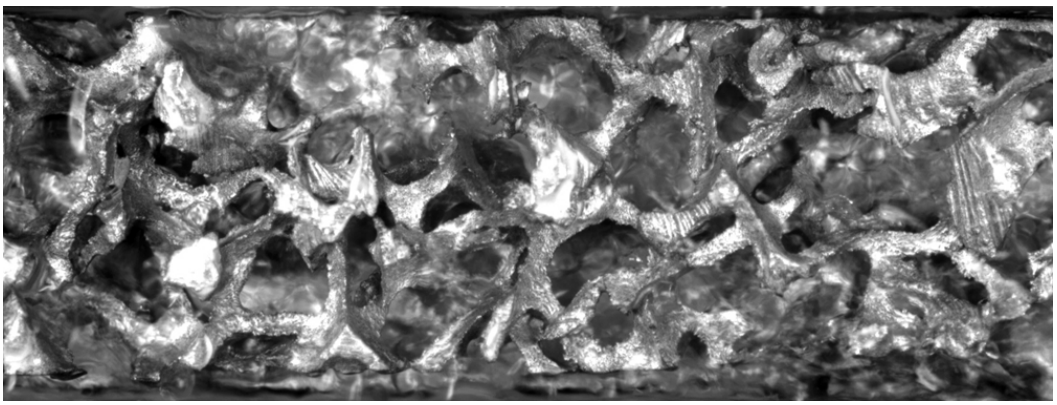

(b) G=50 kg m^{-2} s^{-1}; x=0.50; HF=100 kW m^{-2}

Figure 5.9: Effect of the heat flux on the two-phase flow of R134a at constant inlet vapour quality and mass velocity.

efficient heat transfer process.

Figure 5.12 shows the total two phase pressure gradient plotted against the mean vapor quality as a function of mass velocity; as expected, at constant mass velocity, pressure drop increases as vapor quality increases; furthermore, keeping constant the vapor quality, it increases when increasing mass velocity.

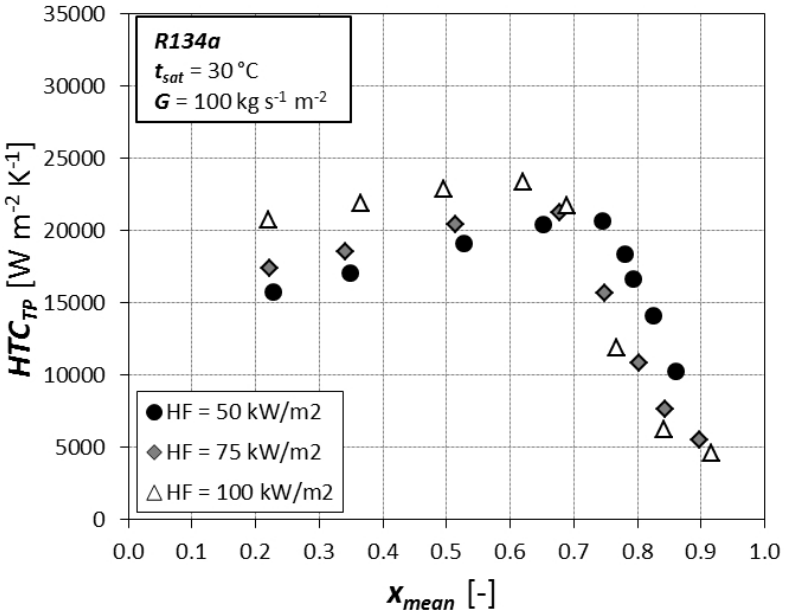

Figure 5.10: R134a two phase heat transfer coefficient as a function of the mean vapor quality at constant mass velocity G=100 kg m^{-2} s^{-1}.

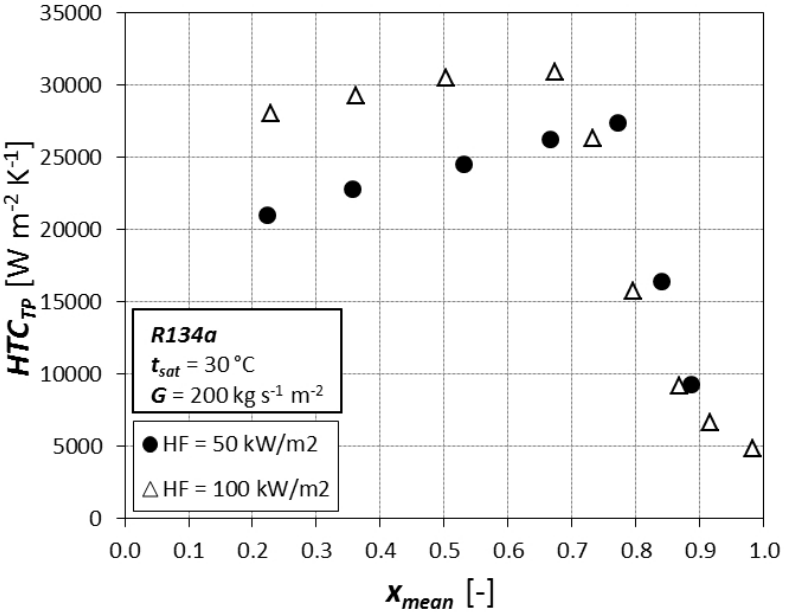

Figure 5.11: R134a two phase heat transfer coefficient as a function of the mean vapor quality at constant mass velocity G=200 kg m^{-2} s^{-1}.

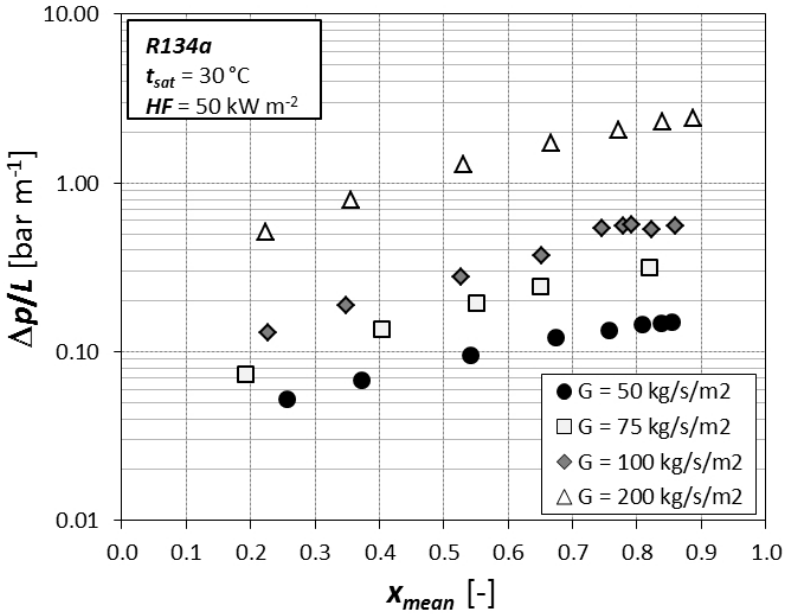

Figure 5.12: R134a total two-phase pressure gradient plotted against mean vapour quality as a function of mass velocity.

5.4.3 R1234ze(E)

Single-phase results

Figures 5.13 and 5.14 shows the heat transfer coefficient and the pressure gradient values measured during single-phase liquid flow of R1234ze(E) inside the tested foam sample. The measurements were carried out keeping the subcooling at the inlet of the test section at least greater than 15 °C, as compared to a saturation temperature of around 40 °C. The refrigerant mass velocity was varied between $G = 50$ kg m^{-2} s^{-1} and $G = 225$ kg m^{-2} s^{-1}. According to the results, both the heat transfer and the pressure gradient increase with the refrigerant mass flow rate. In particular, the heat transfer coefficient is around 3800 W m^{-2} K^{-1}, 5400 W m^{-2} K^{-1}, and 7250 W m^{-2} K^{-1} at 50 kg m^{-2} s^{-1}, 100 kg m^{-2} s^{-1}, and 200 kg m^{-2} s^{-1}, respectively. The pressure gradient is around 0.02 bar m^{-1}, 0.04 bar m^{-1}, and 0.11 bar m^{-1} at 50 kg m^{-2} s^{-1}, 100 kg m^{-2} s^{-1}, and 200 kg m^{-2} s^{-1}, respectively.

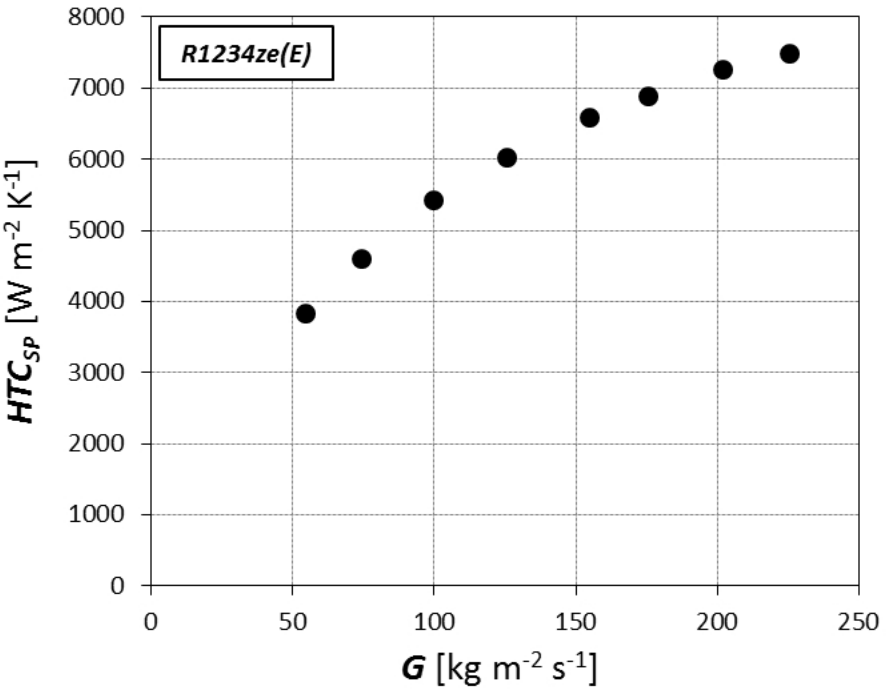

Figure 5.13: R1234ze(E) single-phase heat transfer coefficient plotted against the mass velocity.

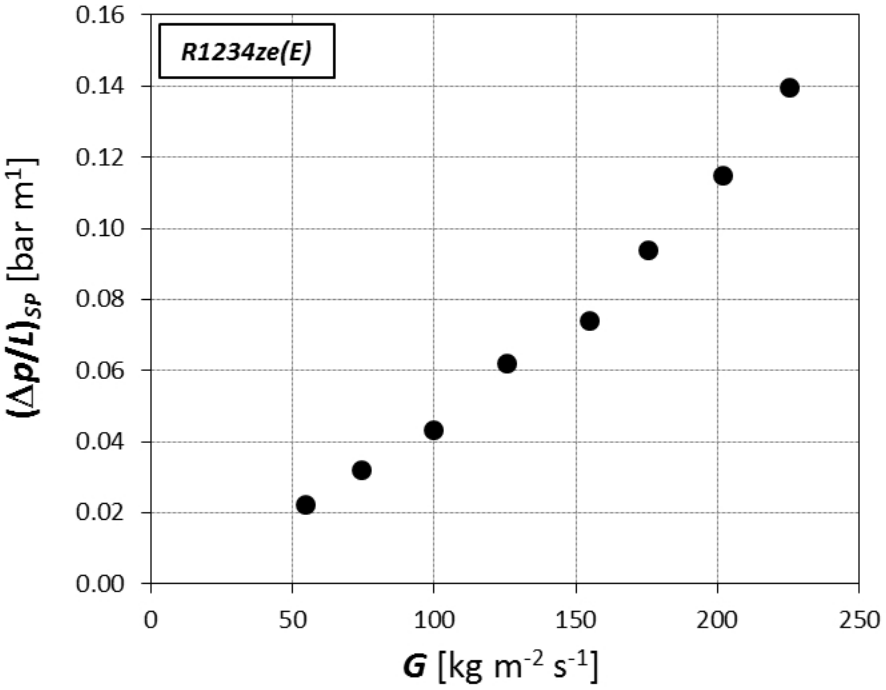

Figure 5.14: R1234ze(E) single-phase pressure gradient plotted against the mass velocity.

Two-phase results

Figure 5.15 shows the effect of the refrigerant mass velocity on the two-phase flow boiling heat transfer coefficient at constant heat flux of 50 kW m^{-2}. Tests have also been run at 75 kg m^{-2} s^{-1} but the heat transfer coefficient felt over those measured at 50 kg m^{-2} s^{-1}, thus their graphical representation is avoided. The HTC_{TP} increases as the vapour quality increases and seems to be independent on the mass flux up to 75 kg m^{-2} s^{-1}, meaning that the nucleate boiling dominates the phase change process. Then, HTC_{TP} increases with the refrigerant mass velocity, meaning that the two-phase forced convection is becoming more and more the dominant term of the phase change process. The critical vapour quality at the onset of the dryout seems not to depend on the mass velocity and it is almost constant ranging between 0.76 and 0.78. After this point, the HTC_{TP} suddenly decreases and all the mass velocities show similar trends of the measured values.

The effects of the refrigerant mass flux on the heat transfer coefficient at constant heat flux of 100 kW m^{-2} are plotted in figure 5.16. In this case, the HTC_{TP}

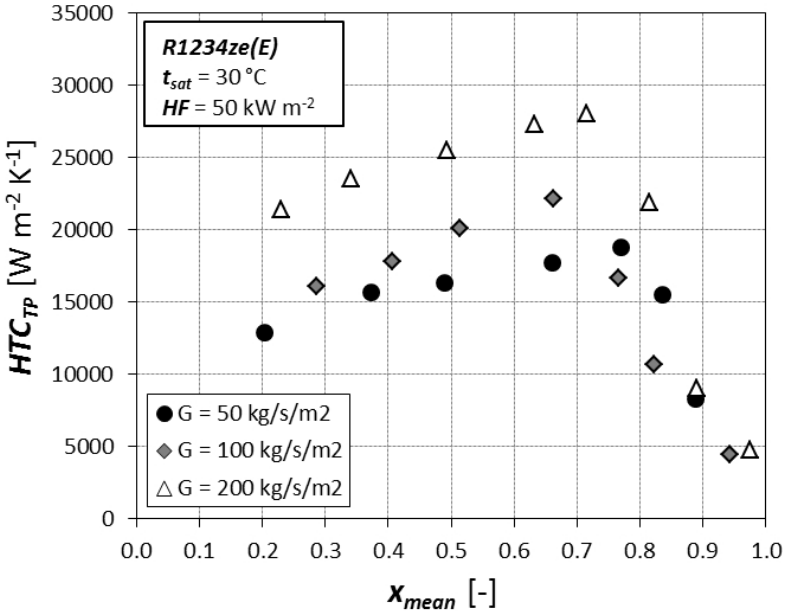

Figure 5.15: R1234ze(E) two phase heat transfer coefficient as a function of the mean vapor quality at constant heat flux HF=50 kW m^{-2} .

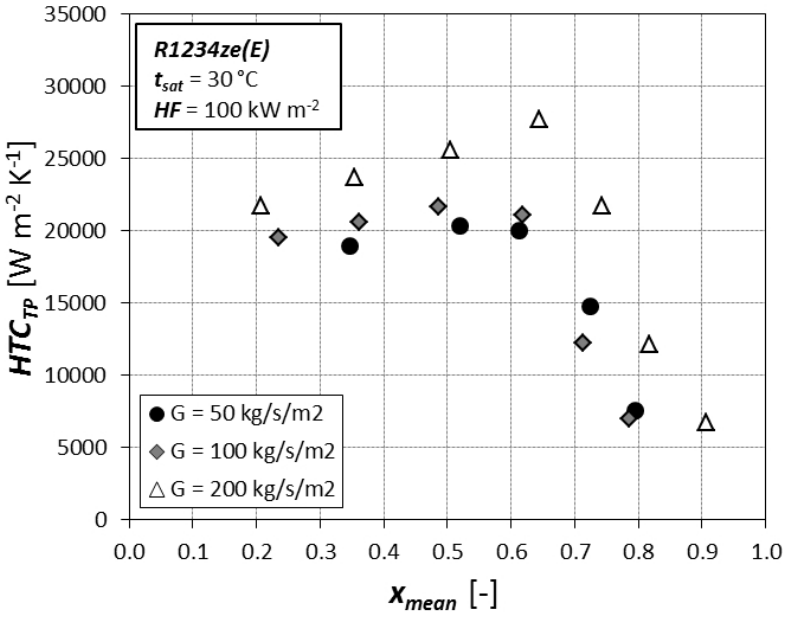

Figure 5.16: R1234ze(E) two phase heat transfer coefficient as a function of the mean vapor quality at constant heat flux HF=100 kW m^{-2} .

is weakly affected by the vapour quality at mass velocities of 50 kg m^{-2} s^{-1} and 100 kg m^{-2} s^{-1}, up to the onset of the dryout phenomenon, after which it decreases. Mass velocity $G = 100$ kg m^{-2} s^{-1} exhibits values of heat transfer coefficient slightly higher than those carried out at a mass velocity of 50 kg m^{-2} s^{-1} at all vapour qualities. The effect of the mass flow rate is again evident when mass velocity varies from 100 kg m^{-2} s^{-1} to 200 kg m^{-2} s^{-1}.

Images of the flow patterns with an imposed heat flux of $HF = 100$ kW m^{-2} are reported in figure 5.17. Figure 5.17a shows the phase change process at $G =$ 50 kg m^{-2} s^{-1}. As highlighted in the case of R134a, also for the R1234ze(E) the refrigerant does not fill the channel, but it flows on the bottom in a stratified-like flow, many bubbles come up from the heated surface and thus the nucleate boiling plays a relevant role during the vaporization process, while the foam structure helps in mixing the bubbles nucleated on the surface avoiding any coalescence process. As a result, the heat transfer coefficient is almost linear as the vapour quality increases, as shown in figure 5.16. Figure 5.17b reports an image taken from the video recorded at $G = 100$ kg m^{-2} s^{-1}. There is entrained liquid from the liquid-vapour interface which is spread and mixed by the foam structure. This behaviour enhances the two-phase forced convection and can explain the increasing of around 6-9% of the heat transfer coefficient when passing from 50 to 100 kg m^{-2} s^{-1}, which was not found in the case of R134a. In figure 5.17c, taken from the video at 200 kg m^{-2} s^{-1}, it clearly appears that liquid and vapour phases are highly mixed and the fluid streams are deviated by the foam structure through a tortuous path; the two-phase forced convection contribute is extremely enhanced, as also shown in figure 5.16.

Figure 5.18 shows the effect of the imposed heat flux on the two-phase heat transfer coefficient as a function of the mean vapour quality at a fixed mass velocity $G = 50$ kg m^{-2} s^{-1}. The two-phase heat transfer coefficient increases when increasing the heat flux for vapour quality lower than those at the onset of the dryout phenomenon. Considering the heat flux of 50 kW m^{-2}, HTC_{TP} increases with vapour quality from 13000 to 18800 W m^{-2} K^{-1}, up to a quality of approximately 0.80, when the onset of the dryout occurs. On the contrary, considering the heat flux of 100 kW m^{-2}, HTC_{TP} remains almost constant with increasing vapour quality at a value of about 20000 W m^{-2} K^{-1}, up to the onset of the dryout, which occurs at a lower vapour quality (0.7) than that of $HF = 50$ kW m^{-2}.

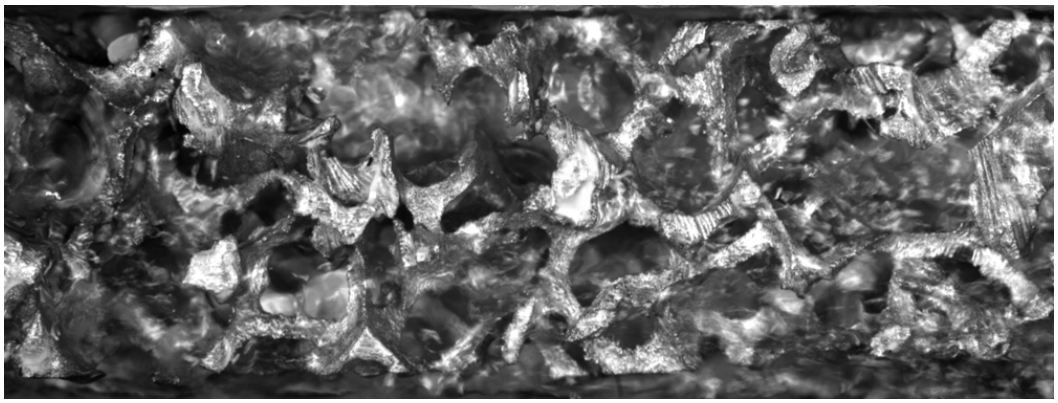

(a) G=50 kg m^{-2} s^{-1}; x=0.50; HF=100 kW m^{-2}

(b) G=100 kg m^{-2} s^{-1}; x=0.50; HF=100 kW m^{-2}

(c) G=200 kg m^{-2} s^{-1}; x=0.50; HF=100 kW m^{-2}

Figure 5.17: Effect of the refrigerant mass velocity on the two-phase flow of R1234ze(E) at constant inlet vapour quality and heat flux.

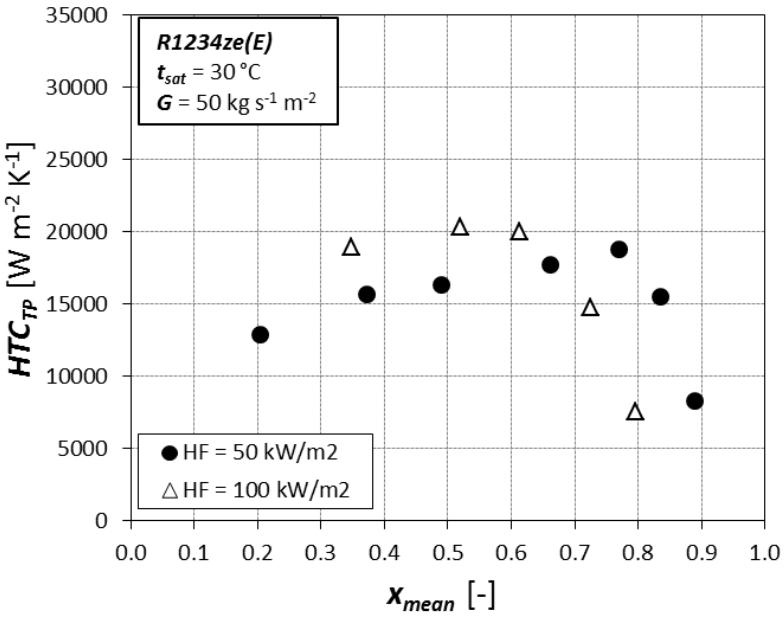

Figure 5.18: R1234ze(E) two phase heat transfer coefficient as a function of the mean vapor quality at constant mass velocity G=50 kg m^{-2} s^{-1}.

Figure 5.19 shows the effect of the heat flux at a fixed mass velocity of 100 kg m^{-2} s^{-1}. The two-phase heat transfer coefficient at heat fluxes $HF = 50$ kW m^{-2} and $HF = 75$ kW m^{-2} exhibit similar heat transfer coefficient prior to the onset of the dryout, and HTC_{TP} increases with increasing vapour quality for both heat fluxes. When increasing the heat flux to $HF = 100$ kW m^{-2}, the two-phase heat transfer coefficients are greater than those measured at $HF = 50$ kW m^{-2} and $HF = 75$ kW m^{-2}, but their values are almost constant at a value of around 20000 W m^{-2} K^{-1}, and then they suddenly decrease. The vapour quality at the onset of dryout is found to decrease when increasing the heat flux.

In the end, figure 5.20 shows the effect of the heat flux at a fixed mass velocity of 200 kg m^{-2} s^{-1}. In this case, the two-phase heat transfer coefficients at $HF = 50$ kW m^{-2} and $HF = 100$ kW m^{-2} exhibit similar values. However, the vapour quality at the onset of the dryout is higher at $HF = 50$ kW m^{-2} rather than at $HF = 100$ kW m^{-2}, being 0.75 and 0.65, respectively.

Figure 5.21 shows the total two phase pressure gradient plotted against the mean vapor quality as a function of mass velocity; as expected, at constant mass velocity,

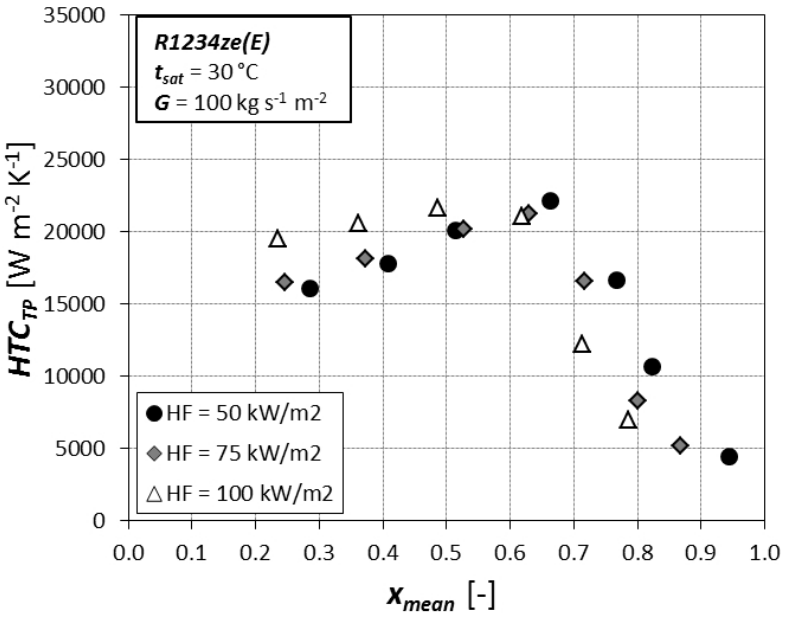

Figure 5.19: R1234ze(E) two phase heat transfer coefficient as a function of the mean vapor quality at constant mass velocity G=100 kg m^{-2} s^{-1}.

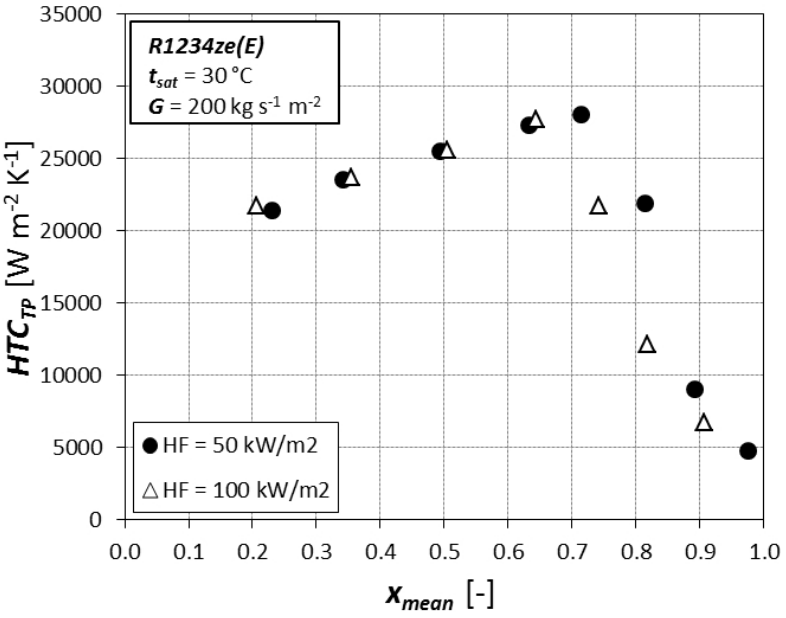

Figure 5.20: R1234ze(E) two phase heat transfer coefficient as a function of the mean vapor quality at constant mass velocity G=200 kg m^{-2} s^{-1}.

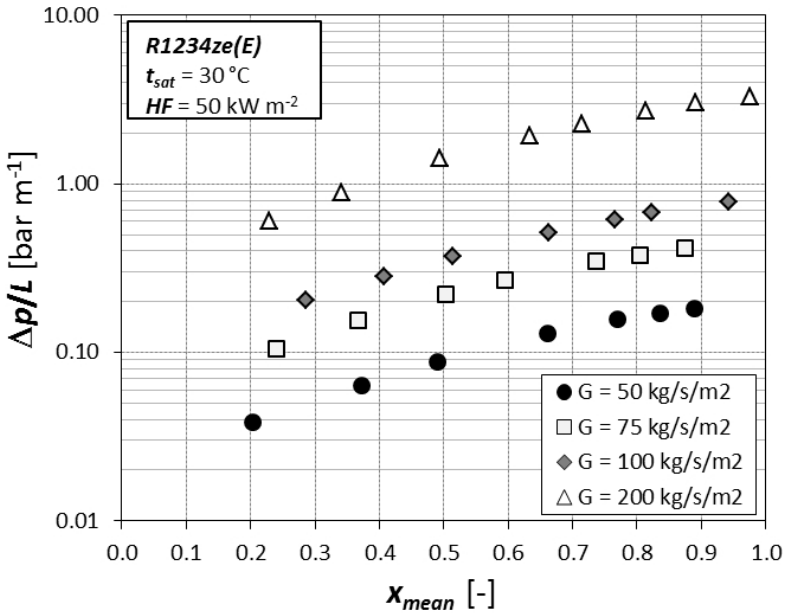

Figure 5.21: R1234ze(E) total two-phase pressure gradient plotted against mean vapour quality as a function of mass velocity.

pressure drop increases as vapor quality increases; furthermore, keeping constant the vapor quality, it increases when increasing mass velocity.

5.4.4 R1234yf

Two-phase results

Figure 5.22 shows the effect of the refrigerant mass velocity on the two-phase flow boiling heat transfer coefficient at constant heat flux of 50 kW m^{-2}. HTC_{TP} increases with vapour quality up to the onset of the dryout phenomenon, which occurs for vapour qualities between 0.7 and 0.8. Mass velocities of 50 and 100 kg m^{-2} s^{-1} exhibit similar values of two-phase heat transfer coefficient, meaning that the nucleate boiling dominates the phase change process. The effect of the mass velocity is evident when increasing from 100 to 200 kg m^{-2} s^{-1}, meaning that also two-phase forced convection starts to play an important role in the phase change process.

Figure 5.23 shows the effect of the imposed heat flux on the two-phase heat transfer coefficient as a function of the mean vapour quality at a fixed mass velocity

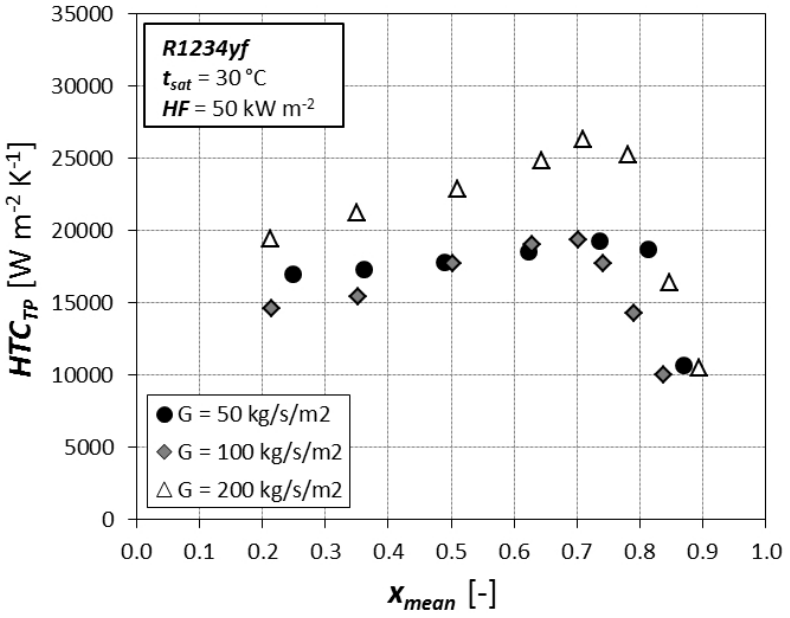

Figure 5.22: R1234yf two phase heat transfer coefficient as a function of the mean vapor quality at constant heat flux HF=50 kW m^{-2} .

$G = 50$ kg m^{-2} s^{-1}. Considering the results carried out with an imposed heat flux of 50 kW m^{-2}, the two-phase heat transfer coefficient slightly increases when increasing vapour quality from 17000 to 19500 W m^{-2} K^{-1}, up to the onset of the dryout quality, which occurs at a quality of about 0.75. On the other hand, heat transfer coefficients with an imposed heat flux of 100 kW m^{-2} are almost constant at a value of about 21000 W m^{-2} K^{-1}, meaning that the nucleate boiling seems to be the dominant heat transfer mechanism at higher heat fluxes. In the latter case, the onset of the dryout occurs at vapor quality of about 0.65, i.e. it occurs at lower vapour quality than that at 50 kW m^{-2}.

Figure 5.24 shows the effect of the imposed heat flux on the two-phase heat transfer coefficient as a function of the mean vapour quality at a fixed mass velocity $G = 100$ kg m^{-2} s^{-1}. The two-phase heat transfer coefficient increases with increasing vapour quality for both heat fluxes, up to then onset of the dryout phenomenon, which occurs at lower vapour quality in the case of heat flux $HF = 75$ kW m^{-2} than $HF = 50$ kW m^{-2}. The two phase heat transfer coefficient carried out at $HF = 75$ kW m^{-2} results higher than those at $HF = 50$ kW m^{-2}.

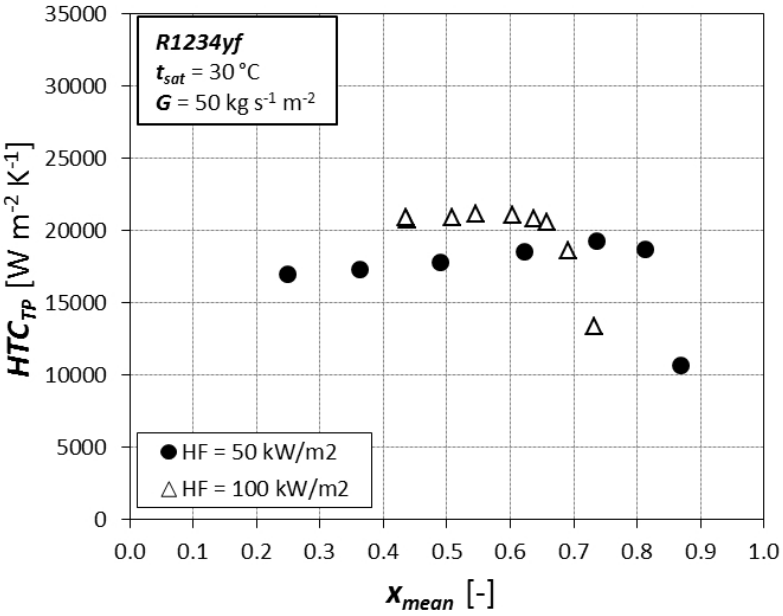

Figure 5.23: R1234yf two phase heat transfer coefficient as a function of the mean vapor quality at constant mass velocity G=50 kg m^{-2} s^{-1}.

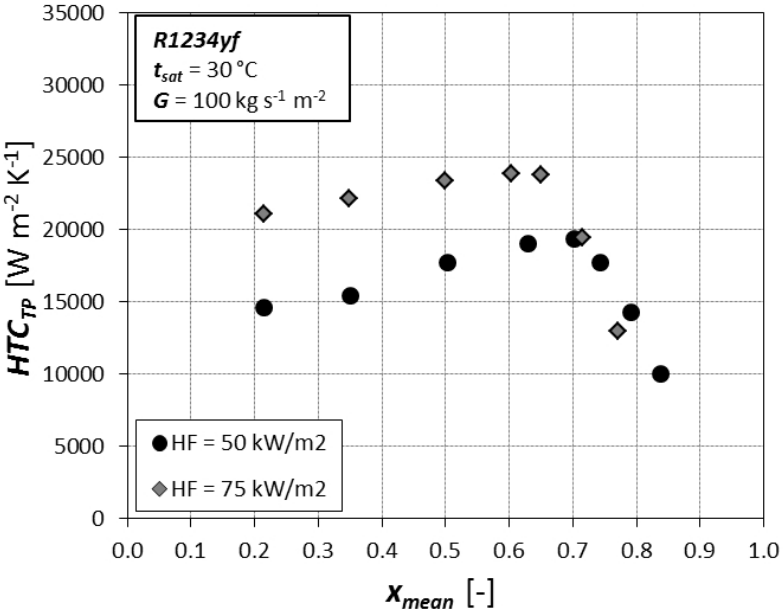

Figure 5.24: R1234yf two phase heat transfer coefficient as a function of the mean vapor quality at constant mass velocity G=100 kg m^{-2} s^{-1}.

Figure 5.25 shows the total two phase pressure gradient plotted against the mean vapor quality as a function of mass velocity; as expected, at constant mass velocity, pressure drop increases as vapor quality increases; furthermore, keeping constant the vapor quality, it increases when increasing mass velocity.

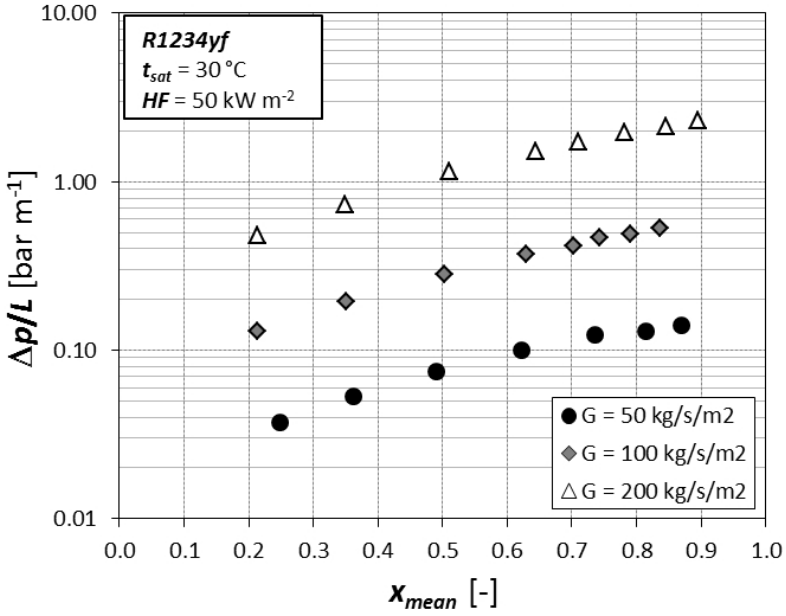

Figure 5.25: R1234yf total two-phase pressure gradient plotted against mean vapour quality as a function of mass velocity.

5.4.5 Comparison among different refrigerants

Table 5.2 reports thermophysical properties of the three tested refrigerants (R134a, R1234ze(E), and R1234yf) at 30 °C of saturation temperature.

Table 5.2: Major thermophysical properties of R134a, R1234ze(E), and R1234yf at 30 °C of saturation temperature. Data from Refprop 9.1 [94].

Property	R134a	R1234ze(E)	R1234yf
p_{sat} [bar]	7.70	5.78	7.84
p_{red} [-]	0.190	0.159	0.232
ρ_L [kg m^{-3}]	1188	1146	1073
ρ_V [kg m^{-3}]	37.5	30.5	43.7
$c_{p,L}$ [J kg^{-1} K^{-1}]	1447	1403	1417
$c_{p,V}$ [J kg^{-1} K^{-1}]	1066	999	1086
h_{LV} [kJ kg^{-1}]	173	163	141
λ_L [W m^{-1} K^{-1}]	0.079	0.073	0.062
λ_V [W m^{-1} K^{-1}]	0.014	0.014	0.014
μ_L [μPa s]	183	188	145
μ_V [μPa s]	11.9	12.5	11.3
$\mathrm{Pr_L}$ [-]	3.35	3.64	3.32
$\mathrm{Pr_V}$ [-]	0.88	0.89	0.86
σ [mN m^{-1}]	7.38	8.21	5.56
$(\mathrm{d}T/\mathrm{d}p)_{sat}$ [K bar^{-1}]	4.5	5.9	4.7

Single-phase comparison

Figures 5.26 and 5.27 present the comparisons between R134a and R1234ze(E) single-phase heat transfer coefficient and pressure gradient, respectively.

R134a and R1234ze(E) show similar values of single-phase heat transfer coefficient. This behaviour can be linked to the values of liquid dynamic viscosity and of

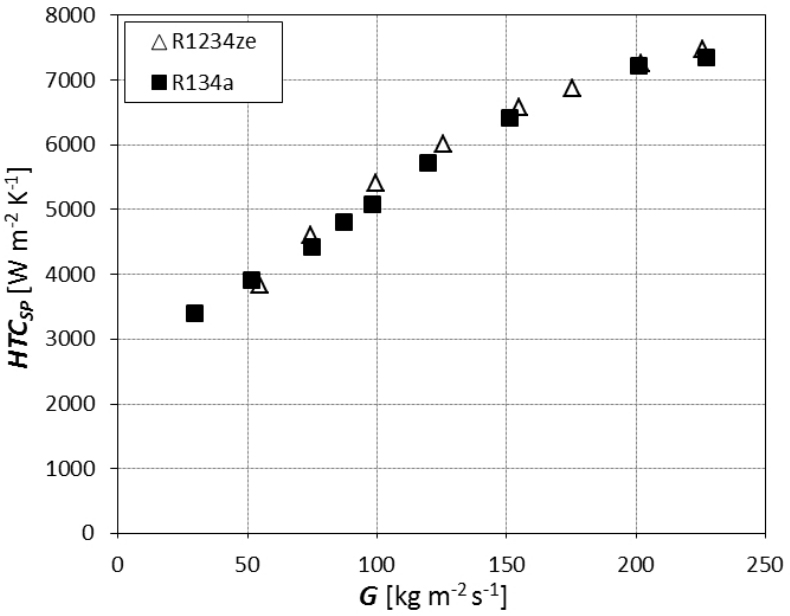

Figure 5.26: Comparison among R134a and R1234ze(E) single-phase heat transfer coefficient.

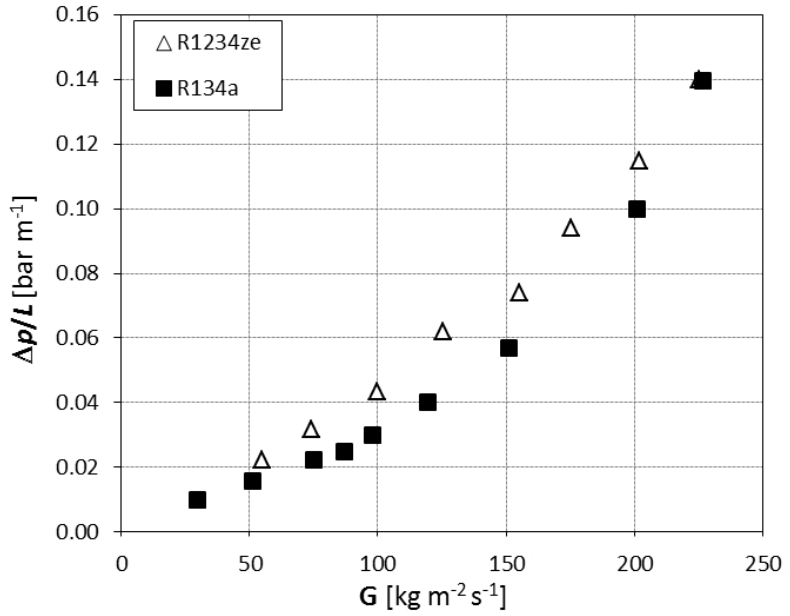

Figure 5.27: Comparison among R134a and R1234ze(E) single-phase pressure gradient.

Prandtl number, which, as it appears in table 5.2, are approximately the same. Considering the pressure gradient values, R1234ze(E) shows similar results, sometimes slightly higher, as compared to those measured for R134a.

Two-phase comparison

The following figures show comparisons between R134, R1234ze(E), and R1234yf two-phase heat transfer coefficients at constant mass velocity and heat flux.

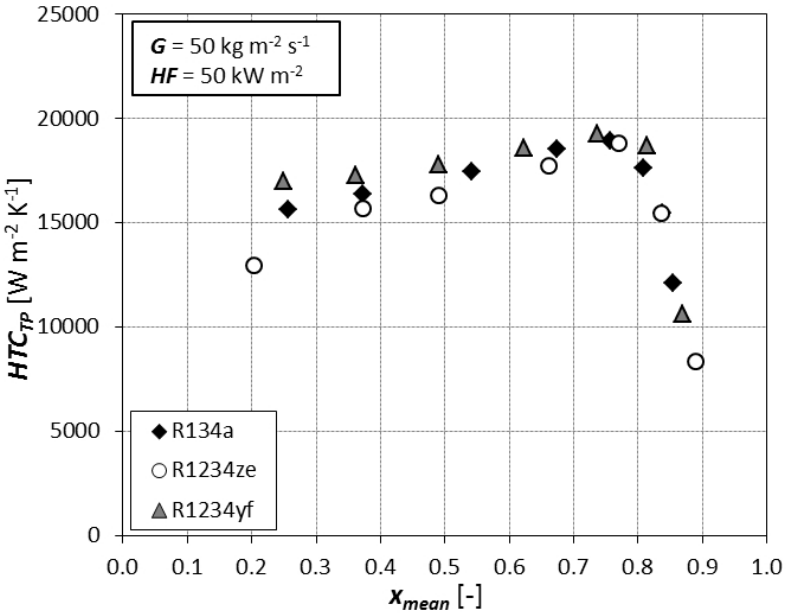

Figure 5.28: Comparison among R134a, R1234ze(E), and R1234yf two-phase heat transfer coefficient at G=50 kg m^{-2} s^{-1} and HF=50 kW m^{-2}.

For a fixed heat flux of 50 kW m^{-2}, no appreciable differences can be observed between the three refrigerants. This behaviour can be explained considering the thermophysical properties reported in table 5.2 and Chen's equation, reported in 4.1.2. At HF=50 kW m^{-2}, nucleate boiling and two-phase forced convection seem to coexist, rather than being competitive. Thus, even though R1234ze(E) might have a better performance in the two-phase forced convection due to its lower vapour density, which implies a higher vapour velocity at constant mass velocity than R134a and R1234yf, it has poorer nucleate boiling characteristics due to its lower reduced

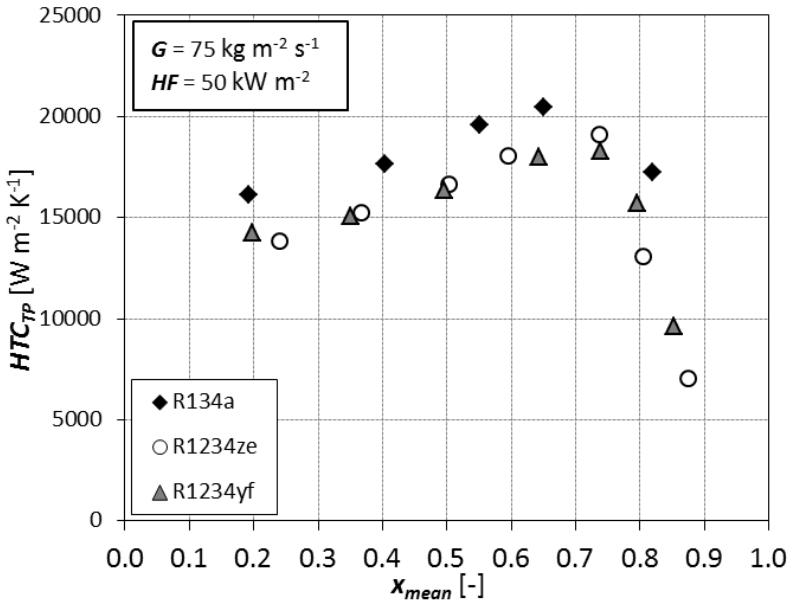

Figure 5.29: Comparison among R134a, R1234ze(E), and R1234yf two-phase heat transfer coefficient at G=75 kg m^{-2} s^{-1} and HF=50 kW m^{-2}.

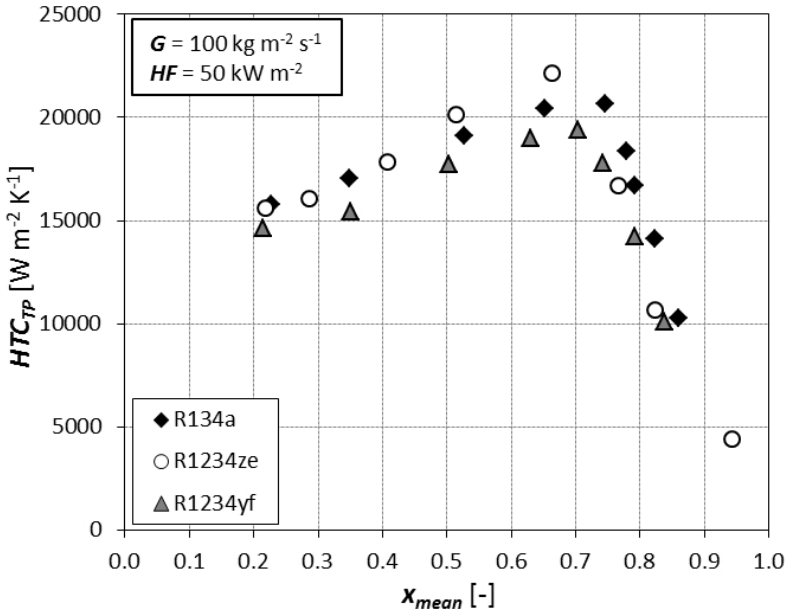

Figure 5.30: Comparison among R134a, R1234ze(E), and R1234yf two-phase heat transfer coefficient at G=100 kg m^{-2} s^{-1} and HF=50 kW m^{-2}.

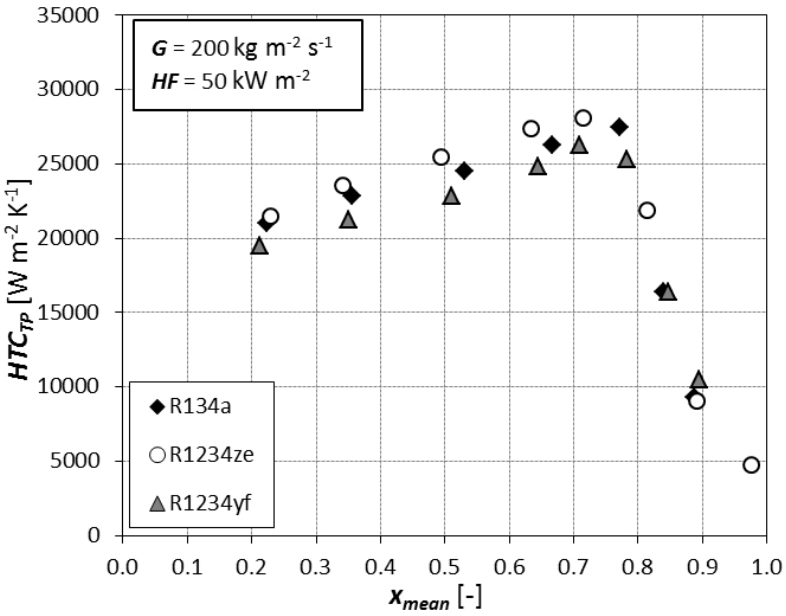

Figure 5.31: Comparison among R134a, R1234ze(E), and R1234yf two-phase heat transfer coefficient at G=200 kg m^{-2} s^{-1} and HF=50 kW m^{-2}.

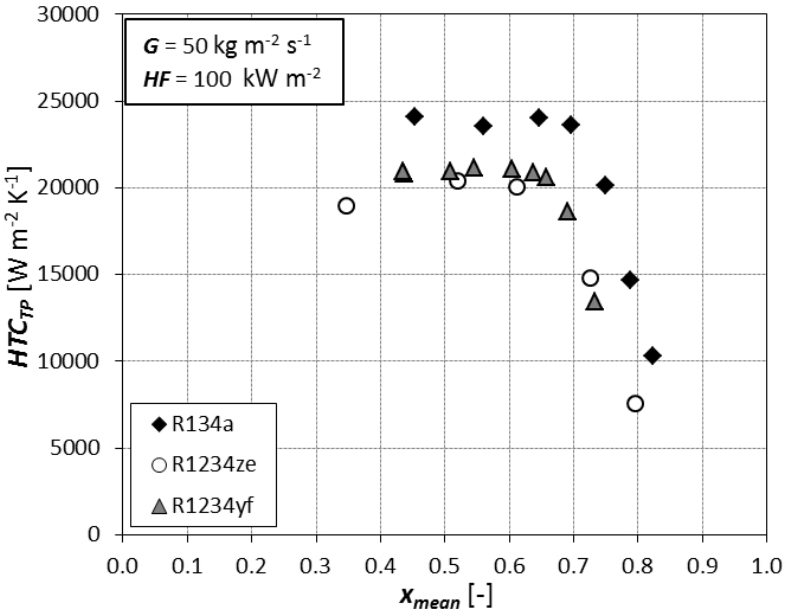

Figure 5.32: Comparison among R134a, R1234ze(E), and R1234yf two-phase heat transfer coefficient at G=50 kg m^{-2} s^{-1} and HF=100 kW m^{-2}.

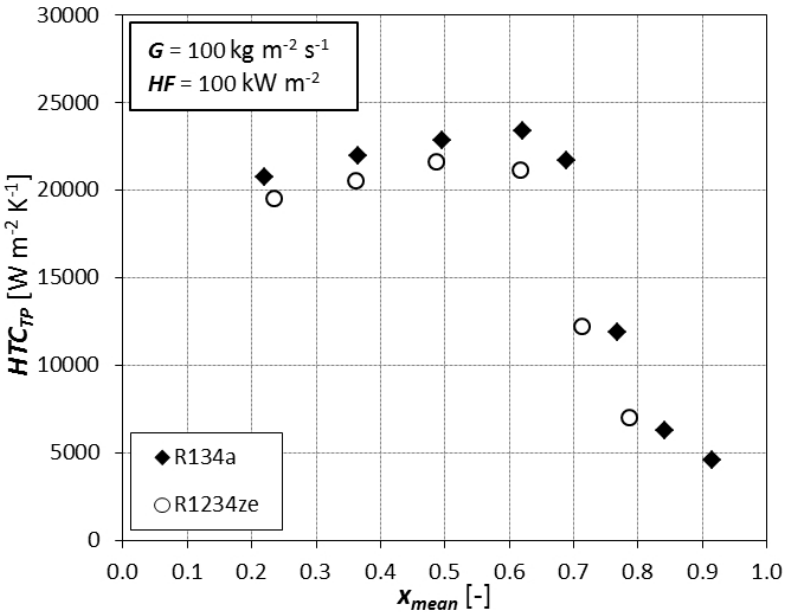

Figure 5.33: Comparison among R134a and R1234ze(E) two-phase heat transfer coefficient at G=100 kg m^{-2} s^{-1} and HF=100 kW m^{-2}.

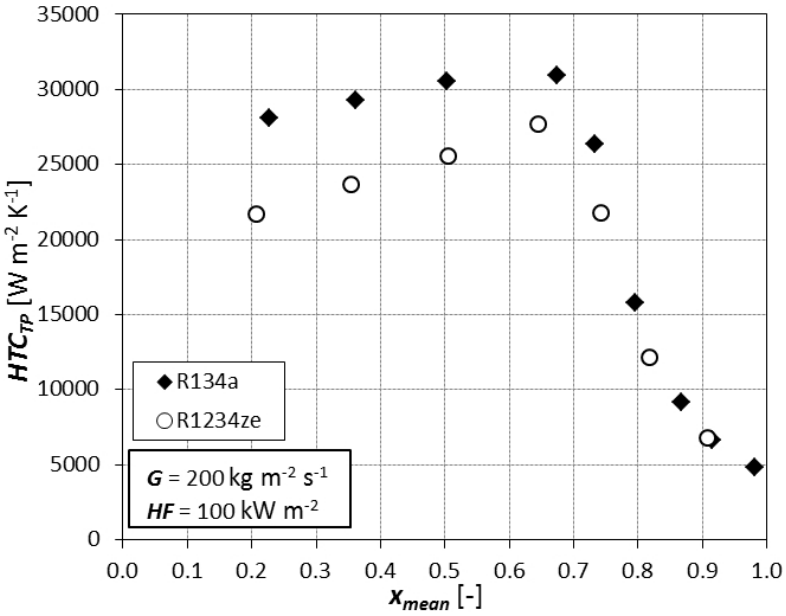

Figure 5.34: Comparison among R134a and R1234ze(E) two-phase heat transfer coefficient at G=200 kg m^{-2} s^{-1} and HF=100 kW m^{-2}.

pressure. Therefore, R1234ze(E) better performance in the two-phase forced convection seems to be neutralized by its poorer nucleate boiling characteristics, leading to approximately the same heat transfer performance at HF=50 kW m^{-2}.

The situation changes at HF=100 kW m^{-2}, where nucleate boiling seems to be strengthened. Unfortunately, no data are available for R1234yf at HF=100 kW m^{-2} with G=100 kg m^{-2} s^{-1} and G=200 kg m^{-2} s^{-1}. In this conditions, thanks to its better thermophysical properties, R134a shows better heat transfer performances.

Figures 5.35-5.37 shows a comparison of the two-phase pressure gradient between the three refrigerant at mass velocity of 50, 100, and 200 kg m^{-2} s^{-1}, respectively. At low vapour quality, the pressure gradient of the three refrigerants is almost the same, in fact they have similar liquid density and thus similar liquid velocity. When increasing the vapour quality, R1234ze(E) shows higher pressure gradient: this might be explained considering the value of the vapour density of the three refrigerants, which is lower for R1234ze(E). Having a lower value of vapour density implies a higher vapour velocity, with a consequent higher shear stress and thus higher pressure gradient. In addition, for the same reasons, the pressure gradient difference between R1234ze(E) and the other two fluids increases as the vapour quality increases.

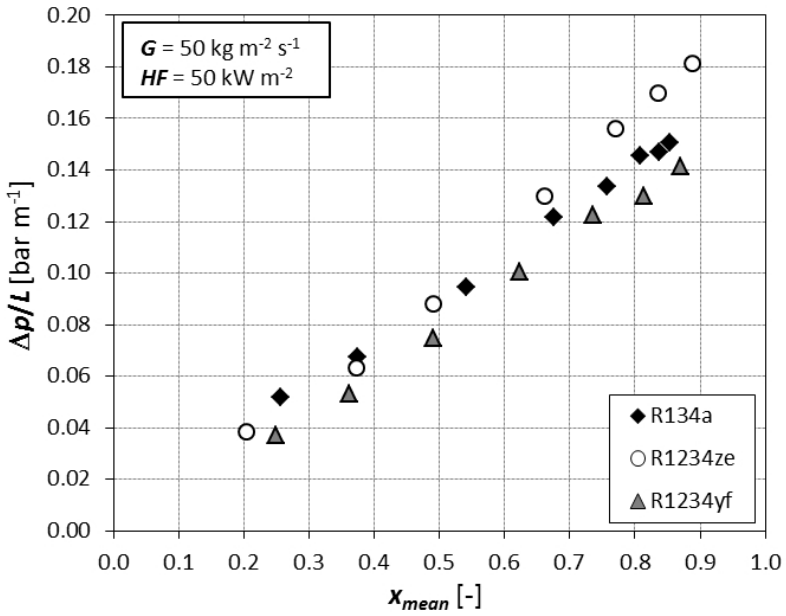

Figure 5.35: Comparison among R134a, R1234ze(E), and R1234yf two-phase pressure gradient at G=50 kg m^{-2} s^{-1} and HF=50 kW m^{-2}.

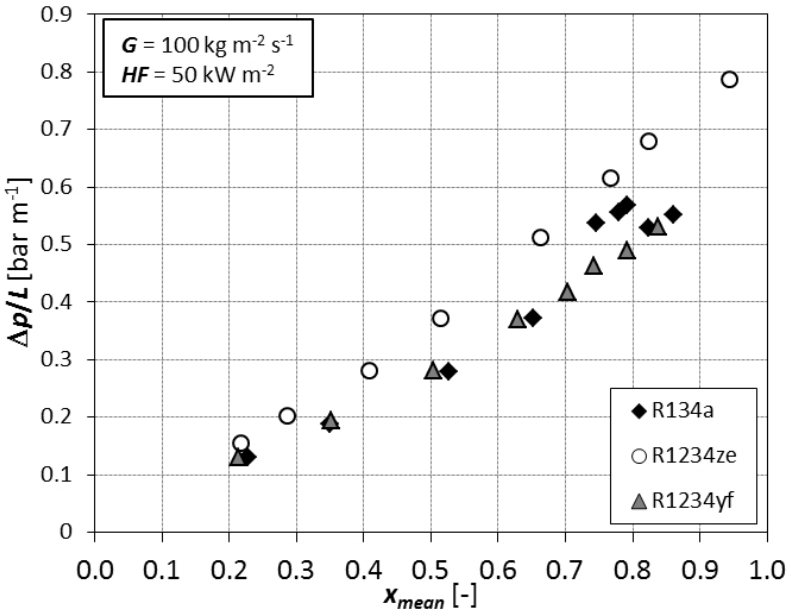

Figure 5.36: Comparison among R134a, R1234ze(E), and R1234yf two-phase pressure gradient at G=100 kg m^{-2} s^{-1} and HF=50 kW m^{-2}.

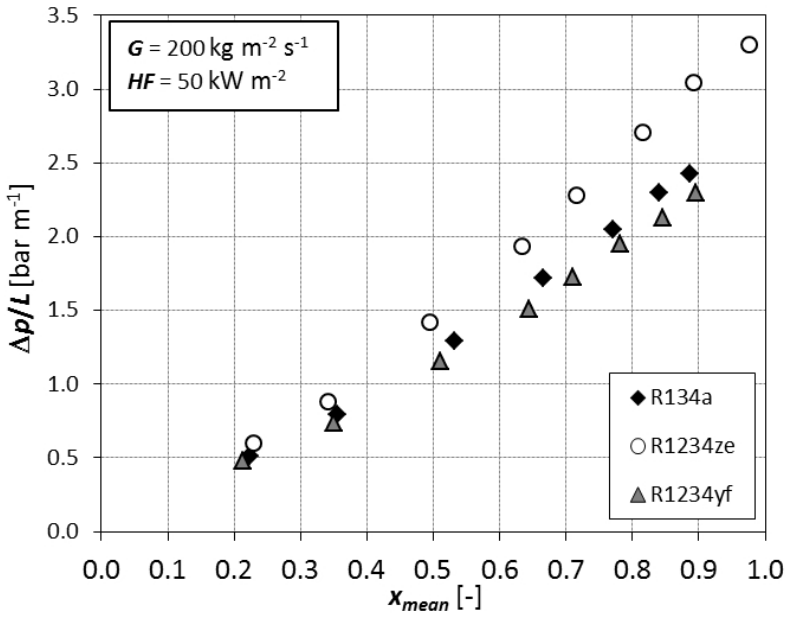

Figure 5.37: Comparison among R134a, R1234ze(E), and R1234yf two-phase pressure gradient at G=200 kg m^{-2} s^{-1} and HF=50 kW m^{-2}.

Chapter 6

Flow boiling inside a microfin tube

6.1 Introduction

The use of synthetic refrigerants with a non-negligible Global Warming Potential or, on the contrary, of natural but flammable or toxic natural fluids calls for the charge minimization of the refrigerating and air conditioning equipment. The refrigerant charge minimization can therefore be considered one of the most important targets for these applications to cope with the new environmental challenges. Traditional microfin tubes are widely used in air and water heat exchangers for heat pump and refrigerating applications during condensation or evaporation. The possible downsizing of microfin tubes can lead to more efficient and compact heat exchangers and thus to a reduction of the refrigerant charge of the systems.

In fact, since Fujie et al. [103] invention, microfin tubes have received a lot of attention because they ensure a large heat transfer enhancement (80-180%) when compared to equivalent smooth tubes under the same operating conditions, with relatively small increase in pressure drop (20-80%). In the last thirty years, this technology has been largely investigated, many experimental and theoretical studies have been conducted and several models to estimate their heat transfer and fluid flow capabilities have been developed and suggested in the open literature. Nowadays, this technology is mature and microfin tubes are widely used as enhanced surfaces for both single phase and two-phase heat transfer in heat pumps, chillers, and HVAC and refrigerating systems.

A huge literature can be found regarding flow boiling inside microfin tubes having an internal diameter higher than 6 mm. Yu et al. [104] experimentally investigated flow pattern and heat transfer of R134a during evaporation in a 10.7 mm diameter smooth tube and a microfin tube, in the ranges of mass velocity between 163 and 408 kg m^{-2} s^{-1}, heat flux between 2.2 and 56.0 kW m^{-2} at a saturation temperature of 6 °C. Depending on the test conditions, wavy flow, intermittent flow, and annular flow were observed. The transition from wavy and intermittent flow to annular flow was found to occur at lower mass flux and quality in the microfin tube than in the smooth tube, resulting in a better heat transfer performance. The heat transfer can be enhanced up to 200% at low mass flux and low quality where annular flow dominates in the microfin tube whereas wavy flow occurs in the smooth tube.

Padovan et al. [105] presented an experimental study on vaporization of R134a and R410A inside a horizontal microfin tube with an inside diameter measured at the fin tip of 7.69 mm, at 30 °C and 40 °C of saturation temperature. Mass velocity ranged from 80 to 600 kg m^{-2} s^{-1}, heat flux from 14.0 to 83.5 kW m^{-2}, and vapour quality from 0.1 to 0.99. The experimental database included measurements of heat transfer coefficient and dryout inception vapour quality. They also proposed an equation to determine the vapour quality at the onset of dryout phenomenon.

Most of the literature about flow boiling inside microfin tubes with internal diameter lower than 5 mm regards CO_2 technology, due to its high working pressure. Gao et al. [106, 107] conducted experiments on flow boiling of CO_2 and oil mixtures in horizontal smooth and microfin tubes. The microfin was a copper tube with an inner diameter of 3.04 mm. The experiments were carried out at mass velocities from 190 to 1300 kg m^{-2} s^{-1}, with a saturation temperature of 10 °C, heat fluxes from 5 to 30 kW m^{-2} and oil recirculation ratio from $\leq$0.01 to 0.72 wt%. In the case of almost pure CO_2, the flow boiling heat transfer is dominated by the nucleate boiling for both smooth and microfin tubes. The dryout quality increases greatly with an increase in mass velocity for the smooth tube and is poorly affected by mass velocity for the microfin tube.

Dang et al. [108] investigated the flow boiling heat transfer of carbon dioxide inside a small sized microfin tube, at a saturation temperature of 15 °C, and heat and mass flux of 4.5-18 kW m^{-2} and 360-720 kg m^{-2} s^{-1}, respectively. Experimental results indicated that heat flux had a significant effect on the heat transfer coefficient, and

the coefficient did not always increase with mass flux, as in the case of conventional refrigerants such as HFCs or HCFCs. Under certain conditions, the heat transfer coefficient at a high mass flux was lower than that at a lower mass flux, indicating that convective heat transfer had a suppression effect on nucleate boiling.

In the last year, some works regarding flow boiling of refrigerants inside small microfin tube begin to appear in the open literature. Wu et al. [109] performed an experimental investigation for convective vaporization of R22 and R410A inside one smooth tube and five microfin tubes with the same outer diameter of 5 mm. Data were for mass velocities ranging from 100 to 620 kg m^{-2} s^{-1} at 279 K of saturation temperature. Considering the effects of microfin on flow boiling, they also proposed correlations for the estimation of the frictional pressure drop and of the heat transfer coefficient.

Kondou et al. [110] experimentally investigated the flow boiling of the potential refrigerant mixture R32/R1234ze(E) in a horizontal microfin tube of 5.21 mm inner diameter. The heat transfer coefficient and pressure drop were measured at a saturation temperature of 10 °C, with heat flux of 10 kW m^{-2} and 15 kW m^{-2}, and mass velocity from 150 to 400 kg m^{-2} s^{-1}. The heat transfer coefficients of R1234ze(E) was found to be lower than those of R32, and the heat transfer coefficient of the mixture R32/R1234ze(E) was even lower than that of R1234ze(E). The heat transfer coefficient was minimized at the composition 0.2/0.8 by mass, where the temperature glide and the mass fraction distribution were maximized.

6.2 Data reduction

The setup described in chapter 4 was used for the experimental tests of refrigerants flow boiling inside the microfin tube. The schematic of the facility is reported in figure 4.25, where the test section is now replaced with the microfin tube under investigation.

The subcooled liquid is pumped to the boiler where it is vaporized and superheated; the refrigerant temperature and pressure are measured at both inlet and outlet of the heat exchanger. The vapour quality at the inlet of the test section depends on the refrigerant conditions at the inlet of the pre-condenser and on the heat flow rate exchanged in the tube-in-tube heat exchanger and obtained from a

thermal balance on the cooling water side as given by:

$$q_{pc} = \dot{m}_{w,pc} \cdot c_{p,w} \cdot (t_{w,pc,out} - t_{w,pc,in}) = \dot{m}_{ref} \cdot (h_{vs} - h_{TS,in}) \tag{6.1}$$

where $\dot{m}_{w,pc}$ is the water mass flow rate at the pre-condenser, $c_{p,w}$ the water specific heat at constant pressure, $t_{w,pc,out}$ and $t_{w,pc,in}$ the water temperatures at the outlet and inlet of the pre-condenser, respectively. Considering the right-hand side of equation 6.1, $\dot{m}_{ref}$ is the refrigerant mass flow rate, while h_{vs} the enthalpy of the superheated gas at the inlet of the pre-condenser, and $h_{TS,in}$ the enthalpy of the refrigerant at the inlet of the test section. The vapour quality at the inlet of the microfin tube (x_{in}) can be calculated from the heat balance, as:

$$x_{in} = \frac{h_{TS,in} - h_L}{h_V - h_L} \tag{6.2}$$

where h_L and h_V are the specific enthalpy of the saturated liquid and vapour, respectively, evaluated at the saturation of the refrigerant measured at the inlet of the microfin tube. The electrical power supplied to the sample is indirectly measured by means of a calibrated reference resistance (shunt) and by the measurement of the effective EPD (Electrical Difference Potential) of the resistance wire inserted in the copper heater. The current can be calculated fron the Ohm's law.

Preliminary heat transfer measurements permitted to estimate the heat losses (q_{loss}) due to conduction through the test section as a function of the mean wall temperature. The tests were run under vacuum conditions by supplying the power needed to maintain the mean wall temperature from around 30 °C to more than 60 °C. The results of these calibration tests are shown in figure 6.1, where the heat lost through the test section is plotted against the mean wall temperature. As it clearly appears, the relationship is linear; in this way. The actual value of heat supplied to the sample can be evaluated.

The heat losses through the test section are given by:

$$q_{loss}[W] = 0.1121 \cdot \bar{t}_{wall}[^\circ\mathrm{C}] - 2.4042 \tag{6.3}$$

where $\bar{t}_{wall}$ is the mean wall temperature; thus, the actual heat flow rate supplied

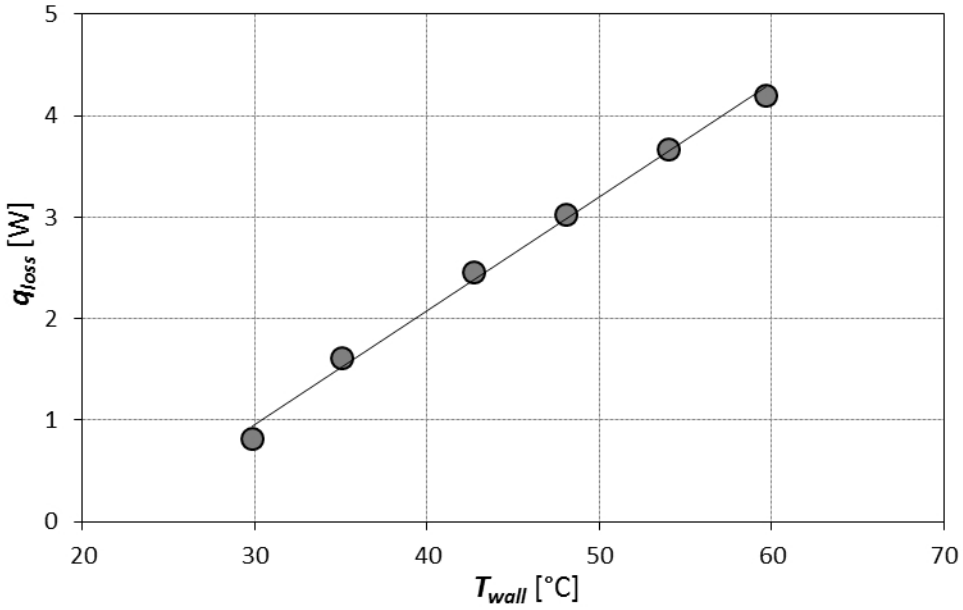

Figure 6.1: Estimated values of heat losses through the test section.

to the foam is given by:

$$q_{TS} = P_{EL} - q_{loss} = \Delta V \cdot I - q_{loss} \tag{6.4}$$

where P_{EL} is the electrical power supplied, ΔV is the electrical potential, and I is the current. It was estimated that the heat lost was always less than 3%. The specific enthalpy at the outlet of the test section can be calculated from the thermal balance applied to the test section:

$$h_{TS,out} = h_{TS,in} + \frac{q_{TS}}{\dot{m}_{ref}} \tag{6.5}$$

Then, vapour quality x_{out} is given by:

$$x_{out} = \frac{h_{TS,out} - h_L}{h_V - h_L} \tag{6.6}$$

In this case, the thermodynamic properties of the refrigerant are evaluated at the outlet saturation pressure. The two phase heat transfer coefficient HTC_{TP}, referred

to the area A_D can now be defined as:

$$HTC_{TP} = \frac{q_{TS}}{A_D \cdot (\bar{t}_{wall} - \bar{t}_{sat})} \tag{6.7}$$

where A_D is the area of a smooth tube with the same inner diameter at the fin tip, $\bar{t}_{wall}$ is the average value of the wall thermocouples, and $\bar{t}_{sat}$ is the average value of the saturation temperatures obtained from the measured values of the pressure, as:

$$\bar{t}_{wall} = \frac{1}{20} \sum_{i=1}^{20} t_{wall,i} \tag{6.8}$$

$$\bar{t}_{sat} = \frac{t_{sat,in}(p_{sat,in}) + t_{sat,out}(p_{sat,out})}{2} \tag{6.9}$$

where $t_{wall,i}$ is the temperature measured by the i-th thermocouple, and $p_{sat,in}$ and $p_{sat,out}$ are the saturation pressures at the inlet and outlet of the test section, respectively. Thermodynamic and transport properties of the refrigerant are estimated from Refprop 9.1 [94].

During two-phase flow inside the microfin tube, the total pressure drop is measured by means of a differential pressure transducer. Generally speaking, the pressure gradient, defined as the ratio of the pressure drop to the length of the tube, is the sum of three terms:

$$-\left(\frac{\mathrm{d}p}{\mathrm{d}z}\right)_{tot} = -\left(\frac{\mathrm{d}p}{\mathrm{d}z}\right)_{f} - \left(\frac{\mathrm{d}p}{\mathrm{d}z}\right)_{g} - \left(\frac{\mathrm{d}p}{\mathrm{d}z}\right)_{a} \tag{6.10}$$

where the subscripts f refers to the frictional term, g to the gravity term, and a to the acceleration term. Considering the term linked to gravity, it depends on the tube inclination (α) and it is:

$$-\left(\frac{\mathrm{d}p}{\mathrm{d}z}\right)_{g} = -(\varepsilon \cdot \rho_V + (1-\varepsilon) \cdot \rho_L) \cdot g \cdot \sin\alpha \tag{6.11}$$

Therefore, if the tube is horizontal, this term is equal to zero. The acceleration term is:

$$-\left(\frac{\mathrm{d}p}{\mathrm{d}z}\right)_{a} = -G^2 \frac{\mathrm{d}}{\mathrm{d}x}\left[\frac{x^2}{\rho_V \cdot \varepsilon} + \frac{(1-x)^2}{\rho_L \cdot (1-\varepsilon)}\right] \tag{6.12}$$

Hence:

$$-\left(\frac{\Delta p}{L}\right)_a = G^2\left[\left(\frac{x^2}{\rho_V \cdot \varepsilon} + \frac{(1-x)^2}{\rho_L \cdot (1-\varepsilon)}\right)_{out} - \left(\frac{x^2}{\rho_V \cdot \varepsilon} + \frac{(1-x)^2}{\rho_L \cdot (1-\varepsilon)}\right)_{in}\right] \cdot \frac{1}{L} \quad (6.13)$$

where L is the length of the microfin tube, and ε is the void fraction, calculated with the equation proposed by Rouhani and Axelsson [111]:

$$\varepsilon = \frac{x}{\rho_V}\left[(1+0.12(1-x))\left(\frac{x}{\rho_V} + \frac{1-x}{\rho_L}\right) + \frac{1.18(1-x)[g\sigma(\rho_L - \rho_V)]^{0.25}}{G\rho_L^{0.5}}\right]^{-1} \quad (6.14)$$

6.3 Uncertainty analysis

The uncertainty analysis is similar to that explained in the previous chapter. The uncertainties on the heat flow rate exchanged in the pre-condenser, on the inlet quality, and on the mean vapour quality can be estimated with equations in paragraph 5.3. Since the reference area to define the two-phase heat transfer coefficient is now different, the uncertainty on the two-phase heat transfer coefficient can be estimated as follows. Deriving equation 6.7:

$$\frac{\partial HTC_{TP}}{\partial q_{TS}} = \frac{1}{A_D \cdot (\bar{t}_{wall} - \bar{t}_{sat})} \quad (6.15)$$

$$\frac{\partial HTC_{TP}}{\partial A_D} = -\frac{q_{TS}}{A_D^2 \cdot (\bar{t}_{wall} - \bar{t}_{sat})} \quad (6.16)$$

$$\frac{\partial HTC_{TP}}{\partial \bar{t}_{wall}} = -\frac{q_{TS}}{A_D \cdot (\bar{t}_{wall} - \bar{t}_{sat})^2} \quad (6.17)$$

$$\frac{\partial HTC_{TP}}{\partial \bar{t}_{sat}} = \frac{q_{TS}}{A_D \cdot (\bar{t}_{wall} - \bar{t}_{sat})^2} \quad (6.18)$$

Thus, the uncertainty on the two-phase heat transfer coefficient can estimated as follows:

$$i_{HTC_{TP}} = \sqrt{\left(\frac{\partial HTC_{TP}}{\partial q_{TS}} i_{q_{TS}}\right)^2 + \left(\frac{\partial HTC_{TP}}{\partial A_D} i_{A_D}\right)^2 + \left(\frac{\partial HTC_{TP}}{\partial \bar{t}_{wall}} i_{\bar{t}_{wall}}\right)^2 + \left(\frac{\partial HTC_{TP}}{\partial \bar{t}_{sat}} i_{\bar{t}_{sat}}\right)^2} \quad (6.19)$$

The uncertainty on the mean wall temperature and on the mean saturation temperature can be calculated as:

$$i_{\bar{t}_{wall}} = \frac{\sqrt{20}}{20} \cdot i_{t_{wall,i}} \tag{6.20}$$

$$i_{\bar{t}_{sat}} = \frac{\sqrt{2}}{2} \cdot i_{t_{sat,i}} \tag{6.21}$$

From the above analysis, the mean uncertainties on the mean vapour quality and on the two-phase heat transfer coefficient, calculated with the instruments accuracy reported in chapter 4 and considering an uncertainty of 1% for the values calculated with Refprop 9.1 [94], are 0.030 and 3.9%, respectively.

6.4 Experimental results

This section presents the experimental results carried out during flow boiling heat transfer of three different refrigerants (R134a, R1234ze(E), and R1234yf) at 30 °C of saturation temperature at the inlet of the microfin tube. The experimental campaign is aimed at investigating the effects of different operating conditions on flow boiling heat transfer inside this new generation of mini microfin tube; in particular, three different heat fluxes were investigated: 10, 25, and 50 kW m^{-2}, the mass velocity (referred to the inner diameter at fin tip) was varied between 190 and 940 kg m^{-2} s^{-1}, while vapour quality from 0.20 to 0.99. In this range of operative conditions, the flow regime before dryout is annular flow, according to Doretti et al. [112].

6.4.1 The microfin tube

A shown in figure 6.2, the tested microfin tube is brazed inside a groove milled in a 20 mm thick, 10 mm wide and 300 mm long copper plate. The pressure taps are located around 50 mm upstream and downstream of the heated tube; a smooth connection was designed and manufactured in order to prevent any possible abrupt pressure losses. The test tube has a heated length of 300 mm whereas the total length for pressure drop measurement is 410 mm. The microfin is heated from the bottom by means of a Nichel-Chrome wire resistance inserted in a 2 mm deep groove

Figure 6.2: Picture of the tested microfin tube brazed in the copper heater.

milled on the bottom face of the copper plate. The heat is supplied by the stabilized DC power supplier, which is able to supply up to 900 W. The instrumented test section is located inside an aluminum housing filled up with 30 mm thick layer of rock wool to limit as much as possible the heat losses.

According to the nomenclature described in figure 6.3, the microfin tube has an outer diameter OD of 4.0 mm, an inner diameter ID at the fin tip of 3.4 mm, it has 40 fins with a fin height of 0.12 mm, the helix angle β is 18°. Twenty calibrated T-type thermocouples are inserted in as many 5 mm deep holes drilled 1 mm under the test tube to measure the wall temperature distribution during the heat transfer process.

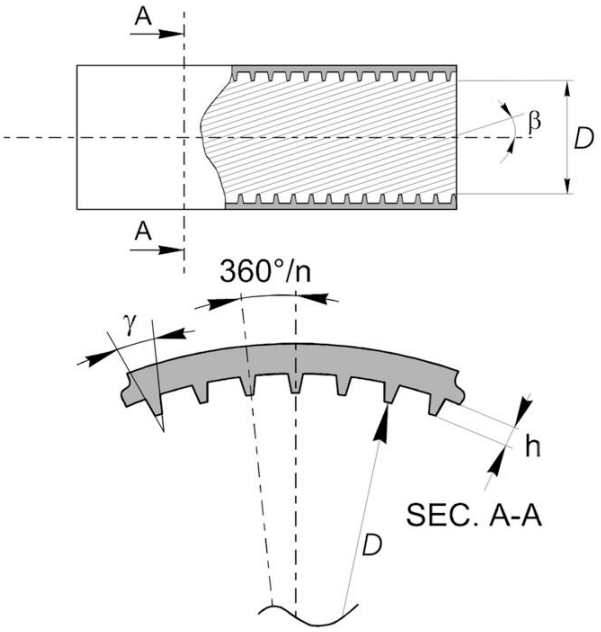

Figure 6.3: Geometrical characteristic of a microfin tube (Cavallini et al. [113]).

6.4.2 R134a

Figure 6.4 shows the two-phase heat transfer coefficient plotted against the vapour quality as a function of the mass velocity, at constant heat flux of 10 kW m^{-2}. Considering the lowest mass velocity, $G = 190$ kg m^{-2} s^{-1}, the heat transfer coeffi-

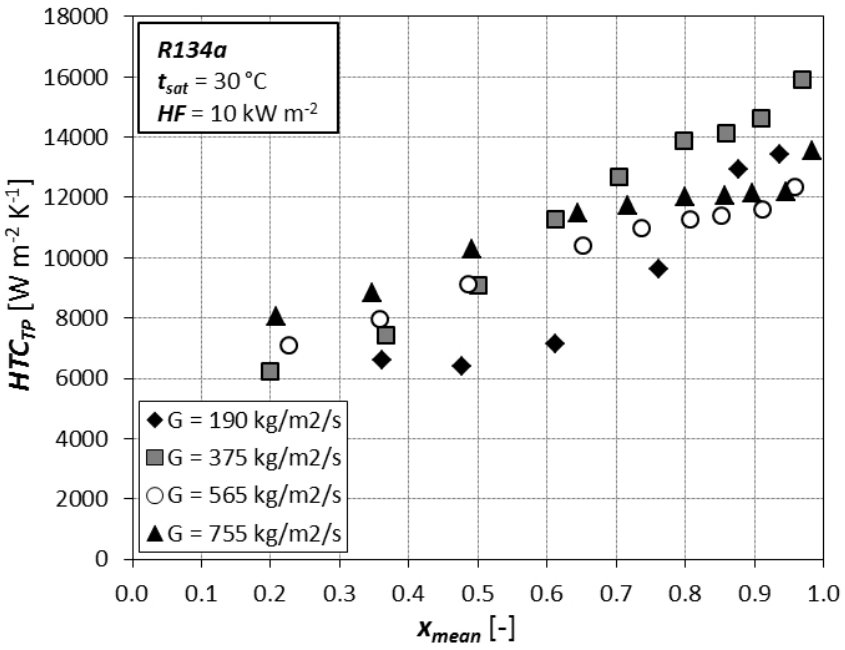

Figure 6.4: R134a two phase heat transfer coefficient as a function of the mean vapor quality at constant heat flux HF=10 kW m^{-2}.

cient remains almost constant at around 6100 W m^{-2} K^{-1} up to a vapour quality of 0.50: this might mean that the phanse change process is controlled by the nucleate boiling; then, it increases with vapour quality. When increasing the mass velocity, the plateau at low vapour quality, where the heat transfer coefficient remains constant, disappears, and the heat transfer coefficient increases almost linearly with the vapour quality meaning that the two-phase forced convection is affecting in the phase change process. It is worthy to point out that, at vapour quality higher than 0.65, the values of the heat transfer coefficient measured at $G = 375$ kg m^{-2} s^{-1} are greater than those measured at higher mass velocities; this can be linked to a particular effect, due to the presence of the helical micro-fins that might be enhanced at this operating test conditions. Furthermore, at this heat flux, no experimental

evidence of the onset of the dryout was observed at any mass velocity.

The two-phase heat transfer coefficient measured at $HF = 25$ kW m^{-2} are plotted against the mean vapour quality as a function of the mass velocity in figure 6.5. At $G = 190$ kg m^{-2} s^{-1}, the heat transfer coefficient shows a plateau, being

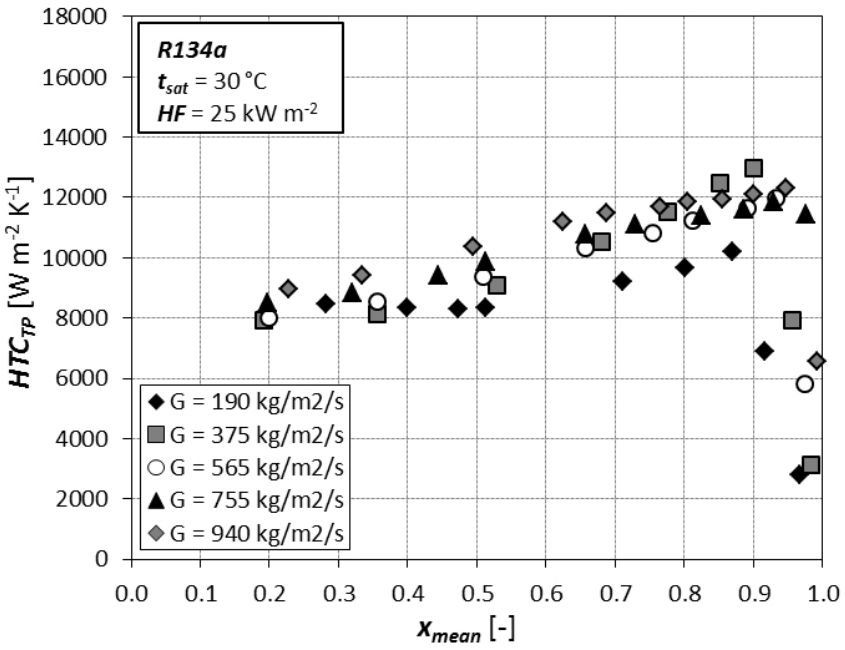

Figure 6.5: R134a two phase heat transfer coefficient as a function of the mean vapor quality at constant heat flux HF=25 kW m^{-2}.

around 8100 W m^{-2} K^{-1}, up to a vapour quality of 0.50, confirming that there is a noticeable enhancement due to high heat flux and thus to the nucleate boiling. When $x_{mean} > 0.50$, the heat transfer coefficient increases with vapour quality, it reaches a maximum value at around $x_{do} = 0.89$ and then it suddenly decreases because the dryout phenomenon occurs. According to what suggested by Wojtan et al. [102], the vapour quality at the onset of the dryout is determined as the last point before the heat transfer coefficient dropped more than 10% from its initial value. When increasing the mass velocity, the plateau where the heat transfer coefficient remains constant reduces to $x_{mean} = 0.35$ at $G = 375$ kg m^{-2} s^{-1}; then, at higher mass velocities, the heat transfer coefficient increases almost linearly with vapour quality, meaning that the two-phase forced convection becomes more and more important on the phase change process. The onset of the dryout phenomenon is delayed as

the mass velocity increases passing from $x_{do} = 0.89$ at $G = 190$ kg m^{-2} s^{-1} to $x_{do} = 0.97$ at $G = 940$ kg m^{-2} s^{-1}. For a given vapour quality, on average, the heat transfer coefficient slightly increases with the mass velocity but, as already mentioned for $HF = 10$ kW m^{-2}, the maximum heat transfer coefficient is exhibited at $G = 375$ kg m^{-2} s^{-1} and $x_{mean} = 0.90$, before the inception of the dryout.

Slightly different the results reported in figure 6.6, where the two-phase heat transfer coefficient is plotted against the mean vapour quality as a function of the mass velocity at constant heat flux HF of 50 kW m^{-2}. At these operating condi-

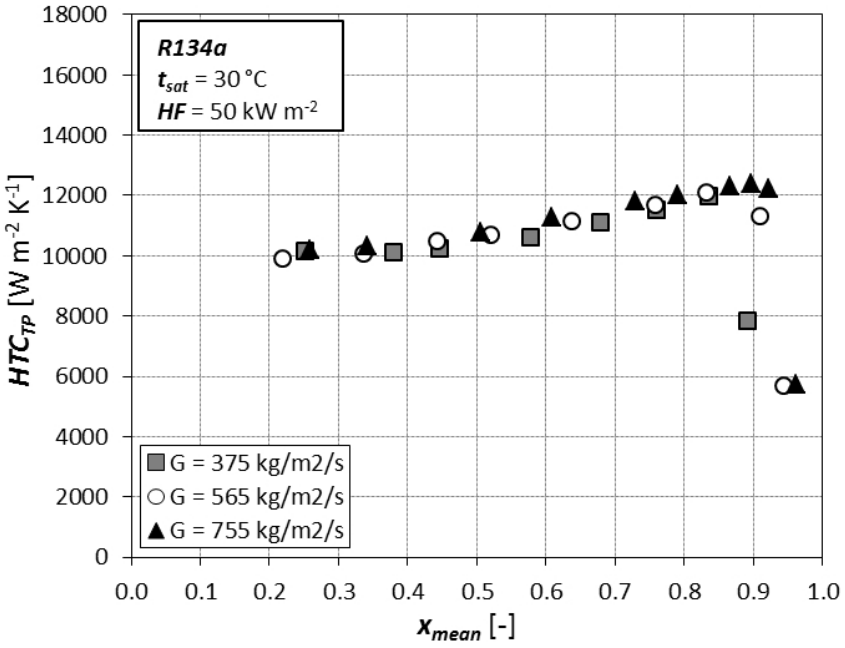

Figure 6.6: R134a two phase heat transfer coefficient as a function of the mean vapor quality at constant heat flux HF=50 kW m^{-2}.

tions, there is not any appreciable effect of the mass velocity on the heat transfer, which seems to be controlled by the nucleate boiling. For vapour qualities lower than 0.50, the heat transfer coefficient, being around 10000 W m^{-2} K^{-1}, is almost constant with the vapour quality at all the investigated mass velocities; as the vapour quality increases, a weak effect on the heat transfer coefficient is shown, which increases as well. The vapour quality at the onset of the dryout is found to increases as the mass velocity increases.

Figure 6.7 permits to highlight the effects of the heat flux on the two-phase heat

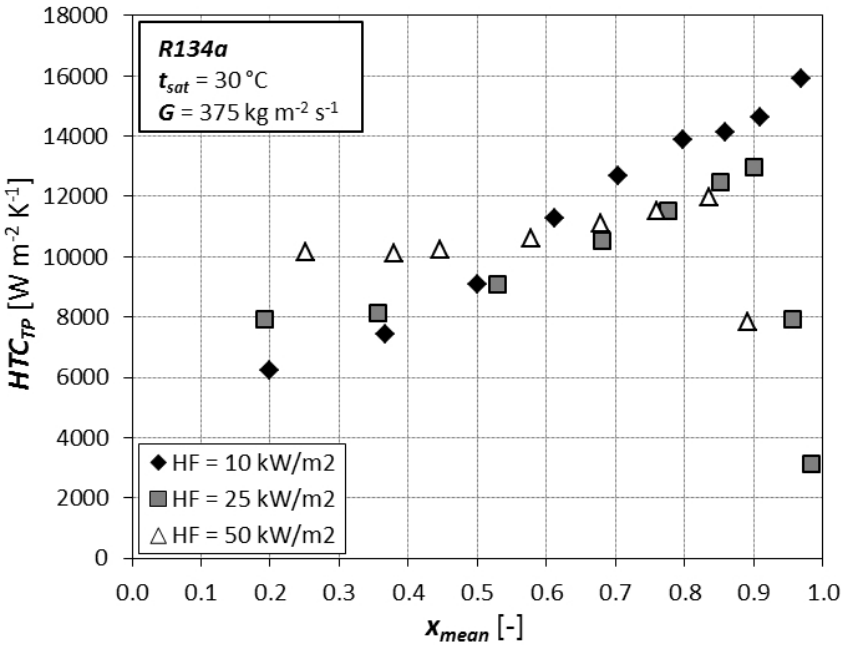

Figure 6.7: R134a two phase heat transfer coefficient as a function of the mean vapor quality at constant mass velocity G=375 kg m^{-2} s^{-1}.

transfer coefficient measured at $G = 375$ kg m^{-2} s^{-1}. It appears that there is a strong relationship between the heat flux and the phase change process. In particular, at $HF = 10$ kW m^{-2}, the heat transfer coefficient increases almost linearly with vapour quality and the dryout phenomenon does not occur. When increasing the heat flux, a plateau where the heat transfer coefficient can be considered constant with vapour quality appears. At $HF = 25$ kW m^{-2}, this plateau ends at $x_{mean} = 0.35$ but at $HF = 50$ kW m^{-2} it can be noticed up to $x_{mean} = 0.60$. Then, the heat transfer coefficient increases with vapour quality. This behaviour can be explained considering the two competitive mechanisms that control the phase change process: nucleate boiling and two-phase forced convection. At low heat fluxes, the flow boiling heat transfer is influenced by the two-phase forced convection, in fact the heat transfer coefficient increases with the vapour quality; when increasing the heat flux, especially at low vapour quality, the nucleate boiling becomes more and more important up to dominate the phase change process; in this region, higher the heat flux, higher the heat transfer coefficient. As the vapour quality increases,

the nucleate boiling mechanism also seems to suppress the two-phase forced convection; as a result, the heat transfer coefficients measured at $HF = 10$ kW m^{-2} are greater than those measured at higher heat flux. Finally, it can be noticed that at $HF = 25$ kW m^{-2} and $HF = 50$ kW m^{-2}, the dryout phenomenon occurs and the vapour quality at its onset decreases as the heat flux increases, passing from around $x_{do} = 0.90$ to $x_{do} = 0.87$, respectively.

Figure 6.8 presents data carried out at a mass velocity of $G = 565$ kg m^{-2} s^{-1}. When increasing the mass velocity, the two-phase forced convection is strengthened and, as shown in the figure, the heat transfer coefficients measured at $HF = 10$ kW m^{-2} and $HF = 25$ kW m^{-2} are almost the same and they increase with the vapour quality, meaning that the two-phase forced convection dominates the phase change process. At $HF = 50$ kW m^{-2}, the heat transfer coefficients are greater than those measured at low heat flux, especially at low vapour quality where it appears a small plateau up to a vapour quality of 0.35; in this region, the nucleate boiling seems to dominate the phase change process. Comparing figures 6.7 and 6.8, at constant heat flux, the vapour quality at the onset of the dryout is delayed when

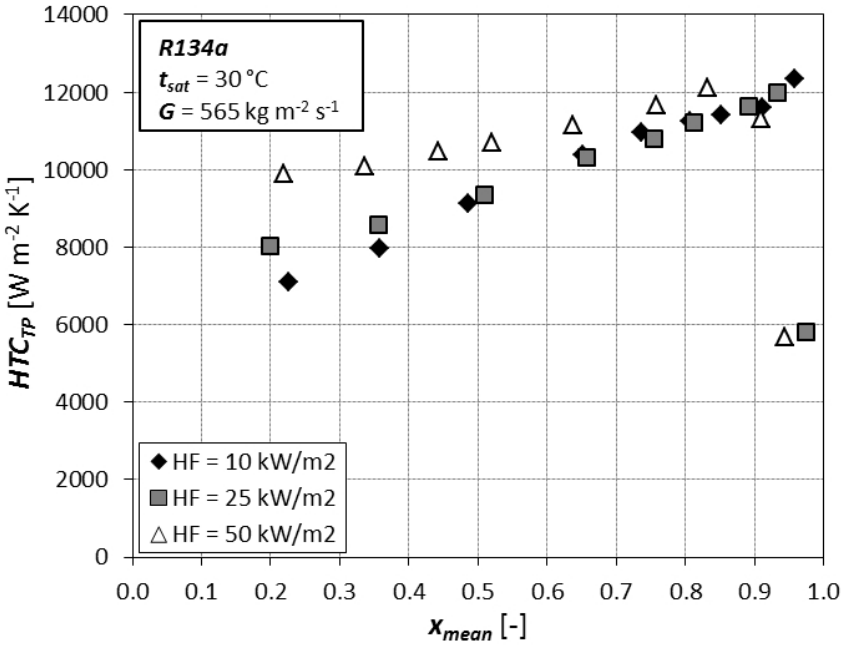

Figure 6.8: R134a two phase heat transfer coefficient as a function of the mean vapor quality at constant mass velocity G=565 kg m^{-2} s^{-1}.

increasing the mass velocity. At $HF = 25$ kW m^{-2} and $HF = 50$ kW m^{-2}, the dryout phenomenon occurs at around $x_{do} = 0.93$ and $x_{mean} = 0.89$, repectively.

Figure 6.9 shows the heat transfer coefficient plotted against the mean vapour quality as a function of the heat flux at constant mass velocity of 755 kg m^{-2} s^{-1}. Similarly to what highlighted before for $G = 365$ kg m^{-2} s^{-1}, the heat transfer

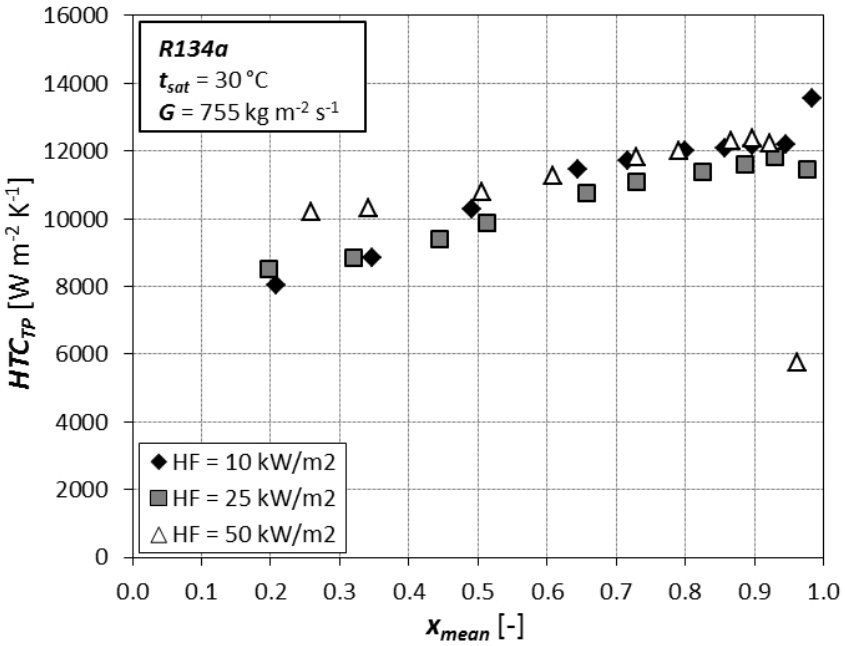

Figure 6.9: R134a two phase heat transfer coefficient as a function of the mean vapor quality at constant mass velocity G=755 kg m^{-2} s^{-1}.

coefficients measured at $HF = 10$ kW m^{-2} and $HF = 25$ kW m^{-2} are almost the same and they increase with the vapour quality, meaning the presence of the two-phase forced convection. At $HF = 50$ kW m^{-2}, the heat transfer coefficient are higher than those measured at lower heat flux, especially at low vapour quality where a small plateau appears up to $x_{mean} = 0.50$; in this region, the nucleate boiling dominates the flow boiling. In fact, at low heat flux, the flow boiling heat transfer coefficient is influenced by the two-phase forced convection, whereas, when increasing the heat flux, especially at low vapour qualities, the nucleate boiling seems to dominate the phase change process. As the vapour quality increases, the two-phase forced convection becomes more important and the heat transfer coefficients are almost similar at all the investigated mass velocities. Finally, it can be noticed

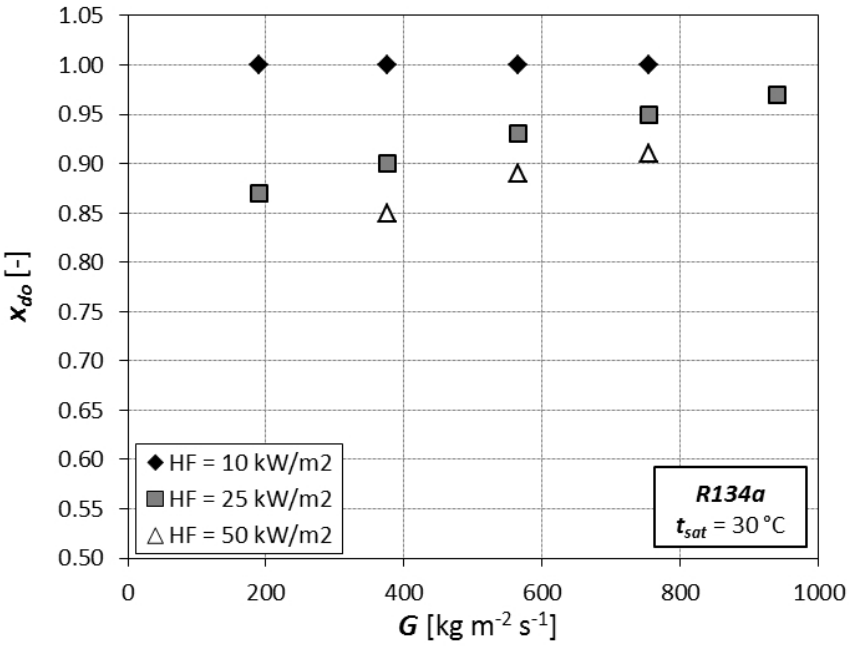

Figure 6.10: Effect of the heat flux on the vapour quality at the onset of the dryout as a function of velocity for the refrigerant R134a.

that the dryout phenomenon only occurs at $HF = 50$ kW m^{-2} and the vapour quality at its onset is around $x_{do} = 0.91$.

Figure 6.10 summarizes the vapour quality at the onset of the dryout. At $HF = 10$ kW m^{-2} the dryout phenomenon was not observed, thus the vapour quality at its onset is conventionally kept equal to 1. At higher heat flux, the vapour quality at the onset of the dryout increases as the mass velocity increases, whereas it decreases as the heat flux increases. At all the investigated operating test conditions, the critical vapour quality is always greater than 0.85.

Figure 6.11 reports the experimental measurements carried out at constant inlet vapour quality $x_{in} = 0.30$ by varying the heat flux up to the onset of the dryout. Three mass velocities were investigated: 190, 375, and 565 kg m^{-2} s^{-1}, in order to highlight the heat transfer behaviour at operating conditions similar to those that can be found in an actual refrigerating machine. The effects of the mass velocity on the heat transfer coefficient can be noticed up to $HF = 30$ kW m^{-2}, in particular it increases as the refrigerant mass flux increases; after that heat flux, the heat transfer coefficient is almost the same at all the investigated mass velocities. As expected,

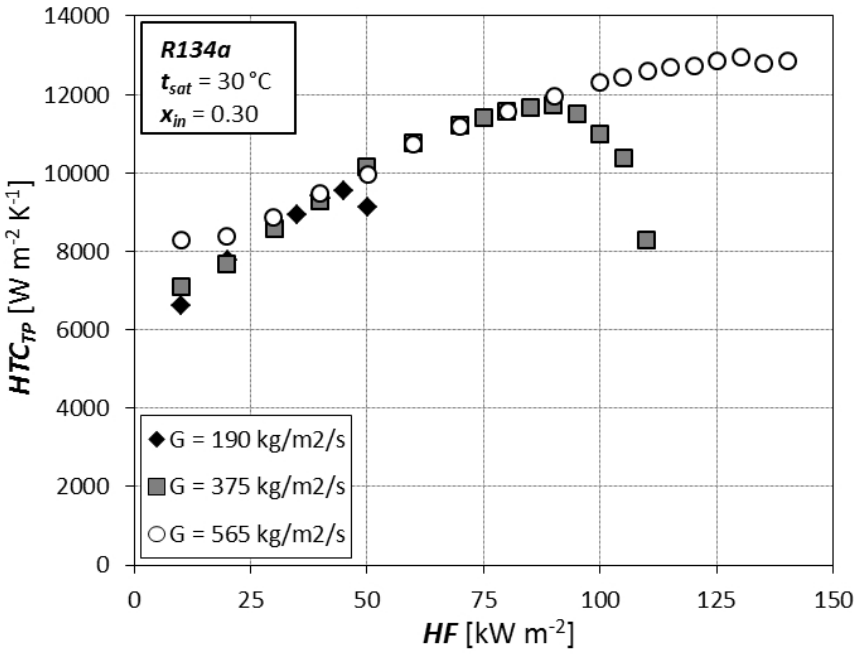

Figure 6.11: Effect of the mass velocity on the R134a heat transfer coefficient at different heat flux.

the heat flux at the onset of the dryout phenomenon increases as the mass velocity increases, being $HF_{do} = 45$ kW m^{-2} at $G = 190$ kg m^{-2} s^{-1}, $HF_{do} = 90$ kW m^{-2} at $G = 375$ kg m^{-2} s^{-1}, whereas at $G = 565$ kg m^{-2} s^{-1} the experimental measurements ended before the critical heat flux could be reached.

The diagram plotted in figure 6.12 shows the two-phase frictional pressure gradients calculated from the measured values of the total pressure drop at $HF = 25$ kW m^{-2}. The Rouhani and Axelsson [111] model was used to estimate the void fraction values to account for the momentum pressure gradients. The results show the effect of the mass velocity and vapour quality on the two-phase frictional pressure gradient; at constant mass velocity, it increases with vapour quality, reaching a maximum value and then it decreases. Finally, at constant vapour quality, the frictional pressure gradient increases as the mass velocity increases. Similar results were also obtained for the other heat fluxes investigated.

Another important parameter in the design of refrigeration systems is the saturation temperature drop due to pressure drop during the phase change process. The saturation temperature drop is a function of the total pressure drop, i.e. it

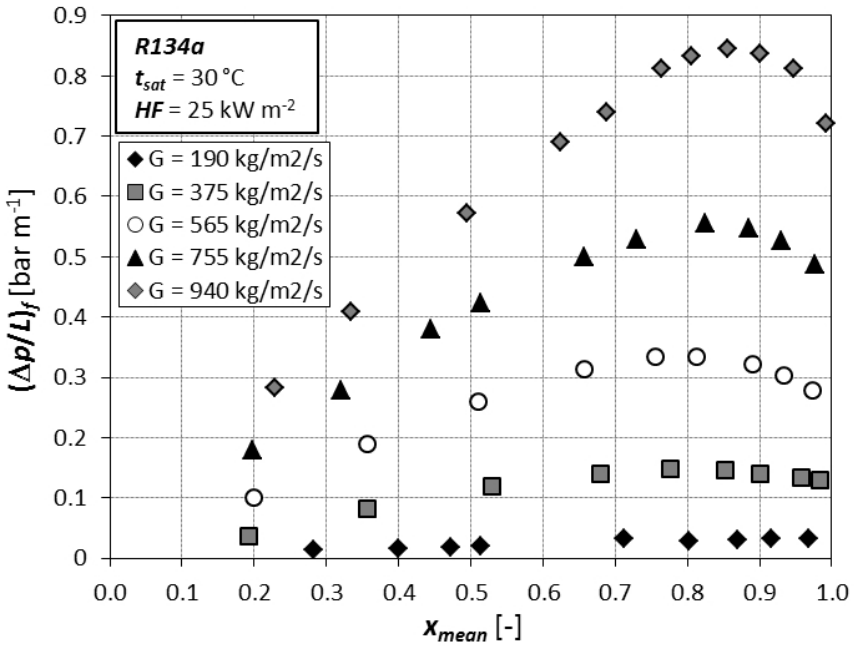

Figure 6.12: R134a two phase frictional pressure gradient as a function of the mean vapor quality at constant heat flux HF=25 kW m^{-2}.

depends both on the friction and on the momentum pressure drop. Figure 6.13 reports the saturation temperature drop as a function of the mean vapour quality at constant heat flux of 25 kW m^2 for five different mass velocities: 190, 375, 565, 755, 940 kg m^{-2} s^{-1}. The trend is similar to that of pressure drops: at constant mass velocity, the saturation temperature drop increases with vapour quality up to a maximum, then it slightly decreases; at constant vapour quality, it increases with mass velocity. Similar results were obtained for the other heat fluxes investigated. Since the momentum pressore drop is a function of the heat flux, the saturation temperature drop slightly increases when increasing the heat flux.

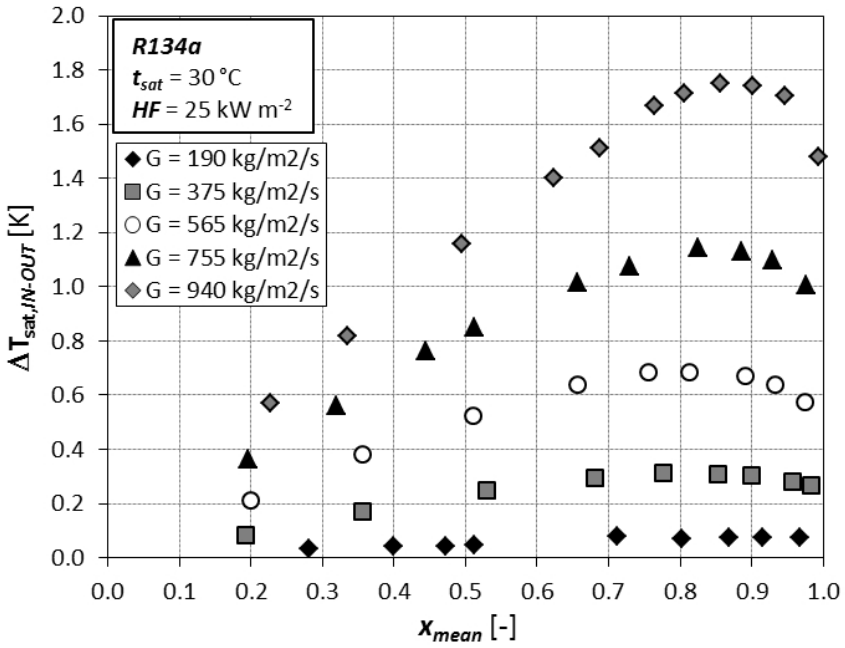

Figure 6.13: R134a saturation temperature drop as a function of the mean vapor quality at constant heat flux HF=25 kW m^{-2}.

6.4.3 R1234ze(E)

Figure 6.14 shows the two-phase heat transfer coefficient plotted against the mean vapour quality at constant heat flux of 10 kW m^{-2}. Generally speaking, the heat

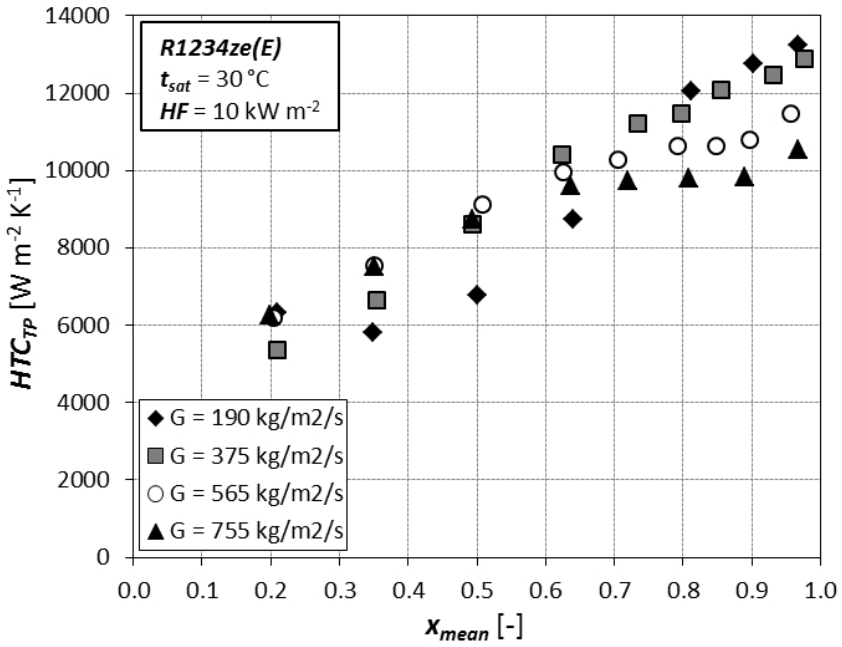

Figure 6.14: R1234ze(E) two phase heat transfer coefficient as a function of the mean vapor quality at constant heat flux HF=10 kW m^{-2}.

transfer coefficient increases with vapour quality for all the investigated mass velocities, meaning that the two-phase forced convection is affecting in the phase change mechanism. It is interesting to highlight that the values of the heat transfer coefficient at $G = 190$ kg m^{-2} s^{-1} are lower than those measured at other mass velocities in the vapour quality range from 0.30 to 0.70, but opposite situation occurs at high vapour qualities, where, at constant vapour quality, the heat transfer coefficient increases when decreasing the mass velocity. At this heat flux, no evidence of the onset of the dryout phenomenon was observed from the experimental measurements.

The thermal results carried out at $HF = 25$ kW m^{-2} are plotted against the mean vapour quality as a function of the mass velocity in figure 6.15. The heat transfer coefficient at $G = 190$ kg m^{-2} s^{-1} shows a plateau, being around 7500 W m^{-2} K^{-1}, up to a vapour quality of 0.4, then the heat transfer coefficient

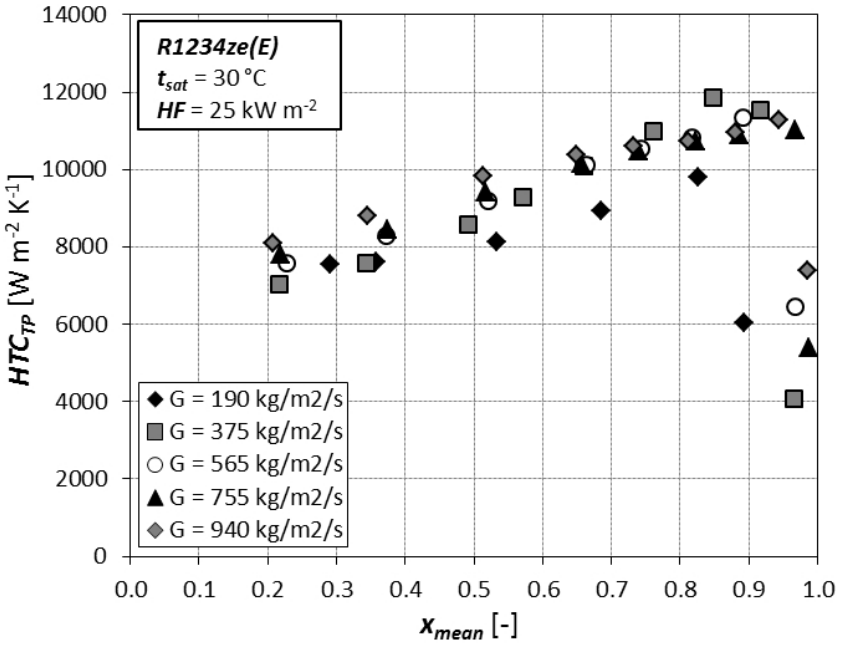

Figure 6.15: R1234ze(E) two phase heat transfer coefficient as a function of the mean vapor quality at constant heat flux HF=25 kW m^{-2}.

increases with vapour quality up to a maximum value at around $x_{do} = 0.85$ and, after this point, it suddenly decreases because the dryout phenomenon occurs. This behaviour can be described considering the two heat transfer mechanisms that control the phase change process: nucleate boiling and two-phase forced convection. In particular, $G = 190$ kg m^{-2} s^{-1}, for $x_{mean} < 0.4$, the nucleate boiling seems to dominate the phase change process, whereas, at higher vapour qualities, the two-phase forced convection seems to become more and more important. When increasing the mass velocity, the plateau at low vapour quality, where the heat transfer coefficient remains constant, disappears and the two-phase heat transfer coefficient always increases with vapour quality, meaning that the two-phase forced convection controls the phase change process. The onset of the dryout is delayed as the mass velocity increases, passing from 0.82 at $G = 190$ kg m^{-2} s^{-1} to 0.97 at $G = 940$ kg m^{-2} s^{-1}. For a given vapour quality, on average, the heat transfer coefficient slightly increases with the mass velocity but the maximum heat transfer coefficient is exhibited at $G = 375$ kg m^{-2} s^{-1} and $x_{mean} = 0.90$, before the inception of the dryout.

Figure 6.16 shows the two-phase heat transfer coefficient plotted against the

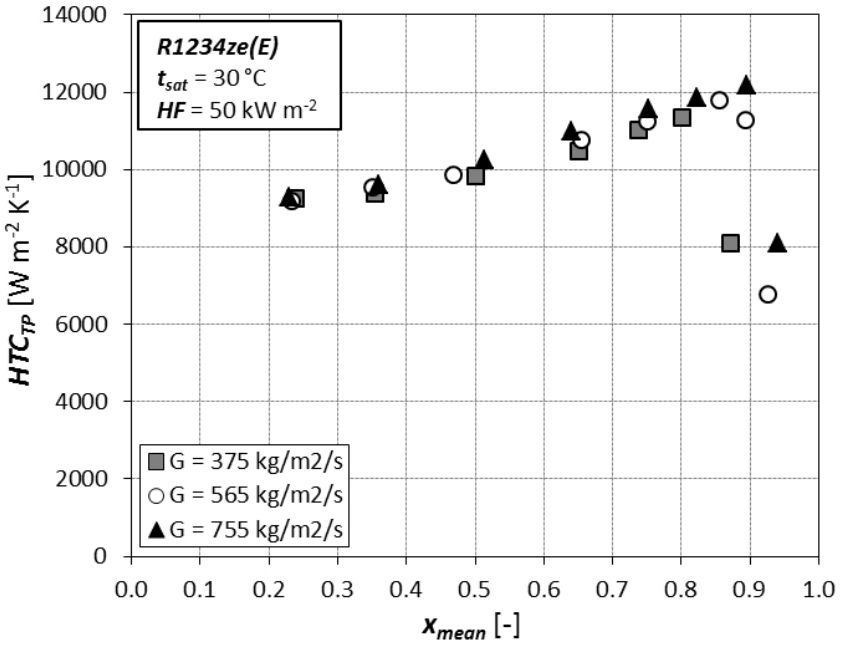

Figure 6.16: R1234ze(E) two phase heat transfer coefficient as a function of the mean vapor quality at constant heat flux HF=25 kW m^{-2}.

mean vapour quality at constant heat flux of 50 kW m^{-2}. In these operating conditions, no effect of the mass velocity can be observed for vapour qualities lower than 0.50, whereas a weak effect of the mass velocity can be noticed at higher vapour qualities. The vapour quality at the onset of the dryout is found to increase as the mass velocity increases, being around 0.82, 0.89, and 0.91 for mass velocity of 375, 565, and 755 kg m^{-2} s^{-1}.

Figure 6.17 permits to highlight the effects of the heat flux on the two-phase heat transfer coefficient measured at $G = 375$ kg m^{-2} s^{-1}. At 10 and 25 kW m^{-2}, the heat transfer coefficient increases almost linearly with vapour quality; at the lowest imposed heat flux, the dryout phenomenon does not occur, while at 25 kW m^{-2}, the onset of the dryout phenomenon is observed at vapour quality of 0.89. At vapour quality lower than 0.35, the heat transfer coefficient increases as the heat flux increases, while at higher vapour qualities the heat transfer coefficient seems to be independent on the heat flux. At $HF = 50$ kW m^{-2}, a plateau where the heat transfer coefficient seems to be weakly dependent on the vapour quality appears, and it ends at around $x_{mean} = 0.40$; then, the heat transfer coefficient increases

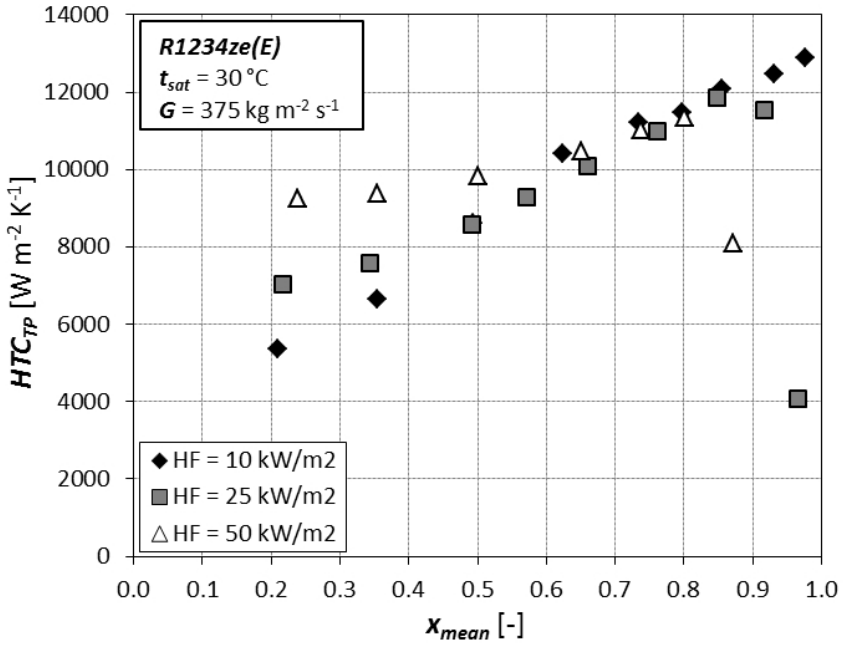

Figure 6.17: R1234ze(E) two phase heat transfer coefficient as a function of the mean vapor quality at constant mass velocity G=375 kg m^{-2} s^{-1}.

with vapour quality. Therefore, at low heat flux, the flow boiling heat transfer is influenced by the two-phase forced convection, in fact the heat transfer coefficient increases with vapour quality. At higher heat flux, especially at low vapour quality, the nucleate boiling becomes more and more important dominating the phase change process; in this region, higher the heat flux, higher the heat transfer coefficient. As the vapour quality increases, the nucleate boiling seems to be suppressed by the two-phase forced convection, and as a result the heat transfer coefficients measured at 10, 25, and 50 kW m^{-2} before the onset of dryout is almost the same. Finally, it can be noticed that at $HF = 25$ kW m^{-2} and $HF = 50$ kW m^{-2}, the dryout phenomenon occurs passing from $x_{do} = 0.89$ to $x_{do} = 0.82$, respectively.

The heat transfer coefficient plotted against the mean vapour quality at fixed mass velocity of 565 kg m^{-2} s^{-1} are reported in figure 6.18. Generally speaking, the two-phase heat transfer coefficient increases with increasing vapour quality for all the investigated heat fluxes. At vapour quality lower than 0.40, the heat transfer coefficient increases when increasing the heat flux, meaning the presence of the nucleate boiling. At higher vapour quality, the values carried out at heat flux $HF =$

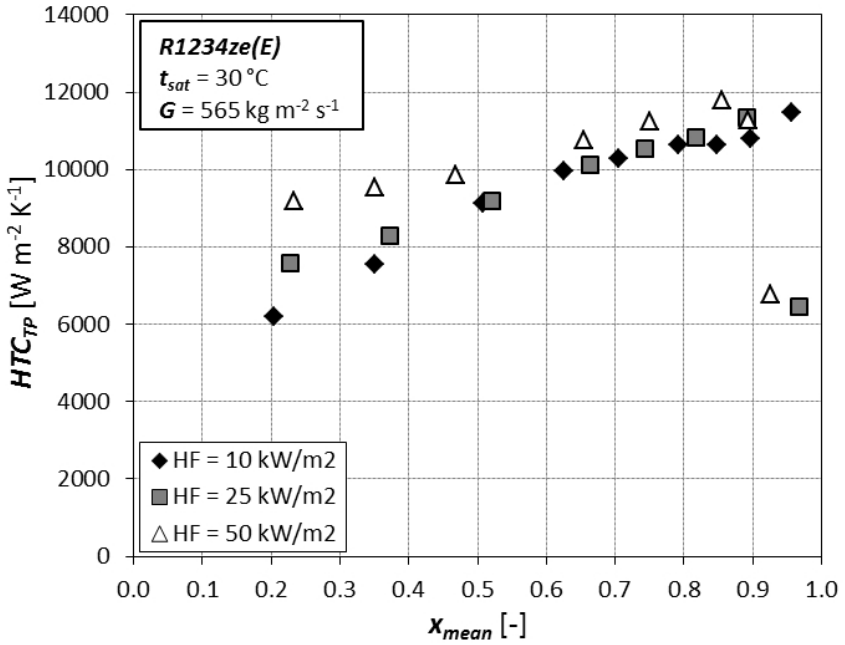

Figure 6.18: R1234ze(E) two phase heat transfer coefficient as a function of the mean vapor quality at constant mass velocity G=565 kg m^{-2} s^{-1}.

10 kW m^{-2} and HF = 25 kW m^{-2} are almost the same, whereas the values at $HF = 50$ kW m^{-2} are slightly higher. Thus, in these operating conditions, the two heat transfer mechanisms, i.e. nucleate boiling and two-phase forced convection, seems to coexist. No experimental evidence of the dryout phenomenon is observed at $HF = 10$ kW m^{-2}, whereas it occurs at $HF = 25$ kW m^{-2} and $HF = 50$ kW m^{-2}, being at $x_{do} = 0.92$ and $x_{do} = 0.89$, respectively.

The results at 755 kg m^{-2} s^{-1} are reported in figure 6.19. When increasing the mass velocity, the two-phase forced convection is strengthened and, as shown in the diagram, at all the investigated heat fluxes, the heat transfer coefficient increases with the vapour quality, meaning the presence of the two-phase forced convection. At constant vapour quality, especially for $x_{mean} < 0.40$, the heat transfer coefficient increases as the heat flux increases. Furthermore, no plateau is exhibited at any heat flux meaning that the two heat transfer mechanisms give their contribute to the phase change without dominating or suppress the other one. The dryout phenomenon occurs at 25 and 50 kW m^{-2} and the vapour quality at its onset decreases as the heat flux increases, passing from $x_{do} = 0.96$ at $HF = 25$ kW m^{-2} to

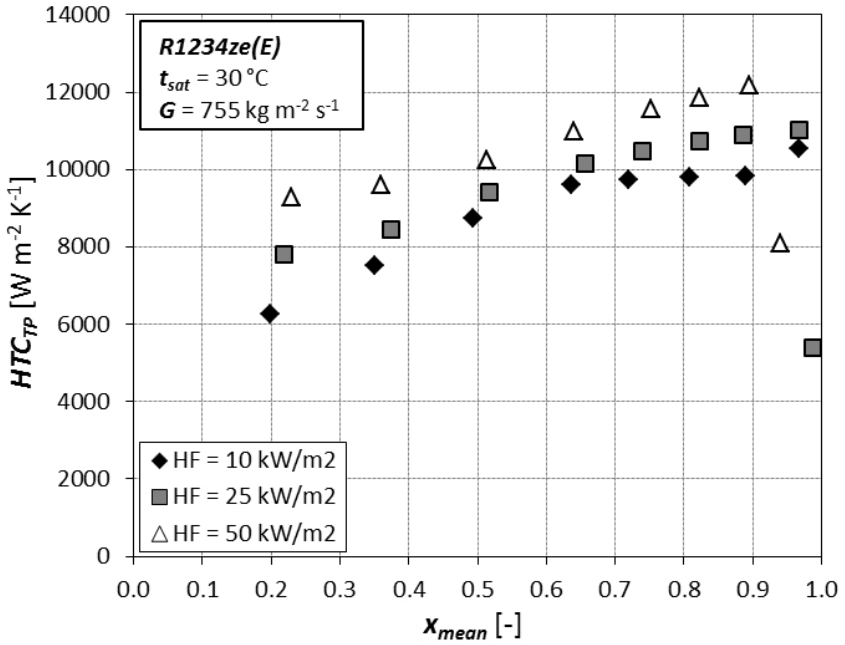

Figure 6.19: R1234ze(E) two phase heat transfer coefficient as a function of the mean vapor quality at constant mass velocity G=755 kg m^{-2} s^{-1}.

$x_{do} = 0.91$ at $HF = 50$ kW m^{-2}. Comparing figures 6.17-6.19, at constant heat flux, the vapour quality at the onset of dryout is delayed when increasing mass velocity. Figure 6.20 summarizes the vapour quality at the onset of the dryout.

Figure 6.21 reports the experimental measurements carried out at constant inlet vapour quality $x_{in} = 0.30$ by varying the heat flux up to the onset of the dryout. Three mass velocities were investigated: 190, 375, and 565 kg m^{-2} s^{-1}, in order to highlight the heat transfer behaviour at operating conditions similar to those that can be found in an actual refrigerating machine. The effects of the mass velocity on the heat transfer coefficient can be noticed up to $HF = 30$ kW m^{-2}, in particular it increases as the refrigerant mass flux increases; after that heat flux, the heat transfer coefficient is almost the same at all the investigated mass velocities before the dryout phenomenon. As expected, the vapour quality at the onset of the dryout phenomenon increases as the mass velocity increases, being $HF_{do} = 40$ kW m^{-2} at $G = 190$ kg m^{-2} s^{-1}, $HF_{do} = 85$ kW m^{-2} at $G = 375$ kg m^{-2} s^{-1}, and $HF_{do} = 135$ kW m^{-2} at $G = 565$ kg m^{-2} s^{-1}.

The diagram plotted in figure 6.22 shows the effects of the mass velocity and

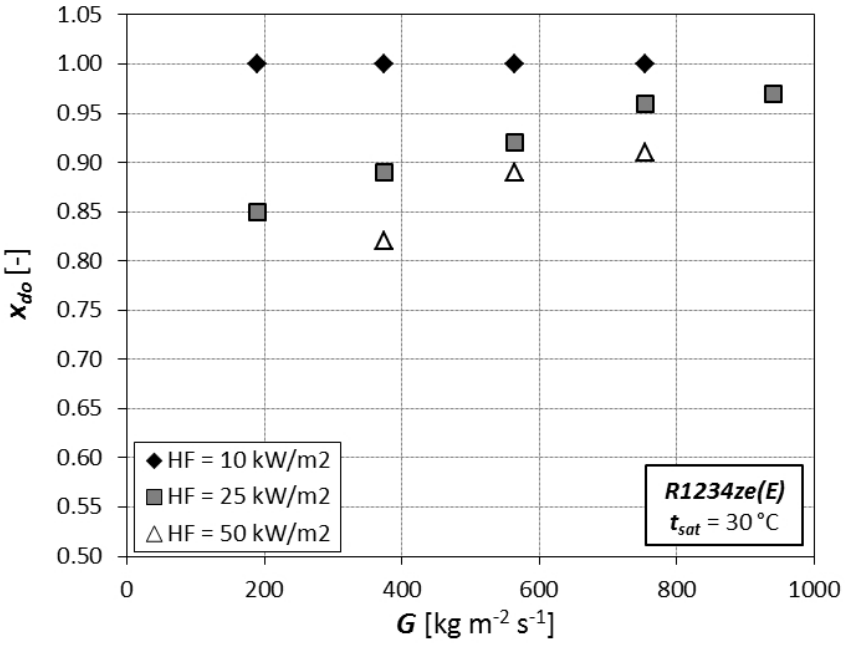

Figure 6.20: Effect of the heat flux on the vapour quality at the onset of the dryout as a function of velocity for the refrigerant R1234ze(E).

vapour quality on the two-phase frictional pressure gradients; the Rouhani and Axelsson [111] model was used to estimate the void fraction values to account for the momentum pressure gradient. The results show that, at constant mass velocity, the frictional pressure gradient increases with vapour quality, reaching a maximum value and, then, it decreases. At constant vapour quality, the frictional pressure gradient increases as the mass velocity increases.

Figure 6.23 reports the saturation temperature drop as a function of the mean vapour quality at constant heat flux of 25 kW m^2 for five different mass velocities: 190, 375, 565, 755, 940 kg m^{-2} s^{-1}. The trend is similar to that of pressure drops: at constant mass velocity, the saturation temperature drop increases with vapour quality up to a maximum, then it slightly decreases; at constant vapour quality, it increases with mass velocity. Similar results were obtained for the other heat fluxes investigated.

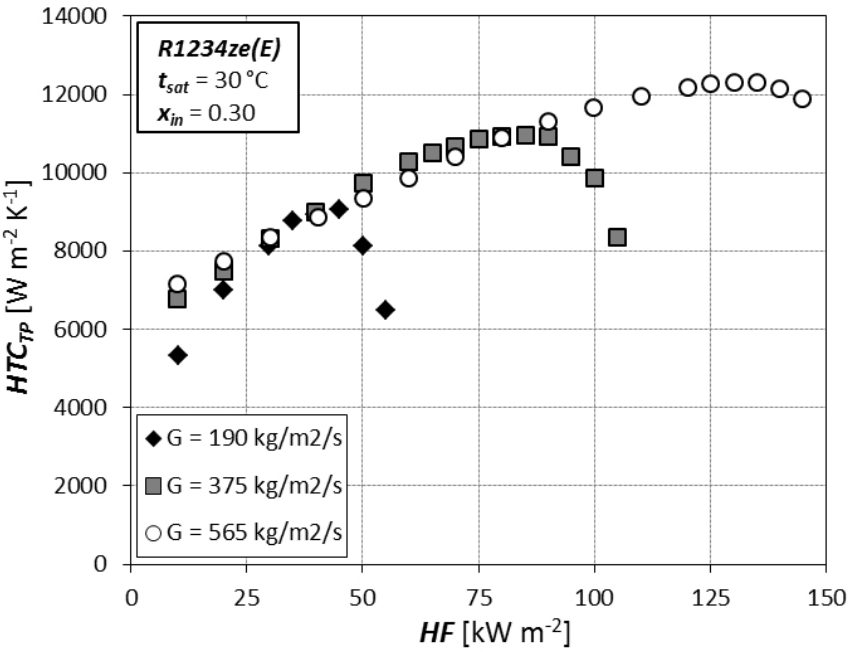

Figure 6.21: Effect of the mass velocity on the R1234ze(E) heat transfer coefficient at different heat flux.

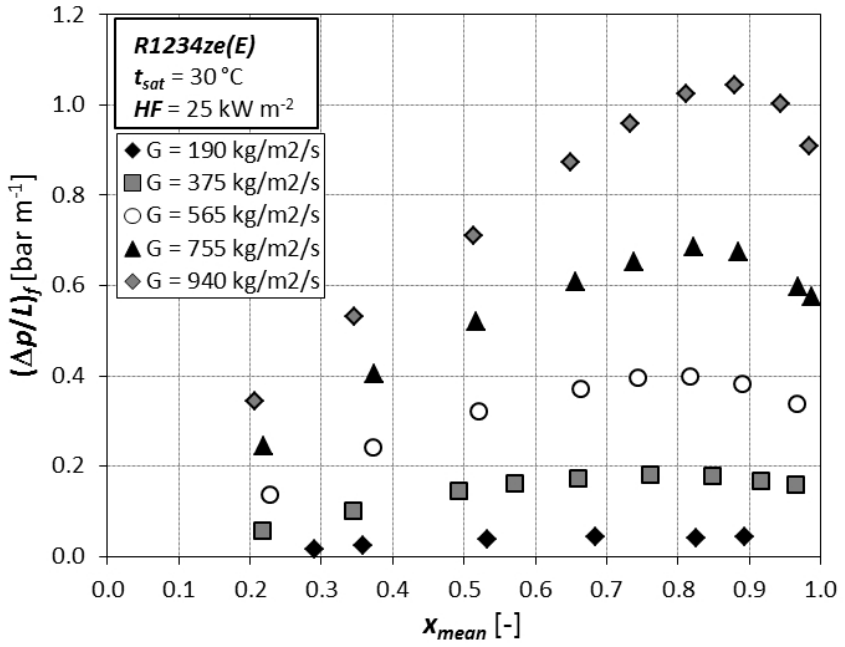

Figure 6.22: R1234ze(E) two phase frictional pressure gradient as a function of the mean vapor quality at constant heat flux HF=25 kW m^{-2}.

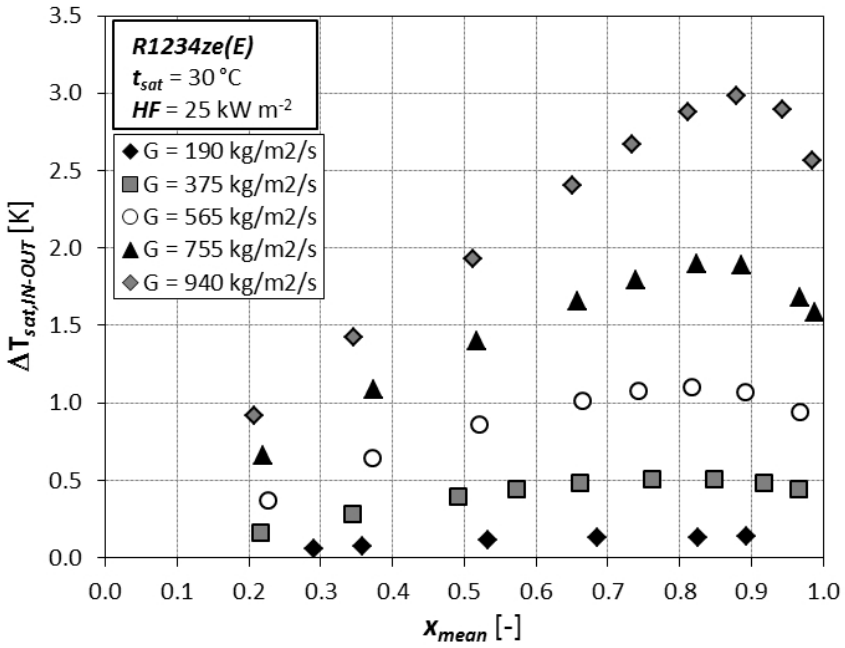

Figure 6.23: R1234ze(E) saturation temperature drop as a function of the mean vapor quality at constant heat flux HF=25 kW m^{-2}.

6.4.4 R1234yf

Figure 6.24 shows the two-phase heat transfer coefficient plotted against the vapour quality as a function of the mass velocity, at constant heat flux of 10 kW m^{-2}. The heat transfer coefficient at the lowest mass velocity (G = 190 kg m^{-2} s^{-1})

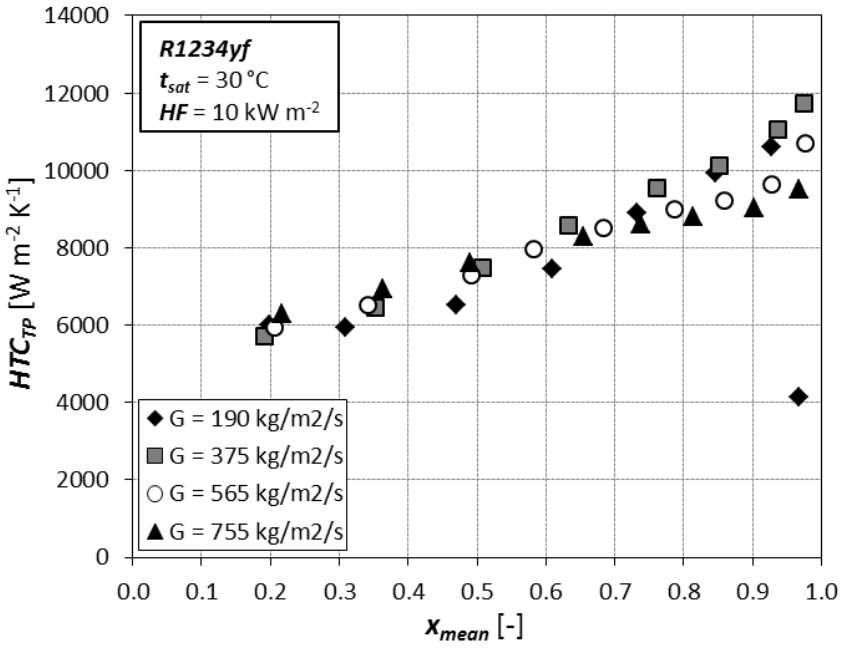

Figure 6.24: R1234yf two phase heat transfer coefficient as a function of the mean vapor quality at constant heat flux HF=10 kW m^{-2}.

is almost constant up to a vapour quality of approximately 0.40, being around 6000 W m^{-2} K^{-1}, then it increases with vapour quality. When increasing the mass velocity, the plateau disappears, and the heat transfer coefficient increases when increasing vapour quality for all the investigated mass velocities. It is interesting to point out that at vapour quality higher than 0.60, the highest heat transfer coefficient is exhibited by the mass velocity G = 375 kg m^{-2} s^{-1}, as previously described for the refrigerant R134a, whereas the lowest value of heat transfer coefficient is shown for the highest mass velocity (G = 765 kg m^{-2} s^{-1}) at vapour quality higher than 0.60. Unlike the previous refrigerants, for the refrigerant R1234yf the dryout phenomenon is observed at HF = 10 kW m^{-2} at the mass velocity of 190 kg m^{-2} s^{-1}.

The results carried out at constant heat flux of 25 kW m^{-2} are shown in figure

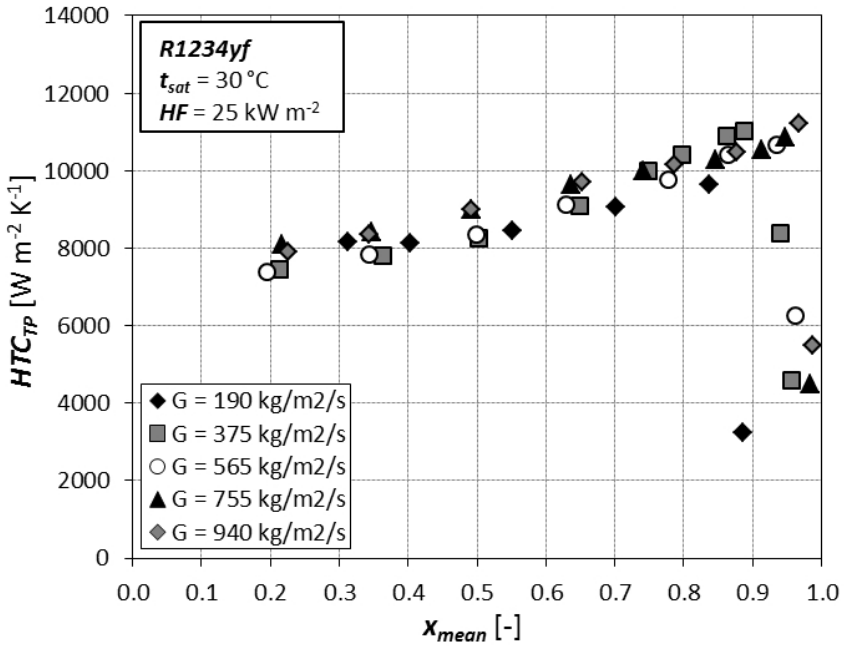

Figure 6.25: R1234yf two phase heat transfer coefficient as a function of the mean vapor quality at constant heat flux HF=25 kW m^{-2}.

6.25. The plateau at $G = 190$ kg m^{-2} s^{-1}, being around 8100 W m^{-2} K^{-1}, is up to a vapour quality of 0.50, thus it seems that the phase change process is controlled by the nucleate boiling; at higher vapour quality the heat transfer coefficient increases with vapour quality, meaning that the two-phase forced convection affects the heat transfer mechanism. The plateau disappears at higher mass velocities. At vapour quality higher than 0.75, the highest heat transfer coefficients are again exhibited by the mass velocity of 375 kg m^{-2} s^{-1}. The dryout phenomenon occurs at all the investigated mass velocities, and it is delayed when increasing mass velocity, passing from vapour quality of 0.85 to 0.96 for mass velocity of 190 and 940 kg m^{-2} s^{-1}, respectively.

Figure 6.26 shows the two-phase heat transfer coefficient plotted against the mean vapour quality at constant heat flux of 50 kW m^{-2}. In these operating conditions, there is not any appreciable effect of the mass velocity on the heat transfer coefficient, which seems to be controlled by the nucleate boiling. There is a plateau for $x_{mean} < 0.50$, where the heat transfer is almost constant at a value of approximately 10000 W m^{-2} K^{-1} for all the mass velocities, and then the two-phase heat

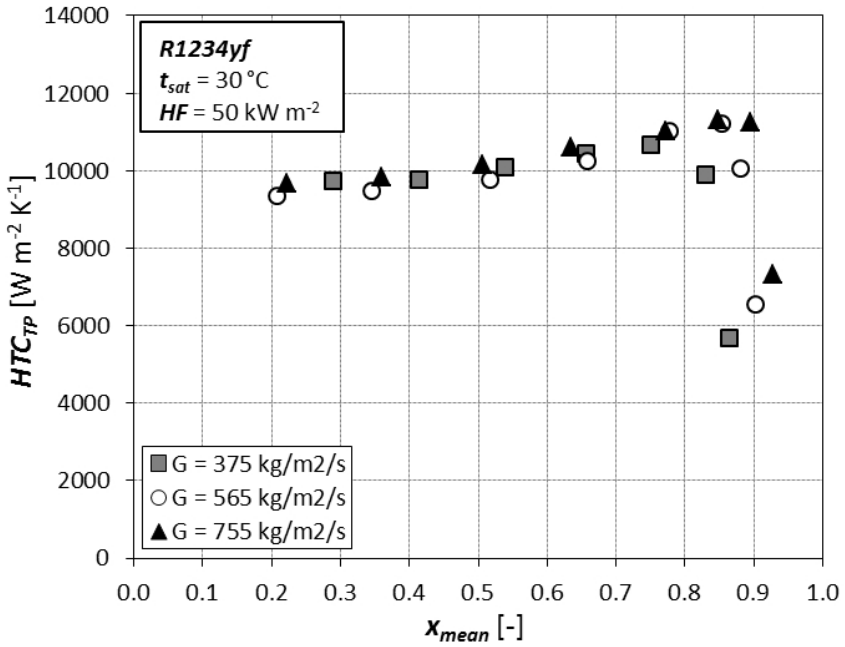

Figure 6.26: R1234yf two phase heat transfer coefficient as a function of the mean vapor quality at constant heat flux HF=25 kW m^{-2}.

transfer coefficient slightly increases with the vapour quality. The values of the vapour quality at the onset of the dryout increases as the mass velocity increases.

Figure 6.27 permits to highlight the effects of the heat flux on the two-phase heat transfer coefficient measured at $G = 375$ kg m^{-2} s^{-1}. There is a strong relationship between the heat transfer coefficient and the heat flux. For vapour quality lower than 0.75, the heat transfer coefficient increases when increasing heat flux. At 10 kW m^{-2} and 25 kW m^{-2}, the heat transfer coefficient increases with vapour quality, whereas it remains almost constant up to $x_{mean} = 0.50$ at $HF = 50$ kW m^{-2}. The dryout phenomenon occurs at $HF = 25$ kW m^{-2} and $HF = 50$ kW m^{-2}, and the vapour quality at its onset decreases as the heat flux increases, passing from 0.89 to 0.82, respectively.

The experimental results carried out at $G = 565$ kg m^{-2} s^{-1} are reported in figure 6.28. In these operating conditions, higher the heat flux, higher the two-phase heat transfer coefficient, at all vapour qualities. The values of the heat transfer coefficient at $HF = 10$ kW m^{-2} and $HF = 25$ kW m^{-2} increase almost linearly with vapour quality, where at $HF = 50$ kW m^{-2} they show a plateau up to $x_{mean} = 0.50$,

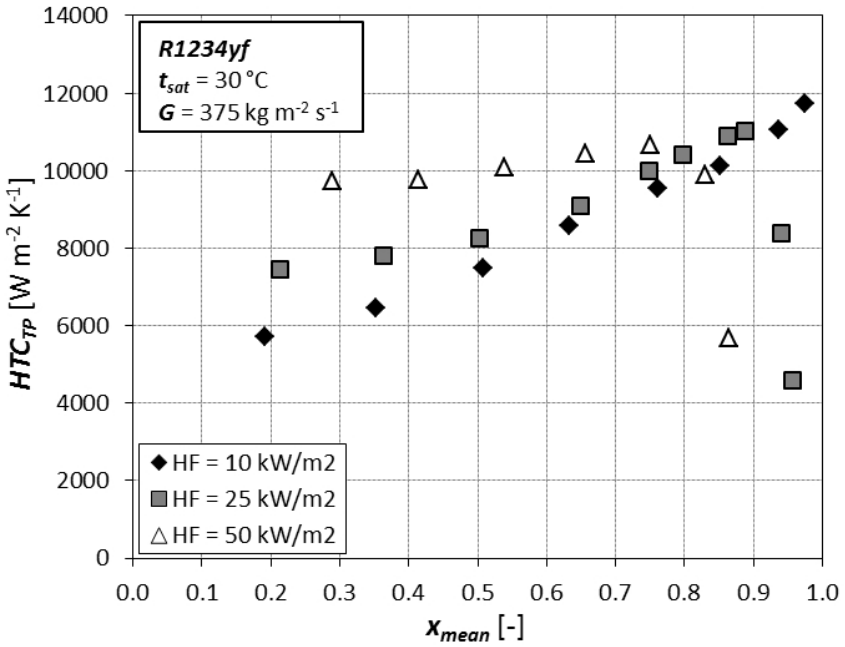

Figure 6.27: R1234yf two phase heat transfer coefficient as a function of the mean vapor quality at constant mass velocity G=375 kg m^{-2} s^{-1}.

where they are constant at about 9500 W m^{-2} K^{-1}. Therefore, it seems that, in these operating conditions, nucleate boiling controls the phase change process at low vapour qualities and high heat fluxes, whereas at higher vapour quality and lower heat flux the two mechanisms, i.e. nucleate boiling and two-phase forced convection, are combined rather than competitive. The dryout phenomenon occurs at $HF = 25$ kW m^{-2} and $HF = 50$ kW m^{-2}, being at vapour quality of 0.94 and 0.86, respectively.

Figure 6.29 shows the two-phase heat transfer coefficient against the mean vapour quality at a fixed mass velocity of 755 kg m^{-2} s^{-1}. At all the investigated mass fluxes, the heat transfer coefficient increases with the vapour quality meaning that the two-phase forced convection dominates the phase change process. At constant vapour quality, the heat transfer coefficient increases as the heat flux increases; furthermore, no plateau is exhibited at any heat flux, meaning that the two heat transfer mechanisms give their contribute without dominating or suppress the other one. The dryout phenomenon occurs at $HF = 25$ kW m^{-2} and $HF = 50$ kW m^{-2}, and the vapour quality at its onset decreases with heat flux, being 0.96 and 0.88,

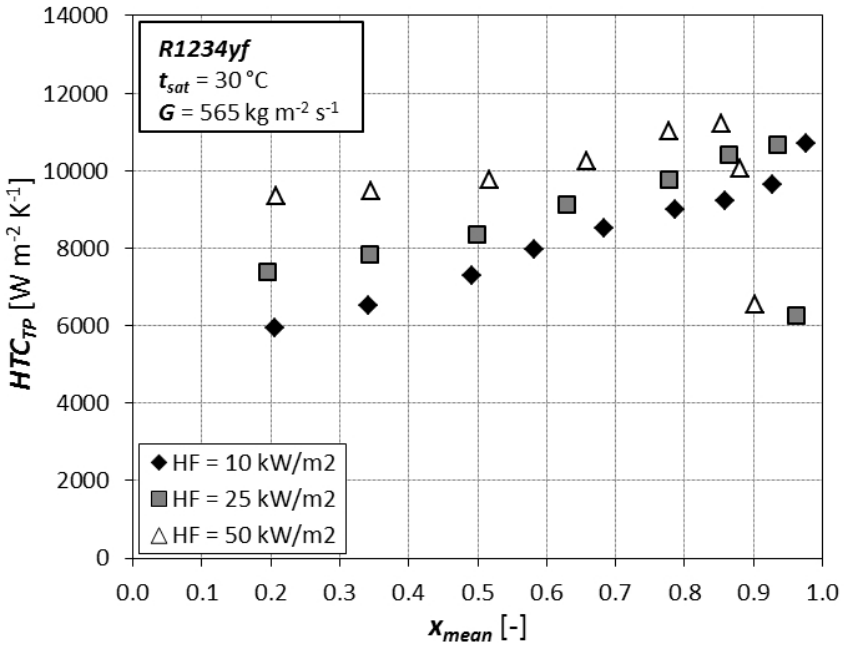

Figure 6.28: R1234yf two phase heat transfer coefficient as a function of the mean vapor quality at constant mass velocity G=565 kg m^{-2} s^{-1}.

respectively. Figure 6.30 summarizes the vapour quality at the onset of the dryout.

Figure 6.31 shows the effect of the mass velocity on the heat transfer coefficient against the heat flux at constant inlet vapour quality of 0.30. The apexes of each curve indicate the critical value of heat flux at the onset of the dryout phenomenon. No appreciable effects of the mass velocity on the heat transfer coefficient can be observed. As expected, the critical heat flux increases as the mass velocity increases, being $HF_{do} = 40$ kW m^{-2} at $G = 190$ kg m^{-2} s^{-1}, $HF_{do} = 80$ kW m^{-2} at $G = 375$ kg m^{-2} s^{-1}, and $HF_{do} = 115$ kW m^{-2} at $G = 565$ kg m^{-2} s^{-1}.

Figure 6.32 shows the effects of the mass velocity and vapour quality on the two-phase frictional pressure gradients; the Rouhani and Axelsson [111] model was used to estimate the void fraction values to account for the momentum pressure gradient. At constant mass velocity, the two-phase frictional pressure gradient increases with increasing vapour quality up to a maximum, after which it decreases. Keeping constant the vapour quality, the pressure gradient increases as mass velocity increases.

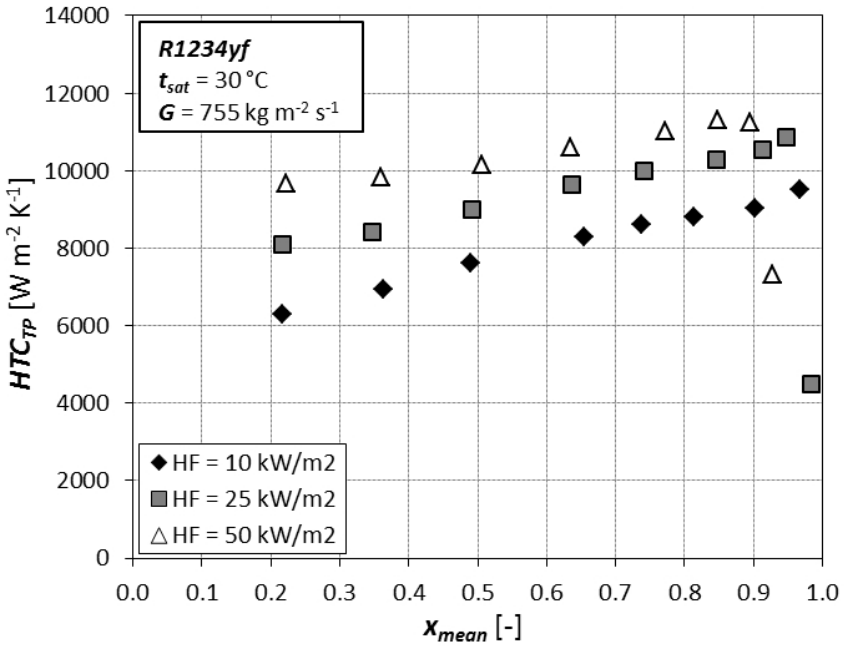

Figure 6.29: R1234yf two phase heat transfer coefficient as a function of the mean vapor quality at constant mass velocity G=755 kg m^{-2} s^{-1}.

In the end, figure 6.33 reports the saturation temperature drop as a function of the mean vapour quality at constant heat flux of 25 kW m^2 for five different mass velocities: 190, 375, 565, 755, 940 kg m^{-2} s^{-1}. The trend is similar to that of pressure drops: at constant mass velocity, the saturation temperature drop increases with vapour quality up to a maximum, then it slightly decreases; at constant vapour quality, it increases with mass velocity. Similar results were obtained for the other heat fluxes investigated.

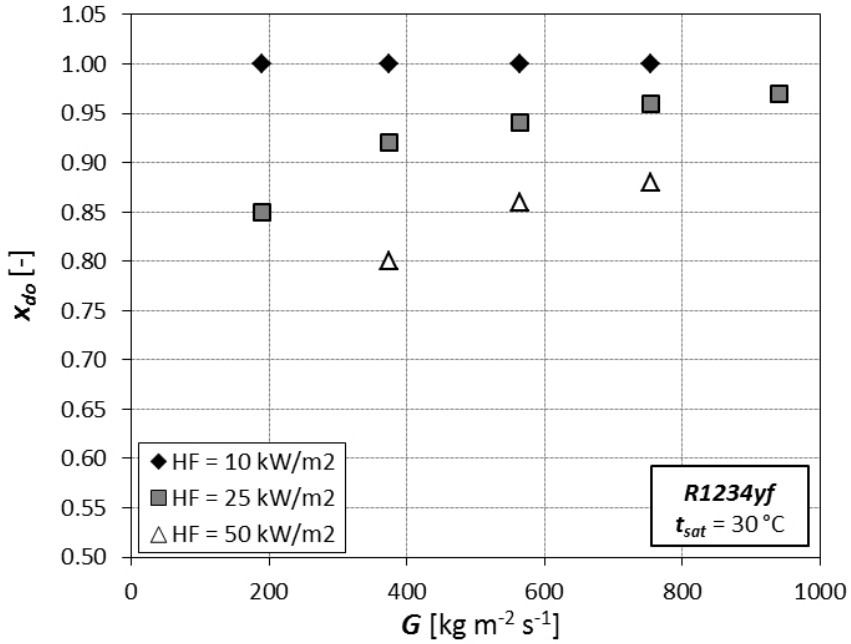

Figure 6.30: Effect of the heat flux on the vapour quality at the onset of the dryout as a function of velocity for the refrigerant R1234yf.

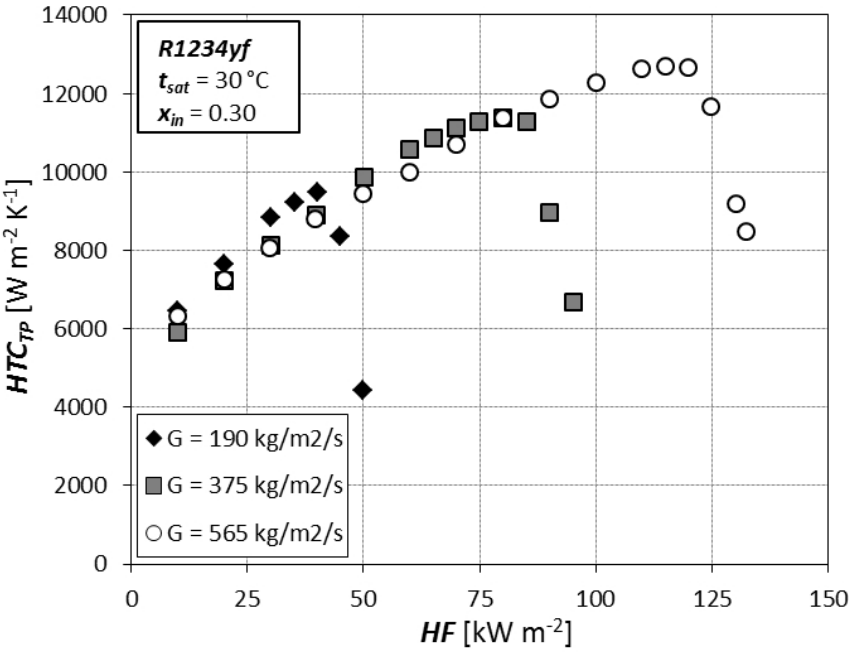

Figure 6.31: Effect of the mass velocity on the R1234yf heat transfer coefficient at different heat flux.

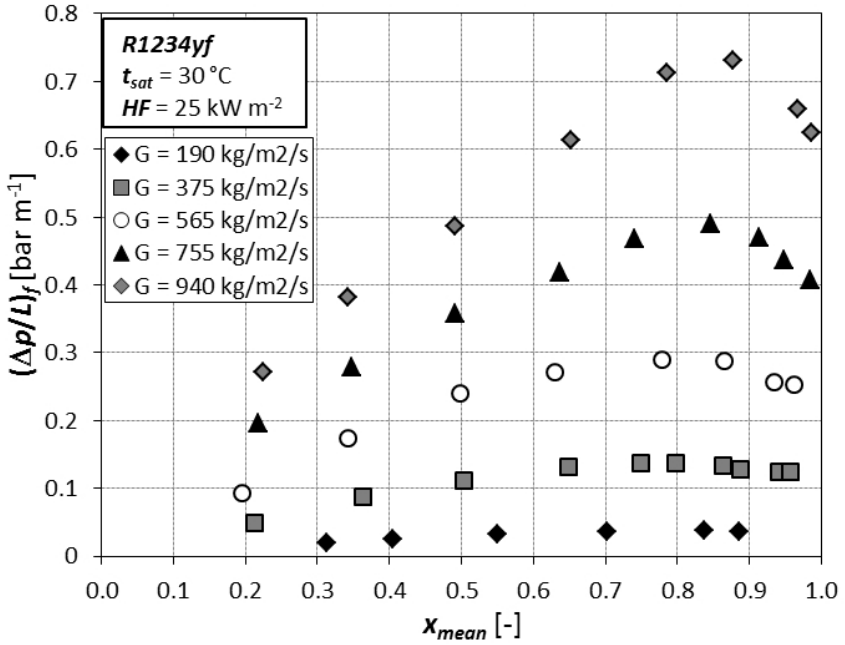

Figure 6.32: R1234yf two phase frictional pressure gradient as a function of the mean vapor quality at constant heat flux HF=25 kW m^{-2}.

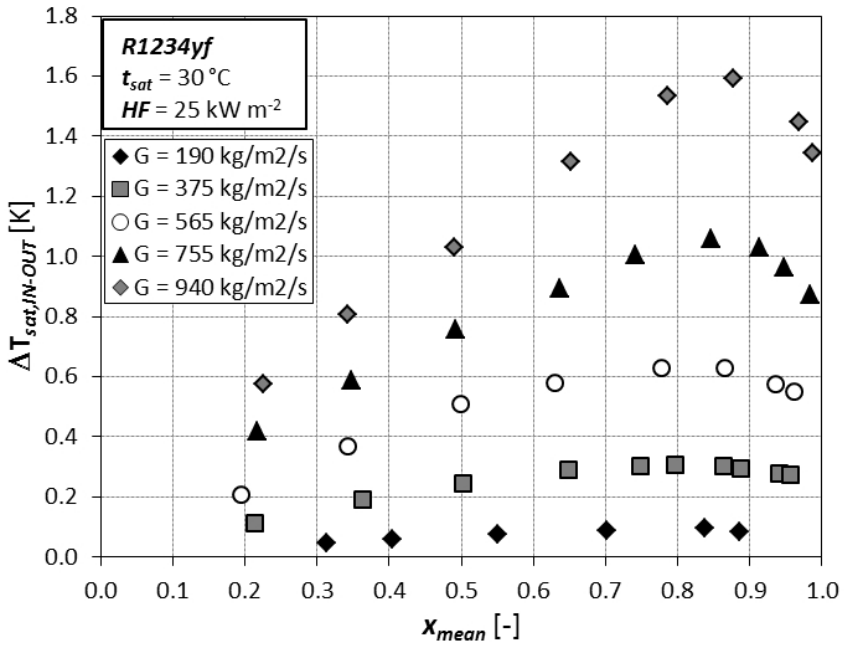

Figure 6.33: R1234yf saturation temperature drop as a function of the mean vapor quality at constant heat flux HF=25 kW m^{-2}.

6.4.5 Comparison among different refrigerants

Figures 6.34-6.45 compare two-phase heat transfer coefficient at fixed mass velocity G and heat flux HF for the three different refrigerants. As it appears from the figures, at fixed heat flux $HF = 10$ kW m^{-2} and $G = 190$ kg m^{-2} s^{-1}, the refrigerant R1234yf has slightly higher two-phase heat transfer coefficient up to a vapour quality of 0.8, after which no differences can be observed among the three refrigerants. At a fixed mass velocity of $G = 375$ kg m^{-2} s^{-1}, R134a shows better thermal performance at vapour quality higher than 0.5, whereas at low vapour quality R1234yf seems to have slightly higher heat transfer coefficient. At $G = 565$ kg m^{-2} s^{-1}, the three refrigerants shows almost the same values of HTC_{TP}. Finally, at $G = 755$ kg m^{-2} s^{-1}, R134a has higher heat transfer coefficient in all the investigated vapour qualities. Therefore, at the lowest tested heat flux, there is not any investigated refrigerant which performs better than the other two. In addition, no dryout phenomenon was observed at $HF = 10$ kW m^{-2} for all the refrigerants for all the investigated mass velocities, except at $G = 190$ kg m^{-2} s^{-1} with the refrigerant R1234yf.

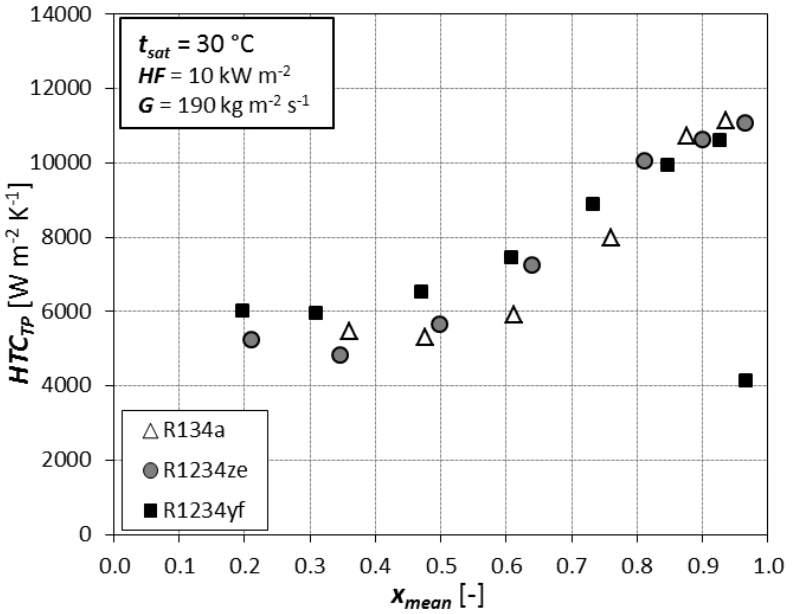

Figure 6.34: Comparison among R134a, R1234ze(E), and R1234yf two-phase heat transfer coefficient at G=190 kg m^{-2} s^{-1} and HF=10 kW m^{-2}.

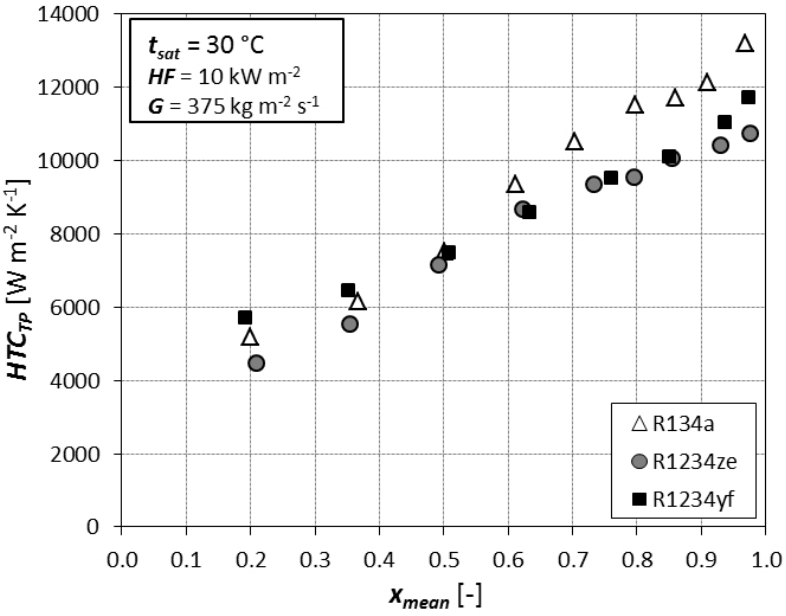

Figure 6.35: Comparison among R134a, R1234ze(E), and R1234yf two-phase heat transfer coefficient at G=375 kg m^{-2} s^{-1} and HF=10 kW m^{-2}.

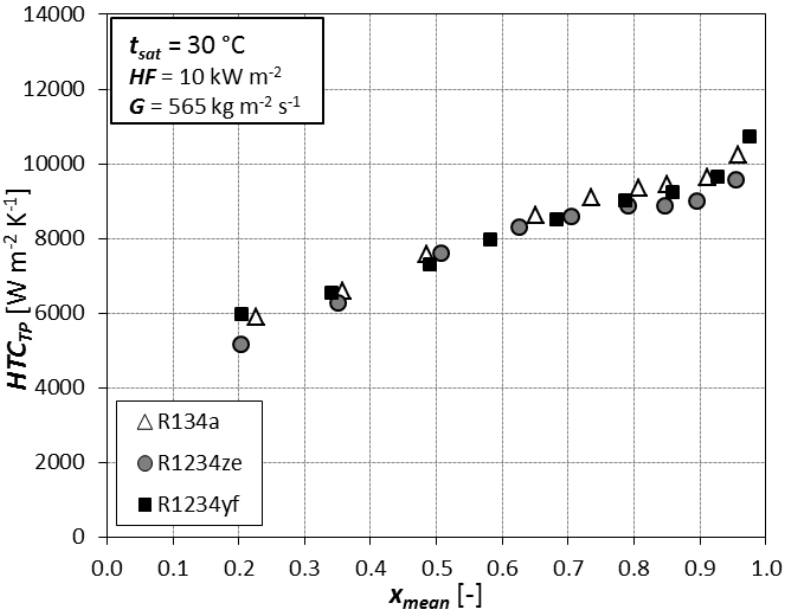

Figure 6.36: Comparison among R134a, R1234ze(E), and R1234yf two-phase heat transfer coefficient at G=565 kg m^{-2} s^{-1} and HF=10 kW m^{-2}.

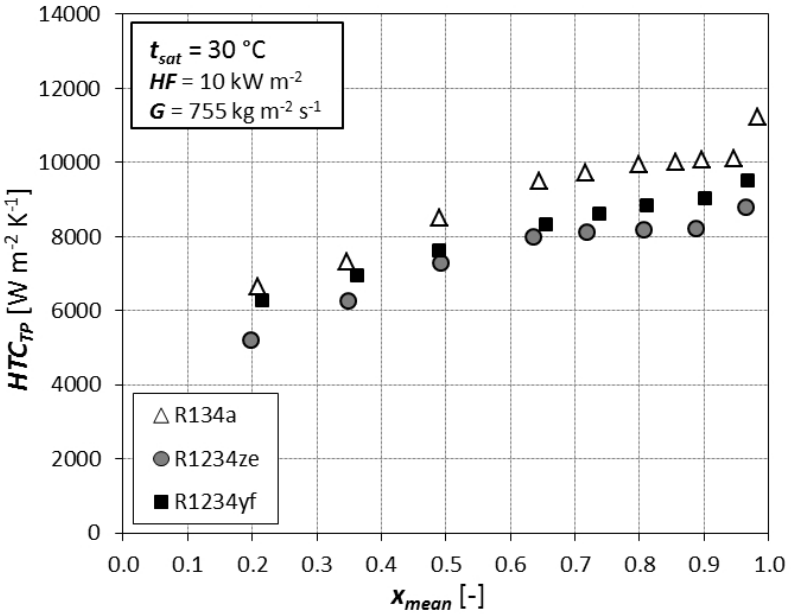

Figure 6.37: Comparison among R134a, R1234ze(E), and R1234yf two-phase heat transfer coefficient at G=755 kg m^{-2} s^{-1} and HF=10 kW m^{-2}.

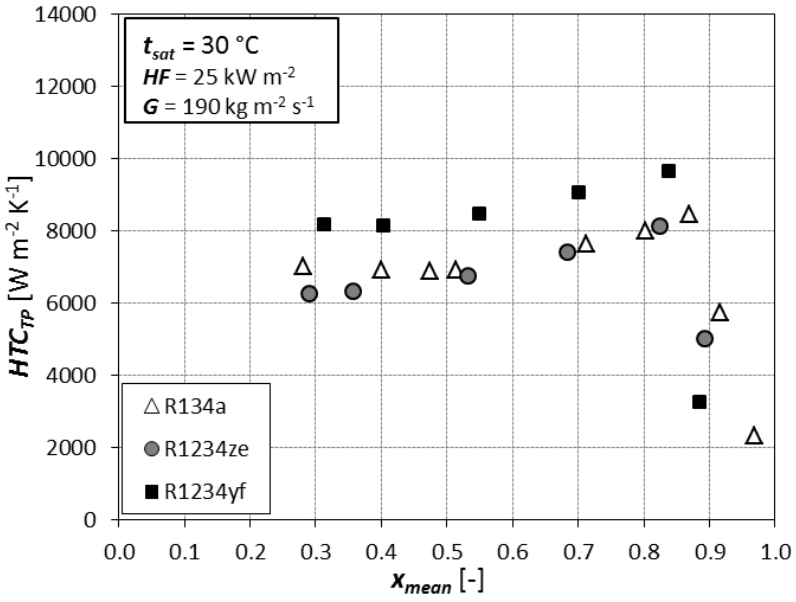

Figure 6.38: Comparison among R134a, R1234ze(E), and R1234yf two-phase heat transfer coefficient at G=190 kg m^{-2} s^{-1} and HF=25 kW m^{-2}.

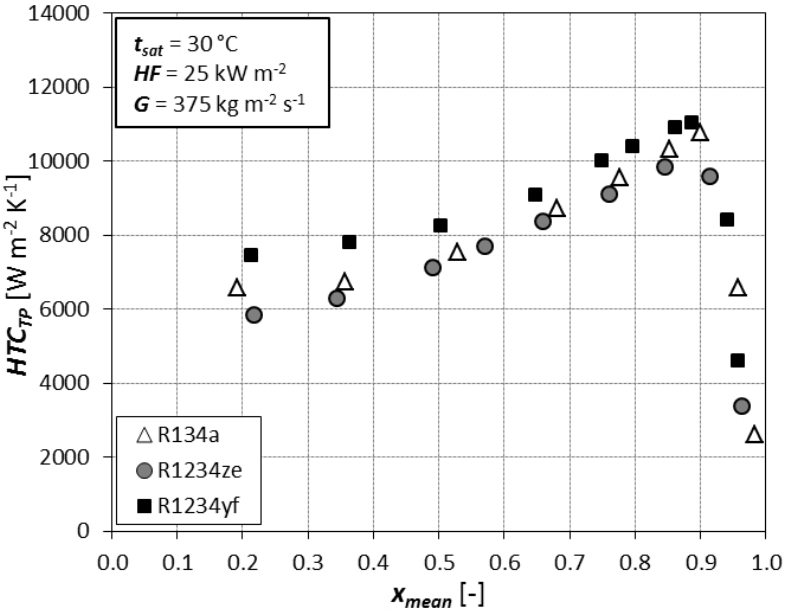

Figure 6.39: Comparison among R134a, R1234ze(E), and R1234yf two-phase heat transfer coefficient at G=375 kg m^{-2} s^{-1} and HF=25 kW m^{-2}.

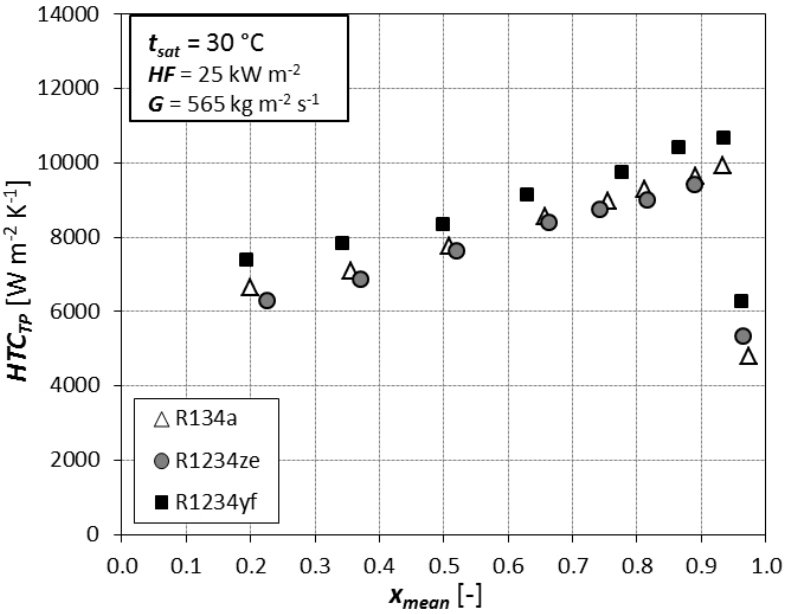

Figure 6.40: Comparison among R134a, R1234ze(E), and R1234yf two-phase heat transfer coefficient at G=565 kg m^{-2} s^{-1} and HF=25 kW m^{-2}.

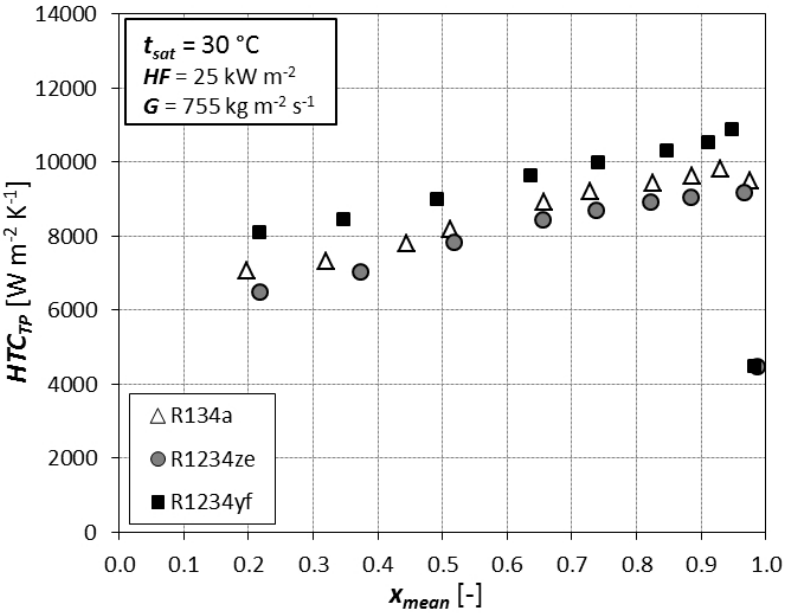

Figure 6.41: Comparison among R134a, R1234ze(E), and R1234yf two-phase heat transfer coefficient at G=755 kg m^{-2} s^{-1} and HF=25 kW m^{-2}.

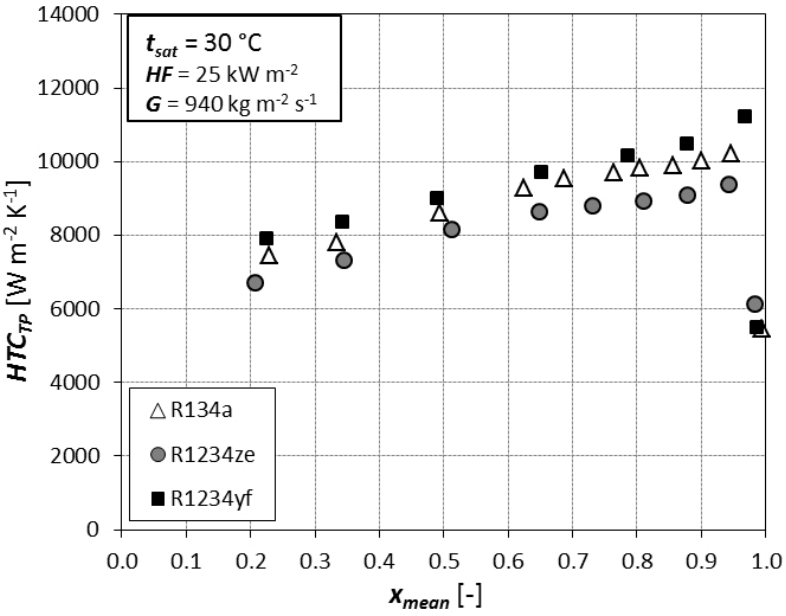

Figure 6.42: Comparison among R134a, R1234ze(E), and R1234yf two-phase heat transfer coefficient at G=940 kg m^{-2} s^{-1} and HF=25 kW m^{-2}.

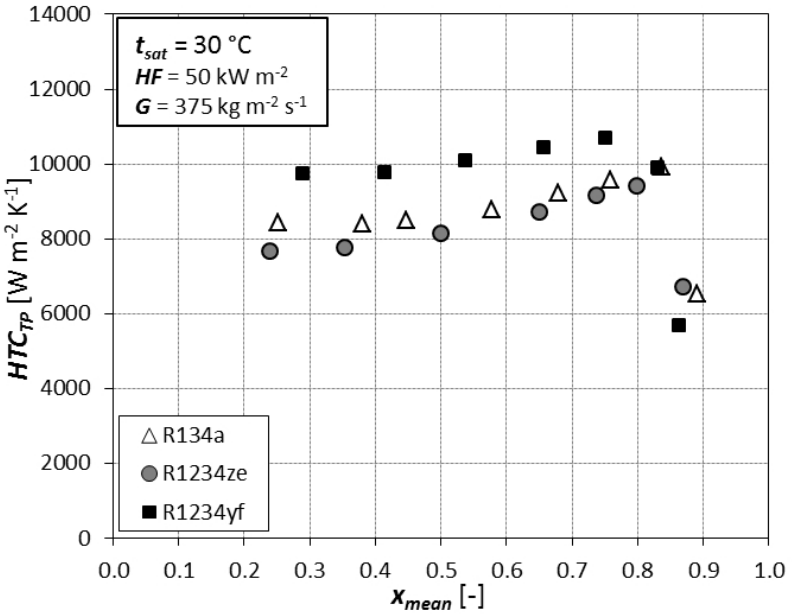

Figure 6.43: Comparison among R134a, R1234ze(E), and R1234yf two-phase heat transfer coefficient at G=375 kg m^{-2} s^{-1} and HF=50 kW m^{-2}.

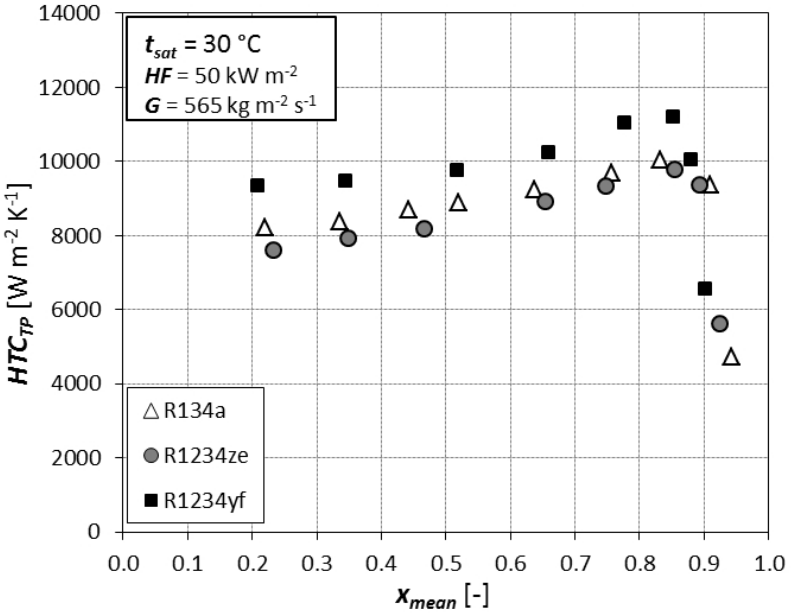

Figure 6.44: Comparison among R134a, R1234ze(E), and R1234yf two-phase heat transfer coefficient at G=565 kg m^{-2} s^{-1} and HF=50 kW m^{-2}.

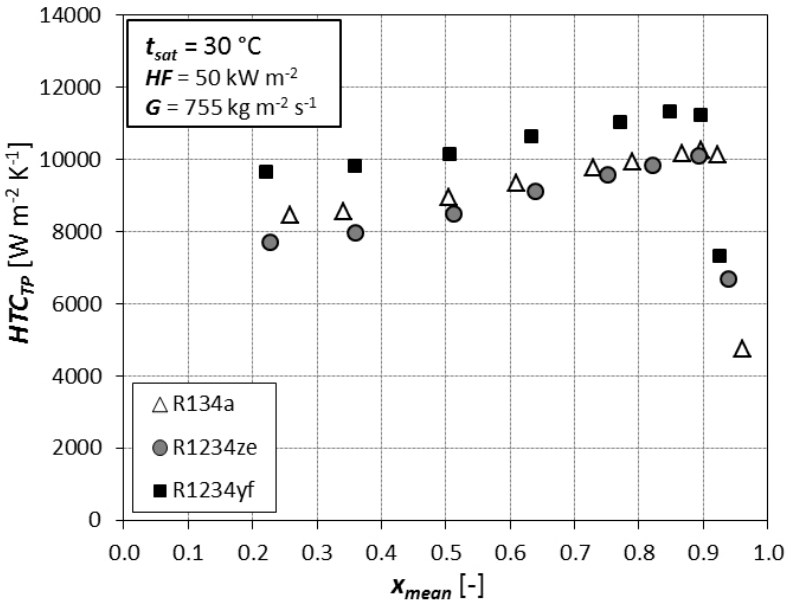

Figure 6.45: Comparison among R134a, R1234ze(E), and R1234yf two-phase heat transfer coefficient at G=755 kg m^{-2} s^{-1} and HF=50 kW m^{-2}.

Different observations can be drawn at heat fluxes of $HF = 25$ kW m^{-2} and $HF = 50$ kW m^{-2}. In these operative conditions, R1234yf shows higher values of the two-phase heat transfer coefficient, whereas R134a and R1234ze(E) have, on average, similar values.

Figures 6.46 and 6.47 show a comparison between vapour qualities at the onset of the dryout phenomenon at fixed heat flux of 25 kW m^{-2} and 50 kW m^{-2}, respectively, among the three investigated refrigerants. At fixed heat flux $HF = 25$ kW m^{-2} and $HF = 50$ kW m^{-2}, R134a, R1234ze(E), and R1234yf show almost the same values of the critical vapour quality, the differences are within the experimental uncertainty on the vapour quality.

The comparison between frictional pressure gradient is shown in figures 6.48-6.51.

At all the investigated mass velocities, R1234ze(E) shows the highest frictional pressure drop. This behaviour can be explained considering the vapour density: R1234ze(E) has the lowest vapour density among the three tested refrigerants, which leads to higher shear stress at fixed mass velocity, and thus to higher pressure drop.

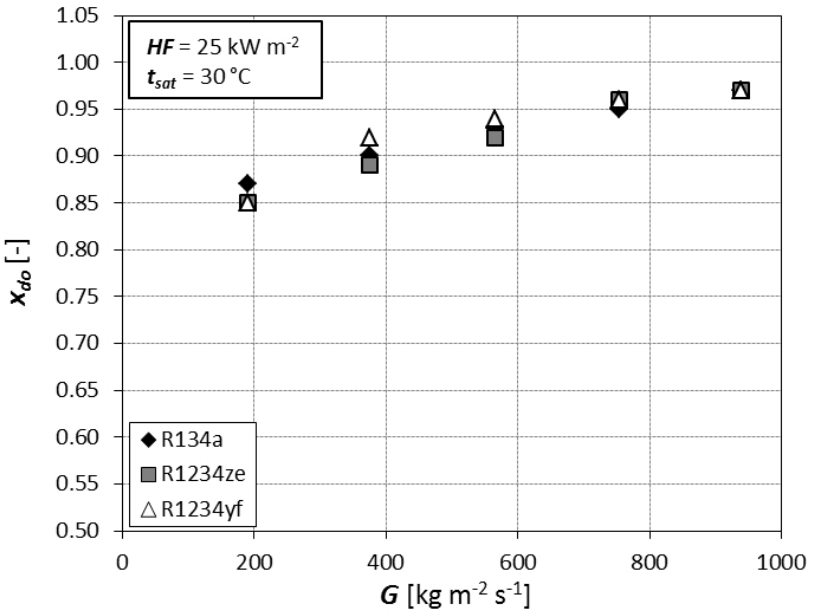

Figure 6.46: Comparison among R134a, R1234ze(E), and R1234yf vapour quality at the onset of the dryout phenomenon at HF=25 kW m^{-2}.

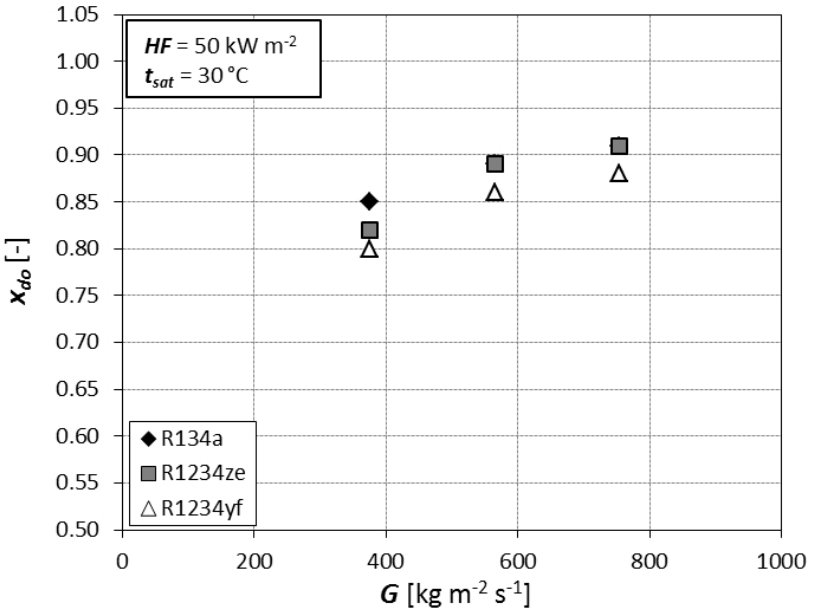

Figure 6.47: Comparison among R134a, R1234ze(E), and R1234yf vapour quality at the onset of the dryout phenomenon at HF=50 kW m^{-2}.

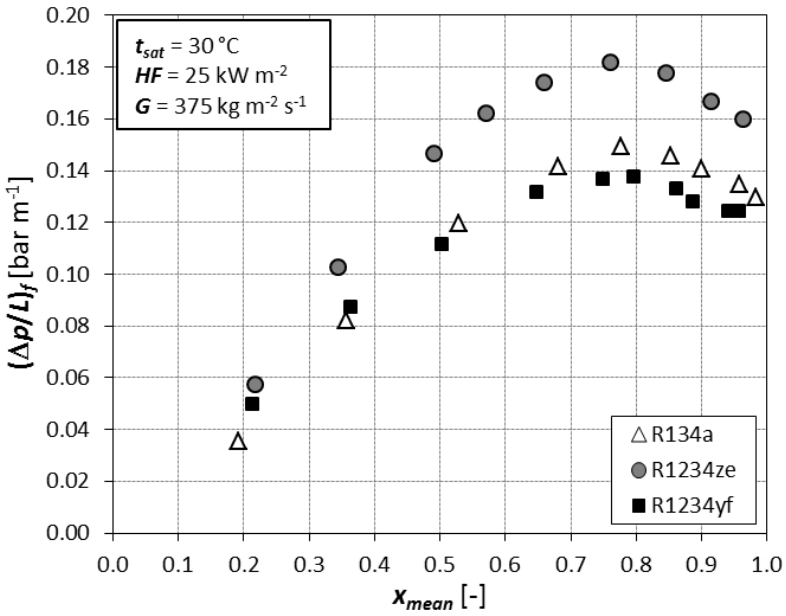

Figure 6.48: Comparison among R134a, R1234ze(E), and R1234yf frictional pressure gradient at G=375 kg m^{-2} s^{-1}.

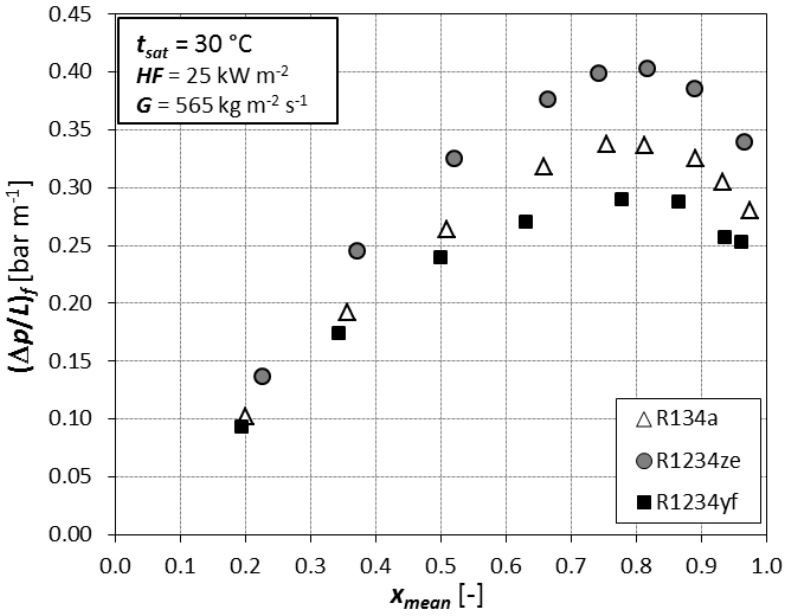

Figure 6.49: Comparison among R134a, R1234ze(E), and R1234yf frictional pressure gradient at G=565 kg m^{-2} s^{-1}.

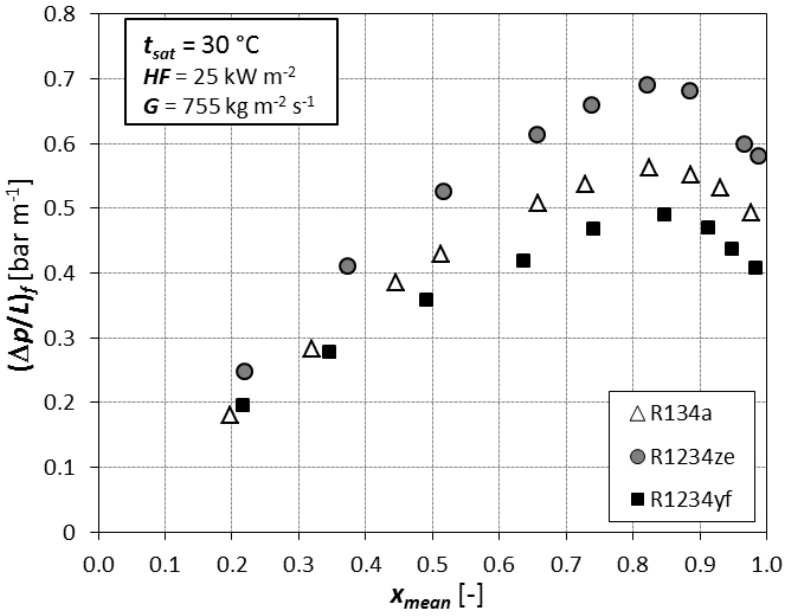

Figure 6.50: Comparison among R134a, R1234ze(E), and R1234yf frictional pressure gradient at G=755 kg m^{-2} s^{-1}.

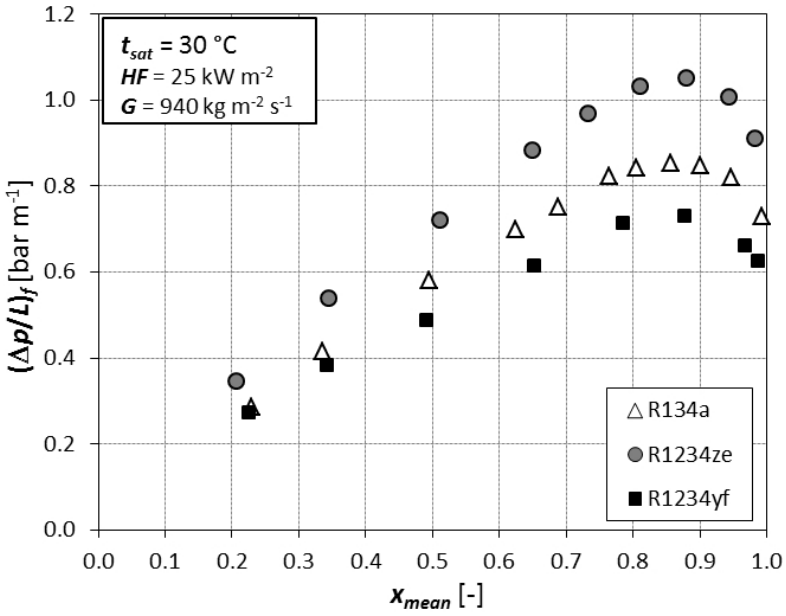

Figure 6.51: Comparison among R134a, R1234ze(E), and R1234yf frictional pressure gradient at G=940 kg m^{-2} s^{-1}.

Figures 6.52-6.54 compare the two-phase heat transfer coefficient as a function of the heat flux with an inlet vapour quality of 0.30 for the three investigated refrigerants. The apexes of the curves represent the critical heat flux, i.e. the value of the heat flux which leads to the onset of the dryout phenomenon. R1234yf presents the lowest values of the critical heat fluxes, whereas the values of R134a are slightly higher than that of R1234ze(E). It has to remember that the latent heat of vaporization at 30 °C of saturation temperature of the three refrigerants (see table 5.2) are 173 kJ kg^{-1}, 163 kJ kg^{-1}, and 141 kJ kg^{-1} for R134a, R1234ze(E), and R1234yf, respectively. In addition, the curves of R1234yf after the critical heat flux are steeper than the other two refrigerants.

Figures 6.55-6.57 compare the saturation temperature drop of the three refrigerants at constant mass velocity of $G = 375$ kg m^{-2} s^{-1}, $G = 565$ kg m^{-2} s^{-1}, $G = 755$ kg m^{-2} s^{-1}, and $G = 940$ kg m^{-2} s^{-1}, respectively. R1234ze(E) shows higher values of saturation temperature drop for all the investigated mass velocities, whereas R134a and R1234yf have similar values. It is interesting to highlight that

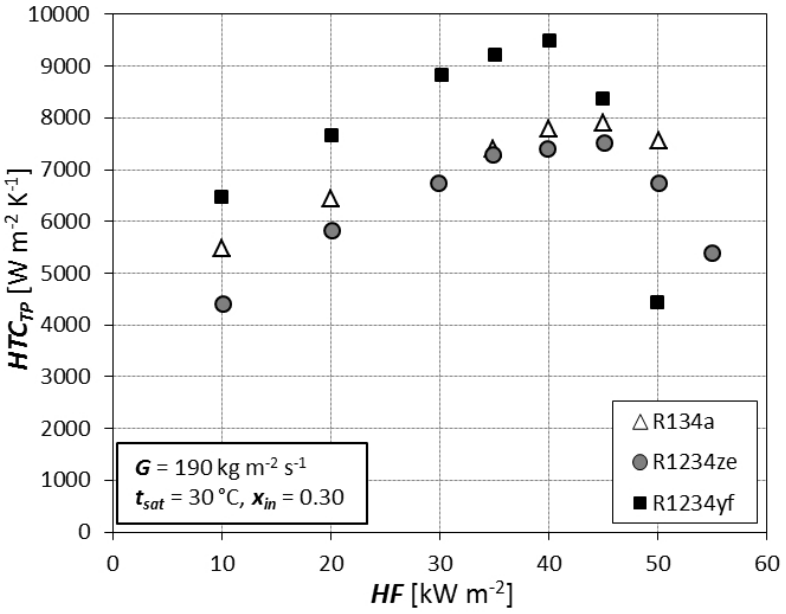

Figure 6.52: Comparison among R134a, R1234ze(E), and R1234yf critical heat flux with an inlet vapour quality of 0.3 at G=190 kg m^{-2} s^{-1}.

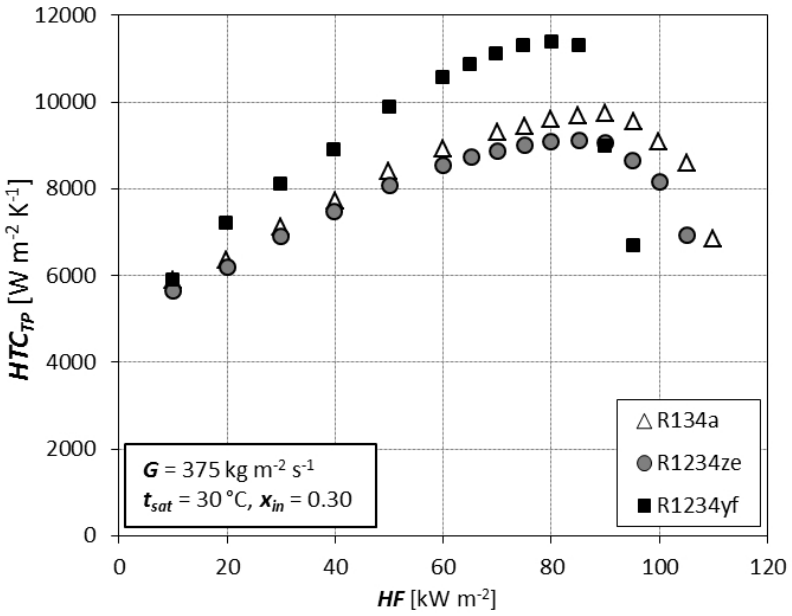

Figure 6.53: Comparison among R134a, R1234ze(E), and R1234yf critical heat flux with an inlet vapour quality of 0.3 at G=375 kg m^{-2} s^{-1}.

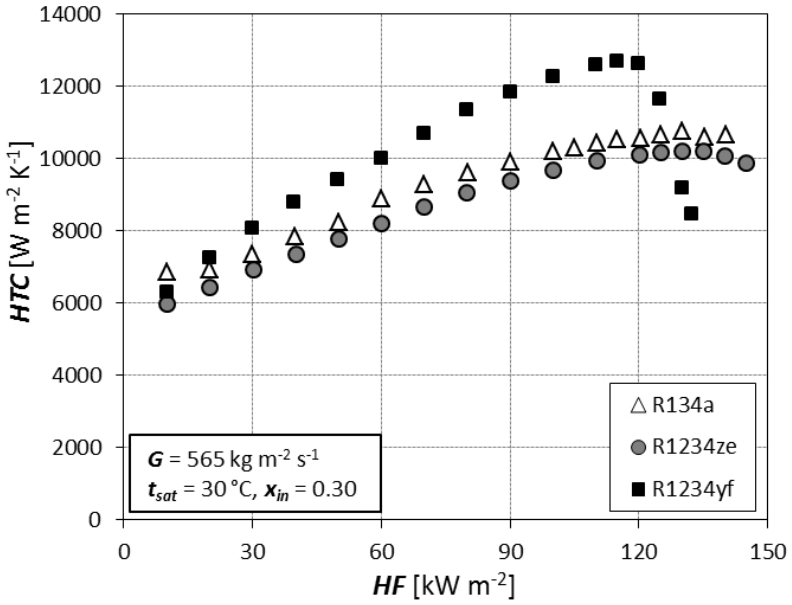

Figure 6.54: Comparison among R134a, R1234ze(E), and R1234yf critical heat flux with an inlet vapour quality of 0.3 at G=565 kg m^{-2} s^{-1}.

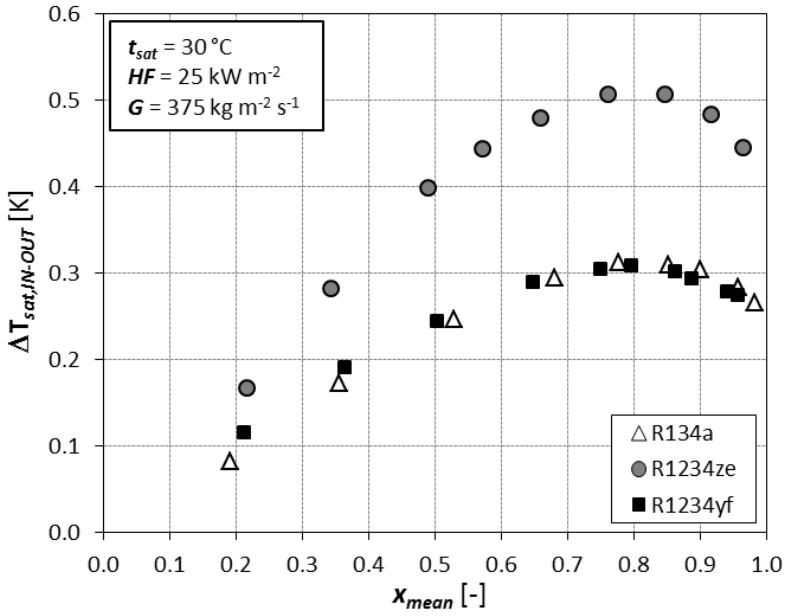

Figure 6.55: Comparison among R134a, R1234ze(E), and R1234yf saturation temperature drop at G=375 kg m^{-2} s^{-1} and HF=25 kW m^{-2}.

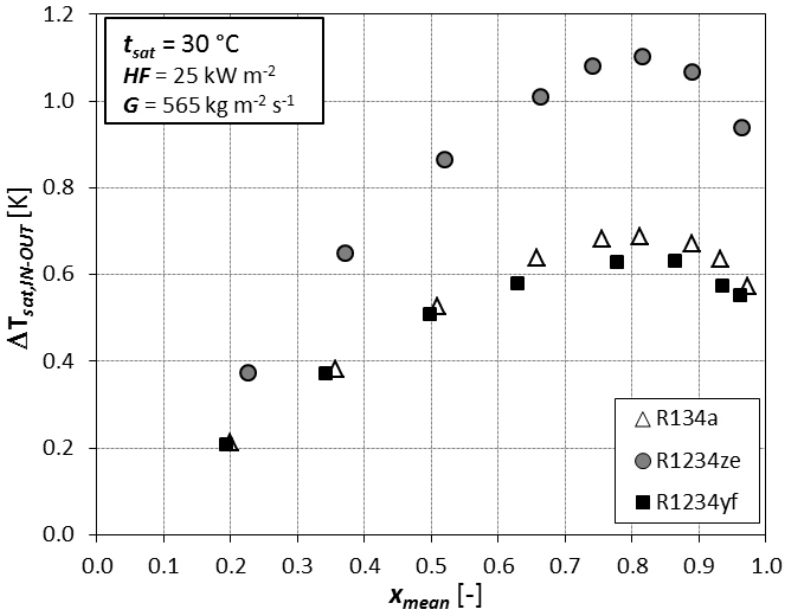

Figure 6.56: Comparison among R134a, R1234ze(E), and R1234yf saturation temperature drop at G=565 kg m^{-2} s^{-1} and HF=25 kW m^{-2}.

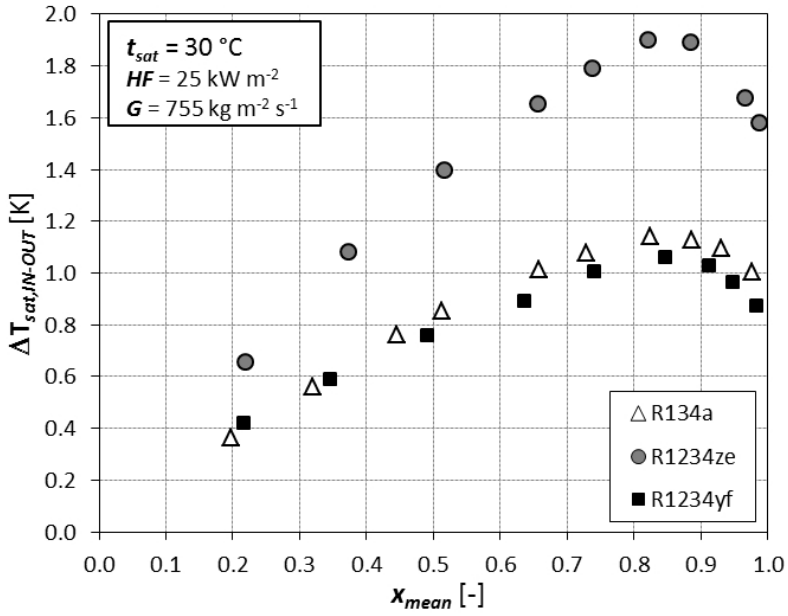

Figure 6.57: Comparison among R134a, R1234ze(E), and R1234yf saturation temperature drop at G=755 kg m^{-2} s^{-1} and HF=25 kW m^{-2}.

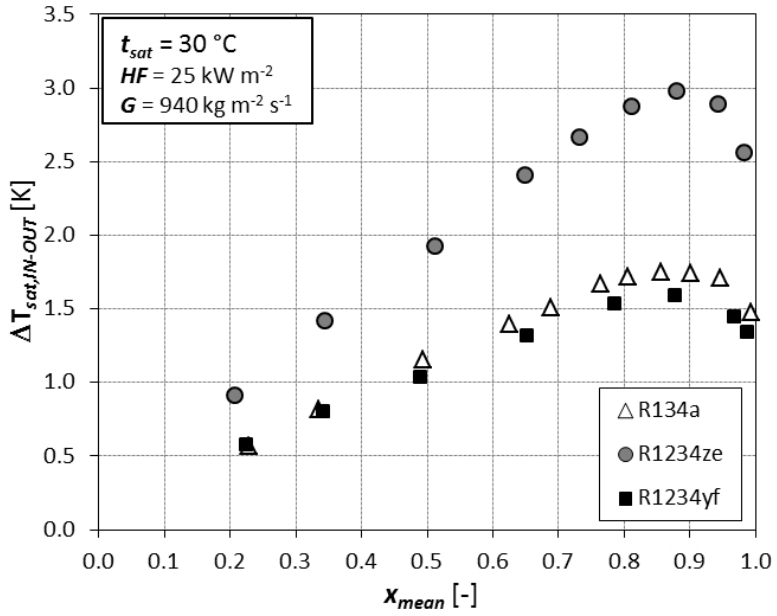

Figure 6.58: Comparison among R134a, R1234ze(E), and R1234yf saturation temperature drop at G=940 kg m^{-2} s^{-1} and HF=25 kW m^{-2}.

the R1234ze(E) penalization in terms of saturation temperature drop is more evident than the penalization in terms of pressure drop. This behaviour can be linked to the parameter $(\mathrm{d}T/\mathrm{d}p)_{sat}$ (see table 5.2), which is higher for R1234ze(E) than that of R134a and R1234yf.

6.5 Comparison against empirical models

6.5.1 Models for the estimation of the frictional pressure drop

Model of Wu et al. [109]

Wu et al. [109] proposed a model for the estimation of the frictional pressure drop during refrigerants flow boiling. The two-phase frictional pressure gradient can be expressed as:

$$\left(\frac{\mathrm{d}p}{\mathrm{d}z}\right)_f = \frac{2 \cdot f_{tp} \cdot G^2}{d_i \cdot \rho_{tp}} \tag{6.22}$$

where f_{tp} is the two-phase friction factor, ρ_{tp} the two-phase density, and d_i the inside diameter at the fin root. The two-phase density and viscosity are calculated as follows:

$$\rho_{tp} = \left(\frac{x}{\rho_V} + \frac{1-x}{\rho_L}\right)^{-1} \tag{6.23}$$

$$\mu_{tp} = \mu_L - 2.5\mu_L\left[\frac{x\rho_L}{x\rho_L + (1-x)\rho_V}\right]^2 + \left[\frac{x\rho_L(1.5\mu_L + \mu_V)}{x\rho_L + (1-x)\rho_V}\right] \tag{6.24}$$

where ρ_V and ρ_L are vapour and liquid density, respectively, μ_V and μ_V the vapour and liquid dynamic viscosity, and x vapour quality. From the knowledge of the two-phase dynamic viscosity μ_{tp} it is possible to calculate the Reynolds number $\mathrm{Re_{tp}}$ as:

$$\mathrm{Re_{tp}} = \frac{G \cdot d_i}{\mu_{tp}} \tag{6.25}$$

Finally, the two-phase friction factor is equal to:

$$f_{tp} = 2\left[\left(\frac{8}{\mathrm{Re_{tp}}}\right)^{12} + \frac{1}{(a+b)^{3/2}}\right]^{1/12} \tag{6.26}$$

with

$$a = \left[2.457 \ln \frac{1}{(7/\,\mathrm{Re_{tp}})^{0.9} + (0.27\,\mathrm{Rx_f})}\right]^{16} \tag{6.27}$$

$$b = \left(\frac{37530}{\mathrm{Re_{tp}}}\right)^{16} \tag{6.28}$$

$\mathrm{Rx_f}$ is an empirically-fitted relative roughness used to model microfin tubes for condensation as suggested by Cavallini et al. [114], which can be expresses as:

$$\mathrm{Rx_f} = \frac{0.18 \cdot (e/d_i)}{0.1 + \cos\beta} \tag{6.29}$$

where e is the fin height and β the helix angle.

Figures 6.59-6.61 report a comparison between experimental and predicted values. Table 6.1 reports relative, absolute, and standard deviations for each refrigerant. As it appears, the correlation is quite accurate, even though it is not able to predict the trend of the frictional pressure drops, which increase with vapour quality up to a maximum, and then they decrease. It is worthy to remember that this correlation was developed from experimental data points whose inlet and outlet vapour quality was fixed, and equal to 0.10 and 0.80, respectively.

Table 6.1: Relative, absolute, and standard deviations between experimental and predicted friction pressure drop by Wu et al. [109].

Refrigerant	dev_{rel}	dev_{abs}	dev_{std}
R134a	19.5%	23.3%	29.5%
R1234ze(E)	20.2%	22.7%	24.2%
R1234yf	16.9%	22.5%	24.8%

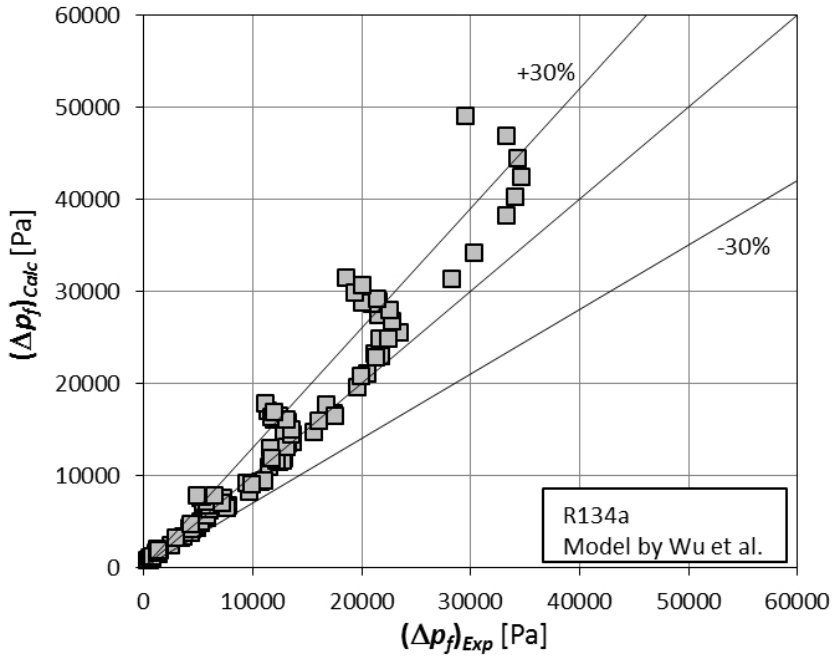

Figure 6.59: Comparison between R134a friction pressure drop and the model proposed by Wu et al. [109].

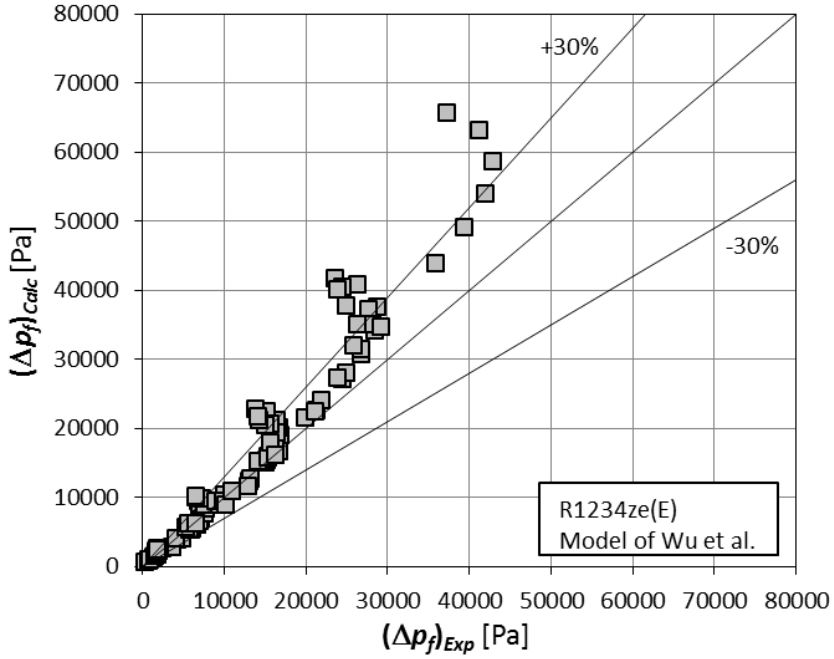

Figure 6.60: Comparison between R1234ze(E) friction pressure drop and the model proposed by Wu et al. [109].

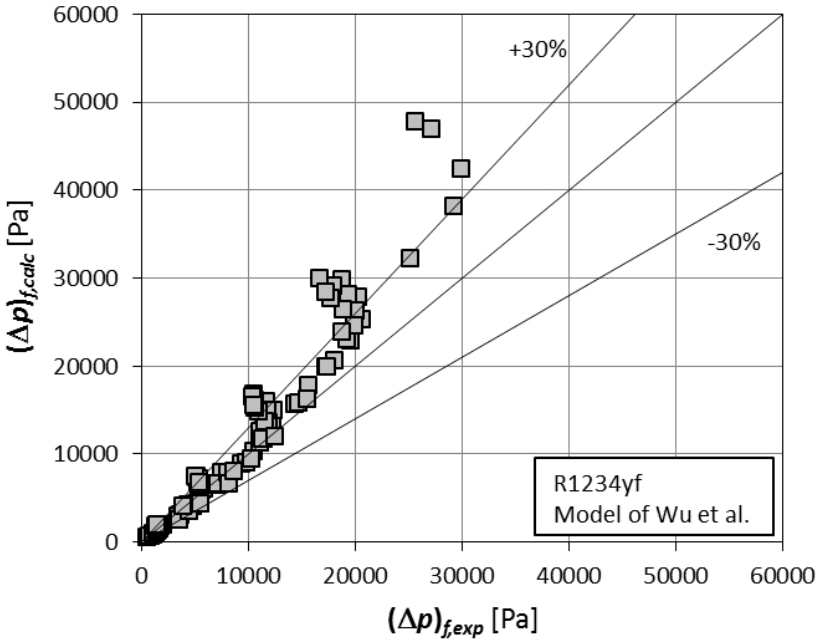

Figure 6.61: Comparison between R1234yf friction pressure drop and the model proposed by Wu et al. [109].

Model of Han and Lee [115]

Based on experimental data, Han and Lee [115] developed a frictional pressure drop correlation with the two-phase frictional parameter Φ_L. The frictional pressure gradient for the two-phase flow was related to the pressure gradient for liquid phase by:

$$\left(\frac{\mathrm{d}p}{\mathrm{d}z}\right) = \Phi_L^2 \frac{f_L\Big[G(1-x)\Big]^2}{2d_i\rho_L} \tag{6.30}$$

where f_L and Φ_L are obtained as follows:

$$f_L = 0.193\Big[\frac{G(1-x)D_i}{\mu_L}\Big]^{-0.024}\left(\frac{p}{e}\right)^{-0.539} \tag{6.31}$$

$$\Phi_L^2 = 2.648X_{tt}^{-1.946} \tag{6.32}$$

with p axial fin pitch, e fin height, and X_{tt} Martinelli parameter.

Figures 6.62-6.64 report a comparison between experimental and predicted values. Table 6.2 reports relative, absolute, and standard deviations for each refrigerant.

Table 6.2: Relative, absolute and standard deviations between experimental and predicted friction pressure drop by Han and Lee [115].

Refrigerant	dev_{rel}	dev_{abs}	dev_{std}
R134a	-10.7%	20.9%	25.8%
R1234ze(E)	-11.0%	21.5%	25.2%
R1234yf	-10.2%	25.2%	29.5%

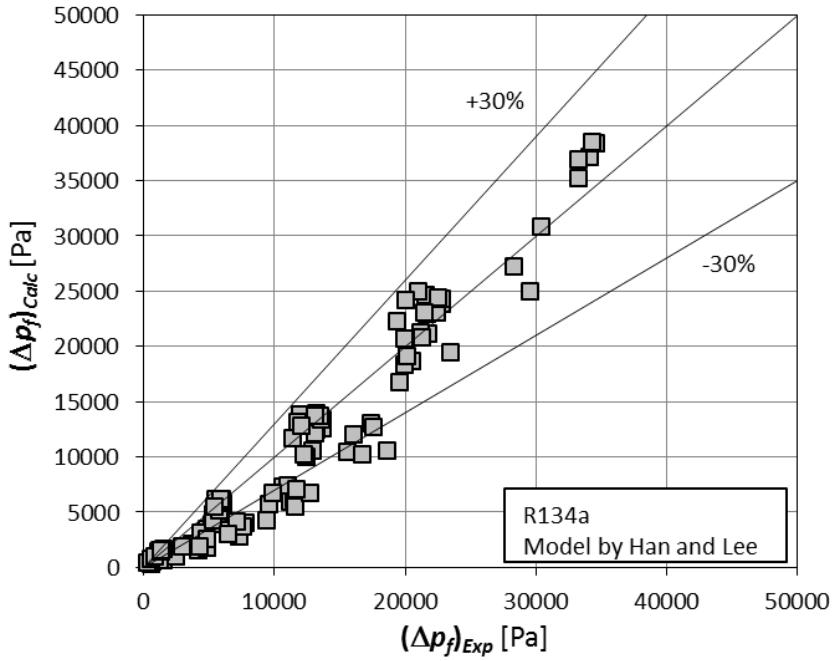

Figure 6.62: Comparison between R134a friction pressure drop and the model proposed by Han and Lee [115].

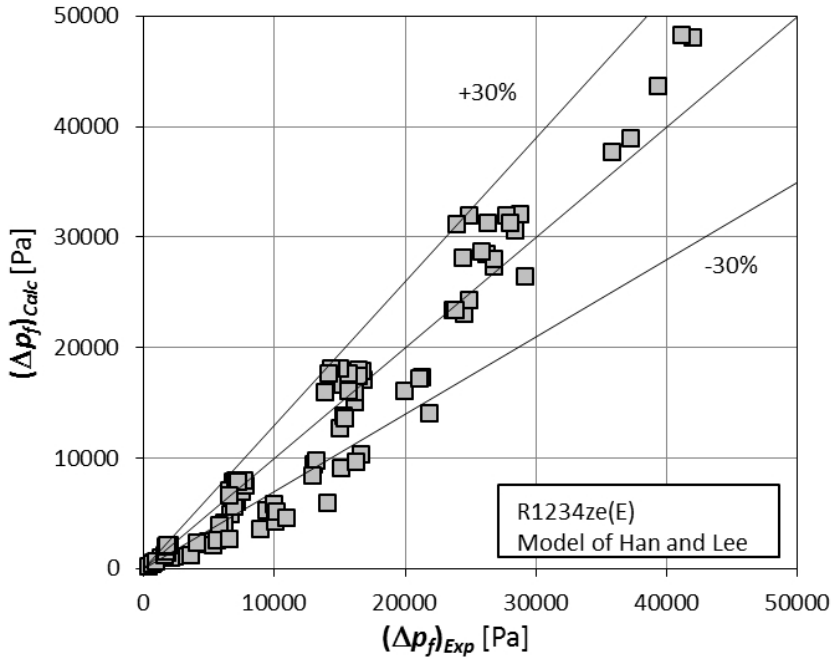

Figure 6.63: Comparison between R1234ze(E) friction pressure drop and the model proposed by Han and Lee [115].

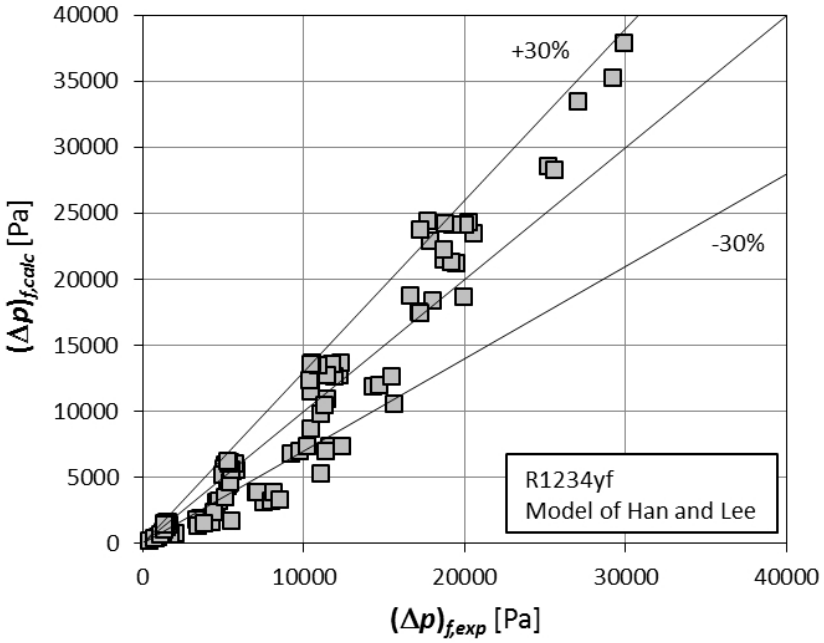

Figure 6.64: Comparison between R1234yf friction pressure drop and the model proposed by Han and Lee [115].

6.5.2 Models for the estimation of the heat transfer coefficient

Model of Wu et al. [109]

The two-phase heat transfer coefficient is given by the contribute of nucleate boiling and two-phase forced convection. Wu et al. [109] suggested to estimate the flow boiling heat transfer coefficient in microfin tubes as:

$$HTC_{tp} = \left[(E_{RB} h_{cb,l})^3 + (S h_{pb})^3 \right]^{1/3} \tag{6.33}$$

where E_{RB} is the enhancement factor introduced to include the enhancement effect of the microfins, S the nucleate boiling correction factor, $h_{cb,l}$ the convective heat transfer coefficient occurring during evaporation at the current vapour quality in the liquid cross section, and h_{pb} the nucleate boiling heat transfer coefficient. The enhancement factor E_{RB} is calculated as:

$$E_{RB} = \left\{ 1 + \left[2.64\, \mathrm{Re}_\delta^{0.036}\, \mathrm{Pr}^{-0.024} \left(\frac{e}{d_i} \right)^{0.212} \left(\frac{p}{d_i} \right)^{-0.21} \left(\frac{\beta}{90} \right)^{0.29} \right]^7 \right\}^{1/7} \tag{6.34}$$

with Re_δ being the Reynolds number based on the film liquid thickness δ:

$$\mathrm{Re}_\delta = \frac{4G(1-x)\delta}{(1-\varepsilon)\mu_L} \tag{6.35}$$

and, assuming no liquid entrainment, the average film thickness δ in intermittent and annular flow can be calculated by means of the following equation based on the actual cross sectional area:

$$\delta = \sqrt{A_c/\pi}(1 - \sqrt{\varepsilon}) \tag{6.36}$$

where ε is the void fraction. $h_{cb,l}$ is calculated as follows:

$$h_{cb,l} = C\, \mathrm{Re}_\delta^{\mathrm{m}}\, \mathrm{Pr}_{\mathrm{L}}^{0.4} \frac{k_L}{\delta} \tag{6.37}$$

and the two constant C and m are 0.014 and 0.68, respectively, and they are based on experimental data. The pool boiling heat transfer coefficient is given by:

$$h_{pb} = 2.8 \times 207 \frac{k_L}{D_b} \left[\frac{(q - q_{ONB}) D_b}{k_L T_{sat}} \right]^{0.745} \left(\frac{\rho_V}{\rho_L} \right)^{0.581} \mathrm{Pr}_\mathrm{L}^{0.533} \tag{6.38}$$

where D_b is the departure bubble diameter calculated as:

$$D_b = 0.51 \left[\frac{2\sigma}{g(\rho_L - \rho_V)} \right]^{0.5} \tag{6.39}$$

and q_{ONB} is the minimum heat flux for the onset of nucleate boiling during evaporation, and it is proposed to be:

$$q_{ONB} = \frac{2\sigma T_{sat} h_{cb,l} E_{RB}}{r_{crit} \rho_V h_{LV}} \tag{6.40}$$

where the critical bubble radius r_{crit} is assumed to be 0.38×10^{-6} m. Finally, the dimensionless parameter S in equation 6.33 is a nucleate boiling correction factor:

$$S = \frac{1}{\xi}(1 - e^{-\xi}) \tag{6.41}$$

$$\xi = 1.96 \times 10^{-5} \times \left(\frac{\rho_L}{\rho_V} \frac{C_{pL}}{h_{LV}} T_{sat} \right)^{1.25} (E_{RB} h_{cb,l}) \frac{D_b}{k_L} \tag{6.42}$$

Figures 6.65-6.67 report a comparison between experimental and predicted values. Experimental data after dryout inception are not considered in comparisons, since the correlation is suitable for intermittent and annular flow. Table 6.3 shows relative, absolute, and standard deviations subdivided by operative conditions. As it appears, this correlations is able to satisfactorily estimate the experimental heat transfer coefficient just in certain working conditions: experimental values are fairly well estimated at mass velocity of 375 and 565 kg m^{-2} s^{-1} for all the three refrigerants, whereas it tends to underestimate the heat transfer coefficient at low mass velocity (G = 190 kg m^{-2} s^{-1}), and to overestimate at high mass velocity (G=755 and 940 kg m^{-2} s^{-1}).

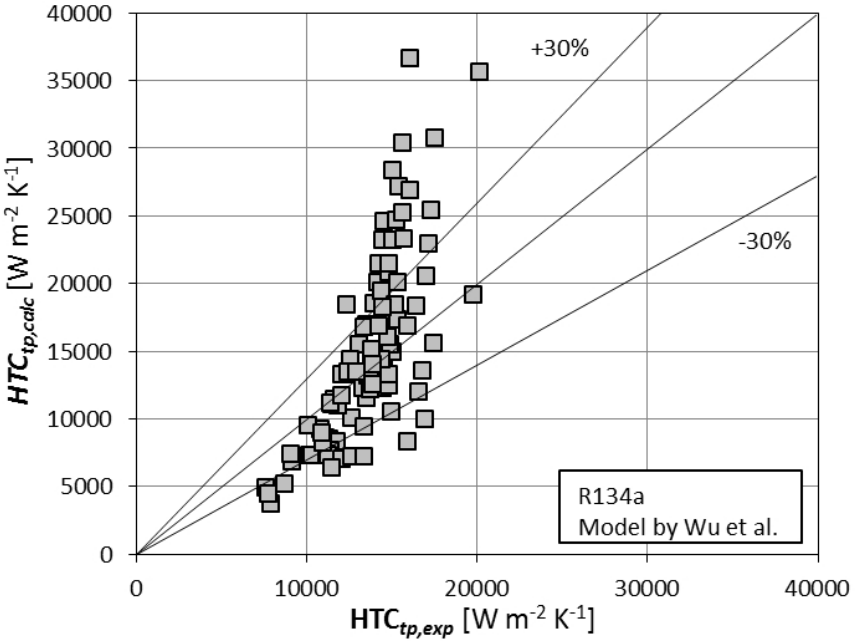

Figure 6.65: Comparison between R134a heat transfer coefficient and the model proposed by Wu et al. [109].

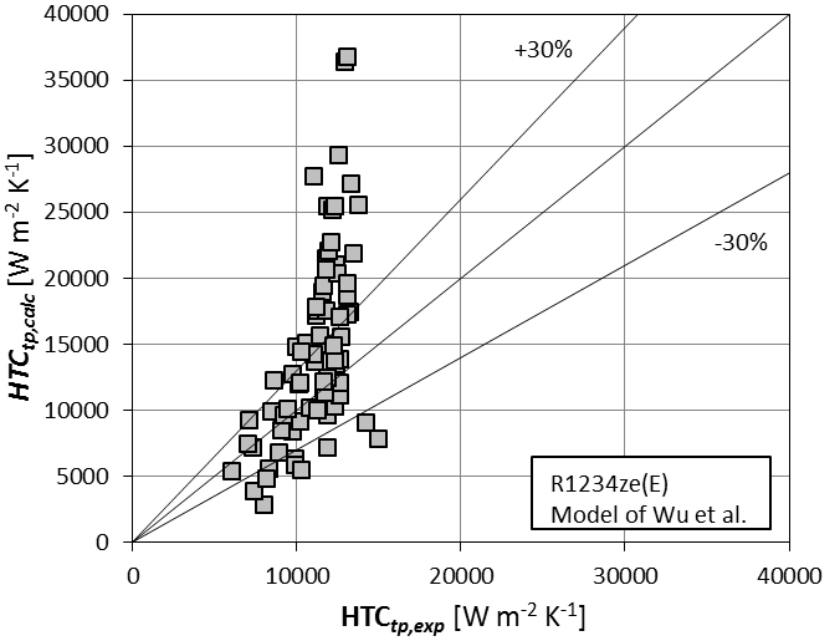

Figure 6.66: Comparison between R1234ze(E) heat transfer coefficient and the model proposed by Wu et al. [109].

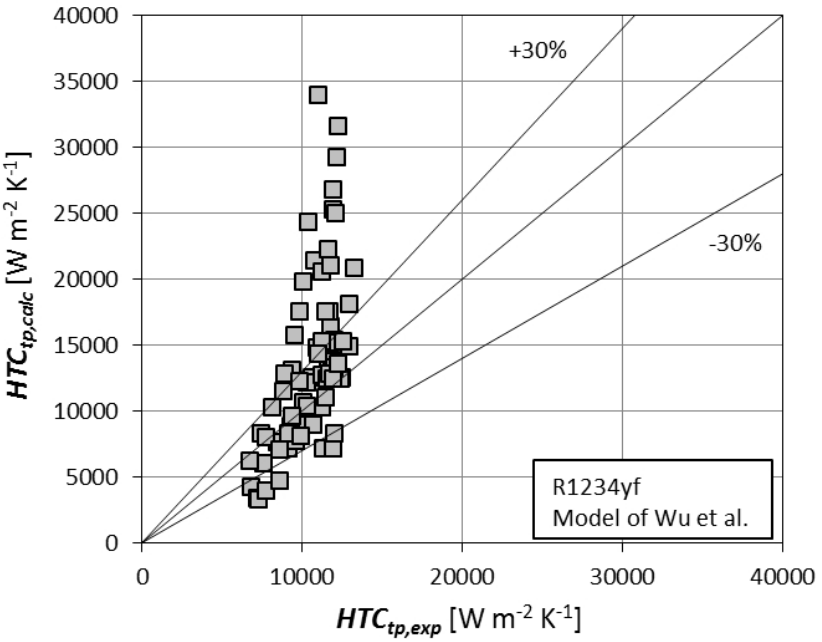

Figure 6.67: Comparison between R1234yf heat transfer coefficient and the model proposed by Wu et al. [109].

Table 6.3: Relative, absolute and standard deviations between experimental and predicted heat transfer coefficient by Wu et al. [109].

Refrigerant	G [kg m^{-2} s^{-1}]	HF [kW m^{-2}]	dev_{rel} [%]	dev_{abs} [%]	dev_{std} [%]
R134a	190	10	-44.4	44.4	4.2
R134a	190	25	-37.0	37.0	5.9
R134a	375	10	-22.4	22.4	9.6
R134a	375	25	-17.9	17.9	10.1
R134a	375	50	-7.9	9.8	7.3
R134a	565	10	16.5	22.1	25.3
R134a	565	25	14.2	24.9	27.2
R134a	565	50	4.5	12.9	18.9
R134a	755	10	25.5	29.5	30.9
R134a	755	25	30.1	35.7	33.4

to next page —

— from previous page

Refrigerant	G [kg m^{-2} s^{-1}]	HF [kW m^{-2}]	dev_{rel} [%]	dev_{abs} [%]	dev_{std} [%]
R134a	755	50	19.3	24.2	25.0
R134a	940	25	52.4	53.7	38.5
R1234ze(E)	190	10	-46.0	46.0	8.5
R1234ze(E)	190	25	-41.9	41.9	4.1
R1234ze(E)	375	10	5.5	11.8	15.3
R1234ze(E)	375	25	-11.2	13.6	13.1
R1234ze(E)	375	50	-10.6	11.2	7.1
R1234ze(E)	565	10	40.2	40.2	29.2
R1234ze(E)	565	25	27.2	30.8	23.8
R1234ze(E)	565	50	8.2	17.5	19.8
R1234ze(E)	755	10	77.2	77.2	46.6
R1234ze(E)	755	25	67.9	67.9	43.4
R1234ze(E)	755	50	35.4	38.7	31.3
R1234ze(E)	940	25	87.6	87.6	49.5
R1234yf	190	10	-44.3	44.3	8.3
R1234yf	190	25	-28.3	28.3	9.3
R1234yf	375	10	2.4	20.4	23.9
R1234yf	375	25	-7.2	12.5	11.8
R1234yf	375	50	10.3	10.3	10.8
R1234yf	565	10	48.3	50.2	37.3
R1234yf	565	25	23.7	31.2	32.3
R1234yf	565	50	17.9	17.9	9.2
R1234yf	755	10	82.5	82.5	60.6
R1234yf	755	25	52.2	56.8	50.4
R1234yf	755	50	23.9	23.9	18.8
R1234yf	940	25	73.3	73.3	51.2

6.5.3 Models for the estimation of the vapour quality at the onset of the dryout phenomenon

Model of Mori et al. [116]

Mori et al. [116] developed an empirical correlation to estimate the dryout quality during refrigerant flow boiling inside microfin tubes. They classified the dryout inception qualities into two characteristic regimes, called $Regime-G1$ and $Regime-G2$. The dryout inception quality x_{do} is given by:

$$x_{do} = \min(x_{do,1}, x_{do,2}) \tag{6.43}$$

where $x_{do,1}$ and $x_{do,2}$ are the values of dryout inception quality calculated for $Regime-G1$ and $Regime-G2$, respectively.

Under $Regime-G1$ conditions, the vapour quality at the onset of the dryout is calculated as:

$$x_{do,1} = 0.92 \tag{6.44}$$

When $Regime-G2$ conditions take place, the vapour quality at the onset of the dryout is calculated as:

$$x_{do,2} = \min(x_{do,2a}, x_{do,2b}) \tag{6.45}$$

with

$$x_{do,2a} = 0.44\,\mathrm{Fr}^{0.04}\,\mathrm{Bo}^{-0.07} \tag{6.46}$$

$$x_{do,2b} = 0.63\,\mathrm{Fr}^{0.02}\,\mathrm{Bo}^{-0.033} \tag{6.47}$$

where Fr and Bo are the vapour Froude number and the boiling number, respectively. They are calculated as:

$$\mathrm{Fr} = \frac{G^2}{g \cdot d \cdot \rho_V(\rho_L - \rho_V)} \tag{6.48}$$

$$\mathrm{Bo} = \frac{q}{G \cdot h_{LV}} \tag{6.49}$$

Figures 6.68-6.70 report the comparison between experimental and predicted values of the vapour quality at the onset of the dryout phenomenon. The correlation results fairly accurate. Relative and standard deviations are reported in table 6.4.

Table 6.4: Relative and absolute deviations between experimental and predicted vapour quality at onset of dryout by Mori et al. [116].

Refrigerant	dev_{rel} [-]	dev_{abs}[−]
R134a	-0.037	0.046
R1234ze(E)	-0.031	0.046
R1234yf	-0.032	0.048

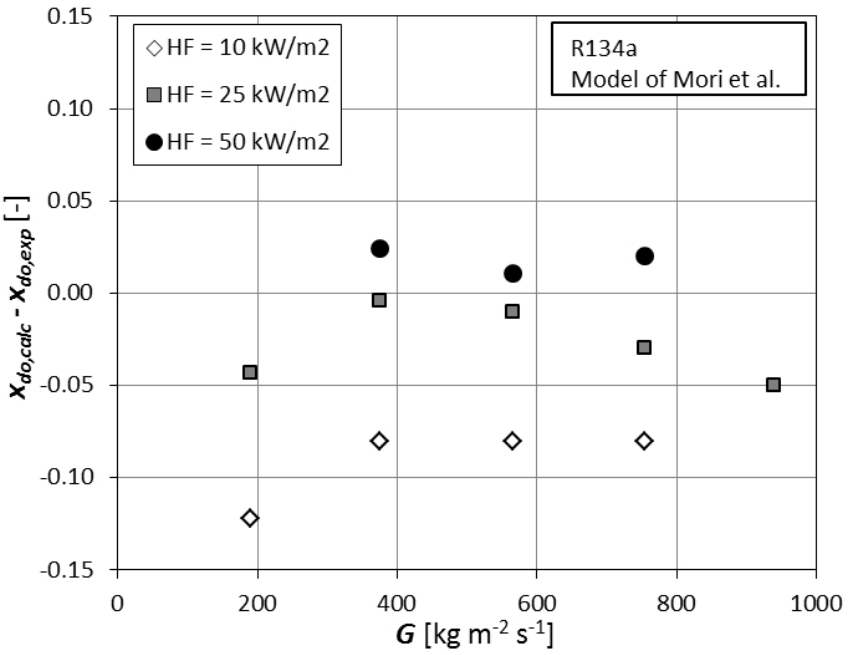

Figure 6.68: Comparison between R134a experimental vapour quality at onset of dryout and the model proposed by Mori et al. [116].

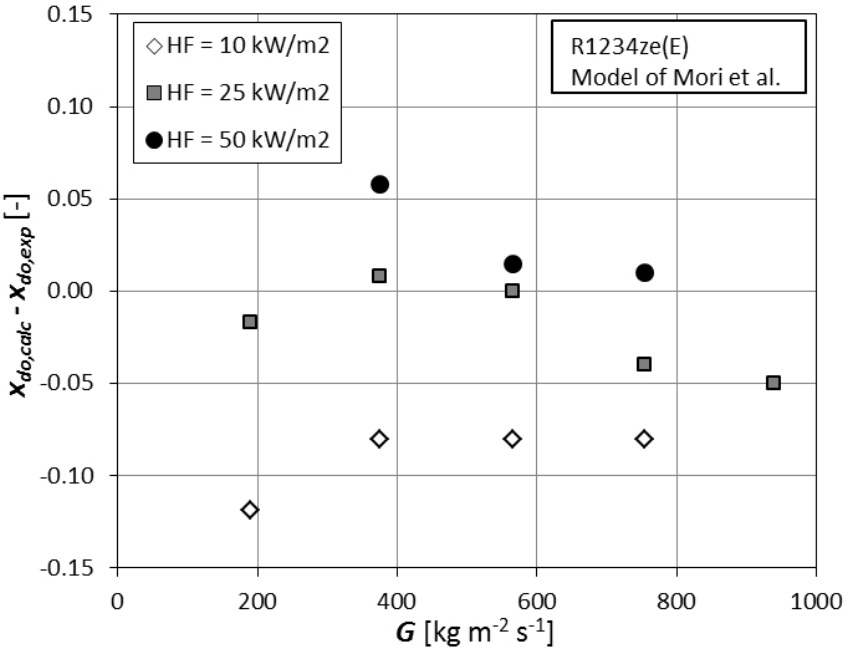

Figure 6.69: Comparison between R1234ze(E) experimental vapour quality at onset of dryout and the model proposed by Mori et al. [116].

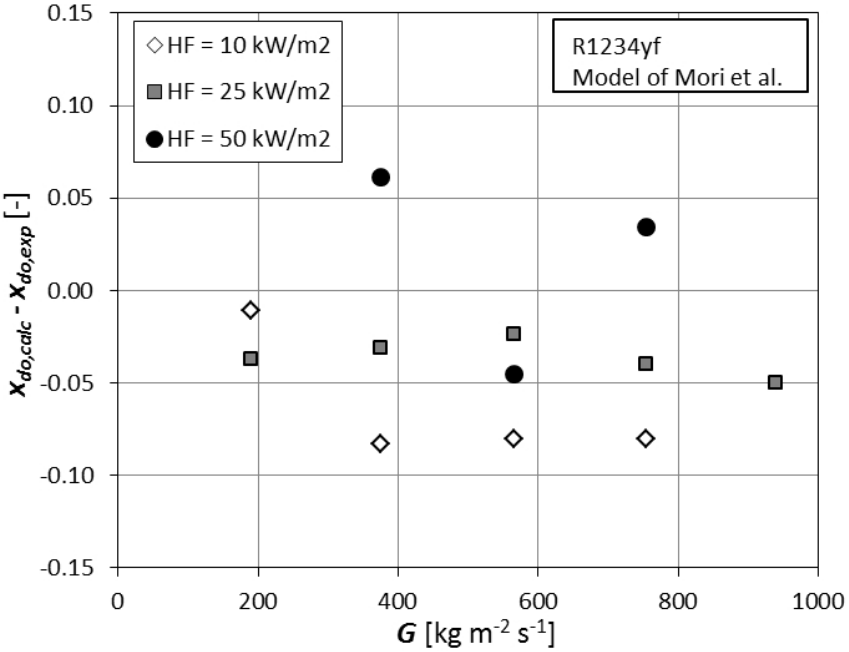

Figure 6.70: Comparison between R1234yf experimental vapour quality at onset of dryout and the model proposed by Mori et al. [116].

Model of Padovan et al. [105]

Padovan et al. [105] modified the Mori et al. [116] correlation. The new correlation came from equation 6.47 for $RegimeG-2a$, and the exponent of the Froude number was changed in order to better describe the dependence on mass velocity:

$$x_{do} = 0.57\,\mathrm{Fr}^{-0.02}\,\mathrm{Bo}^{-0.07} \tag{6.50}$$

Figures 6.71-6.73 report the comparison between experimental and predicted values of the vapour quality at the onset of the dryout phenomenon. The correlation results very accurate. Relative and standard deviations are reported in table 6.5.

Table 6.5: Relative and absolute deviations between experimental and predicted vapour quality at onset of dryout by Padovan et al. [105].

Refrigerant	dev_{rel}	dev_{abs}
R134a	-0.020	0.024
R1234ze(E)	-0.024	0.034
R1234yf	-0.030	0.042

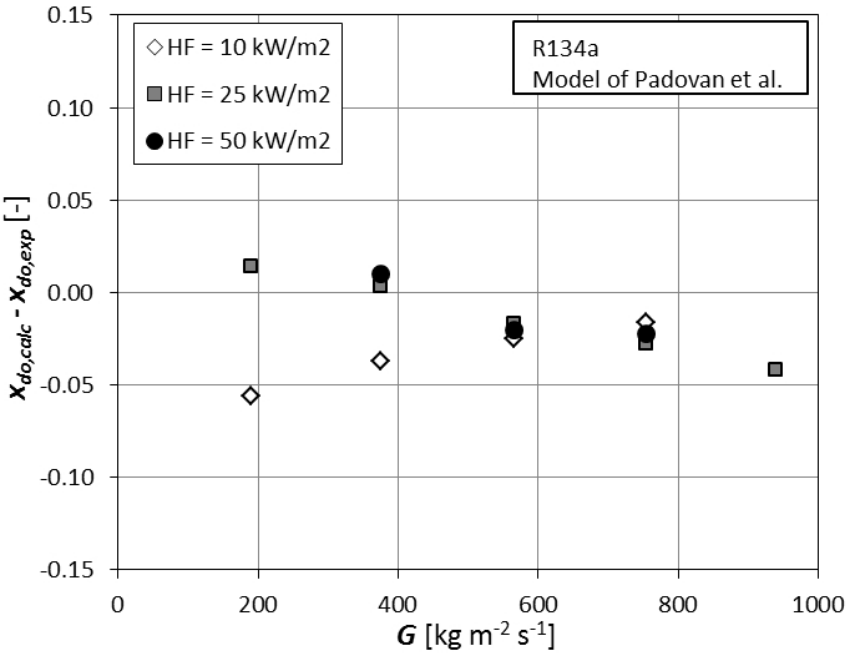

Figure 6.71: Comparison between R134a experimental vapour quality at onset of dryout and the model proposed by Padovan et al. [105].

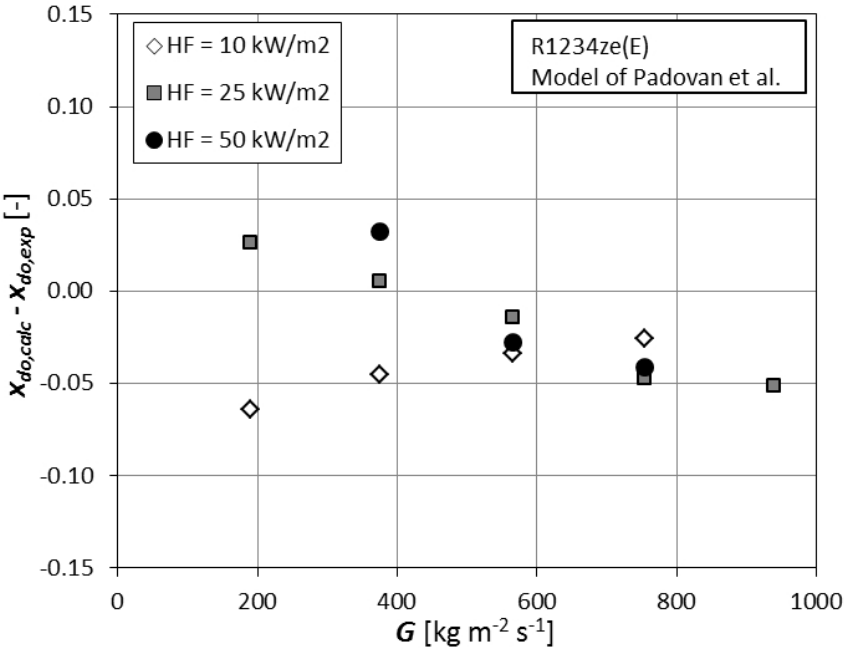

Figure 6.72: Comparison between R1234ze(E) experimental vapour quality at onset of dryout and the model proposed by Padovan et al. [105].

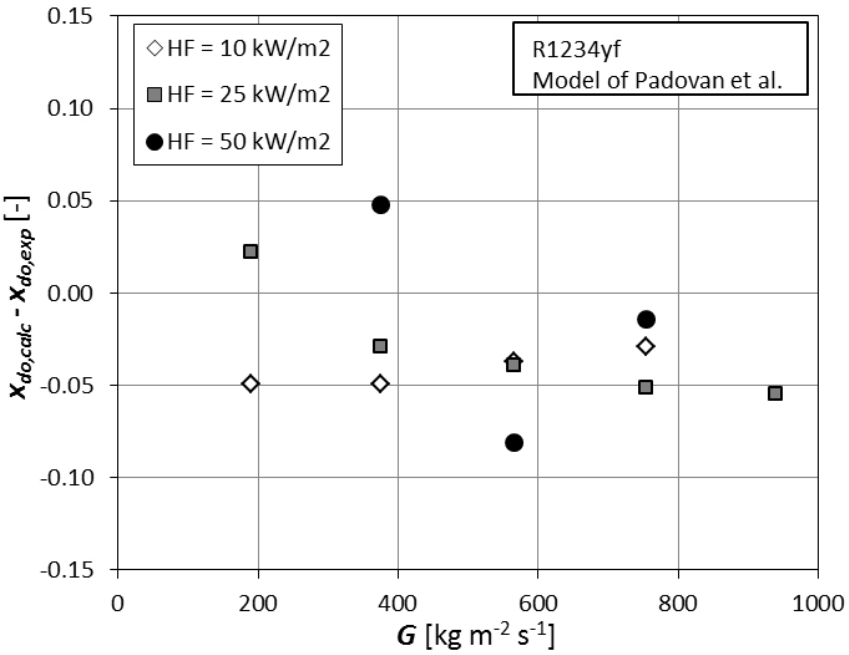

Figure 6.73: Comparison between R1234yf experimental vapour quality at onset of dryout and the model proposed by Padovan et al. [105].

Conclusions

In the first chapter, the air forced convection through metal foams was studied. Nine copper foams, with PPI ranging from 5 to 40, porosity from 0.905 to 0.936, foam core height of 20 mm and 40 mm were experimentally tested in a test facility at the Dipartimento di Ingegneria Industriale of University of Padova. Three different heat flow rates (250 W, 325 W, and 400 W) were imposed at the base of the samples, and the air frontal velocity ranged from about 2.5 m s^{-1} to 5 m s^{-1}. From the experimental measurements, it was possible to calculate the overall heat transfer coefficients and to measure the pressure drops. The analysis of the collected data permitted to understand how each geometrical parameter affects the thermal and hydraulic beheviours of such enhanced materials. For all the tested samples, the heat transfer coefficient did not depend on the imposed heat flux and it increased with the air mass flow rate. At constant porosity and pore density, even if the 20 mm high foams presents half heat transfer area than 40 mm samples, they presents slightly higher or approximately the same values of the overall heat transfer coefficients: this behaviour can be explained considering the foams finned surface efficiency of the 20 mm high foams, which is more than double than that of the 40 mm high samples. Thus, the foam finned efficiency is an important parameter that affects the thermal performance of these enhanced surfaces. The pressure drops were found to increase when increasing the number of pores per linear inch, from the experimental measurements it was also possible to calculate the values of permeability and inertia coefficient. The experimental database, coupled with other experimental measurements previously collected during air forced convection through aluminum foams, permitted to develop a semi-empirical model to estimate both the interstitial heat transfer coefficient and the foam finned surface efficiency. This procedure can be used to design different optimized metal foam heat sinks for any kind of electronic

thermal management applications.

A numerical approach to model the air forced convection through extended surfaces is proposed in the second chapter. The numerical model was validated with experimental values of heat transfer coefficient and pressure drop previously obtained for a reference surface, which was a trapezoidal finned surface which had a rectangular base of 70 $\times$ 100 mm and 6 fins, each one with a base width of 5 mm and a top width of 3 mm. Once validated, the model was extended to different enhanced surfaces: rectangular plain finned and pin finned surfaces. For the plain finned surfaces, the ratio t/H was varied between 0.1 and 0.6, p/H between 0.33 and 1.11, and Reynolds number from 2700 to 10100; for the pin fin surfaces, the ratio S/D was varied from 1.8 to 3.0, T/D from 2.5 to 5.0, H/D from 3.0 to 7.0, and the Reynolds number from 1000 to 4200. In these operative conditions, a turbulent flow was considered both for the plain finned surfaces and for the pin fin surfaces. From the numerical simulations of the rectangular plain finned surfaces, it appeared that, at constant frontal velocity, the heat transfer coefficient increases when decreasing fin pitch and when increasing fin thickness, whereas it does not depend on the fin height. The finned surface efficiency increased when decreasing fin height. The pressure drop increased when decreasing fin pitch and when increasing fin thickness, whereas it was weakly affected by the fin height. For the pin fin surfaces, the streamwise direction dimensionless pin spacing and the dimensionless pin length had a weak effect on the heat transfer coefficient, whereas the heat transfer performance increased when decreasing the transverse dimensionless pin spacing. The surface finned efficiency increased when decreasing the dimensionless pin height, and when increasing the spanwise direction dimensionless pin spacings. The dimensionless pin height did not affect the hydraulic behavior, whereas the decreasing of the streamwise and transverse direction dimensionless pin spacings led to higher pressure drops. Based on the numerical results, four new correlations were proposed to estimate the Colburn j- factor and and the friction factor for both kind of enhanced surfaces. These correlations can be used to optimize finned heat sinks under certain constraints of maximum allowable pressure drop and wall temperature. The numerical analysis can be extended to other enhanced surfaces, such as offset strip fins and wavy fins.

Air forced convection through the real structure of metal foams was numerically

investigated in the third chapter. Pore-scale structures were obtained by micro-computed tomography scanned images of four different copper foams, having about the same relative density (6.4 - 6.6%) but different linear porosity (5, 10, 20, and 40 PPI), with a scan resolution of 20 μm. The experimental results of these 4 copper foams were reported in the first chapter. The scanned samples were reconstructed and meshed employing the commercial software Simpleware. The hydraulic and thermal behavior of these materials was modeled with the commercial software ANSYS Fluent. Experimental conditions reported in the first chapter were considered as boundary conditions, to facilitate a direct comparison between numerical and experimental values. It was observed that the numerical analysis employed in this study predicted pressure gradients very well. Interstitial heat transfer coefficients were compared against values predicted by the empirical correlation proposed in the first chapter. Both the numerical interstitial heat transfer coefficients, and the product between interstitial heat transfer coefficient and foam finned surface efficiency, agreed well with the experimental values. These results validated the analysis procedure based on the μCT technique.

In the fourth chapter a new experimental set up, which was designed and developed in order to study the flow boiling phenomenon inside microstructured surfaces, is presented. The test section was developed by using a commercial CFD software, in order to find the plenum sizes that guaranteed the most uniform velocity distribution at the inlet of the rectangular channel. The most suitable plenum was found to be a cube with the edge of 30 mm. The facility was design and developed to permit either condensation or flow boiling measurements to be performed, thus it had to be as flexible as possible. The refrigerant is pumped through the circuit by means of a magnetically coupled gear pump, it is vaporized and superheated in a brazed plate heat exchanger fed with hot water. Superheated vapour then partially condenses in a pre-condenser fed with cold water to achieve the set quality at the inlet of the test section. The refrigerant enters the test section at a known mass velocity and vapour quality and then it is vaporized by means of the calibrated Nichel-Chrome wire resistance. The fluid leaves the test section and enters in a post-condensers, where it is fully condensed and subcooled. The subcooled liquid passes through a drier filter and then is sent back to the evaporator by the pump. During a calibration campaign, the heat balances at the evaporator and at the pre-condenser were

checked under different working conditions, and the difference between the heat flow rates calculated from the refrigerant side and the ones calculated from the water side were found to be within the experimental uncertainties.

The liquid forced convection and flow boiling measurements of different refrigerants inside a metal foam are showed in the fifth chapter. The metal foam has 5 PPI, a porosity of 0.93, it is 5 mm high, 10 mm wide, and 200 mm long, and it is brazed over a 10 mm high copper plate. Twenty 5 mm deep holes were drilled 1 mm under the foam to monitor the wall temperature distribution by locating as many calibrated T-type thermocouples. Single-phase flow experiments were run with two different refrigerants: R134a and R1234ze(E), keeping the subcooling at the inlet of the test section at least greater than 15 °C, as compared to a saturation temperature of around 40 °C. The two refrigerants behave almost in the same way, showing similar heat transfer coefficients and pressure drops. Two-phase tests were conducted with three different refrigerants: R134a, R1234ze(E), and R1234yf, exploring different operating conditions, in order to explain the effects of vapour quality, mass velocity, and heat flux on the thermal and hydraulic behaviour of such materials. All the experiments were carried at constant saturation temperature of 30 °C. For all the three fluids, at constant heat flux, the phase change process seemed to be controlled by the nucleate boiling up to around $G = 100$ kg m^{-2} s^{-1}, then, passing from 100 to 200 kg m^{-2} s^{-1}, the heat transfer coefficient was enhanced of around 30-35%, highlighting that the two-phase forced convection becomes more and more important. Similar considerations can be drawn for the other tested fluids. For a fixed heat flux of 50 kW m^{-2}, no appreciable differences can be observed between the three refrigerants, whereas at a fixed heat flux of 100 kW m^{-2}, where nucleate boiling seems to be strengthened, R134a showed better heat transfer performances. The hydraulic results showed that for the three fluids, the pressure drops increased with both vapour quality and mass velocity and the R1234ze(E) exhibited higher two-phase pressure drops than those measured for R134a and R1234yf.

The sixth chapter deals with the flow boiling inside a 3.4 ID microfin tube. The measurements were run at constant saturation temperature of 30 °C by varying the refrigerant mass velocity between 190 kg m^{-2} s^{-1} and 940 kg m^{-2} s^{-1} and the vapour quality from 0.2 to 0.99; three different heat fluxes were investigated (10, 25, and 50 kW m^{-2}). The results showed that the flow boiling heat transfer was

controlled by the two well-know phase change heat transfer mechanisms: nucleate boiling and two-phase forced convection; at constant saturation temperature, the actual operative conditions: heat flux, vapour quality, and mass velocity determine which of those dominates the phase change process. The developed measuring technique permitted to find the vapour quality at the onset of the dryout, which occurred at different values depending on the operating test conditions. At a heat flux of 10 kW m^{-2}, the dryout phenomenon did not occur at any mass velocity for R134a and R1234ze(E), whereas it occurred for R1234yf; for a given mass velocity, this value decreased as the heat flux increased. At a heat flux of 10 kW m^{-2}, the three refrigerants showed almost similar values of the heat transfer coefficient, and it was not possible to identify a fluid which performed better than the others, whereas at 25 kW m^{-2} and 50 kW m^{-2} R1234yf showed higher values of the two-phase heat transfer coefficient, whereas R134a and R1234ze(E) had, on average, similar values of the heat transfer coefficient. Pressure drop were found to increase with vapour quality up to reaching a maximum, and then they decreased. Obviously, higher mass velocity led to higher pressure drop. R1234ze(E) was found to have higher pressure drops than those measured for R134a and R1234yf.

The results of this PhD thesis contribute ob the development of a large and reliable experimental database relative to both single and two-phase heat transfer inside microgeometries. Future development of the present work might regard the study of other metal foams, having different material, pore density, and porosity, to highlight the geometrical effects on the thermal and hydraulic behaviour of metal foams during flow boiling of refrigerants, and of a smaller microfin tube.

Bibliography

[1] M. F. Ashby and L. J. Gibson. *Cellular Solids - Structure and properties - Second edition.* Cambridge Solid State Science Series, Cambridge Press, 1997.

[2] V Shapalov. Porous metals. *Mat. Res. Soc. Bull.*, 19:24–28, 1994.

[3] G.J. Davies and S. Zhen. Metallic foams: their production, properties and applications. *J. Mat. Sci.*, 18:1899–1911, 1983.

[4] ERG Materials and Aerospace, http://www.ergaerospace.com/.

[5] V.V. Calmidi and R.L. Mahajan. Forced Convection in High Porosity Metal Foams. *J. Heat Transf.*, 122:557–565, 2000.

[6] W.H. Hsieh, J.Y. Wu, W.H. Shih, and W.C. Chiu. Experimental investigation of heat-transfer characteristics ofaluminum-foam heat sinks. *Int. J. Heat Mass Transf.*, 47:5149–5157, 2004.

[7] S.Y. Kim, B.H. Kang, and J.H. Kim. Forced convection from aluminum foam materials in an asymmetrically heated channel. *Int. J. Heat Mass Transf.*, 44:1451–1454, 2001.

[8] J.J. Hwang, G.J. Hwang, R.H. Yeh, and C.H. Chao. Measurements of Interstitial Convective Heat Transfer and Frictional Drag for Flow Across Metal Foams. *J. Heat Transf.*, 124:2002, 120–129.

[9] N. Dukhan, R. Picon-Feliciano, and A.R. Alvarez-Hernandez. Air Flow Through Compressed and Uncompressed Aluminum Foam: Measurements and Correlations. *J. Heat Transf.*, 128:1004–1012, 2006.

[10] S. Mancin, C. Zilio, A. Cavallini, and L. Rossetto. Heat transfer during air flow in aluminum foams. *Int. J. Heat Mass Transf.*, 53:4976–4984, 2010.

[11] S. Mancin, C. Zilio, A. Cavallini, and L. Rossetto. Pressure drop during air flow in aluminum foams. *Int. J. Heat Mass Transf.*, 53:3121–3130, 2010.

[12] L. Giani, G. Groppi, and E. Tronconi. Heat Transfer Characterization of Metallic Foams. *Ind. Eng. Chem. Res.*, 44:9078–9085, 2005.

[13] H.Y. Zhang, D. Pinjala, Y.K. Joshi, T.N. Wong, K.C. Toh, and M. Fluid Flow and Heat Transfer in Liquid Cooled Foam Heat Sinks for Electronic Packages. *IEEE Trans. Compon. Pack. T.*, 28:272–280, 2005.

[14] M. Odabaee and K. Hooman. Application of metal foams in air-cooled condensers for geothermal power plants: An optimization study. *Int. Comm.*

Heat Mass Transf., 38:838–843, 2011.

[15] G.B. Ribeiro and J.R. Barbosa Jr. Comparison of metal foam and louvered fins as air-side heat transfer enhancement media for miniaturized condensers. *App. Therm. Eng.*, 51:334–337, 2013.

[16] S. De Shampheleire, P. De Jaeger, H. Huisseune, B. Ameel, C. T'Joen, K. De Kerpel, and M. De Paepe. Thermal hydraulic performance of 10 PPI aluminum foam as alternative for louvered fins in an HVAC heat exchanger. *Appl. Therm. Eng.*, 51:371–382, 2013.

[17] K.S. Yang, C.H. Chung, M.T. Lee, S.B. Chiang, C.C. Wong, and C.C. Wang. An experimental study on the heat dissipation of LED lighting module using metal/carbon foam. *Int. Comm. Heat Mass Transf.*, 48:79–79, 2013.

[18] P.C. Huang, C.C. Chen, and H.Y. Hwang. Thermal enhancement in a flat-plate solar water collector by flow pulsation and metal-foam blocks. *Int. Comm. Heat Mass Transf.*, 61:696–720, 2013.

[19] EN ISO 5167-1:1991/A1:1998, Orifice Plates, Nozzles and Venturi Tubes Inserted in Circular Cross Section Conduits Running Full.

[20] S. Mancin, C. Zilio, L. Rossetto, and A. Cavallini. Heat Transfer Performance of Aluminum Foams. *J. Heat Transf.*, 133:060904–1–9, 2011.

[21] Labview 2009, NI, National Instruments, 2009.

[22] Refprop 9.0, NIST, National Institute of Standard and Tecnologies, 2009.

[23] F.P. Incropera and D.P. De Witt. *Fundamentals of Heat and Mass Transfer, third ed.* Wiley, 1990.

[24] I. Ghosh. Heat transfer correlation for high-porosity open-cell foam. *Int. J. Heat Mass Transf.*, 52:1488–1494, 2009.

[25] A. Battacharya, V.V. Calmidi, and R.I. Mahajan. Thermophysical properties of high porosity metal foams. *Int. J. Heat Mass Transf.*, 45:1017–1031, 2002.

[26] J.W. Paek, B.H. Kang, S.Y. Kim, and J.M. Hyun. Effective thermal conductivity and permeability pf aluminum foam materials. *Int. J. Thermophys.*, 21:453–463, 2000.

[27] G.S. Beavers and E.M. Sparrow. Non-Darcy Flow Through Fibrous Porous Media. *J. Appl. Mech.*, 36:711–714, 1969.

[28] K. Hamaguchi, S. Takahashi, and H. Miyabe. Flow friction and heat transfer characteristics of a regenerator matrix (case of foamed metal). *Trans. Jpn.Soc. Mech. Eng.*, 49:1991–2000, 1983.

[29] K. Vafai and C.L. Tien. Boundary and inertia effects on convective mass transfer in porous media. *Int. J. Heat Mass Transf.*, 25:1183–1190, 1982.

[30] S. Ergun. Fluid flow through packed columns. *Chem. Eng. Prog.*, 48:89–94, 1952.

[31] N. Dukhan and P. Patel. Equivalent particle diameter and length scale for pressure drop in porous metals. *Exp. Therm. Fluid Sci.*, 32:1059–1067, 2008.

[32] M. Lacroix, P. Nguyen, D. Schweich, C.P. Huu, S. Savin-Poncet, and D. Edouard. Pressure drop measurements and modeling on SiC foams. *Chem. Eng. Sci.*, 62:3259–3267, 2007.

[33] D.S. Kadle and E.M. Sparrow. Numerical and experimental study of turbulent heat transfer and fluid flow in longitudinal fin arrays. *J. Heat Transf.*, 108:16–23, 1986.

[34] M. Morega and A. Bejan. Plate fins with variable thickness and height for air-cooled electronic module. *Int. J. Heat Mass Transf.*, 37:433–445, 1994.

[35] P. Teertstra, M.M. Yovanovich, and J.R. Culham. Analytical Forced Convection Modeling of Plate Fin Heat Sinks. In *Fifteenth IEEE SEMI-THERM Symposium*, pages 34–41, San Diego, CA, USA, 1999.

[36] I.K. Shwaish, C.H. Amon, and J.Y. Murthy. Thermal/fluid performance evaluation of serrated plate fin heat sinks. In *2002 Intersoc. Conf. Therm. Phenom.*, pages 267–275, San Diego, CA, USA, 2002.

[37] M.S. Mon and U. Gross. Numerical study of fin-spacing effects in annular-finned tube heat exchanger. *Int. J. Heat Mass Transf.*, 47:1953–1964, 2004.

[38] V.P. Malapure, S.K. Mitra, and A. Battacharya. Numerical investigation of fluid flow and heat transfer over louvered fin in compact heat exchangers. *Int. J. Therm. Sci.*, 46:199–211, 2007.

[39] Y. Zhu and Y. Li. Three-dimensional numerical simulation of the laminar flow and heat transfer in four basic fins of plate-fin heat exchangers. *J. Heat Transf.*, 130:111801–1–8, 2008.

[40] Y.T. Yang and H.S. Peng. Numerical study of pin-fin heat sink with un-uniform fin height design. *Int. J. Heat Mass Transf.*, 51:4788–4796, 2008.

[41] E. Galvis, B.A. Jubran, F. Xi, K. Behdinan, and Z. Fawaz. Numerical modeling of pin-fin micro heat exchangers. *Heat Mass Transf.*, 44:659–666, 2008.

[42] A.G. Kanaris, A.A. Mouza, and S.V. Paras. Optimal design of a plate heat exchanger with ondulated surfaces. *Int. J. Therm. Sci.*, 48:1184–1195, 2009.

[43] I. Tari and F.S. Yalcin. CFD analyses of a notebook computer thermal management system and a proposed passive cooling alternative. *IEEE Trans. Comp. Pack. Techonol.*, 33:443–452, 2010.

[44] J. Dong, J. Chen, W. Zhang, and J. Hu. Experimental and numerical investigation of a thermal-hydraulic performance in wavy fin-and-flat-tube heat exchangers. *Appl. Therm. Eng.*, 30:1377–1386, 2010.

[45] Y. Rao, Y. Xu, and C. Wan. An experimental and numerical study of flow and heat transfer in a channel with fin-dimple and pin-fin arrays. *Exp. Therm. Fluid Sci.*, 38:237–247, 2012.

[46] H. Peng, X. Ling, and J. Li. Numerical simulation and experimental verification on thermal performance of a novel fin-plate thermosyphon. *Appl. Therm. Eng.*, 40:181–188, 2012.

[47] W. Yaun, J. Zhao, C.P Tso, T. Wu, W. Liu, and T. Ming. Numerical simulation of the thermal hydraulic performance of a plate pin fin heat sink. .

[48] B.E. Short Jr, P.E. Raad, and D.C. Price. Performance of pin fin cast aluminum codwalls, Part 1: friction factor correlations. *J. Thermophys. Heat Transf.*, 16:389–396, 2002.

[49] B.E. Short Jr, P.E. Raad, and D.C. Price. Performance of pin fin cast aluminum codwalls, Part 2: Colburn j factor correlations. *J. Thermophys. Heat Transf.*, 16:397–403, 2005.

[50] COMSOL Mutiphysics 3.5a, 2008.

[51] A. Cavallin, S. Mancin, L. Rossetto, and C. Zilio. Experimental single phase air heat transfer through an aluminum metal foam. In *Proc. of 8th Gustav Lorentzen Conference on Natural Working Fluids*, Copenhagen, Denmark, 2008.

[52] W.M. Kays and A.L. London. *Compact Heat Exchangers, third ed.* Krieger Publishing Company, Malabar, FL, USA, 1997.

[53] ESDU Data Item 93018, Forced Convection Heat Transfer in Straight Tubes, Part. 2: Laminar and Transitional Flow, ESDU International Plc, Corsham St, London, 1993.

[54] W.S. Churchill. Comprehensive correlating equations for heat, mass and momentum transfer in fully developed flow in smooth tubes. *Ind. Chem. Fundam.*, 16:109–116, 1977.

[55] G.T. Polley and M.M. Abu-Khader. Interpreting and applting experimental data for plate-fin surfaces: problems with power law correlation. *Heat Transf. Eng.*, 26:15–21, 2005.

[56] H.H. Wu, Y.Y. Hsiao, H.S. Huang, P.H. Tang, and S.I. Chen. A practical plate-fin heat sink model. *Appl. Therm. Eng.*, 31:984–992, 2011.

[57] R.K. Shah and A.L. London. *Laminar Flow Forced Convection in Ducts.* Academic Press New York, 1978.

[58] W. Zhi-Qing. Study on correction coefficients of laminar and turbulent entrance region effect in round pipe. *Appl. Math. Mech.*, 3:433–446, 1982.

[59] Y.S. Muzychka and M.M. Yovanovich. Laminar flow friction and heat transfer in non-circular ducts and channels Part I-hydrodynamic problem. In *Proc. of Compact Heat Exchangers, at the 60th Birthday of Ramesh K. Shah*, pages 131–139, year=2002, Grenoble, France.

[60] V. Gnielinski. New equations for heat and mass transfer in tubulent pipe and channel flow. *Int. Chem. Eng.*, 16:359–368, 1976.

[61] R.K. Shah and D.P. Sekulic. *Fundamentals of Heat Exchangers.* John & Wiley Sons, 2003.

[62] Lord Kelvin (Sir William Thomson). On the Division of Space with Minimum Partitional Area. *Philosophical Magazine*, 24:121–134, 1887.

[63] R. Phelan, D. Weaire, and K. Brakke. Computation of Equilibrium Foam Structures Using the Surface Evolver. *Exp. Math.*, 4:181–191, 1995.

[64] K. Brakke. The Surface Evolver. *Exp. Math.*, 1:141–165, 1992.

[65] K. Boomsma, D. Poulikakos, and Y. Ventikos. Simulations of flow through open cell metal foams using an idealized periodic cell structure. *Int. J. Heat Fluid Flow*, 24:825–834, 2003.

[66] A. Kopanidis, A. Theodorakakos, E. Gavaises, and D. Bouris. 3D numerical simulation of flow and conjugate heat transfer through a pore scale model of high porosity open cell metal foam. *Int. J. Heat Mass Transf.*, 53:2539–2550, 2010.

[67] M. Bai and J. N. Chung. Analytical and numerical prediction of heat transfer and pressure drop in open-cell metal foams. *Int. J. Thermal Sci.*, 50:869–880, 2011.

[68] K.C. Leong and L.W. Jin. Effect of oscillatory frequency on heat transfer in metal foam heat sink of various pore densities. *Int. J. Heat Mass Transf.*, 49:671–681, 2006.

[69] Z. Wu, C. Caliot, G. Flamant, and Z. Wang. Numerical simulation of convective heat transfer between air flow and ceramic foams to optimise volumetric solar air receiver performances. *Int. J. Heat Mass Transf.*, 54:1527–1537, 2011.

[70] T. Hornber, C. Rauh, and A. Delgado. Fluid dynamic characterisation of porous solids in catalytic fixed-bed reactors. *Micropor. Mesopor. Mat.*, 154:170–174, 2012.

[71] Q. Yu and B.E. Thompson. A Unit Cube-Based Model for Heat Transfer and Fluid Flow in Porous Carbon Foam. *J. Heat Tranf.*, 128:352–360, 2006.

[72] S.A.M. Karimian and A.G. Straatman. CFD study of the hydraulic and thermal behevior of spherical-void-phase porous materials. *Int. J. Heat Fluid Flow*, 29:292–305, 2008.

[73] S. Krishnan, S.V: Garimella, and J.Y. Murthy. Simulation of Thermal Transport in Open-Cell Metal Foams: Effect of Periodic Unit-Cell Structure. *J. Heat Transf.*, 30:024503–1–5, 2008.

[74] S.R. Annapragada, J.Y. Murthy, and S.V. Garimella. Permeability and Thermal Transport in Compressed Open-Cell Foams. *Num. Heat Transf. Part B: Fundamentals*, 54:1–22, 2008.

[75] M.A. Dawson, J.T. Germaine, and L.J. Gibson. Permeability of Open-Cell Foams Under Compressive Strain. *Int. J. Solids Struct.*, 44:5133–5145, 2007.

[76] T. Fiedler. μ-CT-based finite element analysis on imperfections in open-celled metal foams: Mechanical properties. *Scripta Mater.*, 67:455–458, 2012.

[77] K.K. Bodla, Y.M. Murthy, and S.V. Garimella. Microtomography-based simulation of transport through open-cell metal foams. *Heat Transf. Part A*, 58:527–544, 2010.

[78] M.A.A. Mendes, S. Ray, and D. Trimis. A simple and efficient method for the evaluation of effective thermal conductivity of open-cell foam-like structures. *Int. J. Heat Mass Transf.*, 66:412–422, 2013.

[79] Simpleware Ltd., Exeter, United Kingdom.

[80] Ansys FLUENT 13, 2010.

[81] L.S. Tong and Y.S. Tang. *Boiling Heat Transfer and Two-Phase Flow*. Taylor & Francis, 1997.

[82] Y. Taitel and A.E. Dukler. A Model for Predicting Flow Regime Transitions in Horizontal and Near Horizontal Gas-Liquid Flow. *AIChE J.*, 22:47–55, 1976.

[83] J.G. Collier and J.R. Thome. *Convective boiling and condensation*. Oxford Science Pubblications, 1994.

[84] J.C. Chen. Correlation for boiling heat transfer to saturated liquids in convective flow. *Und. Chem. Process Des. Dev.*, 5:322–329, 1966.

[85] H.K. Forster and N. Zuber. Dynamics of vapour bubbles and boiling heat transfer. *AIChE J.*, 1:531–535, 1955.

[86] V. Khanikar, I. Mudawar, and T. Fisher. Effects of carbon nanotube coating on flow boiling in micro-channel. *Int.J. Heat Mass Transf.*, 52:3805–3817, 2009.

[87] N. Singh, V. Sathyamurthy, W. Peterson, J. Arendt, and D. Banerjee. Flow boiling enhancement on a horizontal heater using carbon nanotube coatings. *Int. J. Heat Fluid Flow*, 31:201–207, 2010.

[88] Y. Sun, L. Zhang, and X. Zhong. Subcooled flow boiling heat transfer from microporous surfaces in a small channel. *Int. J. Therm. Sci.*, 50:881–889, 2011.

[89] K.N. Rainey, G. Li, and S.M. You. FlowBoiling Heat Tranfer From Plain and Microporous Coated Surfaces in Subcoold FC-72. *J. Heat Tranf.*, 123:918–925, 2001.

[90] C.J. Kuo and Y.Peles. Local measurement of flow boiling in structured surface microchannel. *Int. J. Heat Mass Tranf.*, 50:4513–4526, 2007.

[91] C.Y. Zhao, W. Lu, and S.A. Tassou. Flow Boiling Heat Transfer in Horizontal Metal-Foam Tubes. *J. Heat Transf.*, 131:121002–1–8, 2009.

[92] Micro Motion ELITE Coriolis Flow and Density Meter, Product Data Sheet, Micro Motion, EMERSON.

[93] LabVIEW 2011, NI, National Instruments, 2009.

[94] Refprop 9.1, NIST, National Institute of Standard and Tecnologies, 2013.

[95] J. Xu, X. Ji, W. Zhang, and G. Liu. Pool boiling heat transfer of ultra-light copper foam with open cells. *Int. J. Multiphas. Flow*, 34:1008–1022, 34.

[96] W.T. Ji, Z.G. Qu, Z.Y. Li, J.F. Guo, D.C. Zhang, and W.Q. Tao. Pool boiling heat transfer of R134a on a single horizontal tube surfaces sintered with open-celled copper foam. *Int. J. Therm. Sci.*, 50:2248–2255, 2011.

[97] I. Pranoto, K.C. Leong, and L.W. Jin. The role of graphite foam pore structure on saturated pool boiling enhancement. *App. Therm. Eng.*, 42:163–172, 2012.

[98] Z.G. Xu and C.Y. Zhao. Pool boiling heat transfer of open-celled metal foams with V-shaped grooves for high pore densities. *Exp. Therm. Fluid Sci.*, 52:128–138, 2014.

[99] B. Madani, F. Topin, and L. Tadrist. Convective Boiling in Metallic Foam: Experimental Analysis of the Pressure Drop. *Fluid Dynam. Mat Proc.*, 6:351–367, 2010.

[100] B. Madani, L. Tadrist, and F. Topin. Experimental analysis of upward flow boiling heat transfer in a channel provided with copper metallic foam. *Appl. Therm. Eng.*, 52:336–344, 2013.

[101] H. Hu, Y. Zhu, H. Peng, G. Ding, and S. Sun. Effect of tube diameter on pressure drop characteristics of refrigerant-oil mixture flow boiling inside metal-foam filled tubes. *Appl. Therm. Eng.*, 62:433–443, 2014.

[102] L. Wojtan, T. Ursenbacher, and J.R. Thome. Investigation of flow boiling in horizontal tubes: Part I - A new diabatic two-phase flow pattern map. *Int. J. Heat Mass Transf.*, 48:2955–2969, 2005.

[103] K. Fujie, N. Itoh, H. Kimura, N. Nakayama, and T. Yanugidi. Heat transfer pipe, US Patent 4044797, assigned to Hitachi LTD, 1977.

[104] M.H. Yu, T.K. Lin, and C.C. Tseng. Heat transfer and flow pattern during two-phase flow boiling of R-a134a in horizontal smooth and microfin tubes. *Int. J. Refrig.*, 25:789–798, 2002.

[105] A. Padovan, D. Del Col, and L. Rossetto. Experimental study on flow boiling of R134a and R410A in a horizontal microfin tube at high saturation temperatures. *Appl. Therm. Eng.*, 31:3814–3826, 2011.

[106] L. Gao, T. Ono, and T. Honda. Pressure drops of CO2 and oil mixtures in horizontal smooth and micro-fin tube evaporators. In *International Congress of Refrigeration, ICR07-B1-1262*, Beijing, China, 2007.

[107] L. Gao, T. Honda, and S. Koyama. Experiments on Flow Boiling Heat Transfer of Almost Pure CO2 and CO2-Oil Mixtures in Horizontal Smooth and Microfin Tubes. *HVAC&R Research*, 13:415–425, 2007.

[108] C. Dang, N. Haraguchi, and E. Hihara. Flowboiling heat transfer of carbon dioxide inside a small-sized microfin tube. *Int. J. Refrig.*, 33:655–663, 2010.

[109] Z. Wu, Y. Wu, B. Sunden, and W. Li. Convective vaporization in micro-fin tubes of different geometries. *Exp. Therm. Fluid Sci.*, 44:398–408, 2013.

[110] C. Kondou, D. BaBa, F. Mishima, and S. Koyama. Flow boiling of non-azeotropic mixture R32/R1234ze(E) in horizontal microfin tube. *Int. J. Refrig.*, 36:2366–2378, 2013.

[111] S.Z. Rouhani and E. Axelsson. Calculation of void fraction in the subcooled and quality boiling region. *Int. J. Heat Mass Transf.*, 13:383–393, 1970.

[112] L. Doretti, C. Zilio, S. Mancin, and A. Cavallini. Condensation flow patterns inside plain and microfin tubes: A review. *Int. J. Refrig.*, 36:567–587, 2013.

[113] A. Cavallini, D. Del Col, S. Mancin, and L. Rossetto. Condensation of pure and near-azeotropic refrigerants in microfin tubes: A new computational procedure. *Int. J. Refrig.*, 32:162–174, 2009.

[114] A. Cavallini, D. Del Col, L. Doretti, G.A. Longo, and L. Rossetto. Pressure drop during condensation and vaporisation of refrigerants inside enhanced tubes. *Heat and Technology*, 15:3–10, 1997.

[115] D. Han and K.J. Lee. Experimental study on condensation heat transfer enhancement and pressure drop penalty factors in four microfin tubes. *Int. J. Heat Mass Transf.*, 48:3804–3816, 2005.

[116] H. Mori, S. Yoshida, K. Ohishi, and Y. Kakimoto. Dryout quality and post dryout heat transfer coefficient in horizontal evaporators tubes. In *Proc. of 3rd European Thermal Sciences Conference*, Heidelberg, Germany, 2000.

Nomenclature

Latin symbols

A_a	fin surface area [m^2]
A_{base}	base area [m^2]
A_c	fiber cross sectional area [m^2]
A_D	area of the smooth tube with the same inner diameter at the fin tip [m^2]
A_{front}	frontal area [m^2]
a_{sv}	total surface area per unit of volume [m^2 m^{-3}
A_{tot}	total area [m^2]
A_w	wetted area [m^2]
$c_{p,air}$	air specific heat at constant pressure [J kg^{-1} K^{-1}]
$c_{p,L}$	specific heat at constant pressure of the liquid phase [J kg^{-1} K^{-1}]
$c_{p,w}$	water specific heat at constant pressure [J kg^{-1} K^{-1}]
$c_{p,V}$	specific heat at constant pressure of the vapour phase [J kg^{-1} K^{-1}]
$C_{\varepsilon 1}$, $C_{\varepsilon 2}$, C_μ	model constants of equations 2.5 and 2.6 [-]
d	pin diameter [m]
d	diameter [m]
D	diameter [m]
d_f	fiber diameter [m]
D_h	hydraulic diameter [m]
d_p	pore diameter [m]
E_1, E_2	Ergun's constants [-]
e_{abs}	absolute deviation [%]
E_{RB}	enhancement factor [-]
e_{rel}	relative deviation [%]
f	inertia coefficient [-]
f	friction factor [-]
F	friction factor defined in equation 1.75 [-]
f_{app}	apparent friction factor [-]
F_K	friction factor based on the permeability defined in equation 1.79 [-]
Fr	Froude number [-]

g	acceleration due to gravity [m s^{-2}]
G	mass velocity [kg m^{-2} s^{-1}]
h	heat transfer coefficient [W m^{-2} K^{-1}]
H	sample height [m]
h	fin height [m]
HTC	heat transfer coefficient [W m^{-2} K^{-1}]
HTC_{SP}	single-phase heat transfer coefficient [W m^{-2} K^{-1}]
HTC_{TP}	two-phase heat transfer coefficient [W m^{-2} K^{-1}]
HTC^*	overall heat transfer coefficient [W m^{-2} K^{-1}]
h_{fc}	two-phase forced convection heat transfer coefficient [W m^{-2} K^{-1}]
h_L	saturated liquid enthalpy [J kg^{-1}]
h_{lv}	latent heat of vaporization [J kg^{-1}]
h_{NB}	nucleate boiling heat transfer coefficient [W m^{-2} K^{-1}]
$h_{ref,eva,in}$	refrigerant enthalpy at the inlet of the evaporator [J kg^{-1}]
$h_{ref,eva,out}$	refrigerant enthalpy at the outlet of the evaporator [J kg^{-1}]
$h_{ref,pc,in}$	refrigerant enthalpy at the inlet of the pre-condenser [J kg^{-1}]
$h_{ref,pc,out}$	refrigerant enthalpy at the outlet of the pre-condenser [J kg^{-1}]
h_{tp}	two-phase heat transfer coefficient [W m^{-2} K^{-1}]
$h_{TS,in}$	refrigerant enthalpy at the inlet of the test section [J kg^{-1}]
$h_{TS,out}$	refrigerant enthalpy at the outlet of the test section [J kg^{-1}]
h_V	saturated vapour enthalpy [J kg^{-1}]
h_{vs}	superheated vapour enthalpy [J kg^{-1}]
I	current [A]
ID	internal diameter [mm]
j	Colburn j-factor [-]
k	turbulent kinetic energy [m^2 s^{-2}]
K	permeability [m^2]
K_c	contraction coefficient [-]
K_e	expansion coefficient [-]
k_f	thermal conductivity of the foam material [W m^{-1} K^{-1}]
k_{tp}	thermal conductivity of the two-phase flow [W m^{-1} K^{-1}]
l	fiber thickness [mm]
L	length of the sample [m]
m	coefficient used to calculate the fiber efficiency [m^{-1}]
M	coefficient used to calculate the foam finned surface efficiency [m^{-1}]
$\dot{m}_{air}$	air mass flow rate [kg s^{-1}]
$\dot{m}_{ref}$	refrigerant mass flow rate [kg s^{-1}]
$\dot{m}_{w,eva}$	water mass flow rate in the evaporator [kg s^{-1}]
$\dot{m}_{w,pc}$	water mass flow rate in the pre-condenser [kg s^{-1}]

n	fin number [-]
$n_{tc,air,in}$	number of thermocouples at the air inlet section [-]
$n_{tc,air,out}$	number of thermocouples at the air outlet section [-]
Nu	Nusselt number [-]
OD	outer diameter [m]
p	pressure [Pa]
p	fin pitch [m]
P	fiber perimeter [m]
P_{EL}	electric power [W]
PPI	number of pores per linear inch [item in^{-1}]
Pr	Prandtl number [-]
$\mathrm{Pr_L}$	Prandtl number of the liquid phase [-]
p_{red}	reduced pressure [-]
$\mathrm{Pr_{tp}}$	Prandtl number of the two-phase flow [-]
$\mathrm{Pr_V}$	Prandtl number of the vapour phase [-]
$p_{sat,in}$	inlet saturation pressure [°C]
$p_{sat,out}$	outlet saturation pressure [°C]
Re	Reynolds number [-]
$\mathrm{Re_{tp}}$	Reynolds number of the two-phase flow [-]
$\mathrm{Re_d}$	Reynolds number based on the pin diameter [-]
$\mathrm{Re_L}$	Reynolds number based on the liquid phase [-]
R_S	shunt resistance [Ω]
q	heat flux [W m^{-2}]
q_{loss}	heat losses [W]
$q_{ref,eva}$	heat flow rate exchanged in the evaporator from the refrigerant side [W]
$q_{ref,pc}$	heat flow rate exchanged in the pre-condenser from the refrigerant side [W]
q_{TS}	heat flow rate exchanged in the test section [W]
$q_{w,eva,tc}$	heat flow rate exchanged in the evaporator from the water side measured with thermocouples [W]
$q_{w,eva,tp}$	heat flow rate exchanged in the evaporator from the water side measured with thermopile [W]
$q_{w,pc,tc}$	heat flow rate exchanged in the pre-condenser from the water side measured with thermocouples [W]
$q_{w,pc,tp}$	heat flow rate exchanged in the pre-condenser from the water side measured with thermopile [W]
q_y	heat flux along the $y-$direction [W m^{-2}]
q_z	heat flux along the $z-$direction [W m^{-2}]
S	cross section area [m^2]
S	streamwise pin spacing [m]

S	nucleate boiling correction factor [-]
t	fiber thickness [m]
t	fin thickness [m]
T	spanwise pin spacing [m]
$\bar{t}_{air}$	mean air temperature [°C]
$t_{air,in}$	air inlet temperature [°C]
$t_{air,out}$	air outlet temperature [°C]
$t_{ref,in}$	refrigerant temperature at the inlet of the test section [°C]
$t_{ref,out}$	refrigerant temperature at the outlet of the test section [°C]
$\bar{t}_s$	mean saturation temperature [°C]
$t_{sat,in}$	inlet saturation temperature [°C]
$t_{sat,out}$	outlet saturation temperature [°C]
T_x	temperature at the $x-$ coordinate [°C]
t_w	wall temperature [°C]
$\bar{t}_w$	mean wall temperature [°C]
$t_{w,eva,in}$	water temperature at the inlet of the evaporator [°C]
$t_{w,eva,out}$	water temperature at the outlet of the evaporator [°C]
$t_{w,in}$	wall inlet temperature [°C]
$T_{w,mean}$	mean wall temperature [°C]
$t_{w,out}$	wall outlet temperature [°C]
$t_{w,pc,in}$	water temperature at the inlet of the pre-condenser [°C]
$t_{w,pc,out}$	water temperature at the outlet of the pre-condenser [°C]
T_∞	core fluid temperature [°C]
u	velocity [m s^{-1}]
u_{max}	maximum air velocity referred to the minimum cross sectional area [m s^{-1}]
u_i	velocity in the i-direction [m s^{-1}]
u_{in}	inlet velocity [m s^{-1}]
u_j	velocity in the j-direction [m s^{-1}]
V	volume [m^3]
$\dot{V}$	volumetric flow rate [m^3 s^{-1}]
V_{flow}	volume of the air flow [m^3]
V_R	tension measured across the heating element [V]
V_S	tension measured across the shunt [V]
V_{SL}	superficial velocity of the liquid phase [m s^{-1}]
V_{SV}	superficial velocity of the vapour phase [m s^{-1}]
x	coordinate [m]
x	quality [-]
x_{in}	quality at the inlet of the test section [-]
x_{out}	quality at the outlet of the test section [-]

X_{tt}	Martinelli parameter [-]
W	weight [kg]
W	width [m]
z	coordinate [m]
z	coefficient of equation 1.79 [-]

Greek symbols

α	heat transfer coefficient [W m^{-2} K^{-1}]
$\alpha_{numerical}$	numerical heat transfer coefficient [W m^{-2} K^{-1}]
α^*	interstitial heat transfer coefficient [W m^{-2} K^{-1}]
β	helix angle [°]
γ	apex angle [°]
Δp	pressure drop [Pa]
Δp_{app}	apparent pressure drop [Pa]
Δp_c	contraction pressure drop [Pa]
Δp_e	expansion pressure drop [Pa]
Δp_{tot}	total pressure drop [Pa]
ΔT_{ml}	logarithmic mean temperature difference [K]
ΔT_{sat}	difference between wall and saturation temperature [K]
$\Delta T_{w,eva}$	water temperature difference in the evaporator [K]
$\Delta T_{w,pc}$	water temperature difference in the pre-condenser [K]
ε	porosity [-]
$\eta_{1/2}$	efficiency of half strut [-]
θ	angle [°]
λ_{air}	air thermal conductivity [W m^{-1} K^{-1}]
λ_{mat}	thermal conductivity of the foam material [W m^{-1} K^{-1}]
μ	dynamic viscosity [Pa s]
μ_{air}	air dynamic viscosity [Pa s]
μ_L	dynamic viscosity of the liquid phase [Pa s]
μ_t	eddy viscosity [Pa s]
μ_V	dynamic viscosity of the vapour phase [Pa s]
ρ	density [kg m^{-3}]
ρ_{air}	air density [kg m^{-3}]
ρ_L	density of the liquid phase [kg m^{-3}]
ρ_s	density of the material of the foam [kg m^{-3}]
ρ_V	density of the vapour phase [kg m^{-3}]
ρ^*	density of the foam [kg m^{-3}]
σ	core free-flow to frontal-area ratio [-]
σ	surface tension [N m^{-1}]

σ_N	standard deviation [%]
σ_ε, σ_k	model constants of equation 2.4 and 2.5 [-]
Ω	efficiency [-]
Ω^*	finned surface efficiency [-]

List of Figures

List of Tables

List of publications and research activity

Paper on journal with impact factor

- S. Mancin, C. Zilio, A. Diani, L. Rossetto, Air forced convection through metal foams: Experimental results and modeling, Int. J. Heat Mass Transf. 62 (2013) 112-123.
- A. Diani, S. Mancin, C. Zilio, L. Rossetto, An assessment on air forced convection on extended surfaces: Experimental results and numerical modeling, Int. J. Therm. Sci. 67 (2013) 120-134.
- S. Mancin, C. Zilio, A. Diani, L. Rossetto, Experimental air heat transfer and pressure drop through copper foams, Exp. Therm. Fluid Sci. 36 (2012) 224-232.
- A. Diani, S. Mancin, C. Zilio, L. Rossetto, Experimental and numerical analyses of different extended surfaces, J. Phys. Conference Series 395 (2012) 012045-1-8, 6th European Thermal Sciences Conference, Eurotherm 2012, Poitiers, France.

Paper on journal without impact factor

- S. Mancin, C. Zilio, A. Diani, L. Rossetto, Material and height effects on the heat transfer performance of metal foams cooled by air in forced convection, AIP CONFERENCE PROCEEDINGS 1453 (2012) 231-236, Fourth International Conference on Porous Media and its Applications in Science, Engineering and Industries, Potsdam, Germany.

Conference paper with peer-review

- A. Diani, K.K. Bodla, L. Rossetto, S.V. Garimella, Numerical analysis of air flow through metal foams, 68th Conference of the Italian Thermal Machines Engineering Association, ATI 2013, 2013, Bologna, Italy.
- S. Mancin, A. Diani. L. Rossetto, R134a flow boiling heat transfer and pressure drop inside a 3.4 mm ID microfin tube, 68th Conference of the Italian Thermal Machines Engineering Association, ATI 2013, 2013, Bologna, Italy.
- S. Mancin, A. Diani, L. Doretti, L. Rossetto, Liquid and Flow Boiling Heat Transfer Inside a 5 PPI Copper Foam, 8th International Conference on Porous Metals and Metallic Foams, 2013, Rayleigh, NC, USA.
- A. Diani, S. Mancin, L. Rossetto, Experimental analysis of R134a flow boiling inside a 5 PPI copper foam, 31st UIT National Heat Transfer Conference, 2013, Como, Italy.
- A. Diani, S. Mancin, L. Doretti, L. Rossetto, R134a flow boiling inside a high porosity copper foam, Fourth IIR Conference on Thermophysical Properties and Transfer Processes of Refrigerants, 2013, Delft, Netherlands.
- C. Zilio, S. Mancin, A. Diani, L. Rossetto, Aluminum foams as possible extended surfaces for air cooled condenser, 23rd IIR International Congress of Refrigeration, 2011, Prague, Czech Republic.

Conference paper without peer-review

- S. Mancin, A. Diani, L. Doretti, L. Rossetto, Flow boiling in rectangular channel filled with high porosity copper foam: heat transfer measurements and two-phase visualizations, Eighth International Topic Team Workshop on TWO-PHASE SYSTEMS FOR GROUND AND SPACE APPLICATIONS, 2013, Bremen, Germany.
- S. Mancin, A. Diani, C. Zilio, L. Rossetto, Experimental Measurements of R134a Flow Boiling Inside a 3.4 mm ID Microfin Tube, 13th UK Heat Transfer Conference, UKHTC 2013, 2013, London, Great Britain.

- A. Diani, S. Mancin, C. Zilio, L. Rossetto, Experimental measurements of air forced convection through copper foams, International Refrigeration and Air Conditioning Conference, 2012, Purdue University, West Lafayette, IN, USA.
- C. Zilio, S. Mancin, A. Diani, L. Rossetto, Aluminum foams vs conventional extended surfaces for air cooled condensers, 66th Conference of the Italian Thermal Machines Engineering Association, ATI 2011, 2011, Rende (Cosenza), Italy.
- A. Diani, C. Zilio, S. Mancin, L. Rossetto, Experimental and numerical analysis of a finned surface, 29th National Heat Transfer Conference, 2011, Torino, Italy.

During my PhD program, I carried out an experimental campaign in order to study the air forced convection through metal foams. I tested copper foams with different geometrical characteristics (core height, linear density, and porosity). A total amount of approximately 250 experimental measurements of overall heat transfer coefficient and pressure drop were collected, and they permitted to highlight how each geometrical parameter affects the thermal and hydraulic behaviour of such materials. These measurements, coupled these other experimental measurements previously obtained, permitted to validate semi-empirical correlations for the estimation of the overall heat transfer coefficient and pressure drop. In addition, I developed a new correlation to estimate the overall heat transfer coefficient, which can be used to simulate the heat transfer behavior of metal foams as a function of the different geometrical characteristics and under different operating conditions.

I numerically studied the air flow through extended surfaces. First of all, the numerical model was validated against experimental values of heat transfer coefficients and pressure drops during air flow on a reference trapezoidal finned surface. Once validated, the numerical simulations were extended to plain finned and pin fin surfaces, having different geometrical characteristics, such as fin thickness, fin pitch, and fin height for the plain fins, or pin diameter, longitudinal and transversal pitch, and pin height for the pin fin surfaces, in order to highlight the effects of these geometrical parameters on the hydraulic and thermal performance. A total amount of 108 and 51 simulations were performed in the case of plain finned and pin fin surfaces, respectively. In addition, based on the results of the numerical simulations,

I proposed four new equations to estimate the friction factor and Nusselt number during air forced convection through plain finned and pin fin surfaces.

During my period as visiting scholar at the Purdue University, I numerically studied the air forced convection through metal foams. Four experimentally tested copper foams were cut and scanned with a μCT scanner, at a resolution of 20 μm. I reconstructed the real structure of these samples with a commercial software, which also permitted to create mesh for the following numerical analysis. Therefore, the hydraulic and thermal behaviour was simulated, and the numerical results of pressure gradient and heat transfer coefficient were compared with experimental and semi-empirical results.

In addition, I developed a new test section to study the forced convection and flow boiling of refrigerants in microstructured surfaces. The test section was thought to host a metal foam, which is 200 mm long, 10 mm wide, and 5 mm high. I also participated in the design and development of a new experimental facility, which permits either condensation or flow boiling heat transfer measurements to be performed. Once the facility was completed, I run experiments in order to verify the heat balance at the different heat exchangers of the facility. After the testing phase, I started an experimental campaign aimed at studying both the liquid forced convection and the flow boiling phenomenon inside microstructured surfaces. A metal foam with 5 PPI and a porosity of 0.93 was tested during liquid forced convection and flow boiling of refrigerants (R134a, R1234ze(E), and R134a). Single and two-phase heat transfer coefficients and pressure drops were collected. I collected approximately 200 experimental data points, trying to explain the effects of the working conditions (vapour quality, mass velocity, and heat flux) on the thermal and hydraulic behaviour. I also tested a 3.4 mm ID microfin tube during flow boiling of different refrigerants (R134a, R1234ze(E), and R1234yf). Approximately 500 experimental data points were collected under different working conditions (vapour quality, mass velocity, and heat flux) to explain their effects on the heat transfer coefficients, pressure drops, and vapour qualities at the onset of the dryout. This database also permitted to verify empirical correlations to estimate the heat transfer coefficients, pressure drops and vapour qualities at the onset of the dryout.

Acknowledgments

There are a lot of people that I would like to acknowledge. First of all, many thanks to my advisor Prof. Luisa Rossetto, for all of her support during these three years of PhD. Thanks to Simone, for everyday company and for his help. Thanks to Luca Doretti, and also thanks to Claudio Zilio. Thanks to all the ex DFT, from the ground floor to the third floor. Working with all of you has been a fun.

Thanks to Prof. Suresh V. Garimella for hosting me at CTRC labs, and thanks to Karthik and Justin for the support you gave me during my period at Purdue, I spent 4 very useful months.

Thanks to all the guys that completed their Ms thesis period in the lab, among whom I would like to remember Riccardo, Giulia, Michele, Alessandro S., Roberto, Filippo, thanks for your help and company. And also thanks to our visiting student, Tiemi.

The financial support of the European project ICE-E, of the PRIN Project 2009TSYPM7_003, and of the European project POA are very acknowledged.

Finally, the last but the most important, thanks to family, to my grandmother, my parents, Renato, Cristina, and Pancho.